From Tectonic Evolution to Intraplate Stress: The Role of Structural Inheritance and Long-Wavelength Loading

Thesis by

Erin J. Hightower

In Partial Fulfillment of the Requirements for the
Degree of
Doctor of Philosophy

CALIFORNIA INSTITUTE OF TECHNOLOGY
Pasadena, California

2024
Defended October 20th, 2023

ACKNOWLEDGEMENTS

This thesis is the result of a long, hard road and would not have been possible without the wonderful support and guidance of many people. Ultimately, getting a PhD is not just becoming an expert in a particular topic, but it is also becoming an expert in yourself. I would first like to thank my thesis advisor, Mike Gurnis. During one of my undergraduate courses in geology, we read one of Mike's papers on geodynamics and epeirogenic uplift and subsidence, and I began to wonder whether such processes, specifically mantle flow from the sinking Farallon slab, might influence earthquakes in eastern North America. I kept this idea tucked in my back pocket as a potential PhD thesis topic, and when I was applying to graduate schools, I reached out to Mike with my idea. Not expecting to get much of a reply from this professor at Caltech, I was surprised and delighted to receive a long, detailed, and enthusiastic email from Mike about my proposition, in which he encouraged me to apply. And lo-and-behold, here I am today with this finished thesis on that very topic. So, thank you Mike for taking on this project and for taking me on as a student. Thank you also for the opportunity to work on the SISIE project and to participate in the seismic cruise my first year. I have learned so much from you over my time at Caltech: how to be a good scientist, how to approach a project, how to do geodynamic modeling, and how to trust my own instincts. I am a stronger and wiser person today because of this experience.

I would also like to thank my committee members, who have provided valuable support and feedback over the course of completing this thesis. To my academic advisor Joann, thank you for your kindness and guidance over the years. I always enjoy talking with you and appreciate your moral support and detailed feedback. To Mark Simons, thank you for the helpful discussions and for your candor and advice on matters relating to my thesis and to JPL. I find that you provide great scientific intuition and have always given very straightforward and useful advice. To Zach Ross, thank you for your insight and input to my thesis, particularly in regards to Chapter 3. And finally, to Mike Watkins, thank you for your support during the last year of my PhD and for the opportunity to work on the GIA and GRACE project with the folks at JPL. A very sincere thank you also to Jean-Philippe Avouac, who advised me on my second quals project and the work that makes up Chapter 3 of my thesis. I enjoyed getting to work with you on that project and greatly appreciate your counsel, your kindness, and your patience as an advisor.

I would also like to give a very special thank you to Wei Mao, a postdoc in Mike's group during my time here. Wei has devoted countless hours to helping me learn how to use CitcomS, to debugging problems in the code, and to implementing new features within CitcomS that have been critical to the success of this work. I could not have done it without him. Thank you also to the Seismo Fam and the Seismo Lab staff, all of whom make it such a joy to come into work every day, and in particular to my many office mates over the years. A special thank you to Ojashvi Rautela, who has been a dear friend and empathetic support over the past several years.

Thank you also to the team at JPL — Lambert Caron, Eric Larour, and Erik Ivins — with whom I have had the opportunity to work over the last year of my PhD and with whom I will be working in my post-graduate work at JPL. I have learned so much from you all about GIA, ice-sheet modeling, numerical modeling, NASA, and so much more; I look forward to working with you all further in the future.

Thank you as well to numerous sources of support for and collaboration in my research over the years. Thank you to Harm van Avendonk, Sean Gulick, and Brandon Shuck at the University of Texas and to Rupert Sutherland at University of Wellington, New Zealand for their collaboration and leadership in the SISIE project and for their insight and contributions to my work in that project. Thank you to the National Science Foundation for supporting me through the NSF Graduate Research Fellowship. Thank you to the Texas Advanced Computing Center and Purdue University for providing the supercomputing resources needed to conduct this research, and thank you to Computational Infrastructure for Geodynamics for providing me with an additional computing allocation in the last several months of my PhD that was integral to being able to perform some final calculations.

An immense thank you goes out to my family and my partner. To my mom and dad, who have been there every step of the way and who have believed in me no matter what, you both are my rock and I would not have been able to do this without you. To my partner, Bek, you have been a constant source of support and positivity as I have navigated my PhD, and I cannot thank you enough for all of your patience, calmness, clarity, and kindness.

And finally, I would like to acknowledge and thank myself, for daring to embark on this challenging journey and for not giving up.

ABSTRACT

In this thesis, I present a multifaceted exploration of various aspects of deformation and stress in the Earth's lithosphere using a variety of methods in a range of tectonic environments. I begin by examining the evolution of a young subduction zone through a combination of gravity modeling and seismological observations. Chapter 2 details the development a linear 3-D gravity inversion method capable of modelling complex geological regions such as subduction margins. Our procedure inverts satellite gravity to determine the best-fitting differential densities of spatially discretized subsurface prisms in a least-squares sense. We use a Bayesian approach to incorporate both data error and prior constraints based on seismic reflection and refraction data. Based on these data, Gaussian priors are applied to the appropriate model parameters as absolute equality constraints. To stabilize the inversion and provide relative equality constraints on the parameters, we utilize a combination of first and second order Tikhonov regularization, which enforces smoothness in the horizontal direction between seismically constrained regions, while allowing for sharper contacts in the vertical. We apply this method to the nascent Puysegur Trench, south of New Zealand, where oceanic lithosphere of the Australian Plate has under-thrust Puysegur Ridge and Solander Basin on the Pacific Plate since the Miocene. These models provide insight into the density contrasts, Moho depth, and crustal thickness in the region. The final model has a mean standard deviation on the model parameters of about 17 kg/m^{-3}, and a mean absolute error on the predicted gravity of about 3.9 mGal, demonstrating the success of this method for even complex density distributions like those present at subduction zones. The posterior density distribution versus seismic velocity is diagnostic of compositional and structural changes and shows a thin sliver of oceanic crust emplaced between the nascent thrust and the strike slip Puysegur Fault. However, the northern end of the Puysegur Ridge, at the Snares Zone, is predominantly buoyant continental crust, despite its subsidence with respect to the rest of the ridge. These features highlight the mechanical changes unfolding during subduction initiation.

Chapter 3 explores the earthquake interevent time distribution. Earthquakes are commonly assumed to result from a stationary Poisson (SIP) process. We reassess the validity of this assumption using the Quake Template Matching (QTM) catalog and the relocated SCSN catalog (HYS) for Southern California. We analyze the interevent time (IET) distribution and the Schuster spectra after declustering with

the Zaliapin and Ben-Zion (2013) method. Both catalogs exhibit fat-tails on the IET distribution, deviating from the expected exponential distribution. The Schuster spectra of the catalogs are also inconsistent with an SIP process. The QTM catalog shows a statistically significant seasonal signal and a drift in the Schuster probability at long periods, likely due to increased seismicity following the 2010 El Mayor-Cucapah earthquake. This increase is also evident in the yearly IET distributions of the catalog. In contrast, the HYS Schuster spectrum does not show seasonality, but the yearly IET distributions exhibit a decrease in seismicity rate over the duration of the catalog, likely due to seismic network upgrades around 1990. We use synthetic catalogs to test the origin and significance of the observed deviations from the Poisson model. Variations in the QTM annual seismicity rate, around 5.6%, are too small to generate a noticeable departure from an exponential distribution, and the SIP model can not be rejected at the 5% significance level. The synthetic catalogs also suggest the fat-tail is an artefact of incomplete declustering. Overall, variations in the IET distribution for southern California are probably the result of both 1) incomplete declustering and location uncertainty, and 2) transient non-stationarity of the background rate from viscoelastic effects of large earthquakes. However, the stationary Poisson model appears adequate for describing background seismicity at the scale of Southern California and the decadal time scale of the QTM catalog.

Chapters 4 and 5 cover the primary focus of this thesis, exploring the influence of long-wavelength loading on the stress field of continental interiors and intraplate seismicity. The continental interior of eastern North America in particular has hosted many significant historical earthquakes and is undergoing both glacial isostatic adjustment (GIA) and long-wavelength subsidence due to the sinking of the Farallon slab. The regional seismicity concentrates within ancient failed rift arms and other paleo-tectonic structures, which can act as weak zones in the crust where stress accumulates. Within some of these zones, focal mechanism stress inversion shows significant rotational deviation of the maximum horizontal stress (S_{Hmax}) direction from the regional NE-SW trend, which may be explained by long-wavelength stress perturbations in the presence of lithospheric weakness. We focus on two sources of intraplate stress perturbation and seismicity and test the hypotheses that 1) mantle-flow induced epeirogenic subsidence and 2) GIA contribute to intraplate seismicity in eastern North America via reactivation of pre-existing faults.

For the slab loading component of this work, we use high-resolution global, spherical finite-element flow models with CitcomS. To capture realistic temperature fields and

the Farallon slab, we convert seismic tomography models to temperature using a mineralogically constrained depth-dependent scaling factor. We utilize laterally variable temperature-dependent viscosities, upon which we superimpose low-viscosity plate boundary weak zones, as well as lithospheric intraplate weak zones at the locations of failed rifts and other inherited structures in eastern North America. We parameterize the Farallon slab in terms of its buoyancy to determine the degree to which the flow induced by the sinking slab contributes to intraplate stress. Using the modeled stress tensors from instantaneous flow calculations, we compute S_{Hmax}, the stress magnitudes, and the Coulomb failure stress on mapped faults in several major seismic zones. Slab sinking drives localized mantle flow beneath the central-eastern U.S., leading to a stress amplification of 100-150 MPa across the region that peaks over the New Madrid Seismic Zone. This stress amplification introduces a pronounced continent-wide clockwise rotation of the predicted S_{Hmax} direction, reaching as much as ~20° in some seismic zones, particularly when lithospheric weak zones are included. In the New Madrid, Central Virginia, Charlevoix, and Lower Saint Lawrence Seismic Zones, the presence of weak zones loaded by the Farallon slab at depth can explain the pattern of clockwise rotation of the observed focal mechanism derived S_{Hmax} relative to the regional borehole derived S_{Hmax} as reported in previous studies. However, misfits on S_{Hmax} within many of the major seismic zones suggest other sources of stress are needed to properly reproduce the observed stress trends in some areas. We also find that in order for pre-existing lithospheric weak zones to exert appreciable control on intraplate stress under the influence of mantle flow, they must be shallow/sub-crustal and in contact with the crust. These stress perturbations and rotations ultimately bring faults in the NMSZ, the Western Quebec Seismic Zone (WQSZ), and the Lower Saint Lawrence and Charlevoix Seismic Zones closer to failure. In particular, inclusion of the Farallon slab and weak zones produces positive Coulomb failure stresses on some key faults associated with major historical earthquakes, including the Reelfoot Fault in the NMSZ and the Timiskaming fault in the WQSZ. Fault instability is even more likely when assuming weaker faults with lower coefficients of friction.

For the glacial unloading component of this work, we use the global, spherical finite element code CitcomSVE, which models dynamic deformation of a viscoelastic and incompressible planetary mantle in response to surface loading. We supply CitcomSVE with the same seismically constrained viscosity structures computed in the CitcomS models, including those with weak zones, and load the Earth model with the ICE-6G ice history. We perform the same suite of simulations and stress analyses as in the mantle loading problem, using the stress tensor output of the corresponding CitcomS model as the tectonic background stress. We compare the mantle flow and GIA induced stresses, with focus on the present day extant glacially derived stress field. GIA induced stress perturbations are small (~10 MPa), even in the presence of lithospheric weak zones. GIA induced S_{Hmax} alone exhibits a transition from clockwise to counterclockwise rotation moving northeast across the continent. We find that only by inclusion of the mantle flow derived background stress can we reproduce the continental scale clockwise stress rotation observed in stress data, suggesting the effect of mantle loading is more important for explaining these observations than is GIA. In the NMSZ, GIA helps promote stability on the Reelfoot Fault, in opposition to mantle flow, while promoting instability on more non-optimally oriented faults. GIA also helps localize higher Coulomb failure stress within the Charlevoix Seismic Zone and the western half of the WQSZ. In the WQSZ and LSLRS, GIA stress perturbations are large enough that even with only a small reduction in the coefficient of friction, faults that are not likely to fail under the background tectonic and geodynamic stresses alone could slip. Further investigation of the sensitivity of GIA stress to different 3D and 1D viscosity structures and the change in GIA stress with time since deglaciation is warranted to better understand how GIA affects intraplate seismicity. Ultimately, constraining how mantle flow and GIA affect stress and deformation in the presence of laterally variable viscosity is integral to quantifying how long-wavelength loading may alter the spatial distribution of seismic hazard.

PUBLISHED CONTENT AND CONTRIBUTIONS

Hightower, E., Gurnis, M. and Mao, W. "Influence of Farallon Slab Loading on Intraplate Stress and Seismicity in Eastern North America in the Presence of Pre-existing Weak Zones". [Submitted].

E.H. conceptualized the project, performed the data analysis and preparation of model inputs, ran the model calculations using computer allocations provided by M.G., analyzed the results, and wrote the manuscript under the supervision of M.G., with contributions and modifications to the CitcomS code from W.M.

Shuck, B., S. P. Gulick, H. J. Van Avendonk, M. Gurnis, R. Sutherland, J. Stock, and **Hightower, E.** (2022). “Stress transition from horizontal to vertical forces during subduction initiation”. In: *Nature Geoscience* 15.2, pp. 149–155. DOI: https://doi.org/10.1038/s41561-021-00880-4.

E.H. participated in discussions on the paper, helped review and edit the manuscript, and contributed text and information on the gravity data as it relates to Fig. 3.

Hightower, E. (2021). *BayGrav3D*. Version 1.0. CaltechDATA. DOI: https://doi.org/10.22002/D1.2059.

E.H. wrote BayGrav3D and its documentation, performed testing of the code with both simple benchmark cases and more complex geometries, and applied it to the Puysegur Subduction Zone under supervision of M.G.

Hightower, E., M. Gurnis, and H. van Avendonk (2020). “A Bayesian 3D Linear Gravity Inversion for Complex Density Distributions: Application to the Puysegur Subduction System”. In: *Geophysical Journal International* 223, pp. 1899–1918. DOI: 10.1093/gji/ggaa425.

E.H. wrote the gravity inversion software; performed the data processing, modeling, and analysis; and wrote the manuscript under supervision of M.G. and with contributions from H.V.A. to the seismic velocity models.

Gurnis, M., H. Van Avendonk, S. P. Gulick, J. Stock, R. Sutherland, **Hightower, E.**, B. Shuck, J. Patel, E. Williams, D. Kardell, E. Herzig, B. Idini, K. Graham, J. Estep, and L. Carrington (2019). “Incipient subduction at the contact with stretched continental crust: The Puysegur Trench”. In: *Earth and Planetary Science Letters* 520.1, pp. 212–219. DOI: 10.1016/j.epsl.2019.05.044.

E.H. contributed to writing and editing the manuscript and participated in the shipboard operations and data processing for the South Island Subduction Initiation Experiment (SISIE) aboard the Marcus G. Langseth, which this paper summarizes.

TABLE OF CONTENTS

LIST OF ILLUSTRATIONS

LIST OF TABLES

Chapter 1

INTRODUCTION

**Portions of the material described or presented in this chapter were previously published in:*

Gurnis, M., H. Van Avendonk, S. P. Gulick, J. Stock, R. Sutherland, **Hightower, E.**, B. Shuck, J. Patel, E. Williams, D. Kardell, E. Herzig, B. Idini, K. Graham, J. Estep, and L. Carrington (2019). "Incipient subduction at the contact with stretched continental crust: The Puysegur Trench". In: *Earth and Planetary Science Letters* 520.1, pp. 212–219. DOI: 10.1016/j.epsl.2019.05.044.

Hightower, E., M. Gurnis, and H. van Avendonk (2020). "A Bayesian 3D Linear Gravity Inversion for Complex Density Distributions: Application to the Puysegur Subduction System". In: *Geophysical Journal International* 223, pp. 1899–1918. DOI: 10.1093/gji/ggaa425.

Shuck, B., S. P. Gulick, H. J. Van Avendonk, M. Gurnis, R. Sutherland, J. Stock, and **Hightower, E.** (2022). "Stress transition from horizontal to vertical forces during subduction initiation". In: *Nature Geoscience* 15.2, pp. 149–155. DOI: https://doi.org/10.1038/s41561-021-00880-4.

Understanding the structure and deformation of the Earth's lithosphere across different temporal and spatial scales is critical to understanding a wide range of geological phenomena, from the formation of new tectonic plate boundaries to earthquakes to past and future sea-level rise. Lithospheric deformation is a product of the state of stress within the lithosphere. This state of stress results from a combination of far-field tectonic forcing (i.e., ridge push-slab pull), mantle flow, and lithospheric buoyancy forces arising from lateral variations in density, crustal thickness, and topography (Zoback and Zoback, 2007). To first order, the lithospheric stress field is uniform with depth and over broad length scales of up to thousands of kilometers (Zoback and Zoback, 2007). Such coherent stress patterns can be interpreted with respect to long-wavelength lithospheric processes and reflect the balance of forces operating on and within plates and driving plate motions. However, superimposed upon these first order stress provinces are smaller scale stress patterns resulting from local geological or tectonic conditions, such as lithospheric flexure under surface loading, lateral strength variations, or density contrasts (Zoback and Zoback, 2007). In fact, lithospheric heterogeneity can be as important as plate driving forces in governing the stress state within tectonic plates (Humphreys and Coblentz, 2007), and in particular, pre-existing lithospheric or crustal weaknesses play an important role in governing both active tectonic and intraplate deformation and stress. Ultimately, it is the stress, via its magnitude and orientation, that determines the type of deformation and the style of faulting observed within the lithosphere. An understanding of the state, sources, and evolution of lithospheric stress is thus an informative tool by which we can both better assess earthquake hazard and garner a comprehensive understanding of tectonic processes. In this thesis, I present a multifaceted exploration of various aspects of deformation and stress in the Earth's lithosphere using a variety of methods in a range of tectonic environments, from nascent plate boundaries just being born to the ancient cratons of continental interiors.

I begin by examining the evolution of a nascent subduction zone through a combination of gravity modeling and seismological observations. Because the balance of forces on plates is altered by the formation of new subduction zones, understanding the process of subduction initiation is key to characterizing the dynamics of plate motions and the forces that drive and resist those motions. Of particular interest are the state of stress operating throughout the initiation process, which is typically poorly recorded in well-developed arcs, and the material properties of the plate interface and adjacent plates that enable subduction initiation (Gurnis et al., 2019). The transition from forced to self-sustaining subduction, when the negative buoyancy of the downgoing oceanic plate exceeds the resistive force associated with fault friction and plate bending (Toth and Gurnis, 1998), has also been a major unknown in past studies of subduction initiation. To address these questions, I collaborated with a team to investigate the Puysegur Subduction Zone south of New Zealand — a young subduction margin at the intermediate stage of transitioning to a self-sustaining state (Gurnis et al., 2019). Different sections of the Puysegur margin are theorized to represent forced and self-sustaining stages of subduction, but prior to our work, adequate seismic reflection and modeling of the crustal structure did not yet exist for this region. Puysegur has the advantage of being a small subduction zone with a well known plate kinematic history before and during subduction initiation, making it accessible for studying the initiation process and for constructing a regional gravity inverse model at a relatively high resolution.

The Puysegur-Fiordland subduction zone lies between the northern end of the Macquarie Ridge Complex (MRC) and the southern tip of South Island, New Zealand. Present day plate motion is predominantly dextral strike-slip, with highly oblique subduction of the Australian Plate (AUS) northeastwards beneath the Pacific Plate (PAC) at the Puysegur Ridge and Fiordland (Figure 2.3a; DeMets et al. (2010) and Sutherland (1995)). Over the course of its evolution, the Puysegur margin has evolved from spreading ridge to strike-slip plate boundary to subduction zone (Lebrun et al., 2003; Sutherland, 1995), evidenced by the curvilinear fracture zones that merge along the MRC and are prominent in the gravity field and bathymetry. Oblique convergence led to subduction beneath Fiordland starting around 16-10 Ma, beneath the northern extent of the Puysegur segment about 11-8 Ma, and beneath the southernmost extent of the Puysegur Ridge within the last several million years (Sutherland et al., 2006; Lebrun et al., 2003). Puysegur Ridge possesses distinctive, high amplitude gravity anomalies, which prior to this work had poorly constrained structural and compositional interpretations and which have implications for the dynamic processes and mechanical changes unfolding during subduction initiation. The MRC is characterized by long and narrow bathymetric and gravitational highs and lows along strike (Figure 2.3b). The southern part of Puysegur Ridge exhibits a 100 to 150 mGal gravity high adjacent to the -100 to -150 mGal gravity low of the trench. In contrast, a significant -150 mGal gravity low exists over the northern Puysegur Ridge, a region known as the Snares Zone (Figure 2.3; Gurnis et al. (2019) and Hightower et al. (2020)). This region is of particular interest in our study because it has subsided with respect to the rest of Puysegur Ridge by nearly 2 km (Collot et al., 1995). If composed of buoyant crust, ridge subsidence in this location has implications for the subduction initiation process and the force balance on the system. The gravity modeling presented in Chapter 2 addresses both this question of the ridge buoyancy and helps stitch together the information obtained seismically to provide a more complete 3D picture of the structures and rock types in the region.

The crustal structure and tectonics related to the above kinematic history were investigated in detail with seismic reflection, seismic refraction, and bathymetric mapping during the South Island Subduction Initiation Experiment (SISIE) (Gurnis et al., 2019) — a marine geophysical survey in February-March 2018 aboard the R/V Marcus G. Langseth conducted by researchers at Caltech, the University of Texas, and the University of Wellington, New Zealand. We collected 1252 km of multichannel seismic reflection data and two trench perpendicular ocean-bottom seismometer (OBS) seismic refraction profiles, as well as multi-beam swath bathymetry, all of which were essential not only for our direct interpretation of the margin's structure and geology but also as prior constraints on the subsequent gravity modeling.

In Chapter 2, I detail the development of a linear 3-D gravity inversion method applicable to geologically complex regions such as subduction margins. The procedure inverts satellite gravity data, in this case from the Sandwell et al. (2019) free-air gravity map for the Puysegur region, to determine the best-fitting differential densities of spatially discretized subsurface prisms in a least-squares sense. We use a Bayesian approach to incorporate both data error and prior constraints based on the seismic reflection and refraction data from the SISIE expedition. These seismic profiles capture key structural boundaries, including sediment interfaces, the Moho, and the décollement between the subducting and overriding plate, which are used to constrain regions of different density within the gravity model. Based on these data, Gaussian priors are applied to the appropriate model parameters as absolute equality constraints. To stabilize the inversion and provide relative equality constraints on the parameters, we utilize a combination of first and second order Tikhonov regularization, which enforces smoothness in the horizontal direction between seismically constrained regions, while allowing for sharper contacts in the vertical. These models provide insight into the density contrasts, Moho depth, and crustal thickness across and along the Puysegur margin. The final model has a mean standard deviation on the predicted densities of about 17 kg m^{-3} and a mean absolute error on the predicted gravity of about 3.9 mGal, demonstrating the success of the method for even spatially complex density distributions like those present at subduction zones.

The posterior density distribution versus seismic velocity is diagnostic of compositional and structural changes. Along the strike of the Puysegur margin, we infer a thick crustal root composed of predominantly buoyant continental crust below the topographically depressed (and subsided) Snares Zones. Along the southern boundary, the crust is thin but bathymetrically shallow; to the north, the crust is thick but bathymetrically deep. This provides strong evidence for dynamic uplift in the south, reversing to a strong pull force from the Puysegur slab in the north. When the seismic velocities and MCS images are combined with seismic-velocity density relations from the gravity inversion, we also infer the existence of a sliver of oceanic crust emplaced between the nascent thrust and strike slip Puysegur Fault, in contrast to the broadly continental Puysegur Ridge (Hightower et al., 2020; Shuck et al., 2021). The eastern side of the Puysegur Ridge is a continental block and experienced far less stretching than the Solander Basin. This suggests that subduction nucleated adjacent to the boundary between the oceanic crust of the Australian Plate and a crustal block on the Pacific Plate and later jumped outboard onto the Australian Plate (Shuck et al., 2021).

Both the gravity modeling and seismic analysis reveal the significant role that continental crust plays in the evolution of the plate boundary (Gurnis et al., 2019; Hightower et al., 2020). Puysegur had formerly been viewed as an example of induced subduction initiation through transpression along a former spreading center and fracture zone system involving only oceanic crust (Collot et al., 1995; Gurnis et al., 2004). Our results demonstrate that the overriding plate is in fact block-faulted and extended continental crust, providing a density contrast between the converging plates that helps enable subduction initiation (Leng and Gurnis, 2015; Gurnis et al., 2019). This density difference is modeled to have reached its maximum around 15 Ma, consistent with the inferred age of subduction initiation at 15-12 Ma (Sutherland et al., 2006).

The imaged fault geometry along the Puysegur margin also highlights the role inherited structures play in the process of subduction initiation and the evolution of the state of stress throughout that process. The Tauru Fault zone (TFZ) is the most prominent structure imaged in the survey, which was active during the rifting stage around 45-35 Ma and later reactivated as a major fold-and-thrust system during subduction initiation around 16 Ma (Shuck et al., 2022). Identification of similar transitions between normal, reverse, and mixed fault movements record the spatial and temporal evolution of stress along the margin. The timing of initial reactivation of structures as reverse faults indicative of compressional stresses becomes younger moving north to south along the margin, indicating southward propagation of subduction initiation. Extension and subsidence, evidenced by normal faulting, again follow compression at most locations, except in the very south where uplift is ongoing (Figure 1.1). The age of subduction initiation in each locality (16 Ma beneath northern Puysegur and 5 Ma at southern Puysegur), based on plate motions and unfolding of the subducted slab (Sutherland et al., 2006), corresponds to the onset of reverse activity in the upper plate. This phase of compression lasts approximately 8 Myr before relaxation, extension, and subsidence begin, marking the local transition to self-sustaining subduction, which implies 8 Myr is the time needed to weaken the young subduction interface and for the slab to bend into the upper mantle where it can begin undergoing metamorphism (Shuck et al., 2022).

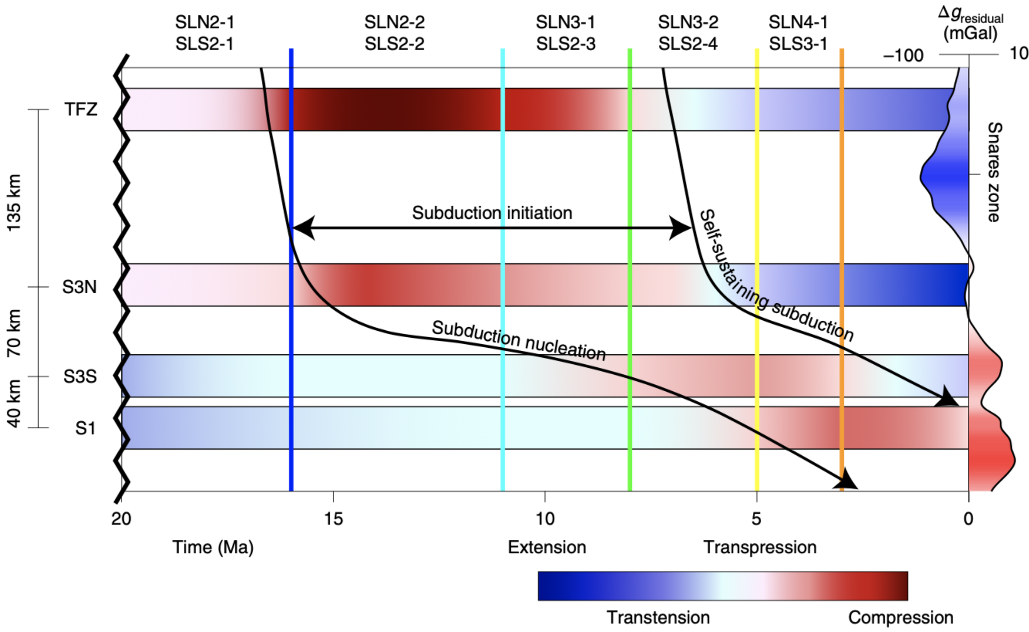

Figure 1.1: Stress evolution along the Puysegur margin from Shuck et al. (2022). Stress states are inferred from periods of normal, reverse, mixed, and quiescent tectonic activity at faults TFZ (Tauru Fault Zone), S3N, S3S, S1. For reference to the location and seismically inferred throw of the faults, the reader is referred to Shuck et al. (2022). The magnitude of the stress is qualitatively inferred from the relative amount of fault throw and the intensity of deformation at each location. Colored vertical lines represent chronostratigraphic horizons from Shuck et al. (2021) and Patel et al. (2020). The present day gravity residual trace, $\Delta g_{\text{residual}}$, was extracted from the free-air gravity anomaly along Puysegur Ridge, removed of its mean. Where $\Delta g_{\text{residual}}$ is negative, Puysegur Ridge is actively being pulled down (i.e., the Snares Zone) and where positive, the ridge is actively being pushed up under horizontal compression. The duration of compression and lag time until the onset of extension are consistent with horizontally forced subduction initiation.

Having revealed that Puysegur subduction initiated with oceanic crust adjacent to continental, there remain no confirmed examples of subduction initiation at an ocean-ocean boundary (Gurnis et al., 2019). Moreover, there is also evidence that the Izu-Bonin-Marianas subduction zone initiated at a relict Mesozoic island arc (Leng and Gurnis, 2015) rather than by juxtaposition of segments of normal oceanic crust differing in age (e.g., Stern and Bloomer (1992)), and even the Tonga-Kermadec system likely originated at the site of an earlier subduction boundary (Sutherland et al., 2010; Sutherland et al., 2020). Likewise, the decrease in duration of the compressive phase from north to south along the Puysegur margin (Figure 1.1) suggests a reduction in initial resistance if adjacent subduction initiation is already underway, owing to an already weakened plate interface (Shuck et al., 2022). These examples and conditions of subduction initiation all serve to highlight the important role that inherited tectonic structures and pre-existing zones of weakness have on plate boundary evolution and tectonic development.

One of the most important datasets available for deciphering the state of stress both at Puysegur and within the lithosphere globally is earthquakes themselves. The majority of the world's stress estimates come from focal mechanism stress inversion (Zoback and Zoback, 2007; Heidbach et al., 2018), which solves for the orientations of the principal stresses and the relative stress magnitude from a set of earthquake focal mechanism solutions (Michael, 1987; Gephart and Forsyth, 1984). Earthquakes provide a wealth of information about stress state, tectonics, and obviously seismic hazard. One of the biggest questions in seismology and seismic hazard analysis is, when is the next big one going to hit? While earthquakes cannot be predicted, much effort has been devoted to better characterizing the occurrence time of earthquakes and assessing the possibility of periodicity. An accurate characterization of earthquake timing is critical for seismic risk evaluation because the distribution of the interevent times of earthquakes directly influences probabilistic seismic hazard assessments.

In Chapter 3, we shift from deformation at nascent plate margins to focusing on the earthquake interevent time distribution at an established plate boundary. Earthquakes are commonly assumed to result from a stationary Poisson (SIP) process. We reassess the validity of this assumption using the Quake Template Matching (QTM) catalog and the relocated SCSN catalog (HYS) for Southern California. We analyze the interevent time (IET) distribution and the Schuster spectra, which identifies periodicity in the seismicity rate, after declustering with the Zaliapin and Ben-Zion (2013) method. Both catalogs exhibit fat-tails on the IET distribution, deviating from the expected exponential trend, though deviation is more prominent on the HYS catalog. The Schuster spectra of the catalogs are also inconsistent with an SIP process. The QTM catalog shows a statistically significant seasonal signal and a drift in the Schuster probability at long periods, likely due to increased seismicity following the 2010 El Mayor-Cucapah earthquake beyond the duration and extent of a typical aftershock sequence, as would be removed by the declustering. This increase is also evident in the yearly IET distributions of the catalog. In contrast, the HYS Schuster spectrum does not show any notable seasonality. Non-stationarity is evident, however, and the yearly IET distributions exhibit a decrease in seismicity rate over the duration of the catalog, likely due to seismic network upgrades around 1990. We use synthetic catalogs to test the origin and significance of the observed deviations from the Poisson model. Variations in the QTM annual seismicity rate, around 5.6%, are too small to generate a noticeable departure from an exponential distribution, and the SIP model can not be rejected at the 5% significance level. The synthetic catalogs also suggest the fat-tail is an artefact of incomplete declustering. Overall, the variations in IET distribution for southern California are probably the result of both 1) incomplete declustering and location uncertainty, and 2) transient non-stationarity of the background rate from viscoelastic effects after large earthquakes. However, the stationary Poisson model appears adequate for describing background seismicity at the scale of Southern California and the decadal time scale of the QTM catalog.

Seismicity and deformation at plate boundaries present a significant seismic hazard to many populated areas throughout the world, and as such, are well-studied. However, large and damaging earthquakes can also occur far from tectonic plate boundaries within the interiors of continents (i.e., intraplate seismicity). From seismicity at active plate boundaries in Chapter 3 and the role of inherited structures at subduction margins in Chapter 2, we transition to the primary focus of this thesis, investigating the deformation of the intraplate lithosphere and the role of pre-existing weaknesses in promoting intraplate seismicity when subjected to long-wavelength sources of stress. Intraplate seismicity is an enigmatic phenomenon potentially resulting from a combination of geodynamic processes and surface loading, with contribution from far-field tectonic forces and pre–existing structures. The continental interior of eastern North America is one of the best regions for studying the interplay between geodynamics and intraplate seismicity, as it has hosted many significant historical earthquakes and is undergoing both long wavelength dynamic subsidence and modern day glacial isostatic adjustment (GIA). Despite the stability of the North American interior, which experiences only about 2 mm/yr of horizontal motion according to GPS data (Stein and Sella, 2002), earthquake shaking can potentially be more hazardous compared to that on plate margins, as the stable continental lithosphere can transmit seismic energy more efficiently (Stein, 2007).

Historic records of major earthquakes in eastern North America date back to at least 1638 (Figure 4.1a), with most seismicity occurring within clearly defined seismic zones. Of these zones, the New Madrid, Central Virginia, Charleston South Carolina, Eastern Tennessee, Northern Appalachian, Western Quebec, Charlevoix, and Lower St. Lawrence River Valley Seismic Zones have experienced destructive earthquakes in recorded history, ranging from M 5 to greater than M 7. These include the famous 1811-1812 New Madrid earthquakes (Figs. 4.1a), which were felt as far away as Ottawa, Canada, caused widespread liquefaction, and even temporarily reversed the flow of the Mississippi River (Johnston and Schweig, 1996). While the largest of these events may have been as high as M 8 (Johnston and Schweig, 1996), more recent estimates suggest the magnitudes were more likely around M 7 (Hough et al., 2000; Stein, 2007). While an intraplate earthquake of magnitude greater than or equal 7 is expected to occur anywhere along the Atlantic margin only every few 1000 years (Brink et al., 2009) and within New Madrid every 550-1100 years (Schweig and Ellis, 1994), earthquake hazard remains significant for the central-eastern United States (CEUS) due to limited earthquake preparedness.

Seismicity in eastern North America tends to concentrate within old aulacogens (failed rifts) or other tectonically inherited structures that can act as weak zones in the crust where stress accumulates (Sykes, 1978; Mazzotti and Townend, 2010; Hurd and Zoback, 2012). These aulacogens and seismic zones are associated with the Proterozoic Iapetan rifted margin and its various failed rift arms (Baird et al., 2010; Withjack et al., 1998) or the Mesozoic rift basins of the extended Atlantic margin (Withjack et al., 1998; Mazzotti and Townend, 2010). Earthquakes and stresses also concentrate in zones of thinner lithosphere around the margin of the North American cratonic lithosphere (Li et al., 2007). Focal mechanism stress inversion shows an increasingly compressive stress regime from the south-central U.S. to southeast Canada (Hurd and Zoback, 2012) with a predominantly NE-SW oriented regional maximum horizontal compressive stress direction (Heidbach et al., 2018). However, some seismic zones exhibit a statistically significant clockwise rotational deviation of the seismically derived maximum horizontal stress (S_{Hmax}) direction from the regional borehole derived S_{Hmax} orientation (Mazzotti and Townend, 2010; Hurd and Zoback, 2012), suggesting multiple stress regimes. Suggested sources of such stress rotations and the associated intraplate seismicity include complex fault intersections (Talwani, 1988; Talwani, 1999; Gangopadhyay and Talwani, 2007), crustal density anomalies, gravitational potential energy forces (Levandowski et al., 2017), and flexure under local loads (Stein et al., 1989). However, the consistency of these stress rotations between seismic zones separated by distances of up to 1500 km cannot be explained by such mechanisms and instead suggests a common long-wavelength source of stress perturbation (Mazzotti and Townend, 2010). Longer wavelength mechanisms include dynamic subsidence, lithospheric flexure, and glacial isostatic adjustment. While these processes typically only induce stress perturbations on the order of 10s of MPa, they may result in stress amplifications by a factor of 5-10 in the presence of a lithospheric weak zone (Grollimund and Zoback, 2001; Mazzotti and Townend, 2010). Thus, under the right conditions, long-wavelength loads may concentrate stresses and lead to intraplate seismicity.

The possible connections between intraplate seismicity and large-scale continental uplift or the sinking of continental platforms (i.e., epeirogeny) remain elusive. Earlier work has demonstrated that sinking slabs, in both regions of active and ancient subduction, create mantle downwelling that exert tractions on the overlying lithosphere, resulting in dynamic subsidence (Hager, 1984; Mitrovica et al., 1989; Gurnis, 1992; Yang et al., 2016; Forte et al., 2010). Initially, the sinking slab stagnates at the 660 km discontinuity due to the viscosity jump and the phase transition between ringwoodite and bridgmanite (Billen, 2008). The negative buoyancy of the accumulated mass is eventually great enough to break through the boundary and continue sinking, initiating a process called slab avalanche, which causes substantial downward asthenospheric flow (Christensen and Yuen, 1984; Tackley et al., 1993; Yang et al., 2016; Yang et al., 2018). Dynamic subsidence has been inferred in eastern North America from Cenozoic shorelines (Spasojevic et al., 2008), under which the remnant Farallon slab lies between 410 and 1700 km depth (Ren et al., 2007; Lu et al., 2019). The presence of the slab beneath the 660 km discontinuity is evidence of potential slab avalanche, as are models of mantle flow localized beneath the NMSZ (Forte et al., 2007). Questions remain as to how this flow-induced continental subsidence affects stress in the lithosphere. While this epeirogenic movement may not cause notable folding or faulting (Gurnis, 1992), it may reactivate pre-existing faults.

In Chapter 4, we use high-resolution geodynamic flow models to explore the hypothesis that mantle flow induced epeirogenic motion and stress perturbation due to the sinking of the Farallon slab contributes to intraplate seismicity in eastern North America via the reactivation of pre-existing faults. To incorporate realistic mantle and lithospheric thermal structure and the negative buoyancy of the Farallon slab, we use geologically and seismically constrained thermal input in our models. This allows us to naturally incorporate plate driving forces due to the thermal buoyancy of the oceanic lithosphere, as well as the effect of variable lithospheric thickness. We parameterize the Farallon slab in terms of its buoyancy to determine the degree to which the flow induced by the sinking slab contributes to intraplate stress. Unlike most previous studies on the effect of mantle flow on intraplate stress, we explicitly impose low viscosity crustal and/or lithospheric weak-zones demarcated by the aulacogens and paleo-rifted margins of eastern North America. Using the mantle convection code CitcomS, we compute the instantaneous flow field and associated stress tensor, with which we calculate the S_{Hmax} direction and deviatoric stress in the crust to determine how stress patterns change in cases of different slab-buoyancies and in the presence of weak-zones. We compare our modeled stresses to those of the World Stress Map (WSM) (Heidbach et al., 2018) and other sources (e.g. Mazzotti and Townend (2010)) and analyze the stress patterns within specific seismic zones. We assess the likelihood of intraplate fault reactivation under these different conditions by computing the Coulomb stress on known faults in several seismic zones.

In addition to loading from the Farallon slab, eastern North America is also the site of ongoing glacial isostatic adjustment (GIA). GIA is the viscoelastic response of the solid earth to the disappearance of major ice sheets following the last glacial maximum (LGM) about 21-26 thousand years ago. At timescales appropriate for post-glacial rebound, the Earth responds to loads viscoelastically (Cathles, 1975; Peltier, 1974), meaning that even after the ice load is gone, there is a time delay to the uplift of the Earth to its pre-glaciation level. During the last glacial maximum, the Laurentide ice sheet covered most of North America, with the thickest ice cover (as much as 3-5 km) positioned at Hudson Bay (Peltier et al., 2015; Lambeck et al., 2017), the site of the largest modern day rebound rates (Sella et al., 2007). It has long been suggested that stresses induced by glacial isostatic adjustment (GIA) may be responsible for many of the anomalous intraplate earthquakes of eastern North America (Wu and Hasegawa, 1996; Wu and Johnston, 2000; Grollimund and Zoback, 2001; Wu and Mazzotti, 2007; Mazzotti and Townend, 2010).

During glaciation, the weight of the ice sheet creates an additional vertical stress in the lithosphere, and the flexure of the lithosphere under the load generates horizontal bending stresses. These additional vertical and horizontal stresses increase all three principal stresses. In terms of Mohr Coulomb failure theory, during glaciation, the weight of the ice-sheet acts to stabilize faults and suppress fault movement (Johnston, 1987; Wu and Hasegawa, 1996; Steffen et al., 2014a). When the ice-sheet melts, the vertical stress from the load decreases, but the GIA induced horizontal stresses do not decrease as quickly because of the viscoelastic nature of the lithosphere and the upward migration of stress from mantle relaxation. Thus, after deglaciation, the vertical stress disappears but the horizontal stress remains, which increases the differential stress, bringing faults closer to failure (Steffen et al., 2014a). Like slab loading, GIA is also a long-wavelength source of stress that in the presence of local lithospheric weak zones could potentially explain the observed stress rotations in seismic zones across eastern North America (Mazzotti and Townend, 2010). Wu and Mazzotti (2007) indeed find that GIA stresses can produce clockwise rotation of the S_{Hmax} direction in the crust above a lithospheric weak zone, and depth-dependent stress rotations in the Charlevoix seismic zone are argued to arise from GIA stress perturbations as well (Verdecchia et al., 2022). Previous GIA models have also demonstrated the influence of GIA induced stresses on both fault reactivation potential and stress orientations in eastern Canada (Wu and Hasegawa, 1996; Wu, 1997) and even in New Madrid (Wu and Johnston, 2000).

In Chapter 5, we explore the hypothesis that glacial isostatic adjustment promotes intraplate seismicity in eastern North America via perturbation to the intraplate stress field and reactivation of pre-existing faults. We develop high resolution global models of the solid earth response to glacial loading and unloading with CitcomSVE (Zhong et al., 2022), a spherical finite-element viscoelastic GIA code built from CitcomS that implements the sea level equation and the ice-loading history of ICE-6G (Peltier et al., 2015) for a fully 3D or 1D Earth viscosity structure. The models use a viscosity structure based on the seismically and geologically constrained thermal structure implemented in the mantle flow models with CitcomS, presented in Chapter 4. Like in the CitcomS models, we test how local-scale, low-viscosity lithospheric weak zones emplaced at the locations of the geologically mapped aulacogens and other structures affect the stress field under loading from GIA. Focusing on the present day GIA induced stresses, we calculate the stress tensor, with which we compute the S_{Hmax} direction, the deviatoric stress magnitude, and the Coulomb stress on known faults. We compare our results to stresses of the WSM (Heidbach et al., 2018) and to those obtained from mantle flow models in Chapter 4 using the same Earth structure.

Investigations into the connection between broad–scale subsidence or uplift and faulting and seismicity can improve how we quantify and assess seismic hazard in intraplate regions, and in some cases are already informing such models. The Canadian seismic hazard model (Adams and Halchuk, 2003; Adams, 2019), for example, has adopted a geodynamic approach to characterizing the spatial distribution of intraplate seismicity that assumes large earthquakes may occur anywhere along the paleotectonic zones encompassing the Late Proterozoic-Cambrian Iapetan rifts and aulacogens (Mazzotti, 2007a). Modeling stress perturbations due to surface loading may also improve our understanding of lithospheric deformation and earthquake hazard in tectonically active regions, such as California, where drought has led to isostatic uplift that can impact regional stresses and seismicity (Johnson et al., 2017b; Johnson et al., 2017a; Kreemer and Zaliapin, 2018; Craig et al., 2017). Lithospheric flexure in response to other surface processes, such as glacial rebound and sea level rise, can potentially impact local and regional stress fields, especially near crustal weak zones and along coastlines, thereby altering the spatial distribution of seismic hazard in the near future. A more thorough understanding of how such long-wavelength loads affect intraplate stress, deformation, and seismicity at the regional and local level is thus important for developing resilient infrastructure and better seismic risk assessment.

Chapter 2

A BAYESIAN 3D LINEAR GRAVITY INVERSION FOR COMPLEX DENSITY DISTRIBUTIONS: APPLICATION TO THE PUYSEGUR SUBDUCTION SYSTEM

Hightower, E., M. Gurnis, and H. van Avendonk (2020). "A Bayesian 3D Linear Gravity Inversion for Complex Density Distributions: Application to the Puysegur Subduction System". In: *Geophysical Journal International* 223, pp. 1899–1918. DOI: 10.1093/gji/ggaa425.

2.1 Introduction

Inverse methods have become increasingly popular for addressing a number of problems in earth science, particularly subsurface mapping. Gravity inversion, for determining either the densities or depths of bodies of known density in the Earth, has been an established method of mapping the Earth's heterogeneities for some time, though often with emphasis on the nonlinear approach. In non-linear gravity inversion, the densities and density contrasts of the subsurface bodies are assumed to be known and one solves for the geometry of the source, usually in terms of depth to a particular interface. These inversions include either methods operating in the spatial domain (Medeiros and Silva, 1996; Camacho et al., 2011; Prutkin and Casten, 2009) or those operating in the wavenumber domain (Oldenburg, 1974; Parker, 1972; Parker, 1995; Chappell and Kusznir, 2008; Cowie and Kusznir, 2012; Bai et al., 2014). However, despite the Fourier method being one of the classical approaches to gravity inversion, wavenumber methods are often less effective in recovering a fully 3D solution with multiple sources and complex geometry (Bear et al., 1995; Geng et al., 2019).

With the linear method, the unknowns are the densities of a discretized array of subsurface rectangular prisms and iteration is not required in order to reach model convergence, except in the case of testing variations in model regularization or other constraints. Solving for the 3D density distribution also indirectly solves for the depth to key interfaces, such as the Moho, because we can interpret such boundaries from sharp transitions in density. While linear gravity inversion is an established method (Bear et al., 1995; Li and Oldenburg, 1998; Silva et al., 2001; Silva Dias et al., 2009; Barnoud et al., 2016; Welford et al., 2018; Geng et al., 2019), many of the studies employing it only do so for relatively simple geological geometries, such as a single sedimentary basin, mafic intrusion, or volcanic feature (Silva et al., 2001; Medeiros and Silva, 1996; Barnoud et al., 2016). Successful application of this method to crustal scale studies and tectonic margins, with variable approaches to the implementation, also exist (Welford et al., 2010; Welford et al., 2018; Geng et al., 2019), but few have applied this method to subduction zones. Subduction margins possess a complicated juxtaposition of structure and rock types and significant and sometimes sharp lateral variations in density, as opposed to passive continental margins, which often exhibit a more gradual change in structure and rock type that is more easily handled by smoothed inversions. We construct a 3D linear gravity inversion for an active subduction zone, demonstrating the successful application of this method to more complex density distributions and bolstering the validity of this method and its use in tectonic applications.

Inversion has the advantage of providing statistical feedback on solution quality. Specifically, within a Bayesian framework, the objective is to determine the posterior distribution of a set of parameters given prior distributions and likelihood functions that describe how the data relate to those unknown parameters (Tarantola, 2005; Aster et al., 2013; De La Varga and Wellmann, 2016; Wellmann et al., 2018). The Bayesian approach is particularly useful for geophysical inverse problems, which are in principle ill-posed because they are inherently non-unique. For example, gravity data cannot distinguish between a narrow density anomaly at depth or a wider source near the surface (Li and Oldenburg, 1998; Geng et al., 2019; Welford et al., 2018). Consequently, one must introduce constraints and *a priori* information in order to transform them into well-posed problems. With the Bayesian formulation, we can account for both error in the data and error in our prior information to reduce how that error may be carried over into the final model, and we can quantify the error on our final solution via the covariance and resolution operators. The Bayesian approach we use here offers improvements over traditional gravity inversion and modeling techniques, where one usually removes the effect of the topography and the Moho and analyzes the residual. Such an approach requires assuming constant layer densities when in fact those densities are often unknowns, and it requires assuming a known Moho depth that has to manually and iteratively be adjusted by the user. This makes it difficult to fully incorporate lateral changes in density. The Bayesian approach is more flexible and capable of handling complex 3D geometries because it allows us to constrain where the boundary is *most likely* to be based on seismic data and what the densities are *most likely* to be, while allowing both to vary in accord with the gravity data, the final boundary location being dependent on the differential density. As such, we are able to draw conclusions about the 3D density distribution in a tectonic setting that would otherwise not be as apparent with traditional forward or inverse gravity methods that require harder constraints or restrictions.

There are a number of common constraints widely used in gravity inversion, including inequality constraints, which specify the lower and upper bounds of parameter estimates; absolute proximity constraints, which specify that model parameters must be close to a specified value, based on geologic information at particular points; and relative equality constraints, which specify that the spatial variation of the model parameter values must be smooth (Silva et al., 2001). Absolute proximity constraints are rarely used alone because there is often not enough prior information available to constrain all model parameters. An exception would be the minimum Euclidean norm, or similarly zeroth order Tikhonov regularization, which requires all parameter estimates to be as close as possible to null values. This type of regularization is biased towards a solution with minimum density and tends to concentrate mass anomalies toward the surface, which is not entirely physical or useful for our interpretation of the subsurface.

Minimum structure inversion, however, is a commonly used method (Last and Kubik, 1983; Farquharson, 2008; Li and Oldenburg, 1998), utilized by codes such as GRAV3D (Li and Oldenburg, 1998). To overcome the inherent insensitivity of gravity to depth and thus the tendency for the inversion to concentrate mass near the surface, these methods often apply a depth weighting (Li and Oldenburg, 1998). Applying absolute proximity constraints and inequality constraints to specific regions of the model, however, overcomes the need for a depth weighting (Geng et al., 2019; Welford et al., 2018). While traditional inverse methods do allow for the adjustment of smoothing parameters, bounds on densities, and variable weighting, they usually do so under hard constraints on predefined boundaries where the density is allowed to vary but the geometry of the boundary remains unchanged (Li and Oldenburg, 1998; Welford et al., 2018). In contrast, the probabilistic approach offers more flexibility. Previous comparisons between such probabilistic methods and approaches such as those used by GRAV3D (Welford et al., 2018) highlight these distinctions as well, and we refer the reader to these sources for a more in depth comparison. These comparisons show that while each method has its advantages and disadvantages, a probabilistic approach using sparse seismic Moho constraints may not always lead to better results, particularly when there are significant lateral variations in crustal thickness and composition, as it tends to concentrate more unreasonable densities into different parts of the model to compensate (Welford et al., 2018). In contrast to previous applications of this probabilistic method (Welford et al., 2018; Geng et al., 2019; Barnoud et al., 2016), our approach directly incorporates constraints on the interface depths *and* on composition via the mapping of seismic velocities to density, not only at the locations of sparse depth to Moho constraints from seismic lines, but interpolated throughout the model domain and weighted according to the spatial extent of the prior data. We also propagate the error on the seismic velocities into the density prior to ensure that the densities obtained vary within a range that is consistent with the error in the seismic velocities and that the seismic data does not too strongly dominate the final model obtained by the inversion, such that it remains predominantly resolved by the gravity. Moreover, the Bayesian approach allows us to directly evaluate the error and statistical validity of our results in a way that does not assume the seismic data is the full truth.

Due to the non-uniqueness of gravity, however, even with absolute proximity constraints, some sort of smoothing or stabilizing functional is needed to produce a meaningful solution. This can come in the form of relative equality constraints such as either first or second order Tikhonov regularization, which spatially minimize the first or second derivative of the physical property, respectively. Relative equality constraints by themselves have a tendency to produce a blurred but still valuable model of the density anomalies (Portniaguine and Zhdanov, 1999; Silva et al., 2001). However, when combined with absolute equality constraints, this inversion technique is often able to produce accurate representations of the source geometry and density (Silva et al., 2001; Medeiros and Silva, 1996). As such, our method employs a combination of absolute and relative equality constraints in the form of Gaussian priors based on existing geophysical data and a combination of first and second order Tikhonov regularization.

There is distinction in the literature between traditional regularization methods and proper Bayesian approaches to inverse problems. Traditionally, regularization modifies the function relating the data to the source of its signal, in an effort to eliminate the unstable problem by replacing it with a similar stable one. This often involves a penalty on the inversion that guarantees a unique solution (Calvetti and

Somersalo, 2018). The Bayesian approach, on the other hand, by modeling the solution as a random variable, allows one to use the exact function relating the data to its source and offers the flexibility of obtaining multiple reasonable solutions, as the final posterior model is in fact a probability distribution. However, the non-uniqueness of gravity inversion in particular requires some form of regularization. The regularization method that best bridges the classical deterministic theory and the Bayesian approach is Tikhonov regularization because instead of modifying the model function, it solves a minimization problem (Calvetti and Somersalo, 2018). In that sense, Tikhonov regularization is essentially a smoothness prior and can be implemented within a probabilistic framework, allowing the inversion problem to remain Bayesian even though it involves regularization.

2.2 Methods

2.2.1 Calculation of Forward Gravity

We model the subsurface density and structure of a defined region and its associated effect on the gravity by discretizing the subsurface into a finite number of rectangular blocks. The gravitational attraction of each rectangular prism is calculated and then summed to compute the gravity field. The gravitational attraction of a homogeneous right rectangular prism relative to an observation point on the surface is given as in Turcotte and Schubert (2014) as

$$\begin{aligned}\Delta g = \Gamma \Delta\rho \sum_{i=1}^{2}\sum_{j=1}^{2}\sum_{k=1}^{2} \mu_{ijk} [\Delta z_k arctan\left(\frac{\Delta x_i \Delta y_i}{\Delta z_k R_{ijk}}\right) \\ - \Delta x_i ln(R_{ijk} + \Delta y_j) - \Delta y_j ln(R_{ijk} + \Delta x_i)] \qquad (2.1)\end{aligned}$$

where $\Delta x_i = (x_i - x_p), \Delta y_j = (y_j - y_p), \Delta z_k = (z_k - z_p)$, and $\mu_{ijk} = (-1)^i(-1)^j(-1)^k$. $\Delta\rho$ is the density contrast of the prism, and Γ is the universal gravitational constant. x_p, y_p, and z_p are the coordinates of the measurement point, and x_i, y_j, and z_k are the coordinates of the corners of the prism, where $(i, j, k) = (1, 2)$. R_{ijk} is the distance from the measurement point to a corner at x_i, y_j, z_k and is given by $R_{ijk} = (\Delta x_i^2 + \Delta y_j^2 + \Delta z_k^2)^{1/2}$.

The sum defines the geometry of the prism relative to the observation point and can be extended to the case of multiple prisms, such that each prism in the domain has a single geometry coefficient for each gravity observation point. We invert gravity data at N observation points to obtain the best fitting estimate of the densities of M subsurface prisms, or M model parameters. Equation 2.1 then results in an N x

M matrix $\mathbf{G}$ that describes the geometry of each prism relative to each observation point times Γ. The gravity anomaly at any observation point due to the combined attraction of all the prisms is the product of this matrix and $\mathbf{\Delta}\rho$, which is an M x 1 vector containing the differential density of each prism, expressed as

$$\mathbf{\Delta g} = \mathbf{G\Delta}\rho. \tag{2.2}$$

2.2.2 Linear Least Squares Inversion

We adopt the method for linear least squares inversion as given in Aster et al. (2013) and Tarantola (2005). For N data points and M model parameters, where $g_i(\mathbf{m})$ is the model prediction of the i^{th} datum (the Δ has been omitted for clarity), the least squares misfit is:

$$F(\mathbf{m}) = \frac{1}{2}\sum_{i=1}^{N}(d_i - g_i(\mathbf{m}))^2. \tag{2.3}$$

For a linear model such as that given in Equation 2.2, the model derivative is independent of the model parameters, and our prediction can be written directly as $\mathbf{Gm}$. The Gauss-Newton solution of the model parameters that minimizes the least squares misfit in Equation 2.3 is thus:

$$\mathbf{m} = (\mathbf{G}^T\mathbf{G})^{-1}\mathbf{G}^T(\mathbf{d}). \tag{2.4}$$

The data $\mathbf{d}$ are the observed gravity anomaly values, and the model parameters to be estimated are the differential densities of each discretized block in the subsurface.

We accommodate data errors and prior constraints on the model parameters in the inversion via a Bayesian approach. Bayes theorem states that the probability of the model parameters, given the data, is proportional to the product of 1) the probability of producing those data with the model and 2) the probability of the model itself.

$$P(\mathbf{m}|\mathbf{d}) \propto P(\mathbf{d}|\mathbf{m})P(\mathbf{m}) \tag{2.5}$$

$P(\mathbf{m})$ is a prior that we use to restrict the model parameters to certain values given our existing geological knowledge.

In including the data error in the least squares solution, we make the key simplifying assumption that the data are independent. In the case of gravity, we are incorporating the relative attraction of both adjacent and distal blocks of mass, and if the data are gridded with some form of interpolation, then they are arguably not truly independent. However, given the complexity of the problem and its physical geometry, the interdependence of the data is difficult to quantify and the simplifying assumption that the data are independent is sufficient to perform the inversion. We assume each data point can be represented by a Gaussian distribution with known error such that we can define a new least squares misfit:

$$F(\mathbf{m}) = \frac{1}{2}\sum_{i=1}^{N}\left(\frac{d_i - g_i(\mathbf{m})}{\sigma_{d_i}}\right)^2, \tag{2.6}$$

where we are now minimizing the difference between the known and predicted gravity, given the error in the gravity data. From Bayes Theorem, minimizing this new misfit $F(\mathbf{m})$ is equivalent to maximizing $P(\mathbf{m}|\mathbf{d})$. To incorporate the data error into the model parameter solution, we define a diagonal and symmetric weight matrix $\mathbf{C_d}$ with the data variance on the diagonal. The solution becomes:

$$\mathbf{m} = (\mathbf{G}^T\mathbf{C_d}^{-1}\mathbf{G})^{-1}\mathbf{G}^T\mathbf{C_d}^{-1}\mathbf{d}. \tag{2.7}$$

2.2.3 Tikhonov Regularization

Linear least squares, even when using the generalized inverse or the truncated generalized inverse to handle small singular values, is often insufficient for many inverse problems due to non-uniqueness and instability, especially for high-dimensional problems. Thus, a form of regularization must be applied. We employ a combination of first and second order Tikhonov regularization, which stabilizes the inversion and acts as a relative equality constraint on the values of the model parameters. First order Tikhonov regularization minimizes the square of the first spatial derivative of the model parameters (i.e., the gradient), thus serving to flatten the solution. Second order Tikhonov minimizes the square of the second spatial derivative of the model parameters (i.e., the curvature) and hence smooths the solution. Zeroth order Tikhonov, on the other hand, favors models that are small and is identical to applying a Gaussian prior with a mean of zero and minimizing the square of the model parameter values themselves.

As Tikhonov regularization is equivalent to applying a prior that enforces either small values, flatness, or smoothness, we can derive the regularized solution by adjusting the misfit equation to reflect the additional minimization of the model parameters or their first or second derivatives.

$$F(\mathbf{m}) = \frac{1}{2}(\mathbf{d} - \mathbf{Gm})^T\mathbf{C_d}^{-1}(\mathbf{d} - \mathbf{Gm}) + \lambda^2(\mathbf{Lm})^T(\mathbf{Lm})$$

$\mathbf{L}$ is either the identity matrix, a first derivative finite difference operator, or a second derivative finite difference operator for zeroth, first, or second order Tikhonov regularization, respectively. λ is a constant controlling the strength of the regularization. As the misfit remains exactly quadratic with the addition of the Tikhonov regularization term, the inverse problem remains linear, and the weighted and regularized linear least squares solution becomes

$$\mathbf{m} = (\mathbf{G}^T\mathbf{C_d}^{-1}\mathbf{G} + \lambda^2\mathbf{L}^T\mathbf{L})^{-1}\mathbf{G}^T\mathbf{C_d}^{-1}\mathbf{d}. \tag{2.8}$$

For three-dimensional models, first and second order Tikhonov are implemented using the sums of the finite-difference approximations to the first or second derivatives in each direction, respectively. Because the discretization of the grid can be different in the x, y, and z directions, we apply three different regularizations, with associated constants α for the x-, β for the y-, and ζ for the z-direction. The derivation of the Tikhonov regularization matrices is given in Appendix A. For three-dimensions, the weighted Tikhonov regularized solution is

$$\mathbf{m} = (\mathbf{G}^T\mathbf{C_d}^{-1}\mathbf{G} + \alpha^2\mathbf{L_x}^T\mathbf{L_x} + \beta^2\mathbf{L_y}^T\mathbf{L_y} + \zeta^2\mathbf{L_z}^T\mathbf{L_z})^{-1}(\mathbf{G}^T\mathbf{C_d}^{-1}\mathbf{d}). \tag{2.9}$$

Without a flatness constraint in the far-field, abrupt density changes at the edges of the model domain result in a classical gravity edge effect. Consequently, to ensure mathematical stability, we impose an infinite edge boundary condition, which allows the gravity to smoothly continue off the edges of the model area. We accomplish this condition by padding the domain with edge prisms that are sufficiently long that they extend far beyond the edge of the gravity grid (on the order of 1000 km for the regional problem with which we test the method). We also enforce this condition during the inversion by using first order Tikhonov regularization with a strong regularization coefficient to minimize the difference between the edge parameters and the adjacent values so that their predicted densities are the same. Thus, we apply different orders and strengths of Tikhonov regularization to the edges and the interior of the model simultaneously. The interior of the model has second order Tikhonov imposed in the horizontal directions to allow for smooth continuity of density bodies in the subsurface, and first order Tikhonov is applied in the vertical direction, as it is better equipped to allow for sharp contacts between layers of rock, while strong first order is applied on the boundary.

As before, this variable order Tikhonov regularization can be achieved by redefining the misfit equation, where separate $\mathbf{L}$ matrices apply different weights to different sets of model parameters and different directions. The full Tikhonov regularized solution, with boundary conditions applied, is

$$\mathbf{m} = (\mathbf{G}^T\mathbf{C_d}^{-1}\mathbf{G} + \mathbf{L})^{-1}(\mathbf{G}^T\mathbf{C_d}^{-1}\mathbf{d}), \tag{2.10}$$

where

$$\mathbf{L} = \alpha^2\mathbf{L_x}^T\mathbf{L_x} + \beta^2\mathbf{L_y}^T\mathbf{L_y} + \zeta^2\mathbf{L_z}^T\mathbf{L_z} + b^2\mathbf{B_x}^T\mathbf{B_x} + b^2\mathbf{B_y}^T\mathbf{B_y}. \tag{2.11}$$

b is the weight of the first order Tikhonov regularization applied to the boundary condition. $\mathbf{B_x}$ and $\mathbf{B_y}$ are the regularization matrices that apply the boundary conditions in the x and y directions, respectively.

2.2.4 Priors

Meaningful solutions consistent with existing geological knowledge are obtained by applying absolute equality constraints as Gaussian priors. In this approach, each parameter is forced to be close to a mean value but is allowed to vary within a specified range. Different regions of the model domain can have different priors depending on 1) what we suspect the densities of the rocks in those areas are, and 2) how confident we are in those values based on their location relative to the other data we have. The prior on each parameter is given by the Gaussian probability density function

$$P(m_k) = \frac{1}{\sigma_p\sqrt{2\pi}}exp(-\frac{1}{2\sigma_p^2}(m_k - \mu_p)^2), \tag{2.12}$$

where m_k is the estimated model parameter value, μ_p is the expected value of that model parameter based on our prior information, and σ_p is the standard deviation of the prior for that parameter.

As with the data error and Tikhonov regularization, we define a new misfit by adding the exponential component of the Gaussian prior to the existing misfit,

$$\begin{aligned} F(\mathbf{m}) = {} & \frac{1}{2}(\mathbf{d} - \mathbf{Gm})^T\mathbf{C_d}^{-1}(\mathbf{d} - \mathbf{Gm}) + \alpha^2(\mathbf{Lm})^T(\mathbf{Lm}) \\ & + \frac{1}{2}(\mu_\mathbf{p} - \mathbf{m})^T\mathbf{C_p}^{-1}(\mu_\mathbf{p} - \mathbf{m}). \end{aligned} \tag{2.13}$$

Defining the prior covariance operator $\mathbf{C_p}$ as an M x M diagonal matrix with the variance of the prior on the diagonal, we arrive at the final data weighted, Tikhonov regularized solution with prior constraints

$$\mathbf{m} = (\mathbf{G}^T\mathbf{C_d}^{-1}\mathbf{G} + \mathbf{L} + \mathbf{C_p}^{-1})^{-1}(\mathbf{G}^T\mathbf{C_d}^{-1}\mathbf{d} + \mathbf{C_p}^{-1}\mu), \tag{2.14}$$

where **L** is defined as in Equation (2.11). This is the final solution vector used in our inversion. The row or column number of the elements along the diagonal of $\mathbf{C_p}$ correspond to the index number of that model parameter. Likewise, μ is an M x 1 vector for which each element corresponds to the density of single prism. To apply different priors to different model parameters, one need only use the coordinates of the model parameter centroids within the desired region to find the appropriate model parameter index and apply a value to that element. If an element on the diagonal of $\mathbf{C_p}^{-1}$ is zero, then no prior is applied to that model parameter.

2.2.5 Quantifying Error

A key advantage of a Bayesian approach is that it allows us to statistically evaluate the solution, via the posterior covariance matrix **C** of the model parameters and the resolution matrix **R**. The covariance matrix is defined as the inverse of the Hessian:

$$\mathbf{C} = (\mathbf{G}^T \mathbf{C_d}^{-1} \mathbf{G} + \mathbf{L} + \mathbf{C_p}^{-1})^{-1}. \tag{2.15}$$

Here the values of **m** estimated by the inversion are the center-points of the posterior Gaussian, and the diagonal values of the covariance matrix **C** are their associated variances.

The resolution matrix is determined from the covariance matrix (Tarantola, 2005):

$$\mathbf{R} = \mathbf{I} - \mathbf{C}\mathbf{C_p}^{-1}, \tag{2.16}$$

where **I** is the identity matrix. If the resolution matrix equals the identity matrix, the model is fully resolved by the data. This particular formulation of the resolution operator primarily allows us to distinguish between those parameters that are resolved by inversion of the gravity data and those that are resolved by the prior. Mathematically, this can be written as:

$$tr(\mathbf{I}) = tr(\mathbf{R}) + tr(\mathbf{C}\mathbf{C_p}^{-1}), \tag{2.17}$$

meaning the total number of model parameters is the sum of the number of parameters resolved by the data and the number of parameters resolved by the prior information (Tarantola, 2005). Higher resolution (values closer to 1) means those parameter values have mostly been determined by the inversion - in other words, we have learned something from the gravity that we did not know *a priori*. On the other hand, low resolution (values closer to 0) means the values of those parameters are almost entirely attributed to the prior. This is the case for regions of the model where the prior is very strong, i.e., a very small prior variance.

Ultimately, solution quality is based on the mean absolute error of the gravity and the mean standard deviation of the model parameters as determined from the diagonal of the covariance matrix, as well as visual inspection of the model to determine its geological reasonability. Even with relative and absolute equality constraints, gravity inversion remains non-unique and there are a number of model solutions that could fit the data. It is possible to obtain a solution that minimizes the misfit as required but that still appears geologically unreasonable and must be disregarded as the most likely posterior distribution of densities. However, the regularization and priors ensure enough stability in the model that with the appropriate regularization parameters α, β, and ζ, the model obtained is geologically sound and in line with our standing geophysical knowledge.

2.3 Synthetic Tests

Estimating optimal regularization parameters is difficult for gravity inversion. We use an iterative technique on a series of synthetic tests to determine α and ζ values that produce 1) the best fit between the predicted and observed gravity, and 2) the most geologically reasonable solution, which for the synthetic models, is a nearly complete recovery of the known density distribution. We conduct these synthetic tests on a simplified lower resolution model of a subduction system. In all synthetic tests, we construct a density model, compute the forward gravity as given by Equation 2.1 and add Gaussian noise to the gravity using a similar standard deviation to that of the data set we will later use (about 1.7 mGal). We invert this gravity for a range of Tikhonov regularization parameters and orders, with or without priors on specific sets of model parameters, while attempting to recover the known density distribution and judging the stability of the inversion.

The performance of the inversion when used with first and second order Tikhonov is tested using a simplified synthetic 3D model of a subduction zone (depicted in representative cross-sections in the bottom row of Figs. 2.1 and 2.2). We test various combinations of the horizontal regularization coefficient α and the vertical regularization coefficient ζ for the cases of only first order Tikhonov, only second order Tikhonov, and a combination of second order in the horizontal and first order in the vertical. For each of these cases, we test four additional classes of constraints: no priors, priors enforced only on parameters within the water column, priors enforced only on parameters within the water and crustal layers, and finally priors on all parameters, including the mantle. The prism size is about 17.5 km in the x-direction, 22.5 km in the y-direction, and increases from about 206 m to 2060 m from shallow to deeper depths in the z-direction. The α and ζ values tested range from 10^{-3} to 10^{8}. There are a total of 10,648 model parameters and 22,500 data points, yielding an over-determined system. The synthetic density model is constructed with a seawater density of 1027 kg/m^3, oceanic crustal density of 2900 kg/m^3, sediment density of 2300 kg/m^3, continental crustal density of 2700 kg/m^3, and mantle density of 3300 kg/m^3. We define differential density, $\Delta\rho$, by subtracting the lateral average of each layer from the true density of each prism in that layer. The prior densities, when applied, match those differential densities. The standard deviation of the priors, when applied, are 5 kg/m^3 for seawater, 80 kg/m^3 for the sedimentary and crustal rocks, and 100 kg/m^3 for the mantle.

The results for these synthetic tests are summarized in Figs. A.1-A.4, which show gridded results for each combination of α and ζ in panels corresponding to the order(s) of Tikhonov regularization used (panel rows) and the set of priors used (panel columns). Gray regions demarcate α and ζ combinations where the regularization strength is too low to produce stable results. The minimum of each test for both the mean absolute error (MAE) on the gravity and the MAE on the model parameters is plotted in each of these figures as well. Fig. A.1 depicts the MAE between the true gravity field of the synthetic model and the gravity predicted by the recovered density distribution. Changes in the gravity misfit are much more dependent on the order of regularization than they are on the presence of a prior. For first order Tikhonov alone, the misfit increases dramatically above α values of 10^4 because the model becomes too flat to correctly reproduce the shorter wavelength variations in the gravity field. For second order Tikhonov, stability is achieved at ζ values of 10^2 in cases with limited priors, above which the gravity error remains reasonably low until α values of about 10^7. For the combination of first and second order Tikhonov, the error remains reasonably low until an α value of 10^7 and between ζ values of 10^{-1} and 10^3. The lowest error on the gravity amongst all the tests is about 1.29 mGal, which is less than the noise level of 1.7 mGal, and occurs for the case of first order Tikhonov with no priors for $\alpha = 10^0$ and $\zeta = 10^{-1}$. The lowest gravity error occurs for the case of no priors because without priors the model is allowed to take whatever shape it must, subject to the smoothness constraint, to fit the data, again highlighting the inherent non-uniqueness of the gravity.

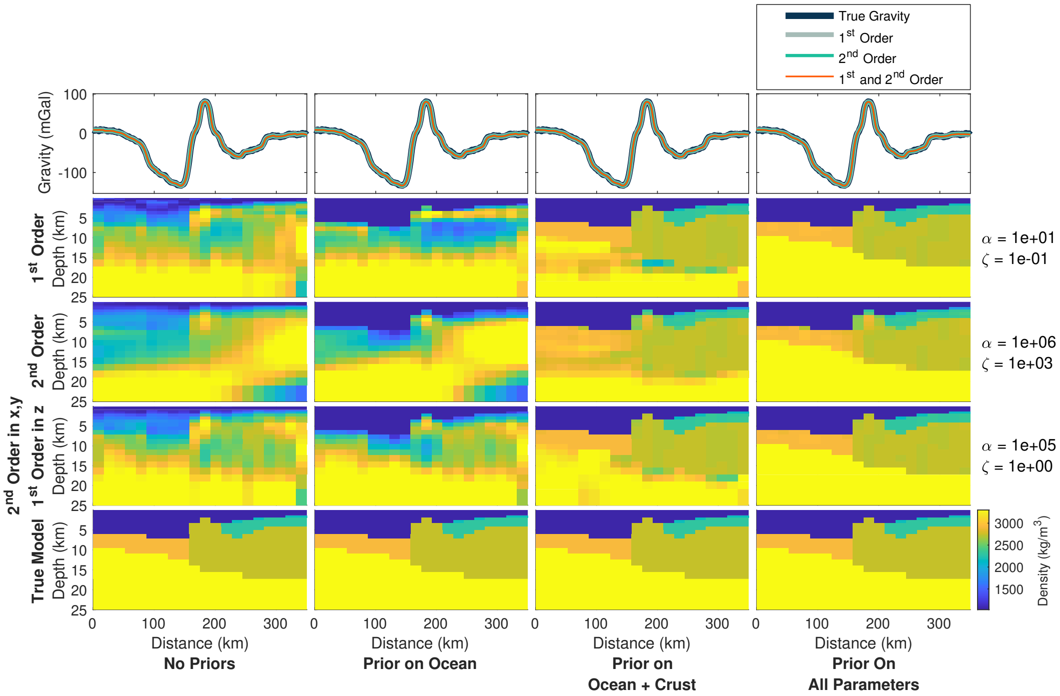

Figure 2.1: Representative cross-section in the x-direction of the synthetic inversion results for α, ζ combinations that produce some of the lowest errors for their respective order of Tikhonov regularization, as determined by comparing the test results depicted in Figures A.1-A.4. **Row 1**: gravity profiles for each of the three cases depicted in the panels below. Dark blue line: true gravity produced by the synthetic model, with noise; gray line: gravity from inversion using only first order Tikhonov; light blue line: gravity from inversion using only second order Tikhonov; orange line: gravity from inversion using second order Tikhonov in the horizontal and first order in the vertical. **Row 2**: cross-sections of the density model recovered from using only first order Tikhonov with $\alpha = 10^1$ and $\zeta = 10^{-1}$ for the cases of no priors, priors only on the ocean water parameters, priors on the ocean and crustal parameters, and priors on all parameters. **Row 3**: cross-sections of the density model recovered from using only second order Tikhonov with $\alpha = 10^6$ and $\zeta = 10^3$ for each of the different prior cases. **Row 4**: cross-sections of the density model recovered from using a combination of first and second order Tikhonov with $\alpha = 10^5$ and $\zeta = 10^0$ for each of the different prior cases. **Row 5**: cross-section of true synthetic density model for comparison.

However, to achieve a geologically reasonable model, priors must be applied. For the case of enforcing a prior on all parameters, the minimum gravity error is still only 1.36 mGal, so the fit to the gravity data is not compromised by adding priors, while the fit to the true density model is dramatically improved. Fig. A.2 illustrates the MAE between the predicted model parameter values and the true model parameter values of the known density model. For most combinations of different regularization orders and priors, too small of an α or ζ value and the regularization is not strong enough to provide a smooth and continuous density distribution, yielding nonphysical fluctuations in the density values (Figs. 2.1 and 2.2, columns 1 and 2). Alternative cross sections with results using different regularization strengths are

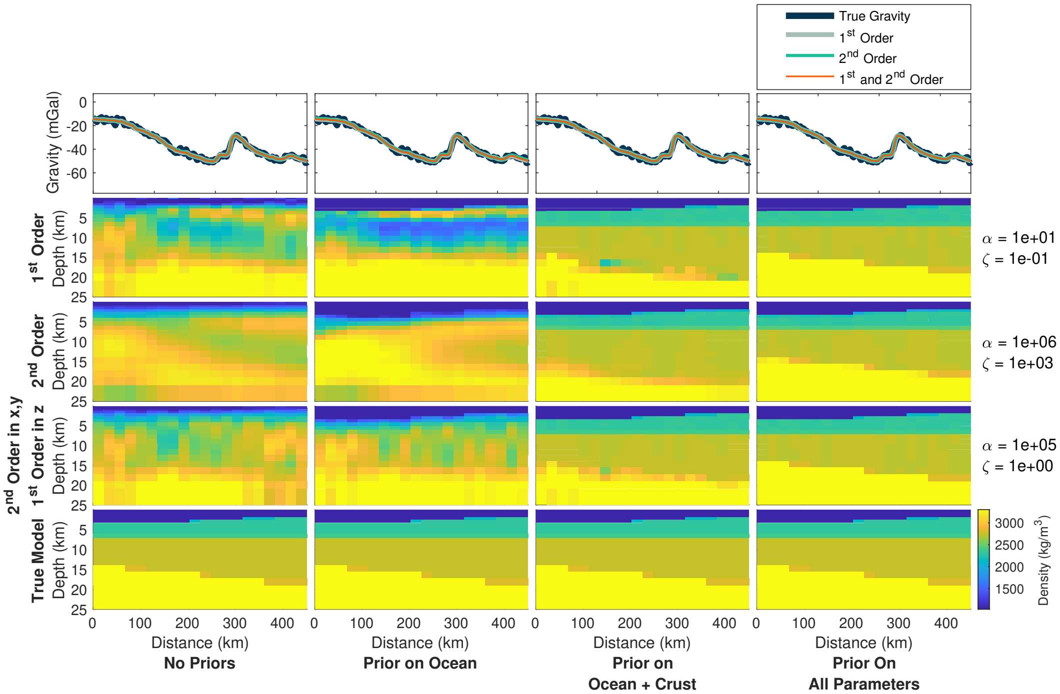

Figure 2.2: Representative cross-section in the y-direction of the synthetic inversion results for α and ζ combinations that produced some of the lowest errors for their respective order of Tikhonov regularization, as determined by comparing the test results depicted in Figures A.1-A.4. **Row 1**: gravity profiles for each of the three cases depicted in the panels below. Dark blue line: true gravity produced by the synthetic model, with noise; gray line: gravity from inversion using only first order Tikhonov; light blue line: gravity from inversion using only second order Tikhonov; orange line: gravity from inversion using second order Tikhonov in the horizontal and first order in the vertical. **Row 2**: cross-sections of the density model recovered from using only first order Tikhonov with $\alpha = 10^1$ and $\zeta = 10^{-1}$ for the cases of no priors, priors only on the ocean water parameters, priors on the ocean and crustal parameters, and priors on all parameters. **Row 3**: cross-sections of the density model recovered from using only second order Tikhonov with $\alpha = 10^6$ and $\zeta = 10^3$ for each of the different prior cases. **Row 4**: cross-sections of the density model recovered from using a combination of first and second order Tikhonov with $\alpha = 10^5$ and $\zeta = 10^0$ for each of the different prior cases. **Row 5**: cross-section of true synthetic density model for comparison.

shown in supplementary Figs. A.5 and A.6. For α values that are too large, the solution smooths over any density variations almost entirely. For cases with no priors or limited priors, the misfit decreases with increasing ζ, but for cases with more priors, the misfit begins to increase again with larger ζ values after achieving its minimum. However, the misfit decreases overall as we apply more priors throughout the model domain, starting with the ocean. Though the results from applying a prior only to the ocean do not look dramatically improved over the case of no priors, in practice, the prior on the ocean is one of the most important constraints because it is the most certain. It eliminates any need for the model to determine where the seafloor is and forces the inversion to put higher densities in the crust and mantle where they belong.

This is evident in the cross-sections in Figs. 2.1 and 2.2. The minimum absolute error on the model parameters amongst all tests is approximately 10.1 kg/m^3 and occurs when using priors on all parameters and $\alpha = 10^1$, $\alpha = 10^4$, and $\alpha = 10^4$, and $\zeta = 10^{-3}$, $\zeta = 10^1$, and $\zeta = 10^{-1}$ for first, second, and combination-first-and-second Tikhonov, respectively.

Comparing the MAE of the model parameters, given the known density distribution, to the standard deviation of the model parameters as determined from the diagonal of the covariance matrix (Fig. A.3) allows us to determine how the covariance matrix reflects uncertainty in the presence of *a priori* model constraints. For all cases except that of second order Tikhonov with no priors, the posterior standard deviation on the model parameters decreases with increasing α and ζ and is consistently lowest for the case where priors are enforced on all model parameters. For the α and ζ values where the MAE on the model parameters was lowest (red square in Fig. A.2, lower right panel), the mean posterior standard deviation on the model parameters is comparatively 56.3 kg/m^3, a value that, while higher, is still reasonably within a range necessary to distinguish one rock layer from another. The standard deviation from the covariance matrix continuously decreases with increasing regularization, while the MAE starts to increase after some minimum when priors are applied, because unlike with the MAE, the minimization in the gradient or curvature between the model parameters enforced by the Tikhonov regularization tends to dominate the definition of the covariance matrix. As the weight of regularization increases, the Tikhonov component of the misfit equation (Equation 2.13) is reduced, and as such, the posterior covariance is reduced as well. Too large of an α or ζ value can cause over-smoothing of the model parameters, and as such the standard deviation of the posterior solution is not always as accurate an estimator of the error on the model parameters away from the "correct" density distribution as the MAE is. However, because we do not know the correct density distribution in a study with real data, as we do in the synthetic tests, we can only use the α and ζ combination of the minimum MAE from the synthetic models as a proxy for what the ideal regularization coefficients must be in order to produce the best geological model. The covariance matrix still provides information on how well the model parameters are estimated, but we should expect errors as high as around 50 – 60 kg/m^3 to be indicative of a good model because we do not want to fully minimize the Tikhonov component.

We can also use the resolution matrix **R** to quantify how much we have actually learned about the subsurface density structure from inverting the gravity data, as opposed to what we already knew from our prior. The mean resolution of all the model parameters for each of the tests is depicted for each combination of α and ζ in Fig. A.4. The resolution should be interpreted as the fraction of that model parameter estimate that can be attributed to the inversion of the gravity data itself, as opposed to the prior. Resolution values close to 1 mean the model is well resolved by the gravity, not the prior. Hence, the tests for the case of no priors have a resolution of 1 because those models are resolved entirely by the gravity. Resolution values close to 0 mean the model is mostly resolved by the prior information alone and not the gravity: i.e., the gravity inversion did not tell us anything we did not already know from the prior. In this way, a resolution of 0 does not necessarily mean the values of the model parameters are wrong in a geologic sense, just that the inversion was not useful. In some regions of the model, such as the ocean layer, where we know the density, it is desirable to have low resolution values because we want these regions to be entirely constrained by the prior and not affected by the inversion. As such there is a clear relationship between the MAE on the model parameters and the resolution: lower σ_p (i.e., a stronger prior) correlates with lower resolution and hence lower MAE on the model parameters. Going from the case of no priors to that of priors on all parameters, we can clearly see that the dependence on the prior increases for a greater number of α, ζ combinations as expected (Fig. A.4). We can also see that the more or the stronger priors we apply, the less regularization is needed to produce a stable and reasonable model (Fig. A.5).

Ideally, we are trying to obtain a model that both best fits the gravity and matches the prior data and so we neither want a model that is entirely determined by the gravity nor entirely determined by the prior. Thus, a very high resolution is not necessarily ideal. Rather, we would expect resolution to increase with distance from the locations where we have prior constraints, exhibiting a spatial dependence. Therefore, a mean resolution somewhere in the middle may be considered reasonable, which is consistent with α and ζ values in the range of 10^4–5×10^6 and 10^{-1}–10^1, respectively (Fig. A.4), as well as the best α and ζ values as determined by the MAE on the model parameters (Fig. A.2). As an example, representative cross sections of the 3D model results, using $\alpha = 10^1$ and $\zeta = 10^{-1}$ for first order, $\alpha = 10^6$ and $\zeta = 10^3$ for second order, and $\alpha = 10^5$ and $\zeta = 10^0$ for combination first and second order, are shown in Figs. 2.1 and 2.2. Similarly, representative cross-sections of the 3D model domain using α and ζ values that produced the lowest MAE on the model parameters for each of the different combinations of regularization order and priors are shown in Figs. A.5 and A.6. The top panel shows the predicted gravity profile produced by each of the models against the true gravity calculated from the known density model. The subsequent three rows depict the resulting models for first, second, and combination first and second order Tikhonov, respectively. The bottom panel illustrates the corresponding cross-section of the true synthetic density model that we are trying to recover in each of these inversions, for comparison. Different α, ζ pairs are ideal for different orders of Tikhonov regularization. Higher regularization constants are needed for second order Tikhonov; those same coefficients would, on the other hand, over-smooth the first order models.

For these combinations of α and ζ, the accuracy of the resulting density models changes drastically across the different applied priors. However, the gravity signal for each model is essentially the same and matches the true gravity well, with an MAE of only about 1.3 to 1.4 mGal for each case, demonstrating the effective non-uniqueness of the gravity (Figs. 2.1 and 2.2, Row 1). Thus, priors are necessary to improve the model. When priors are applied to all parameters, all three regularization options recover the known density model, though at higher values of α, combination first and second order Tikhonov is better at recovering the density distribution. Ultimately, the recovered model is more sensitive to changes in ζ than in α, and for low values of α, first order regularization appears sufficient. However, across all tests, the combination of first and second order Tikhonov consistently produced the most stable results and was the most successful at recovering the known density distribution. Moreover, increasing the resolution of the subsurface model (i.e., adding more model parameters) tends to require increasing the regularization strength, so the combination first and second order Tikhonov is more stable for larger models, as first order becomes too strong, flattening out the model completely, at large α values.

Even without any priors, some semblance of the structure is recovered for the example in Fig. A.5 when using first order regularization, though with such using high α values, structure is better recovered when using the first and second order combination. For first and second order, there is often an unrealistic degree of fluctuation in the density values for the case of no priors and priors only on the ocean (Figs. 2.1 and 2.2). Different combinations of the α and ζ values can yield similarly satisfactory models, but based on the above results for the MAE on the gravity and model parameters and the covariance and resolution matrices, and considering the increase in model resolution for the regional study, using a combination of first and second order Tikhonov with $\alpha = 10^5$ or $\alpha = 10^6$ and $\zeta = 10^0$ with priors of varying certainty on all parameters produces the best results. These are the values that will be applied to the subsequent regional case study of the Puysegur region offshore southern New Zealand.

2.4 Application to the Puysegur Region

Gravity inversion of an active tectonic margin is challenging because of the complicated structures and source geometries and the sharp lateral changes in density across the boundary. Those very compositional contrasts across and along such an active margin play a large role in governing the tectonic processes taking place. Because dynamic processes often dominate the gravity field and influence local topography, gravity modeling at these locations can shed light on important aspects of subduction (Toth and Gurnis, 1998; Krien and Fleitout, 2008). The Puysegur subduction zone is an attractive test case for subduction initiation in particular because of its young age and the transition from developed subduction in the north to incipient underthrusting in the south (Gurnis et al., 2019; Gurnis et al., 2004). As such, the margin provides a progressive snapshot of the subduction initiation process along strike. Puysegur also exhibits unusual gravity anomalies, the origin of which can inform us about the regional dynamics and motivates detailed study of Puysegur with a gravity inversion.

2.4.1 Regional Setting

The Puysegur-Fiordland subduction zone lies at the northern end of the Macquarie Ridge Complex (MRC) and the southern tip of South Island, New Zealand. Present day plate motion is predominantly dextral strike-slip, with highly oblique subduction of the Australian Plate (AUS) northeastwards beneath the Pacific Plate (PAC) at the Puysegur Ridge and Fiordland (Fig. 2.3a; DeMets et al. (2010) and Sutherland (1995)). The Puysegur margin has evolved from a spreading ridge into a subduction zone. Spreading along the PAC-AUS margin began approximately 45 Ma, then became increasingly oblique as the AUS-PAC Euler pole migrated to the southeast during the Miocene, eventually rotating into a strike-slip plate boundary (Lebrun et al., 2003; Sutherland, 1995). This evolution is evident in the curvilinear fracture zones that merge along the MRC and are prominent in the gravity field and bathymetry. Oblique convergence led to subduction beneath the Fiordland boundary starting around 16-10 Ma, beneath the northern extent of the Puysegur segment about 11-8 Ma, and beneath the southernmost extent of the Puysegur Ridge within the last several million years (Sutherland et al., 2006; Lebrun et al., 2003).

The crustal structure and tectonics related to the above kinematic history were investigated in detail with seismic reflection, seismic refraction, and bathymetric mapping during the recent South Island Subduction Initiation Experiment (SISIE) (Gurnis et al., 2019). Puysegur has the advantage of being a small subduction zone with a well known plate kinematic history before and during subduction initiation, making it accessible for studying the process of subduction initiation and for constructing a regional gravity inverse model at a relatively high resolution.

The margin possesses distinctive, high amplitude gravity anomalies, which as of yet have poorly constrained structural and compositional interpretations and which have implications for the dynamic processes taking place in the region. The MRC is characterized by long and narrow bathymetric and gravitational highs and lows along strike (Fig. 2.3B). The southern part of Puysegur Ridge is characterized by a 100 to 150 mGal gravity high adjacent to the -100 to -150 mGal gravity low of the trench. In contrast, a significant approximately -150 mGal gravity low exists over the northern Puysegur Ridge, a region known as the Snares Zone (Fig. 2.3; Gurnis et al. (2019)). This region is of particular interest in our gravity inversion because it has subsided with respect to the rest of Puysegur Ridge by nearly 2 km (Collot et al., 1995). If composed of buoyant crust, this subsidence has implications for the subduction initiation process and the force balance on the system. In addition to addressing questions about these anomalies, gravity modeling can help stitch together the information obtained seismically to provide a more complete 3D picture of the structures and rock types in the region.

2.4.2 Prior Geophysical Constraints

Prior constraints on a gravity inversion can come from a number of geophysical data, including seismic, bathymetric, borehole data and more. For the investigation of the Puysegur subduction system, we utilize bathymetric and seismic data collected from the SISIE marine geophysical expedition (Gurnis et al., 2019; Shuck et al., 2021), as well as sediment thickness estimates from the NOAA sediment thickness database (Straume et al., 2019), to constrain the gravity inversion. These data include the regional NIWA bathymetry grid (Mitchell et al., 2012), horizons picked from seismic reflection profiles, and seismic velocity models constructed from ocean bottom seismometer (OBS) seismic refraction analysis (Gurnis et al., 2019; Shuck

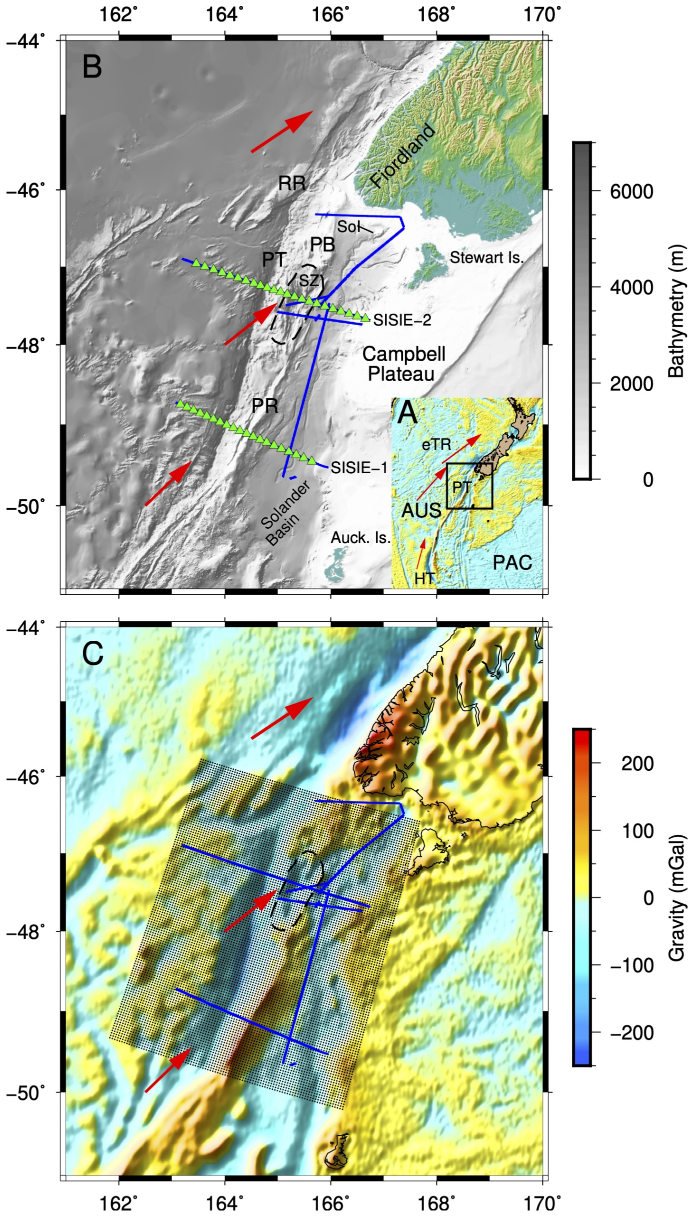

Figure 2.3: Puysegur survey area. **A**. Puysegur survey area, outlined by the black rectangle. The Macquarie Ridge Complex is the long, narrow gravity high/low feature running between the Australian (AUS) and Pacific (PAC) plates from the Hjort Trench (HT) in the south to the Puysegur Trench (PT) in the north. eTR is the extinct Tasman Ridge. Base map is free-air gravity (Sandwell et al., 2019). **B**. Bathymetry of Puysegur region from the NIWA grid (Mitchell et al., 2012). Solid blue lines are MCS lines. Triangles represent the locations of OBS. SISIE-1 and SISIE-2 are combined OBS and MCS lines. Black dashed line outlines the Snares Zone (SZ) bathymetric low. RR: Resolution Ridge; Sol: Solander Island; PB: Puysegur Bank; PR: Puysegur Ridge; and PT: Puysegur Trench. Red arrows are the modern relative plate motion (DeMets et al., 2010) of the AUS plate with respect to the PAC. **C**. Satellite free-air gravity for the Puysegur study region from the Sandwell et al. (2019) global marine gravity grid, v. 29.1. Labels, seismic lines, and plate motion vectors are the same as in A and B. The grid of black dots are the locations of the gravity data points used in the inversion.

et al., 2021). The NIWA grid is based only on shiptrack multibeam data and not calculated from the gravity like the global bathymetry datasets. This ensures the prior remains independent of the gravity data.

The seismic velocity models were constructed using a tomographic inversion of marine seismic refraction data gathered during the SISIE cruise. A total of 43 short-period OBSs were deployed on two east-west transects across the Puysegur Trench (Fig. 2.3a). The wide–angle seismic data records show reflected and refracted arrivals that help constrain the seismic velocities, depth to basement, and Moho of both the Australian and Pacific Plates. We correlated arrival times between neighboring stations to identify refracted and reflected phases and checked the reciprocity on opposite source-receiver pairs. The average maximum source-receiver offset at which we observed seismic refractions was 80 km. We assigned travel-time uncertainties between 40 and 150 ms to account for noise on wide-angle data. We applied a regularized tomographic inversion of the wide-angle travel times to image the seismic velocities of the crust and uppermost mantle along the two transects (Van Avendonk et al., 2004). The resulting seismic velocity models for SISIE-1 and SISIE-2 have an rms data misfit of 90 ms and 80 ms, respectively, which is comparable to the assigned data errors.

The 2-D seismic velocity images along SISIE-1 and SISIE-2 show the nature of the oceanic crust of the incoming AUS plate and the crustal structure of the overriding Puysegur Ridge and Solander Basin (Fig. 2.4). In the deeper parts of the basin, the top of basement was constrained by wide-angle seismic refractions. However, we determined the depth to basement from multichannel seismic reflection images (Shuck et al., 2021) where the sediment cover was thin. We were able to determine the Moho depth outboard of the trench on the AUS plate and beneath the Solander Basin. However, the thickness of Puysegur Ridge is not well resolved from the OBS refraction data alone because the observed wide-angle refractions did not turn to such depths near the plate boundary. The gravity model can thus help constrain the thickness of the crust at the ridge. Nevertheless, Moho depths as determined from the seismic velocity models (deeper bold gray line in Fig. 2.4) are included in our prior. Like the other horizons, the Moho is not a 'hard' constraint but rather a probabilistic constraint on where the top of mantle is most likely to be. This flexibility is a reflection of the fact that there is uncertainty in the seismic data, and the Bayesian method means we do not have to take it completely at face value. The seismic velocities along SISIE-1 and SISIE-2 (Fig. 2.4) confirm that relatively

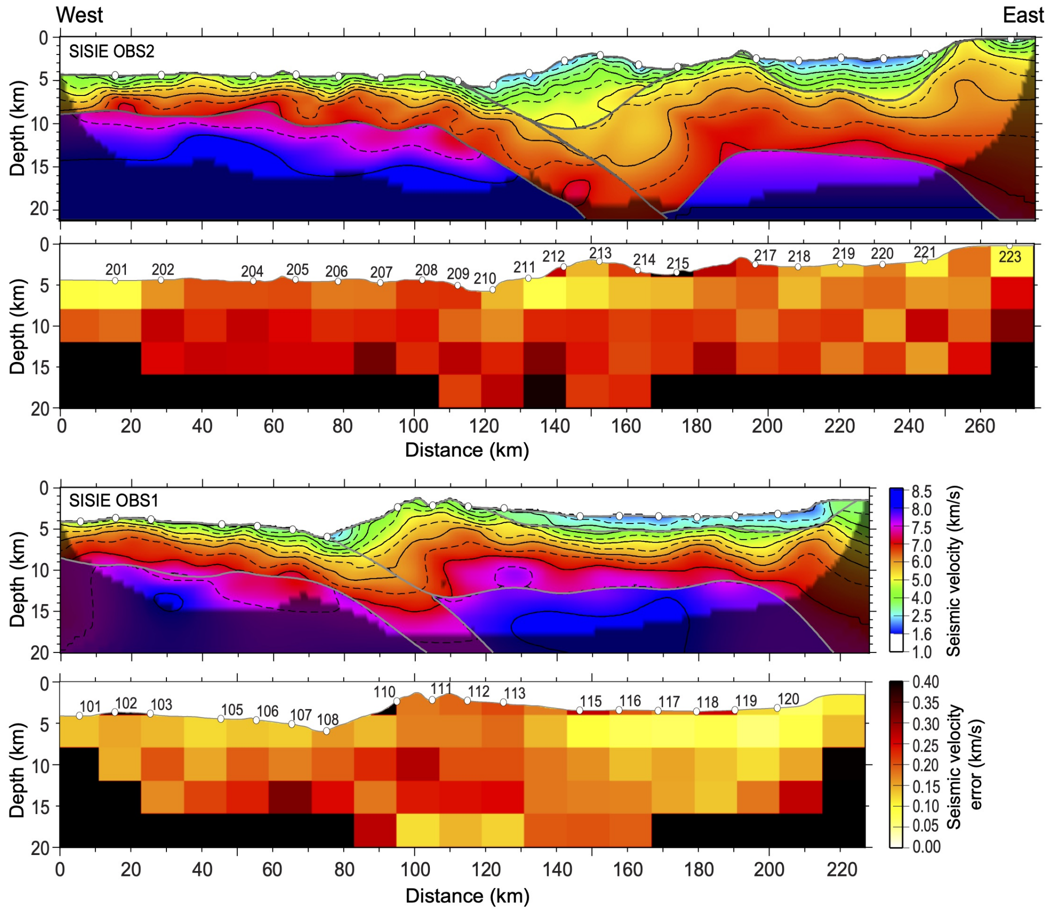

Figure 2.4: Seismic velocity models used in the prior. **A, C**. Seismic velocity profiles for OBS lines SISIE-2 and SISIE-1, respectively. Gray lines are the sediment-basement contact and Moho interpretations. White dots are the locations of OBS. Dark shaded area is where the model has unreliable resolution. **B, D**. Standard deviation of the seismic velocities based on seismic ray tracing for OBS lines SISIE-2 and SISIE-1, respectively. Black regions indicate areas with unreliable velocities. White dots are the locations of OBS and their corresponding numbers.

thin oceanic crust of the AUS plate has higher seismic velocities than the rifted continental crust of the PAC plate (Gurnis et al., 2019). Consequently, there should be a substantial density contrast across the margin that should be evident in the gravity. The composition of Puysegur Ridge appears predominantly continental as well, though this is questionable and a point of interest for the gravity inversion.

Based on the seismic velocities, we can constrain the thickness of the incoming AUS plate to be about 7 km, with isolated pockets of sediment, usually less than 500 m in thickness. Due to the spatial resolution of the gravity model, sediment on the AUS plate usually does not appear in the model except in places where it is relatively thick. The seismic reflection profiles reveal that sediment thickness in the Solander Basin is as thick as 6 km in places, averaging about 2-3 km for the majority of the basin (Shuck et al., 2021). Between our seismic lines, we also constrain the top of basement using the NOAA global sediment thickness database (Straume et al., 2019). The Snares Zone on the northern end of Puysegur Ridge is filled with up to 1 km of sediment, and both the layering observed in the seismic reflection profiles and the low seismic velocities on the western half of Puysegur Ridge suggest it is composed of deformed sediments, more than 10 km in width and 3 km in depth. However, below about 5.5 km depth, the seismic reflection data are inconclusive as to whether the accretionary wedge consists of sedimentary rock or crystalline basement (Gurnis et al., 2019); the gravity inversion can shed light on the compositions of these rocks.

The decollement between the overriding and subducting plates is visible on the seismic reflection images from SISIE-1 and SISIE-2 (Gurnis et al., 2019; Shuck et al., 2021). This horizon is used to constrain the top of the slab in the prior. The vertical, strike-slip Puysegur fault that cuts through the middle of the Snares Zone also appears to be present in the seismic reflection profiles (Shuck et al., 2021). While this fault is not included in the prior information directly, its presence could explain potential density differences observed in the final model.

We invert the Sandwell et al. (2019) global 1 min marine gravity grid, v. 29.1, for the region within the black grid in Fig. 2.3b, which for the Puysegur region has a standard error of about 1.7-2 mGal (Sandwell et al., 2013; Sandwell et al., 2019). We include horizons that represent the seafloor, the sediment-basement contact, and the interpreted Moho from the velocity models (Fig. 2.4). Seismic velocities along the profile lines were converted to density using the empirical Nafe-Drake equation (Ludwig et al., 1970; Brocher, 2005). Those densities were then extrapolated from the 2D SISIE transects to each model parameter using a 3D interpolation scheme. Likewise, surfaces for the horizons are interpolated from the scattered data points of the 2D seismic data and the basement as determined from sediment thickness. For certain regions of the model, the prisms that fall between certain surfaces are assigned a specific prior. For example, prisms that fall between the AUS basement and Moho are given a prior oceanic crustal density of 2900 kg/m^3 and prisms below the interpreted seismic Moho on the PAC plate are assigned a prior density of 3300 kg/m^3, as the estimated seismic velocity in the models falls below an acceptable resolution below about 15 km depth. Otherwise, the prior densities used are those obtained directly from the velocity conversion.

For the prior, we have the highest degree of certainty on the densities of the prisms that lie along our seismic lines. We estimated the local standard deviation in the seismic velocity model with a forward ray–tracing test. The uncertainty assigned to the model was the range in seismic velocity perturbations that would not raise the travel–time misfit more than 5 ms. These errors are for blocks of 10 km by 4 km. The lowest error is approximately 0.05 km/s and the highest is approximately 0.35 km/s. These standard deviations of the velocities are mapped into density using standard error propagation methods and the Nafe-Drake relationship. We 3D interpolate these density errors to the locations of the prism centroids, which then serve as the starting values for the standard deviations on the prior. Certainty on the parameter values decreases from the initial value as we move away from the seismic lines, which we implement in the model by using a higher standard deviation farther from the lines, allowing the gravity to dominate the resulting density values in areas where we do not have seismic data. This is accomplished with a 3D nearest neighbor algorithm that calculates the distance each prism centroid is from its closest data point. The standard deviation determined from propagation of error is then weighted via a smoothly varying functional - exponential decay of the increasing form - of nearest neighbor distance from the seismic and bathymetric data points. In this way, our prior includes both the error on the initial velocity model and the uncertainty due to spatial separation from our prior information. Horizontal slices of the spatially variable prior uncertainty mapped into 3D space are shown in (Fig. 2.5). The Tikhonov regularization then ensures the model retains a smooth solution laterally, so values everywhere are to some degree constrained by those along the seismic lines. The degree to which the solution values are the result of the prior data or the gravity inversion itself can be visualized in the resolution matrix. The majority of the model domain is determined by gravity data and thus not overly biased by the prior information, except in places where we want it to be, such as in the ocean layer.

Ultimately, the final model has 64,000 model parameters with a horizontal resolution of about 9 km and a vertically increasing resolution of about 110 m to 1130 m. We invert 92,953 gravity data points from the marine gravity grid, using a horizontal second order Tikhonov regularization coefficient of 5×10^6 and a vertical first order Tikhonov regularization coefficient of 10^0. We include priors on all parameters, though with spatially varying standard deviation as described above.

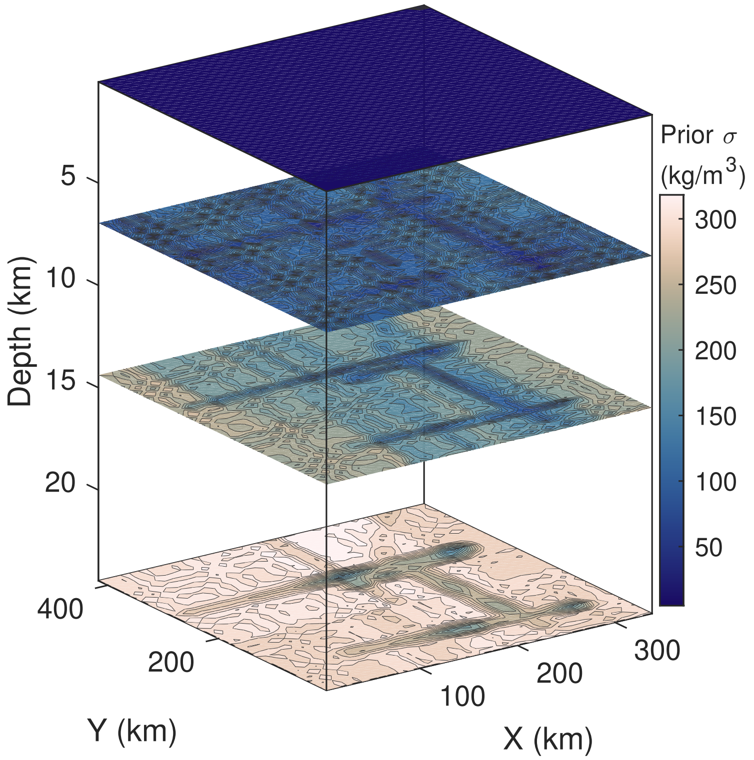

Figure 2.5: Variation of the standard deviation of the prior in 3D space. Because the prior has a higher certainty along the trajectory of the seismic lines, the standard deviation is lowest along the survey lines, and increases exponentially away from the lines and their respective horizons and away from the sea floor. The ocean layer is essentially fixed by the bathymetry and thus has the lowest prior error.

2.4.3 Results

We predict the gravity field from the final density model and compare it to the observed gravity, as well as the residual between the two (Fig. 2.6). The mean absolute error on the gravity produced from the final model is about 3.9 mGals, which is less than 2% of the maximum anomaly in the study area (220 mGal). All the prominent features of the satellite gravity are well-recovered, including the prominent lows in the Snares Zone and the trench and the gravity high over the southern portion of Puysegur Ridge. Some of the finer features in the gravity are not fully recovered due to model resolution. The highest errors on the gravity, as shown by the residual, are mostly concentrated over areas with the largest gravity anomalies and where there is a sharp change in bathymetry, such as over the Puysegur Ridge and the edge of the Campbell Plateau. This is likely due to the trade-off between the regularization trying to smooth features laterally and the inversion trying to match these sharp changes in the gravity and bathymetry. Nevertheless, the highest error on the gravity is only 33.5 mGal, which on the scale of the major anomalies in the study area is still minor.

The model results for the 3D density distribution are presented in representative cross-sections in Figs. 2.7, 2.8, and 2.9, with the prior density distribution and posterior standard deviation plotted for comparison. The resolution and covariance matrices also illustrate the 3D distribution of error in the posterior model (Fig. 2.10). The full resolution matrix exhibits a sharp diagonal with elements close to one, demonstrating that the model parameters are well resolved by the inversion. Looking at only the diagonal components, on the other hand, where each element of the diagonal represents the resolution of a particular model parameter as determined by the gravity, gives us a better sense of how the resolution varies throughout the model domain. As each element is associated with a particular parameter, we can map the diagonal of $\mathbf{R}$ into 3D space (Fig 2.10A). This 3D resolution illustrates which parameters are resolved mostly by the gravity and which are not. The resolution is almost zero in the ocean layer because those parameters are determined entirely by the prior and thus are not resolved by the gravity. The resolution of parameters along the seismic lines is also lower because these parameters are weighted more by the prior. The resolution matrix shows an increase in the degree to which parameters are resolved by the gravity with depth.

However, barring the degree to which the parameters are determined by the prior, there is a fall off in the certainty of the solution with depth, as evident from the posterior covariance matrix, the square root of the diagonal of which is also mapped into 3D space and visualized in Figure 2.10B. This shows the spatial distribution of the standard deviation of the posterior estimate of $\mathbf{m}$. The mean standard deviation on the model parameters as determined from the diagonal of the covariance matrix for the entire model is 17 kg/m^3. There is a fall-off in accuracy with depth, ranging from about 10 – 15 kg/m^3 in the shallow crust along the seismic lines to about 30 kg/m^3 on average in the deepest layer. The maximum model parameter standard error is 68 kg/m^3, concentrated at the bottom and at the edges of the model, where there is less coverage by the gravity data and less constraint by the prior.

The most notable features of the final density model are the densities and structures of the Snares Zone and along Puysegur Ridge. The inversion requires a low density body beneath the central and eastern portion of the Snares Zone, extending to about 18-20 km depth (Fig. 2.7 and 2.9) and is mostly consistent with the prior velocity models. However, the western half of Puysegur Ridge, below about 5.5 km depth, is

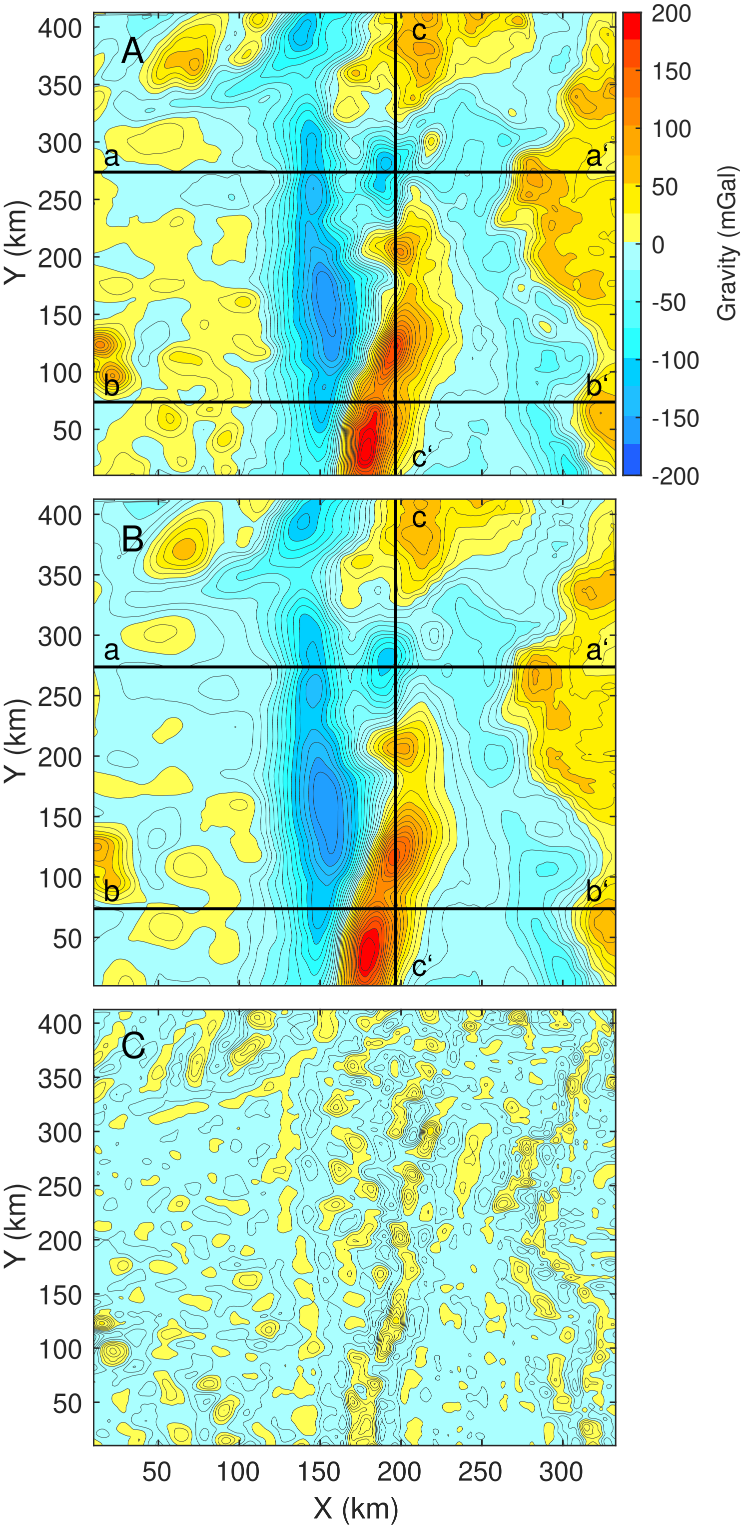

Figure 2.6: Gravity results for the final model. **A**. Observed gravity field as extracted from the Sandwell et al. (2019) gravity grid, v 29.1. Black lines are the locations of cross-sections shown in Figs. 2.7, 2.8, and 2.9. **B**. Gravity predicted from the final density model determined by the inversion. **C**. Residual gravity between the observed and predicted gravity grids, calculated as the absolute difference between each point on the grid.

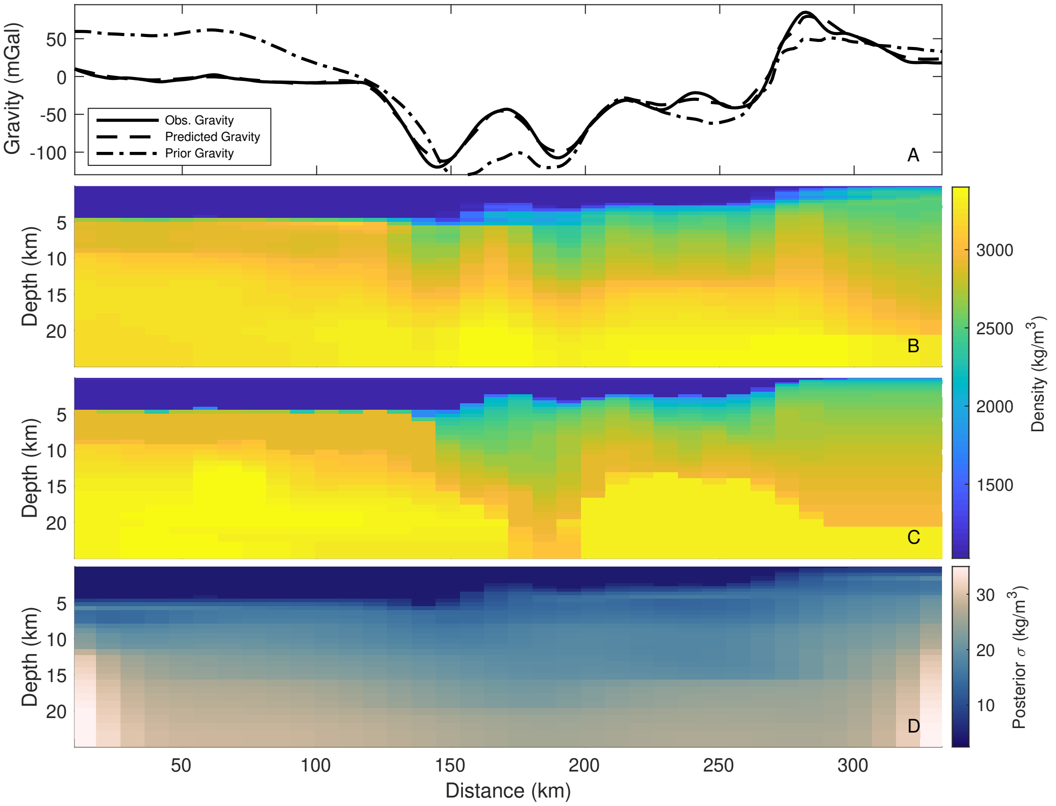

Figure 2.7: East-west cross section of the final 3D density model for line a-a' in Fig. 2.6, roughly parallel to seismic line SISIE-2. **A**. Gravity profiles for the density cross-section. Solid line is the observed gravity; dashed line is the predicted gravity from the final model slice shown in panel B; dashed-dotted line is the gravity from only the prior density model (panel C). **B**. Predicted density distribution from the gravity inversion. **C**. Prior density distribution used to constrain the gravity inversion. **D**. Posterior standard deviation of the density of each prism shown in the cross-section, as determined from the posterior covariance matrix. Colorbar is saturated at 35 kg/m^3. B and D together represent the posterior distribution for the model parameters shown in this cross-section.

consistently higher density than predicted from the velocity models. The southern cross section (Fig. 2.8), on the other hand, shows an elevated mantle beneath the Puysegur Ridge, more–so than suggested by the velocity prior. In all cases, we are mostly unable to resolve a slab structure, despite its presence in the prior.

To get a broad sense of the density and crustal variations within the final model, as well as how they compare to the prior and the seismic velocities, we look at the posterior densities of each prism versus their respective V_p values used to determine the prior (Fig. 2.11). The points are colored by the block of the model in which they reside, as determined by interpolating surfaces between the horizons on the seismic reflection lines from the SISIE survey. Based on these surfaces, prisms are either in the sediments (gray points), the AUS plate crust (blue points), or the PAC plate crust (burnt orange points); prisms within the mantle are not shown

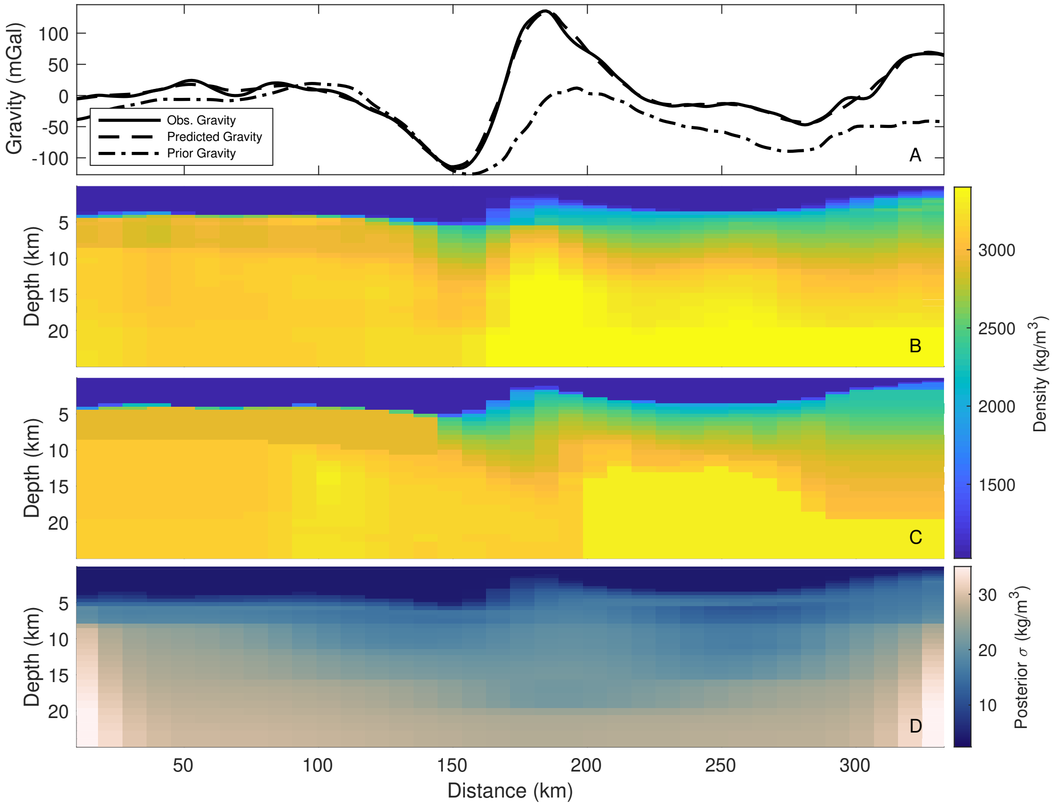

Figure 2.8: East-west cross section of the final 3D density model for line b-b‘ in Fig. 2.6, roughly parallel to seismic line SISIE-1. **A**. Gravity profiles for the density cross-section. Solid line is the observed gravity; dashed line is the predicted gravity from the final model slice shown in panel B; dashed-dotted line is the gravity from only the prior density model (panel C). **B**. Predicted density distribution from the gravity inversion. **C**. Prior density distribution used to constrain the gravity inversion. **D**. Posterior standard deviation of the density of each prism shown in the cross-section, as determined from the posterior covariance matrix. Colorbar is saturated at 35 kg/m^3. B and D together represent the posterior distribution for the model parameters shown in this cross-section.

for clarity. There is scatter even in the prior data points because only the prisms lying along the seismic lines were converted directly with the Nafe-Drake equation; the other prism densities are then 3D interpolated. The scatter is greatest within sedimentary units where rocks can vary over a relatively large range of densities and where there is substantial shallow structural complexity from the velocity models for the interpolation to accommodate. To more clearly illustrate the variation in structure along the ridge, we also determine the Moho depth from the density model, interpreted at the points where the density first exceeds 3200 kg/m^3 (Fig. 2.12B). We also compute the crustal thickness (Fig. 2.12C) by subtracting the bathymetry (Fig. 2.12A) from the Moho. The crust is notably thicker beneath the Snares Zone, about 18 km thick, than it is beneath the southern part of Puysegur Ridge, where it is as thin as 7-8 km. The Moho shallows to around 10-12 km depth under the

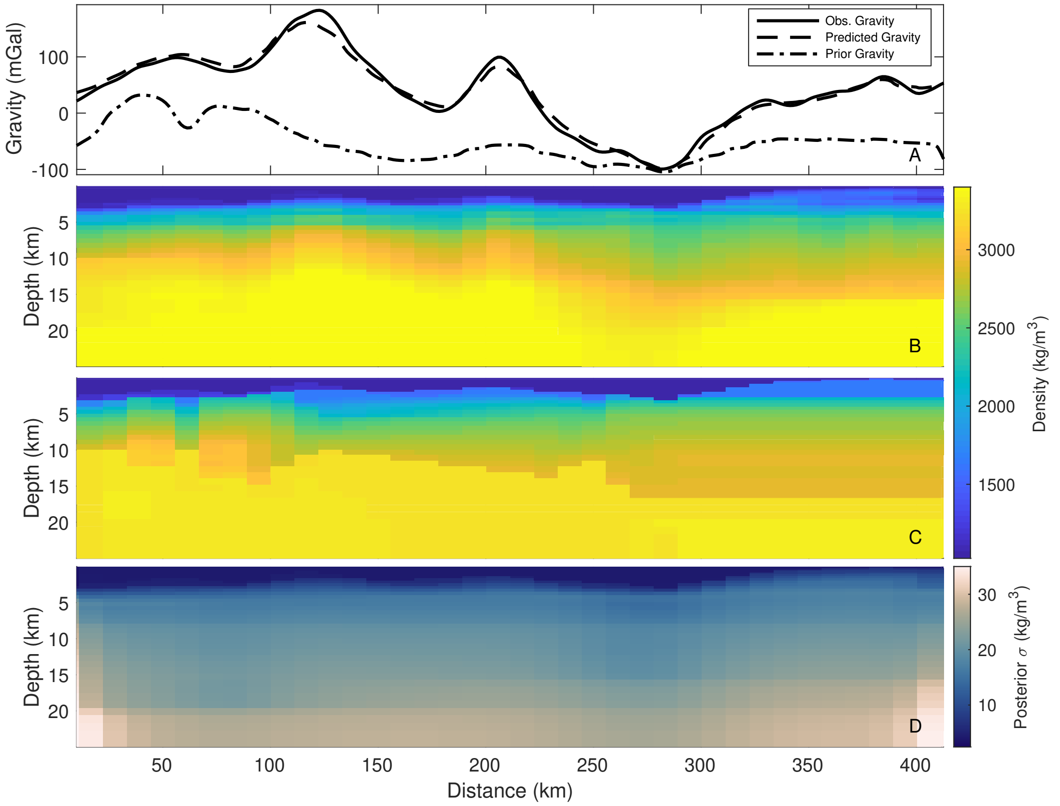

Figure 2.9: North-south cross-section of the final 3D density model for line c-c‘ in Fig. 2.6, roughly parallel to the Puysegur Ridge. **A**. Gravity profiles for the density cross-section. Solid line is the observed gravity; dashed line is the predicted gravity from the final model slice shown in panel B; dashed-dotted line is the gravity from only the prior density model (panel C). **B**. Predicted density distribution from the gravity inversion. **C**. Prior density distribution used to constrain the gravity inversion. **D**. Posterior standard deviation of the density of each prism shown in the cross-section, as determined from the posterior covariance matrix. Colorbar is saturated at 35 kg/m^3. B and D together represent the posterior distribution for the model parameters shown in this cross-section.

southern part of the Solander Basin and deepens to about 18 km in the northern part of the Basin, and even further to 23 km or greater beneath the Campbell Plateau.

2.5 Discussion

The method of linear 3D gravity inversion can be applied not only to simple, local scale structural geometries, but also complex density distributions across active plate margins. The Bayesian method allows for direct inclusion of existing geophysical data as priors and statistical feedback on the quality of the final model. Due to the non-uniqueness of gravity, which is clearly demonstrated by the relative insensitivity of the predicted gravity to changes in the prior (Figs. 2.1 and 2.2), the final model is ultimately dependent on the prior and the strength of the regularization.

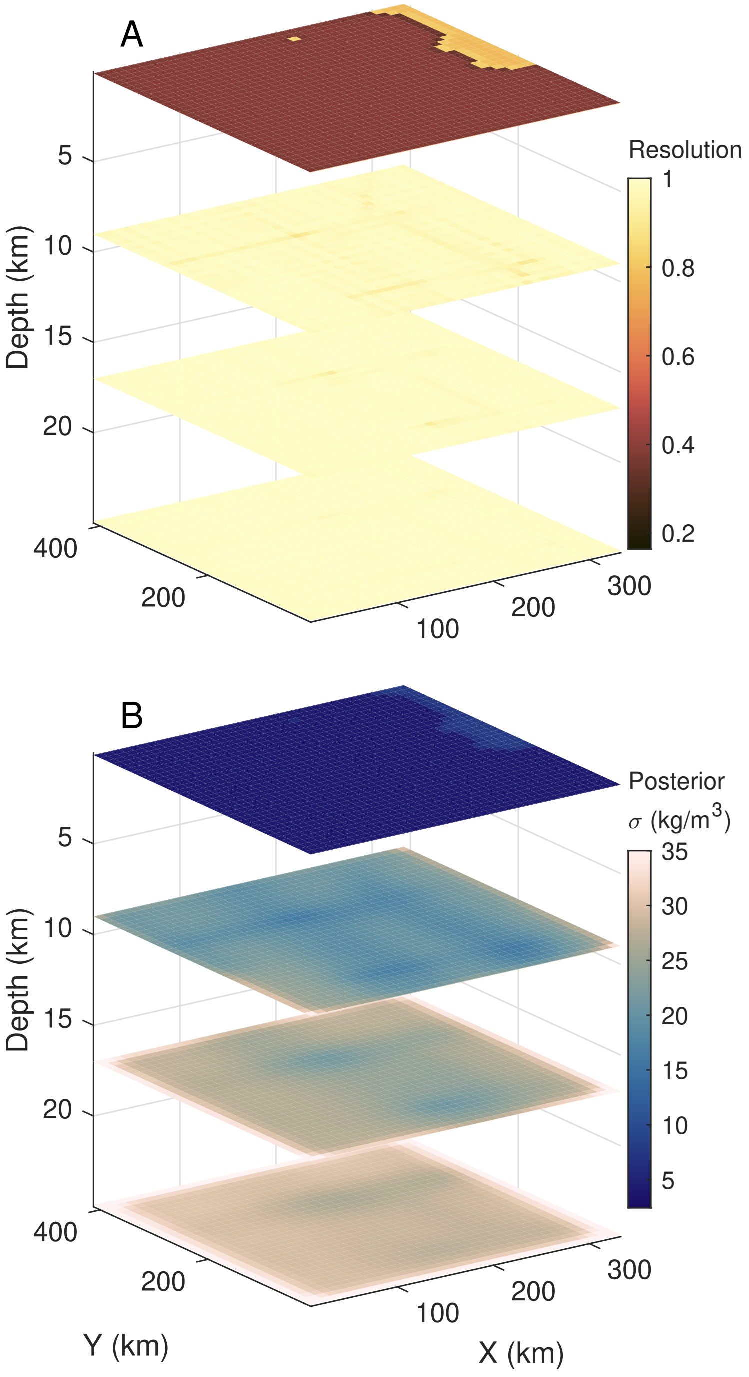

Figure 2.10: 3D mapped resolution and covariance matrices. **A**. Diagonal of the resolution matrix mapped into 3D space. Slices are shown at depths of 1, 9, 17, and 25 km. The resolution represents the fraction of each model parameter value that is resolved by the gravity as opposed to the prior information. **B**. Posterior standard deviation of the model parameters (square root of the diagonal of the covariance matrix) mapped into 3D space. Slice depths are the same as in A. Colorbar is saturated at 35 kg/m^3.

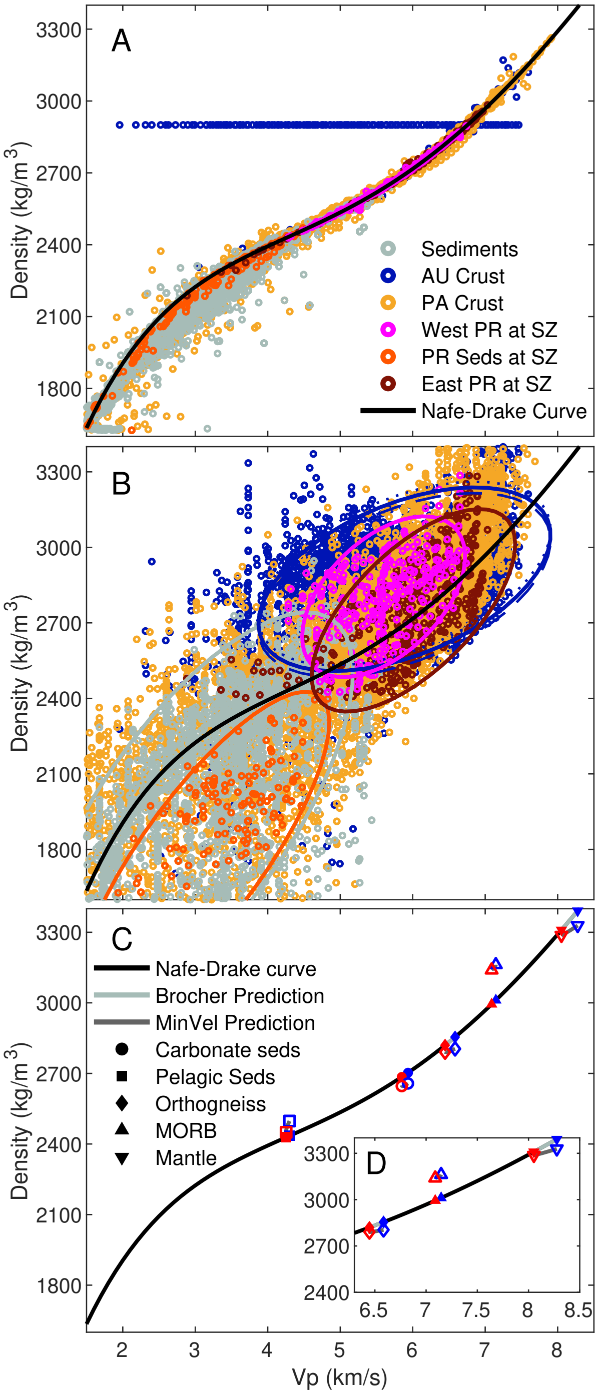

Figure 2.11: Density vs. V_p relative to the Nafe-Drake equation (black line). **A**. Density vs. V_p for the prisms in the prior. Densities were calculated from V_p using the Nafe-Drake equation (black-line) along the seismic lines; the remaining prism centroid densities were 3D interpolated from those points, producing the observed scatter. The prior for the oceanic crust was set to 2900 kg/m^3 instead of using values directly from the equation (blue circles). **B**. Posterior density from the inversion model vs. V_p for each prism centroid. Prisms in the mantle have been omitted for clarity. Colors and their corresponding 2σ error ellipses represent different regions of the model as defined by the structural horizons in the prior. Dotted ellipse represents the shift in the density prediction resulting from low temperature conditions and dashed ellipse represents the shift due to high temperature conditions, as calculated from the MinVel predictions in C. Similar ellipses can be computed for the other crustal blocks, but in all cases, the effect is negligible, so they have been omitted for clarity. Colors are as in A. **C**. Comparison of Brocher (2005) density predictions (filled symbols) to MinVel density predictions (open symbols) for low (surface) temperature conditions (blue symbols) and hotter (25 km depth) temperature conditions (red symbols) for characteristic rock types present in the model domain. Carbonate and pelagic sediment compositions are estimated from values in Li and Schoonmaker (2003) and Patel et al. (2020). Composition of Fiordland Orthogneiss, taken to represent regional continental crustal rock, is from Bradshaw (1990). Composition of MORB and harzburgitic mantle is from Hacker et al. (2003).

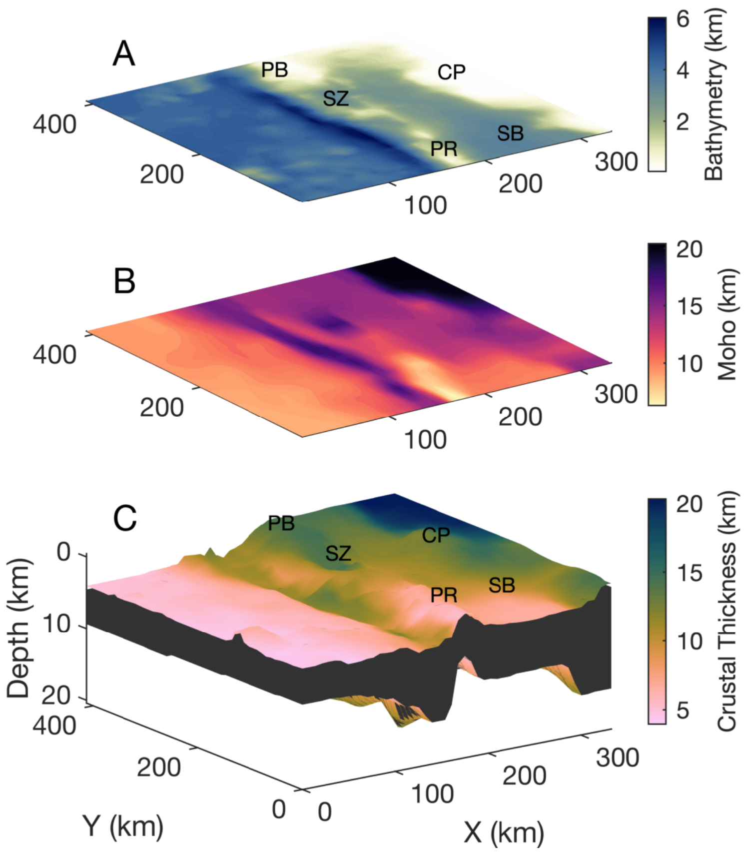

Figure 2.12: **A**. Bathymetry for the Puysegur study area used in the computation of crustal thickness. PB: Puysegur Bank; SZ: Snares Zone; CP: Campbell Plateau; PR: Puysegur Ridge; and SB: Solander Basin. **B**. Moho depth interpreted from the 3D density model at the points where the density first exceeds 3200 kg/m^3. **C**. Crustal thickness for the Puysegur study area calculated by subtracting the bathymetry from the Moho depth and overlain on the bathymetric surface. The crustal volume is filled to the base of the crust using the Moho surface in B. Text labels are as in A.

The synthetic tests demonstrate how the resulting models are often more sensitive to changes in regularization than they are the geophysical prior. The 3D resolution matrix likewise shows how different parameters are determined more by the prior than by the gravity or vice versa. The Tikhonov regularization is a smoothness prior and goes into the definition of the resolution matrix (Eq. 2.16), so when a parameter has a low resolution, the inversion is more strongly constrained by the existing geophysical information *and* the smoothness requirement than by the gravity. Differentiating the degree to which that parameter is determined by the geophysical prior versus the regularization is more difficult. Nevertheless, the majority of the model domain is resolved predominantly by the gravity data. Only within the ocean layers and along the shallow portion of the seismic lines does the prior dominate the posterior solution, demonstrating that in the regions where we do not have seismic coverage, and to some extent in the regions where we do, we have learned something from the gravity.

Ultimately, the goal of obtaining a realistic density model from the inversion is to place constraints on the composition of key features and structures that control subduction and subduction initiation regionally. As the composition of Puysegur Ridge and the origin of the Snares Zone are key motivators for the gravity inversion and for understanding subduction initiation, these regions are highlighted in the comparison of the posterior densities to seismic velocities in Fig. 2.11. Prisms corresponding to the western and eastern halves of Puysegur Ridge at the Snares Zone are shown by pink and maroon points, respectively. The western half of the ridge plots in two distinct regions, a cluster lying predominantly between 2700 kg/m^3 and 2900 kg/m^3 and a cluster lying below 2100 kg/m^3, the latter of which corresponds to the sedimentary units within the shallow portion of the Snares Zone bathymetric depression and the accreted sedimentary portion of the western half of the ridge (Figure 2.11, red-orange points), which is also clearly visible on the seismic reflection images from SISIE-2 (Shuck et al., 2021).

The difference between the western and eastern halves of Puysegur Ridge at the Snares Zone is notable, with the western half averaging around 2803 kg/m^3 and the eastern half averaging around 2750 kg/m^3, the difference of which is more than three times as much as the mean standard deviation of the prisms within the Snares Zone, about 15.1 kg/m^3 (Fig. 2.10). This is especially significant in light of the difference between the final density model and the prior. The prior densities for the Puysegur Ridge at the Snares Zone, particularly for the western half, average around $2500-2700$ kg/m^3 and are consistent with a continental crustal interpretation (Figs. 2.7C and 2.11A). However, the gravity consistently requires the presence of a higher density body of around $2700-3100$ kg/m^3 on the western half of Puysegur Ridge in order to fit the observed gravity signal (Fig. 2.7). These densities, however, are not inconsistent with the velocity models because highly fractured or deformed rock can have a much lower seismic velocity while still maintaining a high density, so what the seismic velocity models seem to indicate is deformed sediment or continental crust, could in fact be fractured oceanic crustal rock (Barton, 1986). We postulate that basement rock of the western half of Puysegur Ridge is compositionally distinct from that of the east and is most likely a sliver of oceanic crust that has been emplaced laterally against the continental crust of the eastern half via the strike slip motion of the Puysegur Fault, which runs through the Snares Zone. This inference is also consistent with the seismic interpretations in Shuck et al. (2021) and Shuck et al. (2022).

The under-prediction of the densities on the western half of Puysegur Ridge by the seismic velocities via the Nafe-Drake curve and the large amount of scatter in the posterior densities relative to that curve put limitations on the degree to which the Nafe-Drake relationship can be used to predict densities without further information, as has been noted by previous authors (Barton, 1986). The Nafe-Drake equation, though valid for velocities between 1.5 km/s and 8.5 km/s, was based empirically on continental crustal data from California (Ludwig et al., 1970; Brocher, 2005) and as such may not be accurate for oceanic crust. However, a comparison between the Nafe-Drake predictions of Brocher (2005) and theoretical seismic velocity and density predictions from mineral physics calculations using the MinVel Subduction Factory Toolbox (Abers and Hacker, 2016; Sowers and Boyd, 2019) reveal that differences between the two predictions are less than 1% on average, though can be as high as 37% for specific rock types (Sowers and Boyd, 2019). There is also the question of whether thermal effects may impact the accuracy of the Nafe-Drake prediction and the model density estimates. However, an analysis of the possible perturbations to the velocity and density estimates of the Brocher (2005) relationship under a hot geotherm calculated using the MinVel toolbox, using the half-space cooling model with a plate age of 25 Ma for rocks in oceanic regimes and a typical continental geotherm with a conservatively high surface heat flux of 120 mW/m^2 for continental regimes, demonstrate that elevated temperature has a negligible impact on the Nafe-Drake predictions relative to the range of densities in our model domain (Fig. 2.11 B,C). The rock compositions used in this analysis include basalt (Hacker et al., 2003), harzburgitic mantle (Hacker et al., 2003), Fiordland orthogneiss (Bradshaw, 1990), and a combination of pelagic clays and biogenic ooze (Li and Schoonmaker, 2003; Patel et al., 2020). The absolute densities estimated for each of these rock types differ insubstantially between low (surface) and warm (25 km depth) temperatures, and the velocity and density both change in accord with one another with that change in temperature, such that the predictive relationship between them remains the same (Fig. 2.11 C, (Sowers and Boyd, 2019)). Puysegur itself is also not a notably hot subduction zone; despite the young age of the subduction front, the crust that is being subducted is not particularly young, spreading in the Tasman Sea having ceased around 53 Ma, though spreading in Emerald Basin south of the study area continued until around 10-20 Ma (Lebrun et al., 2003). Thus, we find it is not necessary to incorporate any thermal effect into our model and that the Nafe-Drake relationship is a reasonable one in light of any possible thermal perturbations and its performance relative to mineral physics estimates.

Some of the differences in density between the prior and posterior also likely arise from error in the 3D interpolation scheme, but the difference in densities between the two even across the Snares Zone, where we have direct seismic data, suggests a significance in the under-prediction of many of the posterior densities by the Nafe-Drake equation. However, this does not invalidate its use as a prior, but rather highlights the advantage of using it in the context of a Bayesian approach. Rather than using seismic velocity as the only indication of a rock's density, we use it as a guide for the rock's possible density and weight that estimate of density accordingly. As such, the Bayesian approach allows for a more reasonable and flexible use of a common velocity-density relationship that otherwise, by itself, may be erroneous in its estimation of rock type.

For this reason, the gravity inversion is an invaluable supplement to our seismic study in estimating rock compositions and structure and in particular to spatially filling the gaps between where we have seismic information. Gravity at short wavelength strongly reflects topography (or bathymetry) (Sandwell et al., 2014; Turcotte and Schubert, 2014); however, if the bathymetry fully is constrained in the inversion and cannot by itself reproduce the gravity signal, then perturbations to the gravity must be coming from other sources, namely lateral density variations that may be governed by Moho geometry. As such, the shape of the interpreted Moho (Fig. 2.12B) strongly mirrors the gravity. Traditional gravity modeling techniques avoid this by removing the signal from the Moho/the isostatic effect and looking at the residual (Oldenburg, 1974; Bai et al., 2014). However, this assumes constant densities in the respective layers and sometimes a fixed interface. Because we do not explicitly impose such assumptions with the Bayesian inverse approach, but rather constrain the 3D densities and hence the structure probabilistically, the resulting Moho, though it does mirror the gravity, is likely a good approximation to the true Moho. Taking the southern line, SISIE-1, as an example, ultimately to match the gravity high over the ridge, there can be either 1) an elevated Moho or 2) anomalously high densities in the crust. In the absence of fixing either of these, the algorithm has no knowledge about which is the correct choice to fit the gravity, and the easiest way to fit the gravity is to create a density distribution increasing in depth with a shape mirroring that of the gravity. This is why inclusion of the Bayesian priors is so important. We can see the effect of the prior versus that of the gravity beneath the Campbell Plateau in Fig. 2.8 B, where there is smearing at the base of the crust relative to the prior in C. The gravity in combination with the regularization wants to put the Moho higher to smoothly mirror the gravity signal. The prior, on the other hand, pulls the Moho down, but not so much so that the predicted gravity is depressed. As we can see in Fig. 2.8 A, the gravity from only the prior is too low to match the observations. This means that, given the inclusion of the prior, the combination of density and structure returned by the gravity inversion is probably the most reasonable estimate of the true structure. In other words, it is the most likely combination of 1) adjusting the Moho depth, and 2) adjusting the density that can be obtained in light of our existing knowledge. It is the Bayesian approach that allows us to do this so effectively. It also means, given we have applied a strong prior along this transect, the fact that the gravity still pulls the Moho up under the Ridge despite the constraint is all the more significant and suggests this is not just an artefact of reflecting the shape of the gravity.

This large gravity high over the southern portion of Puysegur Ridge cannot be explained solely by the bathymetry and requires a mass excess (Fig. 2.8). Similarly, the large gravity low over the Snares Zone also cannot be reproduced by the bathymetry alone, and hence requires a mass deficit to produce the observed gravity (Fig. 2.7). In other words, the density profiles and Moho and crustal thickness maps demonstrate there is relatively shallow mantle beneath the southern Puysegur Ridge and unusually thick crust beneath the Snares Zone; unusual in that the region is bathymetrically low, yet predominantly composed of buoyant continental crust, except for the very western side as previously discussed. The Solander Basin, which is composed of rifted continental margin crust, evidenced by both the seismic data (Gurnis et al., 2019; Shuck et al., 2021) and the densities, progressively thins to the south, where the basin experienced more extension during the rifting phase in the Eocene to Oligocene prior to the development of the strike-slip and subduction margin (Lebrun et al., 2003). Based on the crustal thickness results as estimated from the gravity, we estimate the continent-ocean transition in the southern Solander Basin to be around 50°S or even further south of the model domain, which is roughly consistent with Shuck et al. (2021).

Another notable feature of the inversion results is the inability to resolve a slab structure, despite its presence in the prior and the seismically observable décollement between the two plates on seismic reflection data. The absence of descending crust in the final density model is likely due to the obliquity of subduction. A seismic Benioff zone extending to 150 km depth puts the slab northwards of the gravity study area, beneath Fiordland (Sutherland et al., 2006; Eberhart-Phillips and Reyners, 2001). It is also possible that while the slab is present, it is not required to recover the local scale gravity signal, which is dominated by the bathymetry and shallow crustal structure.

2.6 Conclusions

The inversion technique presented inverts gravity data for 3D density distributions within a Bayesian framework without the need for iteration and with the direct incorporation of prior geophysical constraints. Previous applications of linear gravity inversion, as opposed to the commonly used non-linear and wavenumber domain methods, have predominantly been for geometrically and structurally simpler density anomalies, though have also successfully been applied to crustal scale and tectonic studies. We have demonstrated this method can also be successfully applied to more geologically complex regions with significant lateral variations in density and structure by applying it to an active subduction zone.

The resulting density models provide a more complete picture of the subsurface, filling in the gaps between where there is seismic data and allowing us to estimate the Moho depth and crustal thickness. The crustal thickness and density models reveal the presence of buoyant, yet subsided, continental crust beneath the central and eastern portions of the Puysegur Ridge at the Snares Zone, whereas the western half of the ridge is most likely a sliver of oceanic crust. In contrast, an elevated mantle underlies the southern portion of Puysegur Ridge. The features observed in the Snares Zone and along the Ridge have implications for the structures and rock compositions that control subduction initiation and the changing state of stress during the initiation process, and they support the idea that the margin is transitioning to a state of self-sustaining subduction in the north. These results will allow us to make further calculations of the regional stress and effective topography that can be used to constrain geodynamic models that are the target of future research.

Chapter 3

REVISITING THE POISSON PROCESS ASSUMPTION FOR BACKGROUND SEISMICITY IN SOUTHERN CALIFORNIA USING THE QTM CATALOG

3.1 Introduction

The characterization of the spatio-temporal patterns of earthquake occurrence is important for understanding earthquake physics and is a necessary step in seismic hazard assessment (e.g., Vere-Jones, 1995; Zaliapin and Ben-Zion, 2013). A common view is that any earthquake catalog can be decomposed into background seismicity, consisting of independent events, and clusters, consisting of dependent events. Such a bimodal decomposition emerges naturally from non-parametric analysis of earthquake catalogs (Zaliapin et al., 2008; Marsan and Lengliné, 2008). Following Cornell (1968), the background seismicity is generally considered to result from a Poisson process, which describes points located randomly in space and time according to a single parameter, known as the rate or intensity (Daley and Vere-Jones, 2003). The rate of a Poisson process representing earthquakes can either be stationary (homogeneous) or variable (inhomogeneous) in space and time. To avoid confusion, we use '(non-)stationarity' to characterize the process in time, and '(in)homogeneity' to characterize the process in space. Earthquakes are often considered to be a time-stationary and space-inhomogeneous Poisson (SIP) process (Vere-Jones, 1995; Zaliapin and Ben-Zion, 2013). Space inhomogeneity clearly derives from the fact that earthquakes are not random in space but concentrate along major tectonic plate boundaries and regional faults (Zaliapin and Ben-Zion, 2013) or, equivalently, in zones of high strain rate (Stevens and Avouac, 2021). The time-stationary aspect describes earthquakes as a sequence of independent events that occur randomly in time, except for those associated with aftershock sequences or other seismological phenomena such as swarms. The SIP process seems to provide a good first order model of earthquake statistics at the regional scale (e.g., Stevens and Avouac, 2021; Petersen et al., 2020).

The Poisson assumption stems largely from the work of Gardner and Knopoff (1974), who claimed that the seismicity in Southern California is Poissonian once aftershocks are removed. Their approach was to detect and remove aftershocks from a catalog with the expectation that the remaining set of events was a stationary Poisson point field (Gardner and Knopoff, 1974). This led to a tradition in statistical seismology to test declustering against a stationary process, or against the idea that a catalog isn't truly declustered unless the remaining events are Poissonian. The fact that the Gardner and Knopoff declustering method ignores space and is insensitive to seismicity rate fluctuations has been recognized as a potential source of bias (Luen and Stark, 2012). Despite the fact that a number of studies have challenged the assumptions and procedures used in this approach to declustering (Luen and Stark, 2012; Maurer et al., 2020), seismic hazard studies commonly use the Gardner and Knopoff declustering method (Petersen et al., 2020). The implicit assumption of a stationary Poisson process in this method may make the forecasts that depend on it prone to error (Maurer et al., 2020).

In heuristic models, dependent events are generally modelled as aftershock sequences governed by an Omori-type decay of the seismicity rate with time and a power-law decay with distance from the mainshock. This is the case of the epidemic-type aftershock sequence model (ETAS) (Ogata, 1999), which has been shown to produce very realistic synthetic earthquake catalogs (e.g., Field et al., 2017). The physics-based earthquake simulator RSQSIM (Richards-Dinger and Dieterich, 2012) was also designed to produce such a bimodal representation of seismicity and has been found to fit observations well (Shaw et al., 2018). However, real seismicity catalogs or synthetic catalogs produced using physics-based models can depart from this bimodal representation (Luen and Stark, 2012; Kuehn et al., 2008; Pollitz and Cattania, 2017). Background seismicity might not be stationary due to viscoelastic relaxation associated with the larger events in a given area. This has been observed for example in Southern California, where the background seismicity seems to have been modulated by viscoelastic relaxation following the five M > 6.5 earthquakes that have occurred since 1981 (Pollitz and Cattania, 2017), in particular the M 7.2 El Mayor-Cucapah earthquake of 2010 (Gualandi et al., 2020) (Figure 3.1). The elastic rebound theory and static stress transfer among faults can also lead to quasi-periodicity and synchronization of seismicity not consistent with the hypothesis of a stationary Poisson process (Kuehn et al., 2008; Zöller, 2018; Griffin et al., 2020; Matthews et al., 2002). Departure from Poissonian behavior can also result from synchronization driven by external forcing such as seasonal hydrological loading (Bettinelli et al., 2008; Craig et al., 2017; Johnson et al., 2020), a phenomenon often observed in California (Amos et al., 2014; Kreemer and Zaliapin, 2018). Some authors have even found evidence for synchronization of seismicity at the global scale (Bendick and Mencin, 2020).

In this study, we analyze the temporal pattern of seismicity in Southern California to test whether it includes a background seismicity mode consistent with a stationary Poisson process, as initially argued by Gardner and Knopoff (1974). We use the updated version of the Hauksson, Yang, and Shearer (HYS) SCSN relocated catalog for Southern California (Hauksson et al., 2012), covering a period from 1981 to 2018, and the newer quake template matching (QTM) catalog for Southern California (Ross et al., 2019) (see Data and Resources), which covers a 10 year time period from 2008 to 2017 and boasts a particularly low magnitude of completeness of about 0.3 (Figure 3.1). The large volume of data in the QTM catalog, approximately 900,000 earthquakes, and the shorter period covered make it particularly suitable for such an analysis. The QTM catalog is a valuable resource in this regard, and thus far, other than the Trugman and Ross (2019) foreshock analysis, not much work has been done on the statistics of the QTM catalog. The seismic network has also not changed over that period of time, so it can be assumed that the magnitude of completeness has not changed over that time either, which otherwise might introduce artefacts that can bias the distribution towards appearing non-stationary or non-Poissonian. We resort to a non-parametric decomposition of the seismicity catalog into background mainshock events and clusters following the method of Zaliapin et al. (2008) and Zaliapin and Ben-Zion (2013), which unlike other declustering methods, does not seek a Poisson distribution in the declustered catalog and accounts for both foreshocks and aftershocks. We analyze the interevent time distributions of the mainshock events to test if they are exponentially distributed, as is expected for a Poisson process (Molchan, 2005; Hainzl et al., 2006). We also use the Schuster spectrum method (Ader and Avouac, 2013) to test the quality of the declustering, as well as to test for non-stationarity and the possible synchronization of seismicity.

3.2 Interevent Time Distribution in the Full and Declustered QTM and HYS Catalogs

The interevent time (IET) distribution of earthquakes provides a powerful means to characterize temporal correlation in earthquake time series, where interevent times are calculated as the time between consecutive events ($\Delta t_i = t_i - t_{i-1}$) in the catalog. If the background seismicity in Southern California is consistent with a stationary Poisson process, the interevent times of mainshock events should follow an exponential distribution (Eq. B.1, B.3). When using complete catalogs, including

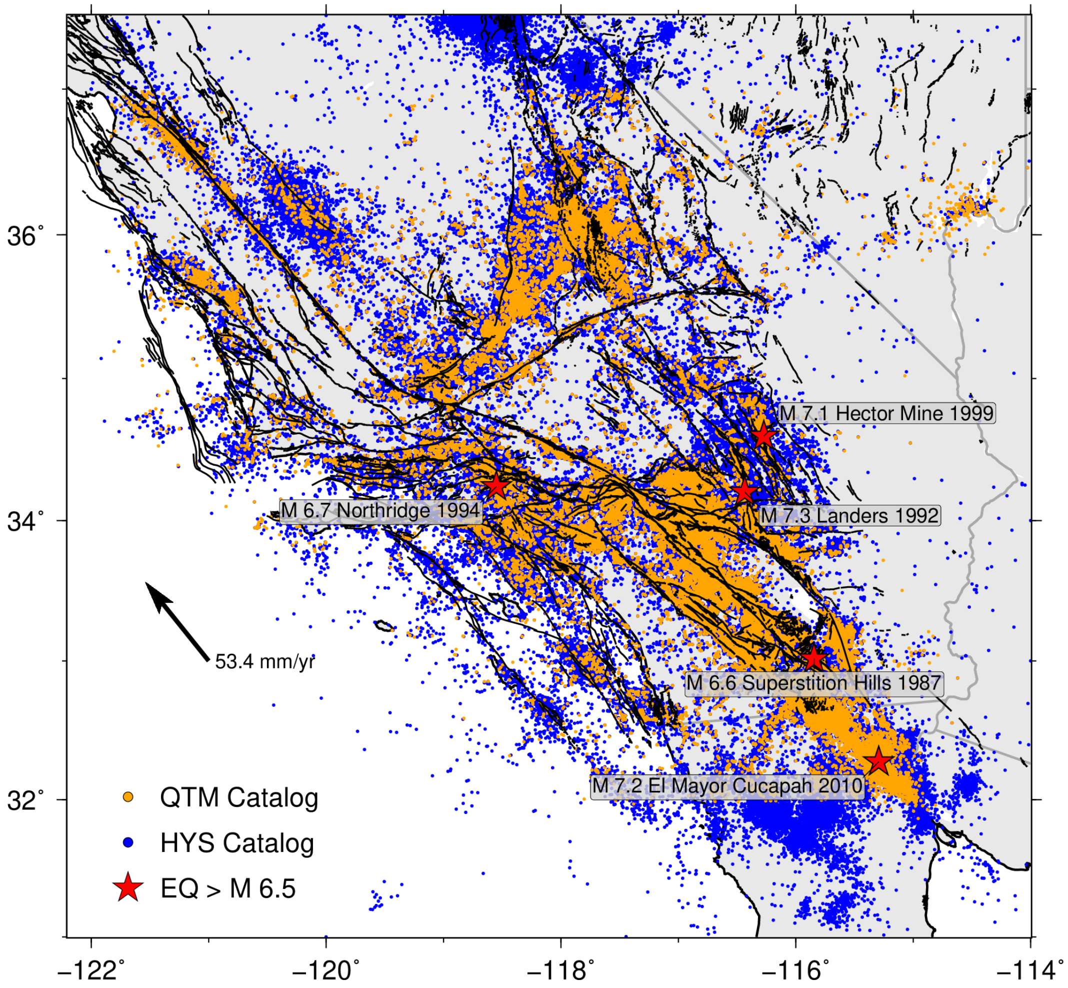

Figure 3.1: Seismicity map of California, showing the locations of earthquakes from the Quake Template Matching (QTM) catalog (Ross et al., 2019) and the relocated SCSN (HYS) catalog from Hauksson et al. (2012) and Lin et al. (2007). Stars mark the locations of earthquakes greater than M 6.5 since 1981 through 2018. Black lines are Quaternary faults. Black arrow is the MORVEL Pacific plate motion, relative to North America, from DeMets et al. (2010).

foreshocks and aftershocks, interevent times are generally observed to follow a gamma distribution (Eq. B.5) (Corral, 2004; Davidsen and Kwiatek, 2013; Hainzl et al., 2006). The exponential distribution is in fact just a special case of the gamma distribution. A gamma distribution is expected to result from the superposition of background seismicity obeying a stationary Poisson process and Omori-type sequences of aftershocks (Molchan, 2005) or events triggered using an ETAS model accounting for both aftershocks and foreshocks (Hainzl et al., 2006), and as such, is often more suited to non-declustered catalogs. In this case, the coefficient $1/\beta$ (Eq. B.6) is argued to quantify the fraction of mainshocks (Molchan, 2005; Hainzl et al., 2006). Both the non-declustered HYS and QTM catalogs are compared with the best-fitting gamma distribution and exhibit good overall fits (Figure 3.2). The mainshock fractions as estimated from the gamma distribution are about 29% and 46% for the HYS and QTM catalogs, respectively. The HYS catalog deviates from the gamma distribution at the highest interevent times, showing a 'fat tail' that leads to the rejection of the gamma distribution for this catalog (Figure 3.2 a). By contrast, the fit with the QTM catalog is more compelling. The IET distributions of the non-declustered catalogs deviate strongly from the exponential distribution, exhibiting a huge fat tail, as would be expected when aftershocks are present in the catalog (Figure 3.2 c-d). Deviations from the gamma distribution suggest that the background seismicity in the HYS catalog, and possibly in the QTM catalog as well, is not consistent with a stationary Poisson process. It is therefore probable that the fit with a gamma distribution does not yield a very reliable estimate of the fraction of mainshocks forming the background seismicity. Investigating that possibility further requires extracting the background seismicity from the catalogs.

We identify and remove aftershocks and foreshocks from the catalogs using the declustering algorithm of Zaliapin and Ben-Zion (2013). The approach identifies the potential parent event of each earthquake based on its distance in time and space from other earthquakes, measured with the Baiesi and Paczuski metric (Eq. B.8) (Baiesi and Paczuski, 2004). This metric depends on the earthquake time, the distance between earthquake hypocenters or epicenters, the magnitude of the possible parent, and the fractal dimension of the earthquake hypocenter distribution, which is typically about 1.6. This distance is split into its space and time components and normalized by the parent magnitude (Eq. B.9). With this approach, the earthquakes are separated into two distinct populations (Figure 3.3). The first mode, where events are close together in space and time, consists of clustered events, and the second mode, where events are farther away in space and time, consists of background events with no parents. In each cluster, only the event with maximum magnitude is selected so that both foreshocks and aftershocks are removed. A key advantage of this approach is that it does not remove aftershocks or foreshocks on the assumption that the remaining field should be Poissonian, as was assumed by Gardner and Knopoff (1974), which makes it a better method for identifying clusters and analyzing the statistics of the remaining point field. The mainshock fraction derived from declustering the HYS catalog is 36%, a value inconsistent with the 29% mainshock fraction obtained from taking $1/\beta$ of the best-fitting gamma distribution, using a logic that assumes that the background seismicity is Poisson and stationary. The mainshock fraction derived from declustering the QTM catalog is 30%, even more inconsistent with the value of 46% obtained from the best-fitting gamma

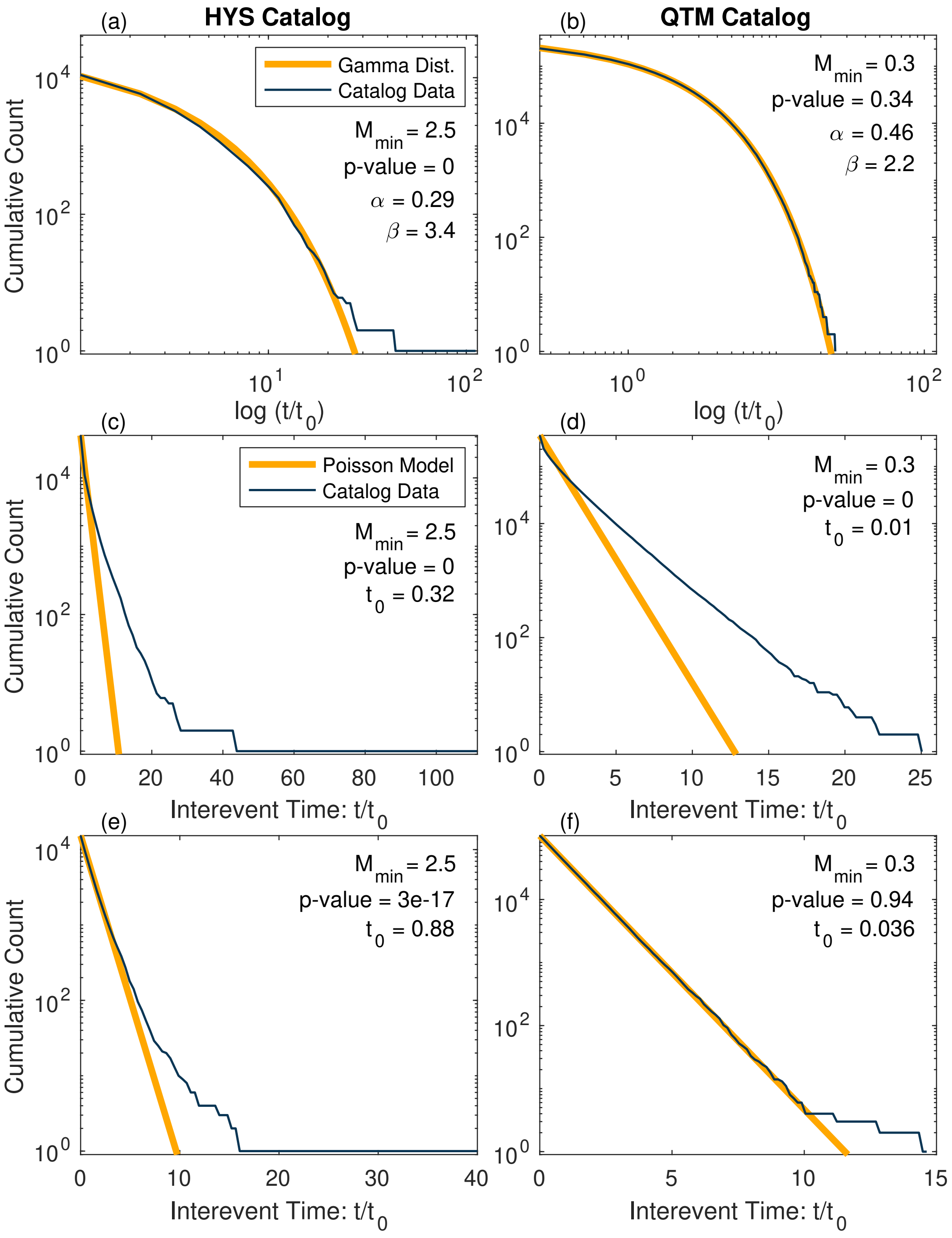

Figure 3.2: Comparison of the earthquake IET for the HYS (a,c,e) and QTM (b,d,f) catalogs for Southern California. (a,b) show the fit of non-declustered catalogs to a gamma distribution. (c,d) show the fit of non-declustered catalogs to an exponential distribution (i.e., Poisson process). (e,f) show the fit of declustered catalogs to an exponential distribution. The IETs of each panel are normalized relative to their respective mean interevent time, t_0. Only IETs from earthquakes above the respective magnitude of completeness, M_c, for each catalog are plotted. The p-value represents the probability that the data come from a gamma or Poisson distribution, respectively.

distribution. This highlights the importance of not assuming a stationary Poisson distribution in the declustering process.

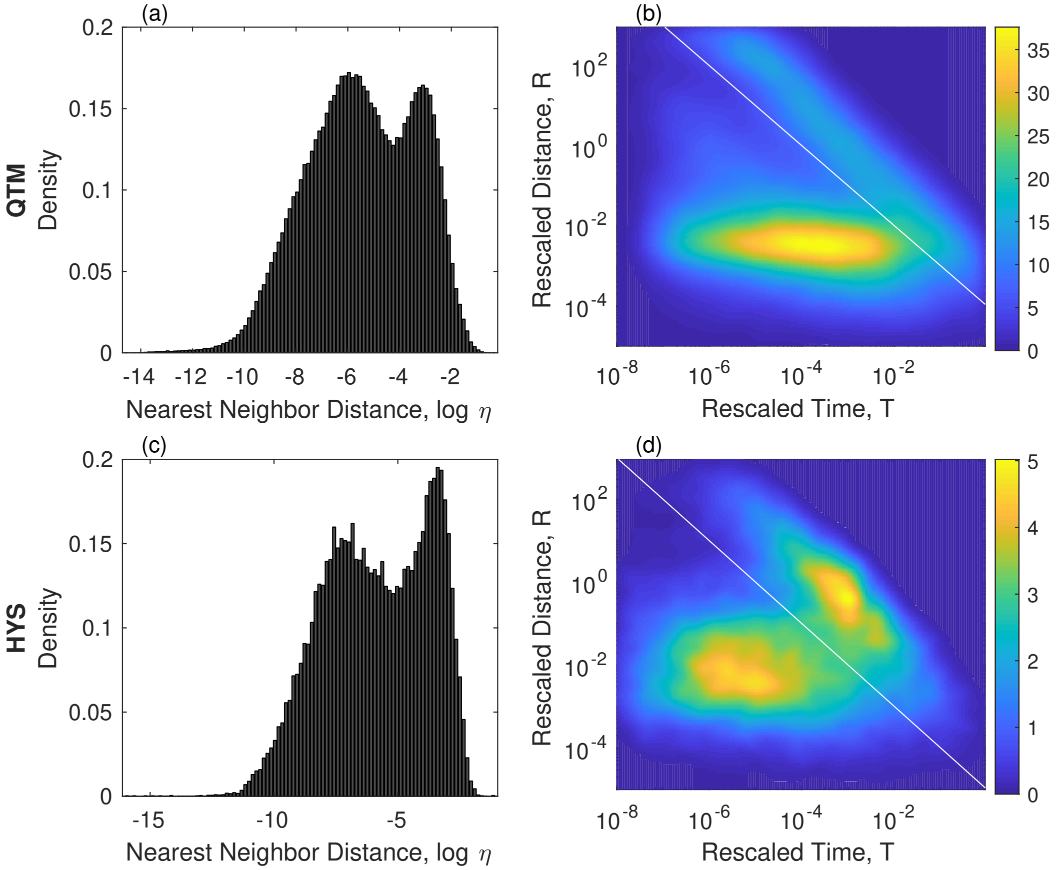

Figure 3.3: Declustering results for the QTM catalog (a-b) and the HYS catalog (c-d). (a,c) Nearest neighbor histogram for all events in the catalog, showing a bi-modal distribution between clustered events and mainshocks. (b,d) Space-time density for all events in the catalog. The lower bright horizontal mode represents the clustered events (foreshocks and aftershocks), and the higher mode represents the background events. For the QTM catalog, the white line that separates the clustered and background modes is selected visually and given by $\log_{10}R + \log_{10}T = -4$, and for the HYS catalog, the line separating the modes is given by $\log_{10}R + \log_{10}T = -5$. The proportion of mainshocks vs. clustered events in the QTM catalog is roughly 30% and 70%, respectively, and for the HYS catalog is roughly 36% and 64%, respectively.

If background events do follow a Poisson process, then the interevent times follow the exponential distribution (Eq. B.3), which depends solely on the mean interevent time t_o. For the QTM catalog, we first select all events with magnitude larger than the reported magnitude of completeness of 0.3 (Ross et al., 2019). The declustered catalog seems fairly consistent with the exponential distribution despite the fat tail at higher interevent times (Figure 3.2f). The magnitude-frequency distribution of earthquakes in the QTM catalog actually departs from the Gutenberg-Richter distribution for magnitudes smaller than about 2 (Figure 3.4a). This is probably due to the fact that the detection threshold of the template matching procedure is inhomogeneous in space. It is probably as low as 0.3 in the vicinity of the earthquakes used as templates and closer to M 2 elsewhere. Importantly for our analysis, this inhomogeneity does not affect the IET distribution since the Poisson test does not require the magnitude of completeness to be uniform in space. A subset of independent events resulting from a Poisson process will still be a Poisson process, albeit characterized by a lower rate. To verify this point, we tested the Poisson model for different cutoff magnitudes and found no sign of any systematic effect (Figure 3.5). The magnitude of completeness of the declustered QTM catalog is about 2 (Figure 3.4a), and the cumulative number of earthquakes with time in the declustered QTM catalog mostly follows a straight line, indicative of a stationary Poisson process (Figure 3.4b). The magnitude of completeness of the HYS catalog is estimated to be about 2.5 (Zaliapin and Ben-Zion, 2015) (Figure 3.4c). The declustered catalog is inconsistent with the exponential distribution due the prominent fat tail at higher interevent times (Figure 3.2e).

The analyses of the HYS and QTM catalogs thus seem to yield somewhat contradictory results. From Figure 3.2 c-f, it is clear that the data of both exhibit a tail, deviating from the Poisson model at higher interevent times, though that of the HYS catalog is significantly larger than that of the QTM catalog, especially in the declustered case (Figure 3.2 e-f). The tails observed in the declustered catalogs are similar in shape to those in the non-declustered set, though not as prominent (note the difference in interevent time range on the abscissa). This raises the question of whether the fat tail is simply due to the presence of remaining aftershocks in the declustered catalogs, as aftershocks are inherently a non-stationary process. A non-stationary background rate would also lead to a departure from the exponential distribution. We test the deviation from the Poisson model to determine its statistical significance, and later test the effect of including aftershocks using a synthetic catalog.

3.3 Schuster Tests of the Declustered QTM and HYS Catalogs

The Schuster test was originally designed to test for possible periodicity in earthquake occurrence due to solid earth tides (Schuster, 1897; Heaton, 1975). In practice, the test is based on a random walk that starts at the beginning of the catalog and steps in the radial direction each time there is an earthquake. If at the end of one cycle, the path returns to the starting point, then it is indeed a random walk, which would be consistent with an SIP process. However, if at the end of one cycle,

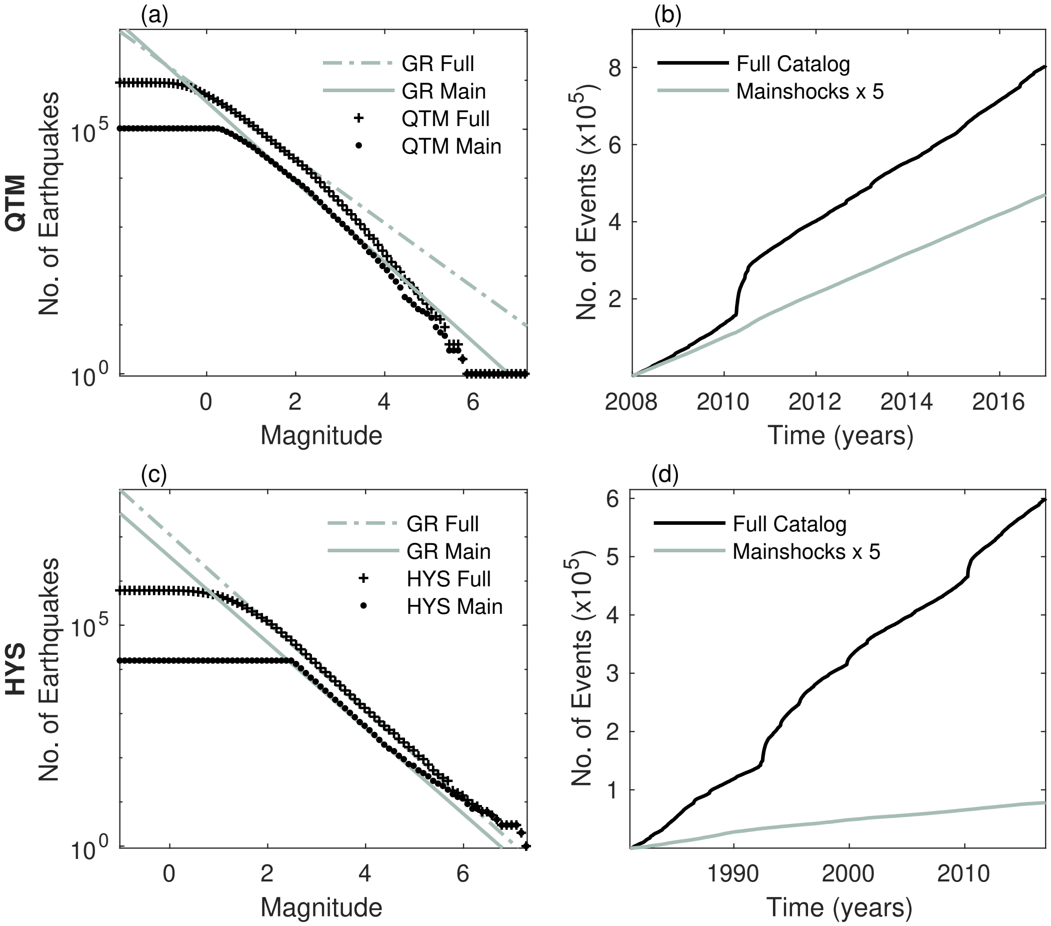

Figure 3.4: Gutenberg-Richter relation and cumulative number of earthquakes with time for the non-declustered vs declustered catalogs. (a) Gutenberg-Richter (GR) relation, determined using the maximum likelihood method, for both the non-declustered (dashed-dotted line and crosses) and declustered (solid line and points) QTM catalog. For the non-declustered catalog, the reported magnitude of completeness (M_c) is 0.3, and the b-value is 0.66. For the declustered catalog, $M_c = 2.0$, and the b-value = 0.82. (b) Cumulative number of earthquakes with time in both the full (black line) and declustered (gray line) QTM catalogs. Mainshock count is scaled by 5 to increase visibility of changes in slope. The QTM mainshocks mostly follow a straight line, indicative of a stationary Poisson process. (c) GR relation for the non-declustered and declustered HYS catalogs. For both the non-declustered and declustered catalogs, $M_c = 2.5$, and the b-value = 0.98. (d) Cumulative number of events with time in the full and declustered HYS catalogs. Mainshock count is again scaled by 5 to increase visibility of the change in slope around 1990.

it has not returned to where it started, then there is some probability that the shift may not be random and there is instead periodicity to the events. The probability that the walk is random is determined based on the radial distance from the start point to the end point and is represented by the dashed circles shown in Figure 3.6 b. The sizes of the random walk circles themselves correlate with the seismicity rate, with larger circles indicating a higher rate. Because the null-hypothesis is that the seismicity results from a uniform random process, this test allows for evaluating

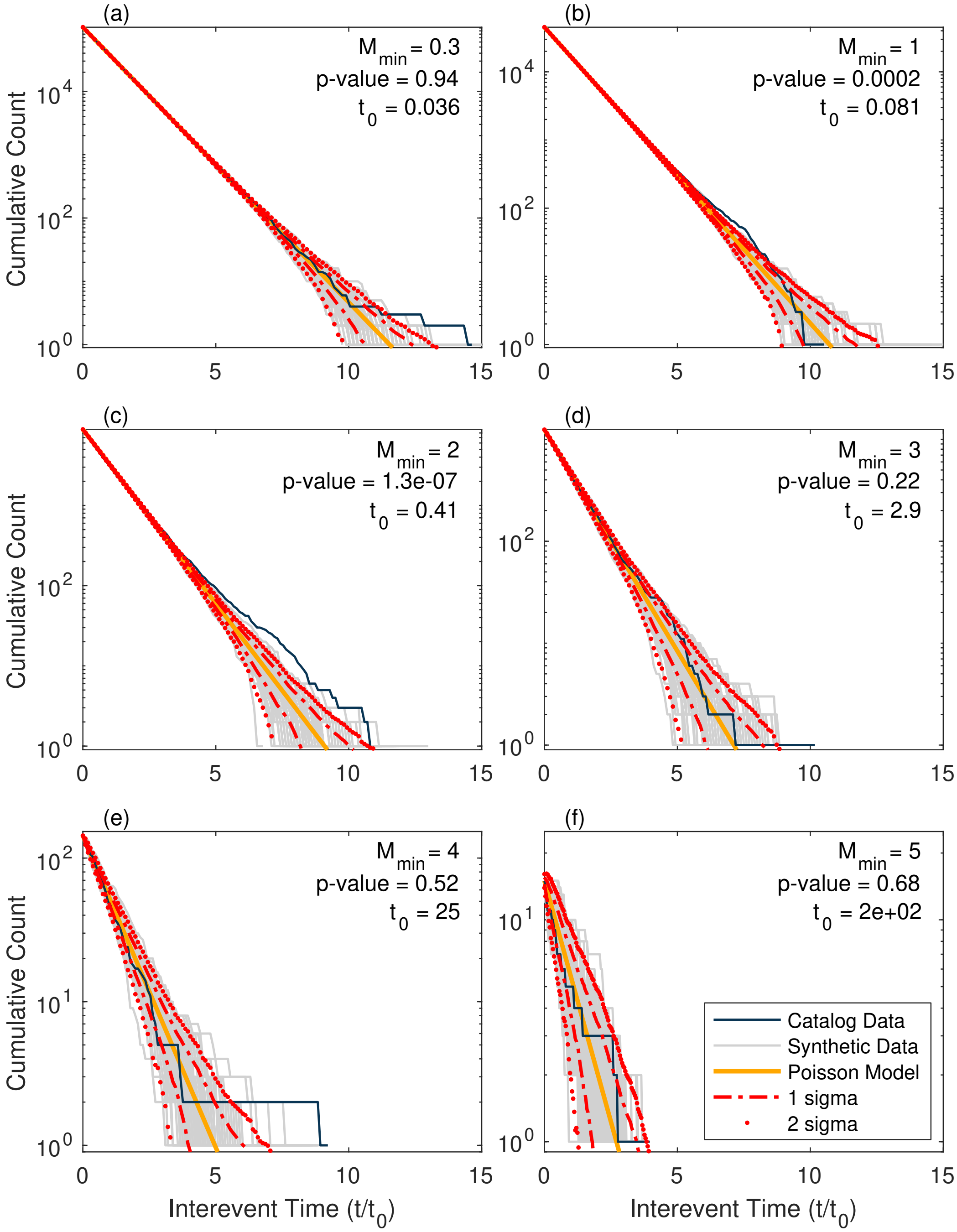

Figure 3.5: Cumulative distribution of interevent times for the QTM data (dark line) versus 100 exponentially distributed synthetic data sets (light grey lines) and the Poisson model (bold straight line), using a mean IET calculated from the data. Each panel shows the IET distribution for a different lower magnitude cutoff: M=0.3, 1, 2, 3, 4, 5. IETs are normalized by the mean IET, t_0, for their respective panel. The dashed line shows the 1σ standard deviation bound calculated from the synthetic data, and the dotted line shows the 2σ standard deviation bound. P-values are given for each M_{min} cutoff, calculated from a standard chi-squared goodness of fit test comparing the QTM count to the Poisson model.

whether the seismicity results from a stationary Poisson process. To do so, we generate a 'Schuster spectrum' (Ader and Avouac, 2013), which shows the probability that the events are from a uniform random process and therefore do not correlate with some periodic perturbation. This measured p-value is compared with the expected p-value for a Poisson process (Figure 3.6a). Thus, any real periodicity, due to tidal forcing or some other periodic source of earthquake triggering, will result in Schuster p-values lower than the expected value. However, a low Schuster p-value does not necessarily imply that the seismicity rate is in fact periodic at the given period (Ader and Avouac, 2013). Either way, for the purposes of our study, a low Schuster p-value does tell us if the interevent times are consistent or inconsistent with a stationary Poisson process, whether it be due to periodicity, clustering, or otherwise.

The Schuster spectrum for the QTM catalog reveals two pronounced characteristics. The first is a strong periodicity at exactly one year, corresponding to a seasonal annual signal. The other is the drift of points moving above the 95% and 99% confidence lines starting at a period of a few months, meaning there is a significant probability that these points are not just due to chance. A drift in the Schuster probabilities such as this is usually indicative not of periodicity, but of a transient period of accelerated seismicity. The shortest period at which the drift is observed quantifies the duration of that period. In our case, the drift starts at a period larger than about one month. Such a transient period of seismicity could be due to remaining aftershocks or earthquake swarms for example. Thus, there is strong indication from the Schuster spectrum that the deviation from the Poisson model that we see in the interevent times is at least in part due to the presence of remaining clusters in the declustered catalog. The low p-value at one year, however, is clearly not related to this drift and shows a true seasonal variation consistent with previous studies (Amos et al., 2014; Johnson et al., 2020; Kreemer and Zaliapin, 2018).

The random walk of the Schuster test (Figure 3.6b) allows for visualizing the two contributions to the low p-value observed at one year. For each year, from 2008 to the end of 2017, the QTM catalog migrates away from its starting point, as shown by the colored points in Figure 3.6b. The chance that this walk is random as a result of a stationary Poisson process is much less than 0.001%. Each year yields a nearly circular random walk of similar radius, indicating a generally small departure from a constant seismicity rate. There is, however, a slightly larger rate of seismicity in the summer, peaking at the end of July, which results in a systematic

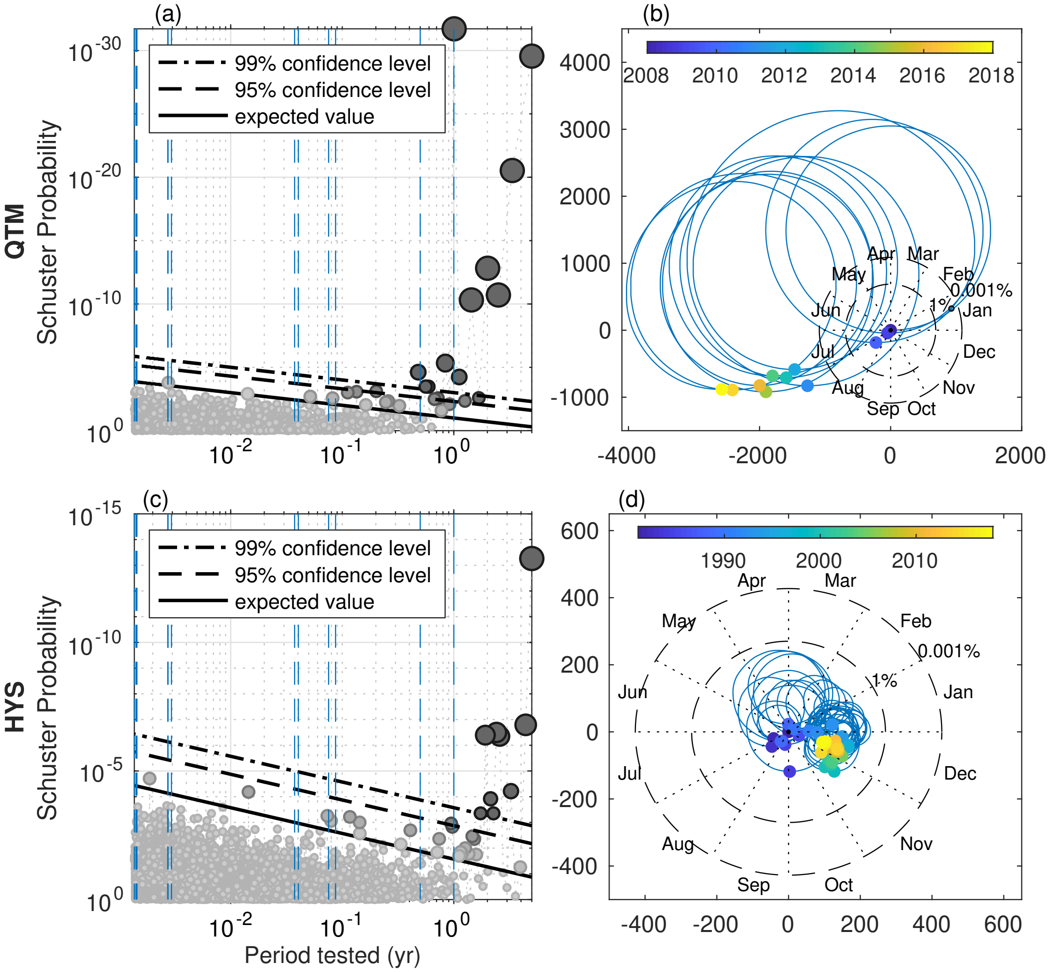

Figure 3.6: Schuster tests for the QTM (a-b) and HYS (c-d) catalogs. (a) Schuster spectrum for the declustered QTM catalog. The period-dependent expected-value line represents the expected minimum Schuster p-value, below which events are consistent with a uniform random process. The 95% and 99% confidence levels correspond to 5% and 1% of the minimum expected values, respectively. Points above these lines have a significant probability not to be due to chance. Dashed lines indicate tidal, half annual and annual periods. There is a notable seasonal periodicity at 1 year, and the drift in the data indicates non-stationarity beginning at times of a few months, likely due to aftershocks. (b) Schuster random walk for the QTM catalog at a period of 1 year. Colored points correspond to the end point of each walk. Dashed circles denote the distance from the start point at which the probability that the walk is random drops to 1% or 0.001%. The migration of the end points with each year indicates annual periodicity. The random-walk circle *sizes*, and thus seismicity *rate*, are roughly the same from year to year. (c) Schuster spectrum for the declustered HYS catalog. There is no detectable periodicity at 1 year, but the drift in the data indicates non-stationarity beginning on the order of about a year, possibly due to aftershocks. (d) Schuster random walk for the HYS catalog at a period of 1 year. There is no significant migration of the end points with each year (all lie within the 1% circle), but the size of the random-walk is highly variable, indicating non-stationarity.

migration of similar amplitude each year. In addition to this clear seasonality, we note a substantially larger gap between 2010 and 2011. The annual loop during that year shows increased seismicity starting in April at approximately the time of the Cucapah-El Mayor earthquake and lasting for a few months.

We perform the same Schuster analysis as detailed above on the HYS catalog as well (Figure 3.6 c-d). Like for the QTM catalog, we observe a drift to low p-values at periods larger than a few months, which suggests non-stationarity of the earthquake rate. Again however, whether this non-stationarity is in the background rate itself or due to aftershocks in the catalog is not obvious. Unlike the QTM catalog, there is no clear seasonal periodicity at one year, and we see no significant migration of the end points in the yearly random walk. For each cycle, the probability that the endpoint location is still the product of a random walk is greater than 1% (Figure 3.6d). The plot however shows considerable variation of the size of the annual loops, suggesting that the non-stationarity of the process is not due to a single transient period of increased seismicity, as was the case for the QTM catalog. Based on the QTM Schuster spectra though, we see two factors contributing to the departure from the hypothesis of a stationary Poisson process, one being the seasonal variations of seismicity and the other being a transient increase of the rate of mainshocks in 2010. The HYS catalog also suggests apparent variations of the background seismicity rate. However, the test does not show whether the apparent non-stationarity of the background rate in both catalogs is true or due to remaining aftershocks.

3.4 Testing for Variations of the Background Seismicity Rate

The largest event in the QTM catalog is the April 2010 M 7.2 El Mayor-Cucapah earthquake in Mexico, the aftershock activity for which clearly shows up in the cumulative number of events with time in the non-declustered catalog (Figure 3.4b). The declustered QTM catalog shows only a slight increase in the number of events after the 2010 earthquake that may influence the resulting IET distribution. Afterslip and viscoelastic relaxation can induce time dependent stress variations in the crust that are reflected in the temporal behavior of aftershock occurrence and the seismic cycle (Gualandi et al., 2020), and could be a source of non-stationarity in the earthquake occurrence rate. To test for non-stationarity due to this event and in the QTM catalog more broadly, we cut the catalog before and after the El Mayor-Cucapah event to analyze the IET distribution separately for the time periods Jan 2008 to Dec 2009 and Jan 2011 to Dec 2017, omitting the year 2010 entirely. The results reveal that the period prior to the earthquake had a lower earthquake occurrence rate, with a mean IET of about $t_0 = 0.0367$ days, while the time period after the earthquake had a mean IET of about $t_0 = 0.0361$ days (Figure 3.7a). The two IET distributions for the two periods are likewise different as they have slightly different Poisson parameters (Figure 3.7b). However, individually both sets of the catalog still follow an exponential distribution and appear to be stationary.

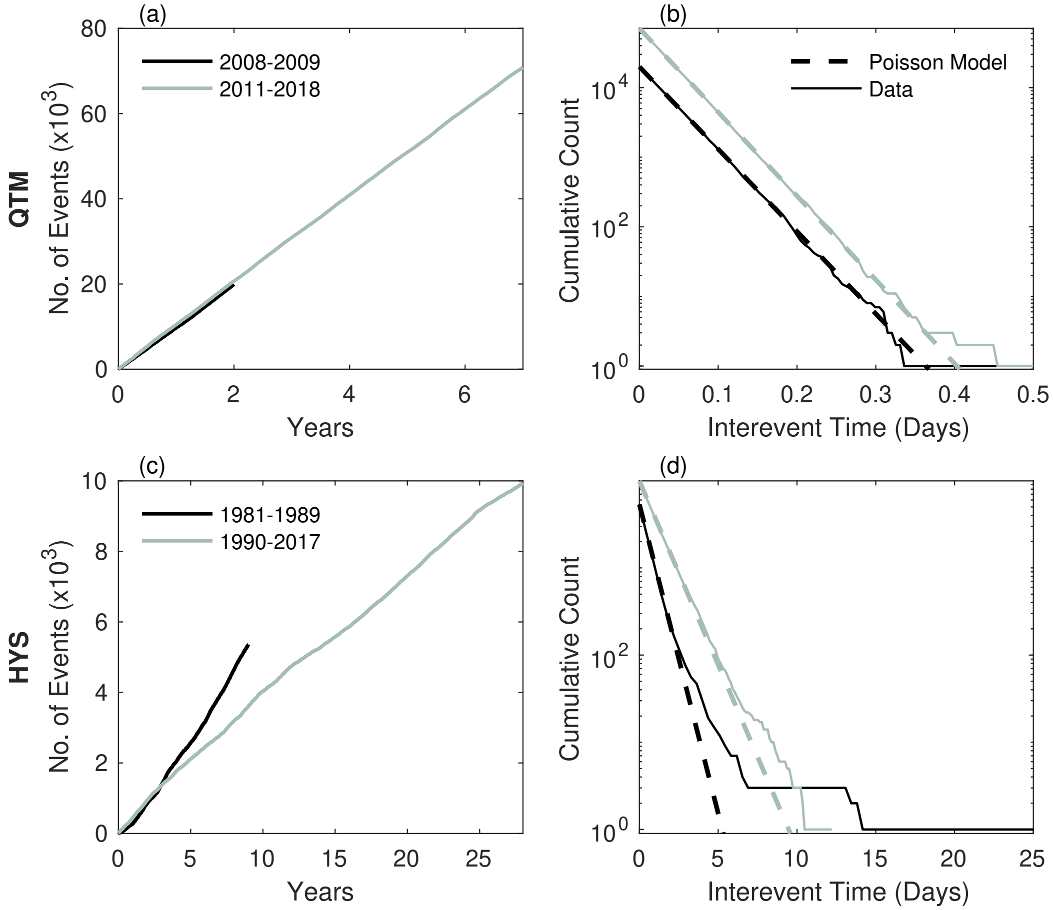

Figure 3.7: IET distributions of the QTM and HYS catalogs split before and after historical changes in the earthquake rate. (a) Cumulative number of events with time and (b) the interevent time distribution from the QTM catalog for events before (Jan. 2008 – Dec. 2009; black line) and after (Jan 2011 – Dec. 2017; gray line) the 2010 El Mayor Cucapah M 7.3 earthquake in Mexico, omitting the year 2010. Dashed lines in (b) are the Poisson models for each subset of the catalog and solid lines are the QTM data. (c) Cumulative number of events with time and (d) the interevent time distribution from the HYS catalog for events before (Jan. 1981 – Dec. 1989; black line) and after (Jan. 1990 – Dec.2017; gray line) 1990, where there is a notable change in the mean earthquake rate. Dashed lines in (d) are the Poisson models for each subset of the catalog and solid lines are the HYS data.

To further investigate non-stationarity, we also examine earthquake occurrences for each year in the catalog individually, to see if the earthquake rate, or equivalently the mean interevent time, is changing systematically year to year. Figure 3.8 illustrates

(a) the number of events with time for each year in the catalog plotted separately against days in the year, and (b) the IET distributions for each individual year. All of the years, except 2010, have roughly the same mean IET, averaging about 0.0357 days. Only that of 2010, with an IET of 0.0304 days, is significantly different from the others, falling more than two standard deviations lower than the mean IET across all years (Figure 3.8c). This drop in mean interevent time, meaning a higher earthquake occurrence rate, coincides with the El Mayor-Cucapah event, suggesting there are still a number of remaining aftershocks and/or an increase of the background seismicity following the El Mayor-Cucapah earthquake. Likewise, the individual IET distributions of each year more-or-less collapse onto a single exponential distribution and their variation is within that expected for the Poisson model, as discussed below. The only distribution that notably differs is that of 2010 (Figure 3.8b). These results suggest that the slight tail on the IET distribution of the QTM catalog is a signature of temporary non-stationarity due to the presence of remaining aftershocks in the declustered catalog. The lower mean IET of 2010 when included in the whole catalog acts to skew the associated Poisson model to the left, giving the appearance of a fat-tail. Non-stationarity, however, does not appear to be long-lived past the end of the aftershock sequence, as the mean IET returns to its pre-El Mayor-Cucapah value. Note that the large size of the catalog allows for detecting very small changes of the background seismicity rate of only a few percent.

The 2010 event is also present in the HYS catalog, but the other large events that could affect the seismicity rate and IET distribution in this catalog are the Landers 1992 and Hector Mine 1999 earthquakes. However, in the non-declustered catalog, the seismicity rate, and hence the slope of the number of events with time in Figure 3.4d, changes instead at around 1990. To investigate the effect of this change on the IET distribution, we cut the catalog before and after 1990. The catalog subsets then yield relatively straight cumulative events with time curves (Figure 3.7c), possibly suggesting stationarity. However, their corresponding IET distributions (Figure 3.7d) both still exhibit significant fat tails, though with a stronger one on the period from 1981-1989.

Breaking the HYS catalog down into yearly subsets reveals a much more pronounced change in the seismicity rate with time, as was also suggested by the random-walk paths in the Schuster test (Figure 3.6d). There is a systematic shift in the number of events with time over the years of the catalog, from higher rates of earthquake

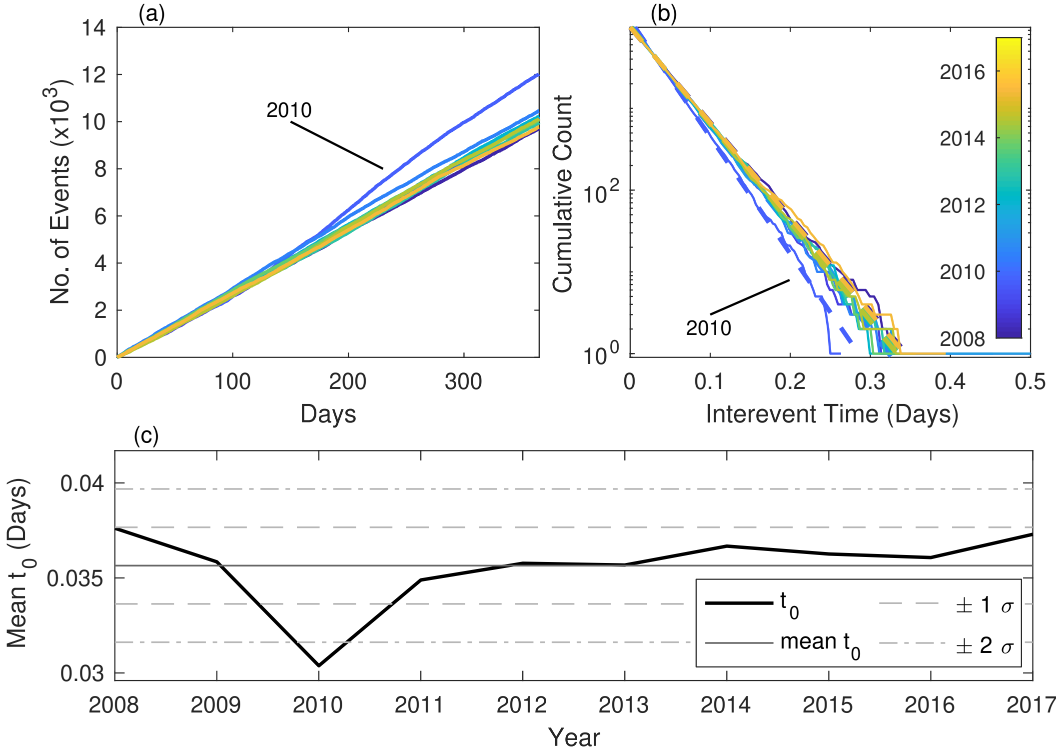

Figure 3.8: Interevent time results for the QTM catalog split between each consecutive year to examine temporal variations in the earthquake occurrence rate. (a) Total number of events with time within each separate year against days in the year. Shading represents the year. The slope of 2010 notably differs from those of the other years. (b) Interevent time distribution for each of the individual years. Each year other than 2010 collapses onto more or less the same distribution. (c) Change in the mean interevent time with year. 2010 exhibits a significant reduction in mean interevent time outside the 2σ bound due to the abundance of events in the aftermath of the El Mayor-Cucapah quake.

occurrence in the 1980s to generally lower rates in the 2000s (Figure 3.9a). This is inversely seen in the general increase in the mean IET over the length of the catalog (Figure 3.9c), which likewise affects the associated IET distribution (Figure 3.9b). When each year is considered individually, the deviation of the data from the exponential curve is not significant, as was also the case for the QTM catalog, but taken together, the mean produced by the entire catalog does not produce a model that is an accurate representation of the earthquake interevent times due to the non-stationarity in the rate.

Unlike the QTM catalog, the change in the earthquake rate for the HYS catalog does not directly correlate with any particular year and actually happens before the Landers and Hector Mine earthquakes, suggesting that non-stationarity may be a more long-lived characteristic of the background seismicity rather than a result of the presence of aftershocks from any one large quake. However, the lower

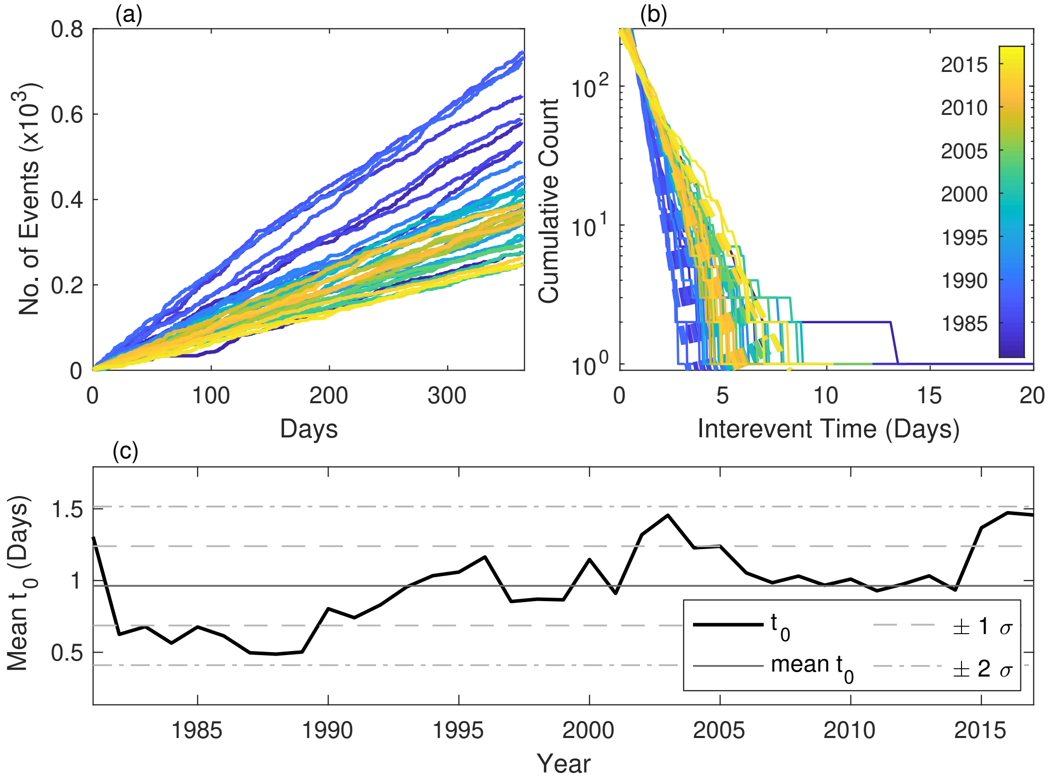

Figure 3.9: Interevent time results for the HYS catalog split between each consecutive year to examine temporal variations in the earthquake occurrence rate. (a) Total number of events with time within each separate year against days in the year. Shading represents year. There is a systematic decrease in the seismicity rate over the course of the catalog. (b) Interevent time distribution for each of the individual years. The shift in mean interevent time is again evident in the data. (c) Change in the mean interevent time as a function of year. There is a long-term increase in the mean interevent time of the catalog, pointing to non-stationarity in the seismicity rate.

completeness of this catalog compared to the QTM could create artefacts of non-stationarity, especially considering that the magnitude of completeness has likely decreased with time as the detection capability of the network improved. That effect alone, if we were using a magnitude of completeness lower than the value in the early 1990s, could have resulted in an apparent increase of the seismicity rate. This is actually opposite to what we observe, however.

The overall apparent decrease in the earthquake rate since the early 1990s may in fact be an artifact due to improved location uncertainties resulting from the increased density of seismic stations (Ben-Zion and Zaliapin, 2020). Zaliapin and Ben-Zion (2015) demonstrate that reducing location errors results in statistically smaller distances between parent and offspring events, which means a larger proportion of events will be identified as clustered after the locations are improved, starting in the early 1990s (Ben-Zion and Zaliapin, 2020). If more events are identified as clustered for the later years in the catalog, then this could artificially result in fewer mainshocks per year, and hence a lower apparent seismicity rate, as seen in the later half of the HYS catalog. If fewer events are identified as aftershocks in the period before 1991 due to location error, then the likelihood that some of those aftershocks will remain in the catalog after declustering is higher. This means a higher proportion of events with shorter interevent times than there would have been had they been identified as aftershocks, which skews the mean interevent time, and equivalently increases the seismicity rate of the catalog, leading to a fat tail. This could explain why the tail of the catalog subset for the period prior to 1990 is substantially larger than that of the later subset of the catalog (Figure 3.7d). As the location error decreases and the number of events in the catalog increases, as in the case of the QTM catalog, the earthquake IET distribution should approach the exponential distribution.

3.5 Analysis of Synthetic Catalogs

We further analyze the interevent time distribution by using synthetic catalogs to test the significance of the deviation from the Poisson model, to test the degree to which the fat tail of the IET distribution is a declustering artifact or due to temporal changes in the background seismicity rate, and to validate the procedure used to extract the background events.

3.5.1 Hypothesis Testing with Synthetic Interevent Times

In order to test the statistical significance of the deviation from the Poisson model, we first generate a set of 100 synthetic IET sequences, distributed according to an exponential distribution with the same mean interoccurrence time as the QTM data. The standard deviation of the synthetic data tends to increase with greater interevent times, so for each IET, we calculate the mean of the count over all 100 tests, then calculate the associated standard deviation, σ_s, of the synthetic data from the expected value (the count predicted by the Poisson model) at that particular interevent time. We then plot the predicted count from the Poisson model $\pm\ \sigma_s$ to determine whether the tail of the data significantly falls outside the one or two standard deviation bound and thus to test the hypothesis that the interevent times of the QTM catalog are consistent with an exponential distribution. Figure 3.5 shows the 100 synthetic distributions plotted along with the QTM catalog data, the Poisson model, and the standard deviations of the synthetic data relative to the Poisson model for six different minimum magnitude cutoffs. The tail of the QTM data, for the most part, clearly does not lie outside the tails of the synthetic data sets.

To verify this, we calculate the p-value using a standard chi-squared goodness of fit test for the QTM data with the null hypothesis that the interevent times of the catalog data are from an exponential distribution. The chi-squared test yields high p-values for all the M_{min} tested except for $M_{min} = 1, 2$ (Figure 3.5), such that for most magnitude windows, there is at least a 22% chance that the count of the interevent times in the QTM data exceeds that predicted by the Poisson model and still comes from an exponential distribution. Thus, in most cases, there is not enough evidence to reject the Poisson model for the QTM earthquake IET distribution at the 5% significance level. In the cases of $M_{min} = 1, 2$, however, the p-value is very low (2e-4 and 1.3e-7, respectively), meaning the Poisson hypothesis can be rejected for these particular magnitude cutoffs, even though the deviation is not visually extreme. The reason why the Poisson model can be rejected for some magnitude cutoffs may possibly be due to random error, but is most likely a result of incomplete declustering and/or non-stationarity of the earthquake occurrences, as examined above with the Schuster spectrum and the annualized IET distributions. The seasonal variation of seismicity detected with the Schuster test seems to have no detectable effect on the IET distribution, and this source of non-stationarity cannot be detected easily based on the departure from the exponential distribution expected for a stationary Poisson process.

3.5.2 Testing the Effect of Non-Stationarity and Aftershocks with Full Synthetic Catalogs

With the previous analyses (Figures 3.6 – 3.9), there is already strong indication that it is merely the presence of aftershocks that has the strongest effect on the Poissonian (or non-Poissonian) nature of the catalog, but deviations from stationarity in the background rate, as shown in Figures 3.8 and 3.9, may play a role as well. To determine whether non-stationarity alone or incomplete declustering is responsible for the observed fat tail, we generate full synthetic catalogs using a simple-type aftershock sequence model (STAS). We generate non-stationary Poissonian distributed mainshocks using the same annualized t_0 as in the QTM and HYS catalogs. Magnitudes are distributed according to the Gutenberg-Richter law, and aftershock sequences for each earthquake are generated according to the modified Omori's Law (see supplementary material for details on the generation of the synthetic catalogs).

We create a total of 50 synthetic catalogs for each of the HYS and QTM based mainshock sequences.

We determine the cumulative distributions of the IETs in the same way as before, for both the mainshocks alone (Figure 3.10 a-b) and for the full catalog separately (Figure 3.10 c-d). The IET distributions of the mainshocks alone are plotted against the Poisson model obtained using the mean t_0 of the HYS or QTM catalogs, respectively, and the IET distributions of the full catalog simulations are plotted with the Poisson model calculated using the mean t_0 of that simulation, including the aftershocks. We compare the two distributions to see if the trends previously seen in the IET CDF of the QTM and HYS data are characteristic of the presence of aftershocks.

Comparing the CDF of the IETs of the synthetic mainshock catalogs, where events are known to come from a Poisson distribution, albeit a non-stationary one, reveals the effect that the magnitude of the non-stationarity has on the IET distribution. The mainshock IET distributions (Figure 3.10 a-b) mostly follow the Poisson model as expected, even with the non-stationarity. Most of the deviation is well within the expected error for synthetic data, as discussed above based on Figure 3.5. Only for the non-stationary case using the t_0 of the HYS data is there a more significant tail on the distribution, where the lower standard deviation bound of the synthetic data is actually just above the Poisson model (Figure 3.10a). This suggests that non-stationarity may indeed contribute to the observed tail on the mainshock data. Non-stationarity does not have as strong an effect for the QTM-based synthetic catalog as it does for the HYS-based synthetics, but the variation in t_o in the HYS catalog is also an order of magnitude larger than in the QTM, suggesting the variability in the earthquake rate must be above a certain level before it can actually have an effect on the IET distribution.

The IET distributions and the associated Poisson models for the entire catalog with aftershocks, on the other hand, are strikingly different and reveal the effect that the presence of aftershocks has on the IET distribution (Figure 3.10 c-d). When the mean interevent time used in the exponential model is calculated from the interevent times of the full catalog, the resulting model is extremely skewed due to the overabundance of lower magnitude events with shorter interevent times, reducing the overall mean t_0. This generates the appearance of a large fat tail in the data. Indeed the synthetic data for the complete catalogs always tails-off to the right (thin light gray lines in Figure 3.10 c-d) relative to their respective Poisson models (dark

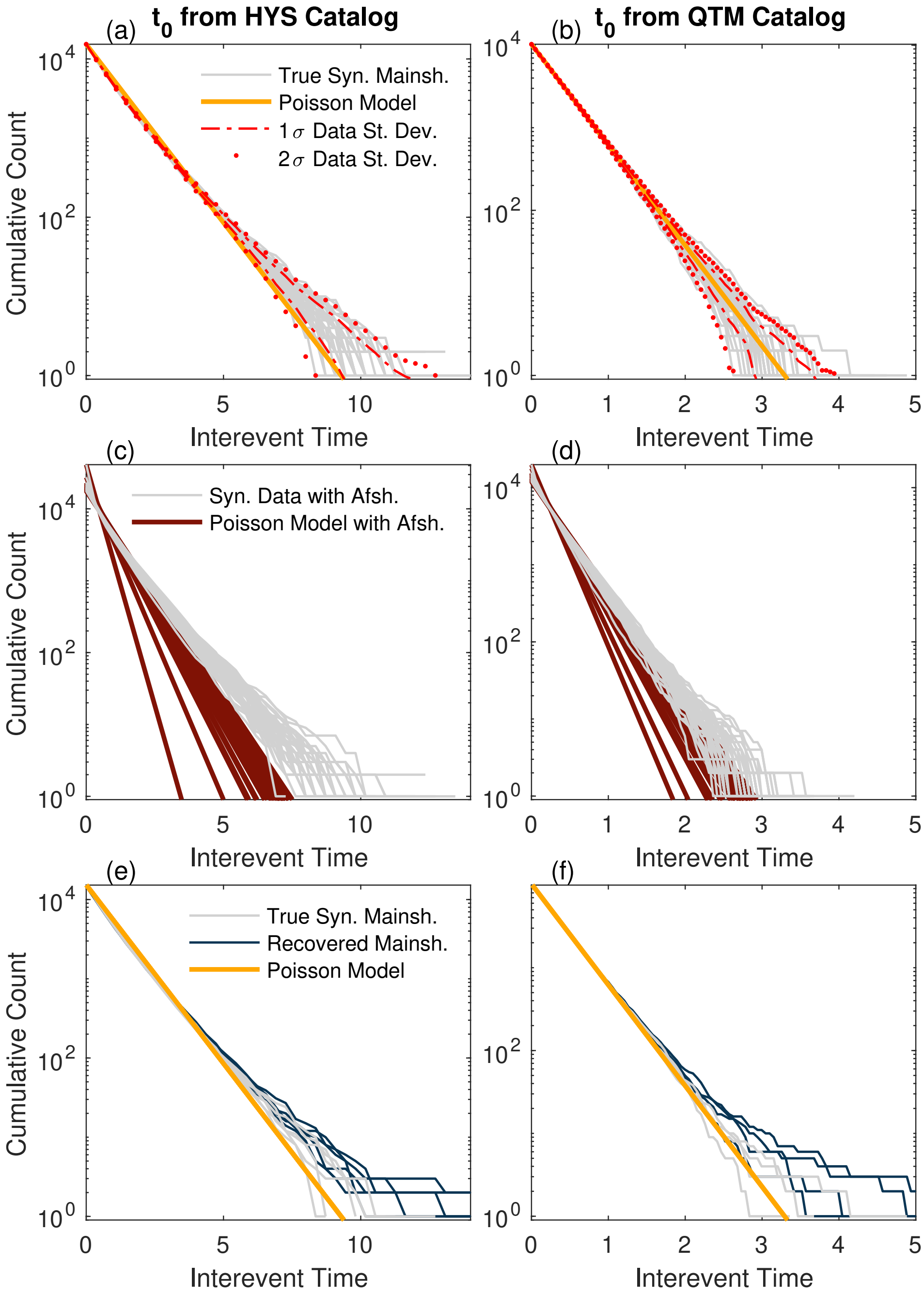

Figure 3.10: IET distributions of 50 synthetic catalogs for: (a) Mainshocks generated using the non-stationary annualized t_0's from the HYS catalog (light gray lines), plotted against the corresponding Poisson model using the mean IET of the whole HYS catalog. (b) Same as (a) but using the non-stationary annualized t_0's from the QTM catalog. (c) Full synthetic catalogs with aftershocks using the HYS-based mainshocks in (a), with the corresponding Poisson models for each simulation. (d) Same as (c) but using the QTM-based mainshocks in (b). (e) Synthetic mainshocks recovered from declustering the HYS-based synthetic catalogs (dark lines) for simulations that have at least one M > 7 earthquake, versus the true synthetic mainshock distributions for those same simulations (light gray lines) and the known Poisson model, as in (a). (f) Same as (e) but for the QTM-based synthetic catalogs.

thick lines) for all simulations, as expected. This same deviation is what we observe in the undeclustered catalogs, as well as to some extent in the declustered ones.

To test whether the observed tail is an artefact of remaining aftershocks after declustering, we decluster the synthetic simulations that contain at least one M > 7 earthquake using the Zaliapin and Ben-Zion (2013) algorithm. This yields 6 declustered catalogs from the simulations based off the HYS data and 4 declustered catalogs from the simulations based off the QTM data. (See supplementary material Figures S1-S10 for results of the synthetic catalog generation and declustering.) The interevent time distributions for the recovered mainshocks obtained from the declustering are shown in Figure 3.10 (e-f) against the distributions for the true synthetic mainshocks for those same simulations and the known Poisson model for the mainshocks as in Figure 3.10 (a-b). For most of the simulations, the Zaliapin and Ben-Zion (2013) declustering predicts the correct proportion of mainshocks to within about 3.8% on average. However, the interevent time distributions of the recovered mainshocks always exhibit a slight fat tail. To determine whether this deviation is significant, given the existing deviation in the synthetic mainshocks, we again perform a basic chi-squared goodness of fit test as was done on the real data. For the HYS-based synthetic catalog, only two cases out of the six that were declustered were significant enough to reject the Poisson model, but for the QTM-based synthetic catalog, the deviations of all but one of the four declustered simulations were significant enough to reject the Poisson hypothesis. This suggests that in the case of the HYS catalog, aftershocks remaining in the catalog after declustering are not the primary cause of the deviation, but rather the non-stationarity itself, since, as was mentioned above, the variation in the earthquake rate of the HYS catalog is greater than that of the QTM catalog. In the case of the QTM catalog on the other hand, the presence of remaining aftershocks in the declustered catalog, even if only a small amount, is enough create a significant fat tail. The synthetic catalogs presented here demonstrate that the fat tail on the earthquake IET distribution is in part due to background non-stationarity, but is also largely an artefact of the presence of aftershocks.

3.6 Discussion

Analysis of the earthquake interevent time distribution of the QTM and HYS catalogs for Southern California reveals that earthquakes do appear to follow a Poisson process, albeit with temporary variability in the earthquake occurrence rate. Comparison of the QTM data to synthetic interevent times generated according to an exponential distribution (Figure 3.5) shows that the fat tail of the data does not significantly lie outside the expected error for the interevent times of a stationary Poisson process for most magnitude cutoffs. Nevertheless, there are cases where the deviation of the data beyond the spread of the synthetic error is statistically significant and for which the Poisson model can be rejected. Moreover, the Schuster tests and annualized analysis of the catalogs show evidence of non-stationarity and/or the influence of aftershocks that warrant an explanation of the deviation. Overall, there are a number of sources that can explain the fat tail, all of which likely contribute to the IET distribution of the catalog.

The first is the limited number of events and the completeness of the catalog. There is greater error at longer interevent times, and even more so when we look at only larger magnitudes because those earthquakes have longer interevent times just by the nature of the Gutenberg-Richter relationship. This spread is the result of numerical error from having only a finite number of events, since to truly generate a Poissonian distributed set of data one cannot specify the number of events a priori, as it would technically lead to a violation of the independent scattering property of Poisson processes (Daley and Vere-Jones, 2003). If we had an infinite number of events, or at least a really long and/or totally complete catalog, then those data sets would collapse onto the exponential distribution expected for a Poisson process, but we are limited both in our simulated data and in the real data by a finite number of events. This is, however, why the tail on the QTM catalog is less significant than in other catalogs - it is simply a more complete catalog. This highlights the importance of using a more robust and complete catalog when performing any analysis of earthquake occurrences in time. Nevertheless, the question stands: is the deviation of the data from the Poisson model consistent with the numerical deviation we expect due to a limited number of events, or it is more so and thus attributable to some physical process intrinsic to the seismic cycle itself?

From most of the results of the synthetic interevent times in Figure 3.5, our results indicate that the deviation is not beyond what is expected from numerical error and that the QTM earthquakes do indeed follow a Poisson process. However, it is worth noting that the tail on the catalogs is always above the exponential line, while the exponentially distributed synthetic data varies equally both above and below the model. Thus, although the QTM data, for instance, usually does not exceed the error we would expect for the exponential distribution, the fact that it is uni-directional in its deviation implies that the tail we do observe is in fact not random. This is also supported by the Schuster spectrum. Moreover, the size and completeness of the

QTM catalog allows for tracking rather small temporal variations in the background seismicity rate, which are on the order of about 5% at the annual scale for all of southern California. The existence of this variability is significant because it hearkens back to debates about the estimated foreshock fraction. When assuming a stationary Poisson process, up to 70% of mainshocks may appear to be preceded by statistically significant foreshock sequences (Trugman and Ross, 2019), but when taking into account fluctuations in the background seismicity rate, Ende and Ampuero (2020) argue that the presence of a foreshock sequence is often just due to random chance and that the percentage of mainshocks preceded by true foreshock sequences is closer to 10-20%. The existence of variability in the background rate as determined from the QTM catalog supports the argument that the Trugman and Ross (2019) foreshock percentage is likely overestimated. This of course assumes that our selection of mainshocks is in fact accurate and robust to sources of non-stationarity. There are limits to any declustering method, but the synthetic catalogs demonstrate that the Zaliapin and Ben-Zion (2013) algorithm predicts the correct fraction of mainshocks to within 3.8% error on average, and it is, in principle, not biased towards a Poisson distribution. However, the synthetic catalog simulations also demonstrate that the QTM fluctuations in seismicity rate alone are not enough to push the synthetic data to the right of the exponential (Figure 3.10b). In a more limited catalog, however, or one with more significant variability in t_0, such as the HYS, in which the annual temporal variation is on the order of about 28%, the tail begins to emerge (Figure 3.10a). Of course, the variability is dependent on the size of the catalog: with more events, we would expect the variability to decrease, which is why the QTM catalog provides a more robust estimate of any true background variability. Nevertheless, from the results of the Schuster tests and the synthetics, we argue that the tail is not a random deviation due to a limited number of events in the catalogs but is a result of real characteristics of the catalog. However, such characteristics likely reflect incomplete declustering or changes in the quality and density of both the seismic network and seismic data rather than any underlying geophysical process.

In the QTM catalog, changes in t_0 and the interevent time distribution correlate with 2010, and as such, the tail in this catalog is most likely an artefact of remaining aftershocks from the El Mayor-Cucapah sequence in the declustered catalog. Recent work has shown that post-seismic deformation due to the 2010 El Mayor-Cucapah event has persisted for an extended period of time (Gualandi et al., 2020). The work of Gualandi et al. (2020), which used variational Bayesian Independent Component

Analysis to examine the El Mayor-Cucapah aftershock sequence in both the spatial and temporal near- and far-field, revealed that viscoelastic relaxation affected the seismicity rate across a region several times the fault rupture length and for seven years after the mainshock. The anomalously large space and time length scales of the aftershocks from the mainshocks enabled by the viscoelastic response may explain why such aftershocks were not identified and removed in the declustering. It may be argued that they are not proper aftershocks since they were not triggered directly by the co-seismic stresses. Cutting the QTM catalog into periods before and after 2010 indeed shows a slight change in the mean earthquake occurrence rate between the two time periods (Figure 3.7 a-b). Thus, the effect of the Earth's viscoelastic response to an earthquake on the seismic cycle and the IET distribution are grounds for considering non-stationarity or time-dependent distributions when constructing hazard models, at least within the relaxation time period after an event. However, examining the IET distribution of each year in the catalog individually reveals that the mean IET returns to its pre-event mean value within about a year or so after the 2010 earthquake, demonstrating that the events within different time windows are still Poisson distributed and that the catalog at large may be considered stationary.

Changes in t_0 in the HYS catalog on the other hand are not associated with any particular earthquake. However, the apparent non-stationarity in the HYS catalog also likely results from excess aftershocks in the declustered catalog due to the dependency of aftershock detection on improvements in the seismic network, starting in the 1990s, as discussed above. This possible sensitivity of changes in the earthquake rate to improvements in location errors highlights the importance of the spatio-temporal scale considered when modeling the earthquake IET distribution. At the scale of all of Southern California, fluctuations in the mean interevent time due to forcing factors or localized memory effects are likely averaged out, resulting in an SIP process, as seen broadly in the QTM catalog. At a more local scale, however, such as that directly affected by the post-seismic effects of the El Mayor-Cucapah earthquake, the seismic rate variations may not be insignificant, as evidenced both in the seismicity itself and in geodetic data (Gualandi et al., 2020). This is particularly true in light of work from Ben-Zion and Zaliapin (2020) demonstrating progressive localization of seismicity in the 1-2 years before large mainshocks, in particular the Landers, Hector Mine, and El Mayor Cucapah earthquakes, as a result of localization and intensification of rock damage by the preceding background seismicity. This also has the effect of creating a real and/or apparent decreasing intensity of the background seismicity (Ben-Zion and Zaliapin, 2020), consistent with an increasing

t_0, as observed in the HYS catalog. Our study focuses specifically on the temporal distribution of earthquakes, but given the connection between temporally varying spatial localization of seismicity and changes in the seismicity rate, use or analysis of the earthquake IET distribution should in the future incorporate both the spatial and temporal structure of earthquake occurrence, especially as it relates to informing seismic hazard.

While the deviation of the QTM earthquake interevent time distribution is for the most part insignificant, it is real and not random, though limitations in the size of a catalog do contribute to the size of the tail. However, our results reveal that the fat tail observed on the IET distribution is a reflection of transient non-stationarity in the seismicity rate due to either 1) excess aftershocks remaining in the declustered catalog, possibly due to changes in the seismic network, and/or 2) viscoelastic effects in the aftermath of large events. Such non-stationarity becomes more important at the local level and over shorter timescales. Ultimately, seismic hazard assessment needs to address potential risk from earthquakes at a local scale, from place to place, where it directly impacts people and infrastructure. At the scale of all of southern California, however, a stationary Poisson process is still a sufficient model for representing earthquake occurrences at the decadal time scale and spatial scale of the QTM catalog.

Data and Resources

Earthquake data from the relocated SCSN catalog from Hauksson et al. (2012) (HYS catalog) is available from the Southern California Earthquake Data Center (SCEDC): https://scedc. caltech.edu/data/alt-2011-dd-hauksson-yang-shearer.html (last accessed Feb. 17th, 2021). The QTM catalog for Southern California is also available from the SCEDC: https://scedc.caltech.edu/da- ta/qtm-catalog.html (last accessed Feb. 10th, 2021). Appendix B contains equations and details on the declustering algorithm and the generation of the synthetic catalogs, as well as figures showing the GR distribution, cumulative events with time, magnitude with time, and the declustering results for each synthetic catalog containing at least one M > 7 earthquake.

Chapter 4

GEODYNAMIC CONTROLS ON INTRAPLATE SEISMICITY IN EASTERN NORTH AMERICA I: THE INFLUENCE OF MANTLE LOADING FROM THE FARALLON SLAB

**A version of this chapter has been submitted for publication as:*

Hightower, E., Gurnis, M. and Mao, W. "Influence of Farallon Slab Loading on Intraplate Stress and Seismicity in Eastern North America in the Presence of Pre-existing Weak Zones". [Submitted].

4.1 Introduction

Intraplate seismicity is an enigmatic phenomenon not directly associated with plate boundary tectonics, potentially resulting from a combination of geodynamic processes and surface loading, with contribution from far-field tectonic forces and pre–existing structures. The continental interior of eastern North America is one of the best regions for studying the interplay between geodynamics and intraplate seismicity, as it has hosted many significant historical earthquakes and is undergoing both modern day glacial isostatic adjustment (GIA) (Wu and Hasegawa, 1996; Wu and Johnston, 2000; Grollimund and Zoback, 2001) and long-wavelength dynamic subsidence (Spasojevic et al., 2008; Forte et al., 2010). Despite the stability of the North American interior, which experiences only about 2 mm/yr of horizontal motion according to GPS data (Stein and Sella, 2002), earthquake shaking is potentially more hazardous compared to that on plate margins, as the stable continental lithosphere can transmit seismic energy more efficiently, and peak ground acceleration may be almost twice that of plate boundary zones for a given earthquake magnitude (Stein, 2007).

Historic records of major earthquakes in eastern North America date back to at least 1638 (Figure 4.1 a), with most seismicity occurring within clearly defined seismic zones (Figure 4.1 b). Of these zones, the New Madrid, Central Virginia, Charleston South Carolina, Eastern Tennessee, Northern Appalachian, Western Quebec, Charlevoix, and St. Lawrence River Valley Seismic Zones have experienced destructive earthquakes in recorded history, most notably the 1811-1812 New

Madrid earthquakes. The largest of these events may have been as high as M 8, but more likely around M 7 (Hough et al., 2000; Stein, 2007). These and other significant events ranging from M 5 to M 7 are depicted in Figure 4.1a and listed in Table 4.1. While an intraplate earthquake of magnitude greater than or equal to M 7 is expected to occur anywhere along the Atlantic margin only every few 1000 years (Brink et al., 2009), earthquake hazard remains significant for the central-eastern United States (CEUS) due to limited earthquake preparedness.

Major Historical Earthquakes in Eastern North America

Year	Magnitude	Location
1638	6.5	Central New Hampshire
1663	7	Charlevoix, Quebec
1732	6.3	Montreal, Quebec
1755	5.9	Cape Ann, Massachusetts
1811-1812	7.3-8	New Madrid
1882	6.6	Fort Collins
1886	7.0	Charleston, South Carolina
1897	5.6	Giles County, Virginia
1925	6.3	St. Lawrence River Valley, Quebec
1929	7.2	Grand Banks, Newfoundland
1935	6.2	Timiskaming, Canada
1971	5.5	Labrador Sea
1978	6.1	North Atlantic
1982	5.7	New Brunswick
1989	6	Ungava, Canada
2011	5.8	Mineral, Virginia

Table 4.1: Major historical earthquakes greater than M 5.5 in Eastern North America since 1600. Data from the USGS ANSS Comprehensive Earthquake Catalog (ComCat), queried on Feb. 8th, 2021.

Hypotheses for the drivers of intraplate seismicity include gravitational body forces (Levandowski et al., 2017; Levandowski et al., 2018), far-field tectonic stresses (Humphreys and Coblentz, 2007), prolonged viscoelastic relaxation in the aftermath of large events (Kenner and Segall, 2000; Kenner and Simons, 2005), hydrologic and seasonal loading (Craig et al., 2017), glacial rebound (Grollimund and Zoback, 2000; Grollimund and Zoback, 2001; Wu and Johnston, 2000; Wu and Mazzotti, 2007), and mantle flow (Forte et al., 2007; Saxena et al., 2021). Across these different factors, intraplate seismicity exhibits common characteristics, including correlation with paleotectonic structures, the apparent lack of any significant recent deformation on existing structures or faults, and low intraplate strain rates (Mazzotti, 2007a). Globally, about two-thirds of continental intraplate earthquakes occur

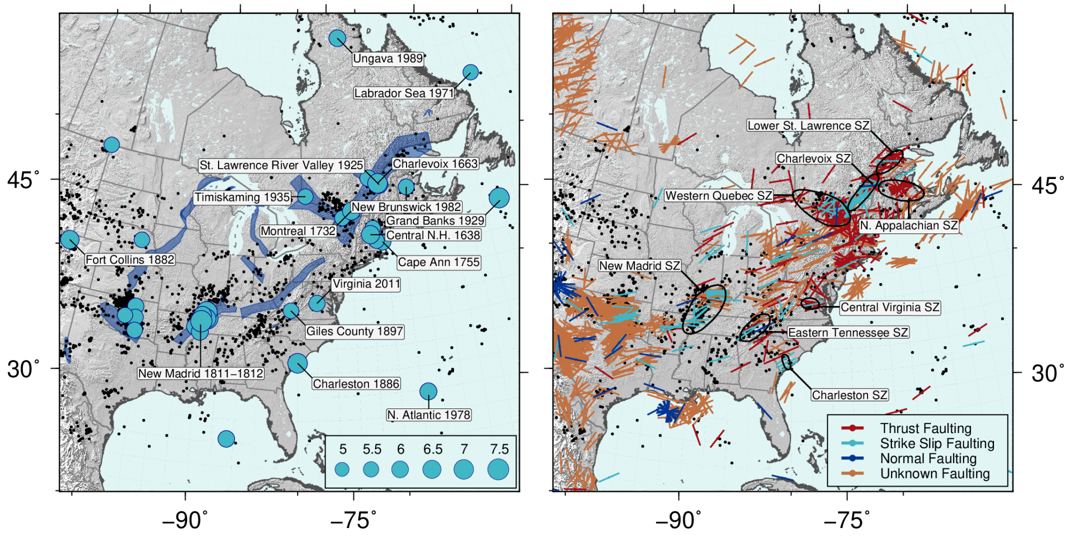

Figure 4.1: Regional setting. a) Historical seismicity in eastern North America. Large blue circles are significant historical intraplate earthquakes of M ≥ 5.5. Black dots are background seismicity of M ≥ 3 from the USGS-ANSS Comprehensive Earthquake Catalog. Indigo polygons are geologically mapped ancient aulacogens from Whitmeyer and Karlstrom (2007). b) Stress field (S_{Hmax}) of eastern North America from the World Stress Map Database (WSM) (Heidbach et al., 2018), colored by faulting style. Black dots are background seismicity as in (a). Black ellipses outline major named seismic zones.

within Mesozoic or older crustal extensional structures, such as rifted margins, aulacogens (failed rift arms), and extensional basins (Johnston et al., 1994; Mazzotti, 2007a), which can act as weak zones in the crust where stress accumulates.

Likewise, seismicity in eastern North America tends to concentrate within these ancient aulacogens (Sykes, 1978; Hurd and Zoback, 2012). The New Madrid Seismic Zone (NMSZ) (Reelfoot Rift) and Western Quebec Seismic Zone (WQSZ) (Ottawa-Bonnecherè Graben) are associated with Proterozoic (700-550 Ma) Iapetus failed rift arms (Baird et al., 2010). The Lower St. Lawrence, Charlevoix, Montreal, and Eastern Tennessee Seismic Zones are associated with the Iapetus rifted margin itself (Mazzotti and Townend, 2010), and the Northern Appalachian, Central Virginia, and Charleston Seismic Zones are spatially correlated with Mesozoic rift basins of the extended Atlantic margin (Withjack et al., 1998; Mazzotti and Townend, 2010), as well as other inherited tectonic structures. Earthquakes and modeled stresses also concentrate in zones of thinner lithosphere around the margin of the North American craton (Li et al., 2007), where it transitions to the Grenville province and the rifted margin. Even more enigmatic is that there is little association between the earthquake locations and active faults, despite the correlation between seismicity and these inherited structures. This is due in part to poorly located hypocenters and limited data on historic events but may also be due to the intrinsically low strain rates characteristic of intraplate regions (Mazzotti, 2007a). For example, earthquake statistics alone may predict a few kilometers of total seismic deformation over the last million years (Mazzotti and Adams, 2005), but seismic reflection surveys of the Charlevoix and New Madrid Seismic Zones indicate total accumulated deformation on particular structures to be no more than a few tens of meters (Lamontagne and Ranalli, 1996; Schweig and Ellis, 1994; Van Arsdale, 2000). Such low strain rates, typically on the order of 10^{-9} yr^{-1} or less based on GPS (Mazzotti and Adams, 2005; Mazzotti et al., 2005; Calais et al., 2006), do not, however, rule out the possibility of future large earthquakes (Kenner and Segall, 2000).

Mechanical models from Kenner and Segall (2000) demonstrate that relaxation of local lithospheric weak zones can transfer stress to the upper crust and trigger slip on faults, resulting in an earthquake sequence that continues until the weak zone fully relaxes, which can be prolonged by cyclic stress transfer from co- and post-seismic slip reloading the lower crust (Kenner and Segall, 2000; Kenner and Simons, 2005; Dicaprio et al., 2008). Such weak zone relaxation and stress cycling can trigger earthquake sequences with large slip events every 500-1000 years with shear strain rates on the order of 10^{-7} yr^{-1} to 10^{-9} yr^{-1} for high stress intraplate regions and 1.8×10^{-8} yr^{-1} to 5.5×10^{-9} yr^{-1} for lower stress regions, despite surface deformation rates often having been below the GPS detection threshold (Kenner and Segall, 2000).

Likewise, mechanical modeling of the 1811–1812 New Madrid earthquakes has revealed that intraplate seismic zones tend to stay in a stress shadow for hundreds to even thousands of years after large events, owing to the difficulty of full stress restoration due to the strength of the ambient crust and low regional strain rates (Li et al., 2007; Stein and Liu, 2009). Such findings imply seismicity in this region may be non-stationary, with mainshocks clustered in time (Kenner and Simons, 2005; Dicaprio et al., 2008; Stein and Liu, 2009). This would suggest the New Madrid earthquakes of 1811–1812 and the ensuing seismicity are transient in nature and that seismic hazard in the mid-continent may be overestimated (Newman et al., 1999). This idea is supported in part by paleoseismic evidence demonstrating an elevated slip rate on the Reelfoot Fault during the two most recent major earthquake cycles (Van Arsdale, 2000). However, paleoseismicity also records a Holocene slip rate that is four orders of magnitude greater than that in the Cretaceous and Cenozoic and a slip rate as high as 4.4 mm/yr over the last 2400 years alone (Van Arsdale, 2000).

The increase in slip rates over the past several thousand years may be tied to uplift from Laurentide deglaciation. Likewise, paleoseismological and geodetic evidence suggestive of recurrence times anywhere between 400 – 1100 years in combination with the lack of accumulated deformation on faults suggests places like the NMSZ may have become active recently and that the seismic zone itself is only a couple tens of thousands of years old (Schweig and Ellis, 1994). In general, intraplate earthquakes tend to be episodic and clustered (Stein and Liu, 2009), and seismicity may migrate between similar structures due to long-term deformation (Stein, 2007). This migration and the reactivation of particular structures may result from regional stress changes due to GIA (Wu and Johnston, 2000; Mazzotti et al., 2005; Steffen et al., 2014a), epeirogenic subsidence (Spasojevic et al., 2008), or even denudation and erosion (Craig et al., 2017; Calais et al., 2010). In light of the possibility of stress cycling, however, one must consider whether hazard is highest where seismicity has recently been concentrated or uniform within regions with similar structures.

Another common explanation for intraplate seismicity is the role of gravitational potential energy (GPE), where lateral lithospheric density and topography variations lead to regions of high deviatoric stress. Some geodynamic models find that while GPE tends to play a lesser role than mantle tractions in governing lithospheric stresses and plate velocities, both are necessary to accurately reproduce the observed stress data and plate motions (Ghosh et al., 2009; Ghosh et al., 2013). With respect to seismicity, Levandowski et al. (2017) found that for the Great Plains region of North America body forces control the state of stress and style of earthquakes without influence from mantle flow or need for pre-existing crustal weaknesses. Ghosh et al. (2013), on the other hand, find that weak zones at plate boundaries are necessary for determining the style of stress. Other studies argue for more persistent sources of stress that are concentrated by local structures (Levandowski et al., 2018; Heidbach et al., 2018), since the significant variability and local deviations within some of the seismic zones in the eastern U.S. are generally inconsistent with the continental-scale stress field that would be predicted for far-field tectonic forcing alone (Levandowski et al., 2018; Mazzotti and Townend, 2010).

In fact, focal mechanism stress inversion shows an increasingly compressive stress regime from the south-central U.S. to southeast Canada (Hurd and Zoback, 2012). While these focal mechanisms are mostly in agreement with the regional NE-SW oriented stress field, some aulacogens exhibit rotational deviation, suggesting multiple stress regimes (Hurd and Zoback, 2012; Mazzotti and Townend, 2010; Verdecchia et al., 2022). Within the Central Virginia, Lower St. Lawrence, and Charlevoix seismic zones, there is as much as a 30-50° statistically significant clockwise rotation of the seismically derived direction of maximum horizontal compressive stress (S_{Hmax}) relative to the regional borehole-derived S_{Hmax} orientation (Mazzotti and Townend, 2010). Significant depth-dependent rotations of up to 40-60° are observed within the Charlevoix Seismic Zone as well, which are argued to result from a combination of weak fault zone crust and post-glacial rebound stress (Verdecchia et al., 2022). Similar but slightly smaller rotations are observed in the Northern Appalachian and New Madrid Seismic Zones. These stress rotations occur over distances of up to 1500 km and require stress perturbations at mid-seismogenic depths of at least 160–250 MPa (Mazzotti and Townend, 2010). Potential sources of these stress rotations and the associated seismicity include complex fault intersections (Talwani, 1988; Talwani, 1999; Gangopadhyay and Talwani, 2007), crustal density anomalies and GPE forces (Levandowski et al., 2017; Ghosh et al., 2009), and flexure under local loads (Stein et al., 1989). These sources, however, cannot explain the consistency of stress rotations over spatial scales of 100s-1000s of km (Mazzotti and Townend, 2010). On the other hand, long-wavelength sources like dynamic topography, lithospheric flexure, and GIA, which typically only induce stress perturbations on the order of 10-100 MPa, may result in stress amplifications by a factor of 5-10 in the presence of a lithospheric "weak-zone" (Grollimund and Zoback, 2001; Wu and Mazzotti, 2007). Thus, under the right conditions, long–wavelength vertical movements may perturb the intraplate stress field, leading to seismic activity in an otherwise stable continental interior.

While some argue lithospheric mantle heterogeneity alone is the primary control on intraplate seismicity (Saxena et al., 2021; Levandowski et al., 2017; Zhan et al., 2016), there is cause for considering the role of epeirogeny in augmenting stress in these regions. Assuming a low-viscosity sub-lithospheric upper mantle, mantle flow due to the sinking of the Farallon slab can create significant surface depression (Forte et al., 2010) and localize bending stresses within the NMSZ possibly capable of triggering earthquakes (Forte et al., 2007). Zhan et al. (2016) point out that crustal or lithospheric loading resulting from displacements in a mantle low-velocity zone would likely be insignificant under far-field stresses alone, but could be catalyzed to a significant degree by unloading processes like GIA or even changes in drainage networks. Strain rates associated with intraplate seismicity are also on the same order of magnitude as, or even slightly smaller than, those of post-glacial rebound (Mazzotti and Adams, 2005; Calais et al., 2006; Stein, 2007).

Mechanical models from Mazzotti (2007a) suggest that a weak low-viscosity layer in the presence of regional strain consistent with that of GIA can load an upper-crust fault system and amplify the surface velocity gradient, improving the fit to GPS data for the St. Lawrence Valley. Other authors have also found GIA to be a significant driver of seismicity in the St. Lawrence River Valley (James and Bent, 1994; Wu and Hasegawa, 1996) and the NMSZ (Wu and Johnston, 2000; Grollimund and Zoback, 2001). Additionally, just as annual periodicity of seismicity in California reflects a seasonal modulation of the earthquake rate (Chapter 3, Figure 3.6), observations of the correlation between micro-earthquakes in the NMSZ and annual and multi-annual hydrologic loading cycles in the Mississippi embayment demonstrate that long-wavelength changes in continental water-storage can produce observable crustal deformation and modulate the regional seismicity (Craig et al., 2017). Such observations highlight the degree to which small changes in loading from long-wavelength processes can promote localization and enhancement of crustal stresses that impact seismicity rates.

Saxena et al. (2021) assess how both GPE and mantle flow from an inferred lithospheric drip influence stress and seismicity in eastern North America using tomography-constrained regional geodynamic models with a heterogeneous mantle lithosphere. Their results suggest that upper mantle flow alone, without lithospheric heterogeneity, is not sufficient to reproduce the observed intraplate stress field (Saxena et al., 2021). However, while their predicted S_{Hmax} directions are locally consistent with some data (e.g., Levandowski et al., 2018), they are broadly inconsistent with the general southwest-northeast trending S_{Hmax} from the World Stress Map (Heidbach et al., 2018) (Fig. 4.1b), and their predicted regional stress regime is opposite to that obtained from focal mechanism stress inversion across the CEUS and parts of Canada (e.g., Hurd and Zoback, 2012). Saxena et al. (2021) attribute such mismatches to the absence of long wavelength compressive tectonic stresses or spatially limited crustal weak zones in their models. In contrast, Zhan et al. (2016) investigated the role of pre–existing weakness in their models of the NMSZ by altering the mechanical properties within the ancient rifts and testing different degrees of mantle heterogeneity. They find that a large low-viscosity mantle region beneath the NMSZ can reload the layer above it, concentrating stresses in the upper mantle through displacement. The strength of the lower crust enables elevated stresses to transmit to the base of the ancient rift, potentially reactivating faults.

These studies highlight the importance of local weak zones in controlling intraplate seismicity, as stresses from tectonics, topography, or density contrasts are typically too small to trigger intraplate failure on their own. The integrated strength of a lithospheric section under a cold geotherm like that of eastern North America is estimated to be 5-10 times larger than plate driving forces (Mazzotti, 2007a). Thus, because cratons are too cold and stable to deform easily, even localized weak-zones may require very low viscosities in the lower crust and/or upper mantle (10^{19} Pa s or less) to achieve seismic strain rates. Such weakness can be due to either conditions that reduce the strength and viscosity of the entire lithosphere, such as elevated heat flow, or conditions that allow for high stress and strain rates in a weak deforming layer that loads the brittle upper crust. A weak zone may also result from the presence of a mechanically weak crust, such as a wet quartz-diorite with low effective viscosity, even under a cold geotherm; high pore fluid pressure; or an exceptionally weak fault zone with low-friction fault gouge material (Mazzotti, 2007a).

Despite the work reported to date, the possible connections between intraplate seismicity and large-scale continental uplift or the sinking of continental platforms (i.e., epeirogeny) remain elusive. Geodynamic modeling has demonstrated that sinking slabs, in regions of both active and ancient subduction, create mantle downwelling that generates tractions within the overlying lithosphere, resulting in dynamic subsidence (Hager, 1984; Mitrovica et al., 1989; Gurnis, 1992; Yang et al., 2016; Forte et al., 2010). Initially, sinking slabs can stagnate at the 660 km discontinuity due to the viscosity jump and the phase transition between ringwoodite and bridgmanite (Billen, 2008). The negative buoyancy of the accumulated mass is eventually great enough to break through the boundary and continue sinking, initiating a process called slab avalanche, which causes substantial downward asthenospheric flow (Christensen and Yuen, 1984; Tackley et al., 1993; Yang et al., 2016; Yang et al., 2018). Dynamic subsidence has been inferred in eastern North America from Cenozoic shorelines (Spasojevic et al., 2008), under which the remnant Farallon slab lies between 410 and 2200 km depth (Ren et al., 2007; Lu et al., 2019). The presence of the slab predominantly beneath the 660 km discontinuity implies possible slab avalanche, as do models of mantle flow localized beneath the eastern U.S. (Forte et al., 2007), but questions remain as to how this flow-induced continental subsidence affects stress in the lithosphere. Moreover, the increasing degree of stress rotation moving northeastwards into the Canadian margin is consistent with increasingly compressive stress regimes and stress rotations observed above deep slabs far inland of the trench, such as in Sundaland (Yang and Gurnis, 2016; Yang et al., 2018).

While this epeirogenic movement may not cause notable folding or faulting (Gurnis, 1992), it may reactivate pre-existing faults.

We explore the hypothesis that mantle flow caused by the sinking of the Farallon slab contributes to intraplate seismicity in eastern North America via perturbation to the stress field and reactivation of pre-existing faults. We develop high-resolution global geodynamic flow models with CitcomS (Zhong et al., 2000; Tan et al., 2006; Moresi et al., 2014), a spherical finite-element thermochemical mantle convection code. The models use an initial thermal structure constrained by seismic tomography and geology to accurately reflect lithospheric and mantle structure, adequately capture the Farallon slab at depth, and reproduce observed plate motions. As we are interested in the current state of stress, we calculate the instantaneous flow field and associated stress tensor, with which we compute the S_{Hmax} direction and the deviatoric stress in the crust and lithosphere. We evaluate our results against the stresses in the World Stress Map Database (Heidbach et al., 2018) and Mazzotti and Townend (2010). Our work improves upon previous investigations of this topic by 1) using global rather than regional scale convection models that naturally incorporate far-field tectonic forcing, 2) purposefully testing the impact of the Farallon slab on the stress field by parameterizing its negative buoyancy, 3) explicitly including local-scale, low-viscosity lithospheric weak-zones at the locations of the geologically mapped aulacogens, and 4) quantifying the likelihood of fault reactivation by resolving the modeled Coulomb stress onto mapped faults within the seismic zones of eastern North America.

4.2 Geological Background and Regional Setting

New Madrid Seismic Zone

The NMSZ is predominantly associated with the Reelfoot Rift — part of a system of intracratonic faults that resulted from late-stage crustal extension during and following the breakup of super-continent Rodinia and the opening of the Iapetus ocean (Thomas and Powell, 2017). At its northeast end, it merges with the eastward trending Rough Creek Graben, which serves as a sinistral strike-slip offset between the Reelfoot Rift and the Rome Trough (Figure 4.1). However, despite the fact that earthquakes mainly occur within the rift, most appear to have little systematic relationship to the known graben-boundary faults (Thomas and Powell, 2017). The basement of the NMSZ has been deformed by a combination of extensional fracturing within a releasing bend between the Reelfoot and Rough Creek grabens during

Iapetan rifting and contraction of those previously extended basement rocks within the Reelfoot Rift, which reactivated extensional faults in the Appalachian-Ouachita orogeny during the assembly of Pangea (Thomas and Powell, 2017). Such repeated deformation and reactivation could result in a weakened basement at lower crustal depths that concentrates seismicity in the NMSZ. However, the high-velocity lower crust, often interpreted as a mafic pillow, beneath the NMSZ is inconsistent with a weakened low-viscosity rheology at these depths.

Rather, low-velocity zones are identified in the upper mantle beneath the NMSZ, extending from the base of the crust to as deep as 300 km (Thomas and Powell, 2017; Nyamwandha et al., 2016; Chen et al., 2016). Moreover, Zhan et al. (2016) demonstrate in regional lithospheric models of the NMSZ that the differential stress needed to explain the observed seismicity requires a combination of weak rift, strong lower crust, and low-viscosity upper mantle, and that without the weak rift zone, the differential stress is elevated but broadly distributed rather than localized. The passage of a mantle plume is also often used to explain the crustal structure and associated concentration of seismicity in the NMSZ (Chu et al., 2013). Chen et al. (2016) conclude a combination of thermal variations, compositional heterogeneity, and water content are needed to explain the observed variations in seismic velocity beneath the NMSZ and the Illinois Basin, since a small increase in temperature alone would not be enough to create a large strength difference between the rift and surrounding region, but both increased iron content and hydration in addition to temperature will sufficiently weaken olivine. Rifting would have introduced iron, water, and basalt into the host peridotite of the region, refertilizing the lithospheric mantle and reducing its seismic velocities. The partial melting and mafic material that intruded the lower crust can explain the high velocity layer at the base of the crust below the Moho and above ~ 70 km. The weakening of olivine from hydration and greater iron content would result in a low-viscosity weak zone in the upper mantle beneath the rift, which by creeping faster than surrounding areas can transfer stress and load the crust (Thomas and Powell, 2017; Kenner and Segall, 2000).

Eastern Tennessee and Central Virginia Seismic Zones

Unlike the NMSZ, the Eastern Tennessee Seismic Zone (ETSZ) is not associated with an aulacogen or other rift arm but instead with the New York-Alabama (NY-AL) magnetic lineament. This structure formed as a sinistral continental transform fault between proto-Laurentia and Amazonia during the assembly of supercontinent Rodinia and the Grenville orogeny (Thomas and Powell, 2017). Seismic anisotropy from SKS shear wave splitting indicate a strong shearing component parallel to the lineament (Thomas and Powell, 2017; Wagner et al., 2012; Long et al., 2016). A prominent low velocity zone exists in the basement beneath the ETSZ at depths of 5-25 km, consistent with a sheared crust (Powell et al., 2014). Sheared crust is often accompanied by soft phyllosilicate minerals such as talc, phlogopite, and antigorite, particularly if deformed in the presence of hydration (Chen et al., 2016). Such minerals are inherently weak and lower in viscosity due to their layered structure and exhibit significantly reduced shear strengths. In eastern Tennessee, this sheared crust is interpreted to be a weak zone bounded by en echelon conjugate shears and normal faults beneath the NY-AL lineament (Thomas and Powell, 2017). Magnetotelluric (MT) imaging of this region (Murphy and Egbert, 2017) also reveals a contrast in lithospheric electrical properties between the Appalachian highlands and the Piedmont and Coastal Plain lowlands to the east; the former, near the ETSZ, is underlain by more conductive crustal and mantle material between 25 and 55 km depth, which can be interpreted as a viscosity contrast between the two domains ranging anywhere from 1 to 6 orders of magnitude (Murphy and Egbert, 2017; Murphy et al., 2019). The NY-AL lineament itself is a narrow feature, at most 25-50 km wide (Thomas and Powell, 2017). The deeper portion of this potential low viscosity structure, as indicated by the MT data, however, ranges from 25 to 125 km wide (Murphy and Egbert, 2017). For this reason, we represent the weak zone associated with the ETSZ by a roughly 50-100 km wide low-viscosity zone between 15 and 50 km depth, with narrower widths at shallower depths, which allows us to capture at least 2 elements width in our models.

MT imaging has also captured the lithospheric structure to the north of the ETSZ in the vicinity of the Rome Trough and the Central Virginia Seismic Zone (CVSZ). Highly conductive asthenosphere beneath the central Appalachians imaged by the MAGIC array (Long et al., 2020; Evans et al., 2019) reveals thin lithosphere on the order of 80 km thick. Regions of high conductivity extend from 80 to 200+ km depth across the entire width of the Appalachian Mountain chain, the position of which is consistent with earlier shear velocity models that show a pronounced 300 km wide low velocity zone extending from the base of the lithosphere to near 660 km, known as the Central Appalachian Anomaly (CAA) (Schmandt and Lin, 2014). Such an anomaly could be caused by extensive hydration of the mantle due to fluids derived from the relict Farallon slab, which would lower mantle viscosity. Beneath the Rome Trough, conductivity is sufficiently high to be consistent with some degree of partial melt and hence lower viscosity (Evans et al., 2019). Conductive solid phases, such as sulphides and graphite indicative of metasedimentary shear fabrics developed during continental suturing, surround this region of possible partial melt and are consistent with those imaged by seismic reflection profiling across the Grenville province and across the ETSZ (Culotta et al., 1990). Thus, we include a low viscosity weak zone between 80 and 200 km depth parallel to the Rome Tough and approximately 400-600 km in width.

Lower Saint Lawrence River, Charlevoix, and Western Quebec Seismic Zones

The Lower Saint Lawrence Rift System (LSLRS) as a whole contains all of the Lower Saint Lawrence Rift, the Ottawa-Bonnechere Graben, and the Saguenay Graben, as well as the Western Quebec, Charlevoix, and Lower Saint Lawrence Seismic Zones (Figure 4.1). The latter is confined to the northernmost end of the LSLRS. Within this seismic zone and throughout the LSLRS, earthquakes predominantly occur within the Precambrian Shield between depths of 5 to 25 km on steeply dipping normal faults that were formed during the opening of the Iapetus Ocean (Lamontagne and Ranalli, 2014). There is evidence of strong decoupling between the Appalachians and Canadian Shield along the Logan Line (Castonguay et al., 2010), and the Appalachians are for the most part aseismic, with earthquakes occurring beneath the Appalachian Nappes and within the Precambrian Shield (Lamontagne and Ranalli, 2014). The Lower Saint Lawrence Seismic Zone (LSLSZ) is the least seismically active of those in the LSLRS.

The Charlevoix Seismic Zone (CXSZ), on the other hand, has the highest seismic hazard of continental eastern Canada (Lamontagne and Ranalli, 2014). In the CXSZ, earthquakes cluster along or between the mapped Iapetan rift faults of the St. Lawrence Rift (Lamontagne and Brouillette, 2022), but the CXSZ is also the site of an ancient impact structure. It has been suggested that this comparatively weak damaged volume has lower elastic moduli that influence the stability of the rift faults that intersect it, promoting a localization of low level seismicity within the crater and larger events near the perimeter and outside the crater (Baird et al., 2010; Thomas and Powell, 2017; Lamontagne and Brouillette, 2022). The rift faults themselves are believed to have lower Mohr-Coulomb frictional strength (Baird et al., 2010), meaning the predominant source of weakness may lie in the crust, not the mantle. The effect of post-glacial rebound on the near surface ancient rift faults may be amplified by a weaker crust with low frictional strength and semi-brittle rheology (Verdecchia et al., 2022). Moreover, the CXSZ exhibits depth-dependent crustal stress rotation and strength variations, primarily in the middle crust between

13-26 km depth (Verdecchia et al., 2022). The seismicity itself ranges from 0-26 km depth, with the largest stress rotations occurring between 12 and 16 km, yielding a total clockwise rotation of about 30° between shallow and deeper focal mechanisms (Verdecchia et al., 2022). The largest stress rotation from the regional borehole direction (up to 60°) is at mid-crustal depths between 20-26 km. Similar clockwise rotations of 44°-49° are reported for the LSLSZ north of the CXSZ (Verdecchia et al., 2022).

The Western Quebec Seismic Zone (WQSZ) is likewise associated with Precambrian to early Paleozoic Iapetan rift arms and aulacogens, specifically the Ottawa-Bonnechere and Timiskaming Grabens, which are characterized by both NW-SE and NE-SW striking, steeply dipping faults (Rimando and Peace, 2021). The majority of earthquakes in the WQSZ occur at 8-18 km depth and follow a linear NW-SE trend slightly adjacent but parallel to the Ottawa-Bonnechere Graben (Figure 4.1). In addition to aulacogens, it has been suggested that the passage of the Great Meteor Hotspot during the Mesozoic or an extension of the New England Seamount Chain track, whose path aligns with the orientation of the WQSZ, enabled thermo-mechanical weakening of ancient faults and shear zones and emplaced strength contrasts between felsic rocks and mafic intrusions in the mid-crust (Sykes, 1978; Ma and Eaton, 2007). The hotspot theory is supported in part by lithospheric velocity anomalies at around 200 km depth (Ma and Eaton, 2007), but there is no surface geological expression of a hotspot (Lamontagne and Ranalli, 2014). The WQSZ also exhibits thinner crust than the surrounding Grenville Province, which typically ranges from 30-48 km thick (Ma and Eaton, 2007). Despite local structural complexities that no doubt play a role in controlling seismicity throughout the LSLRS, the ancient rift itself likely provides a source of lower crustal or upper mantle weakness. In our models, we position weak zones at the locations of the LSLRS and its rift arms within and below the lower crust into the top of the lithospheric mantle, between 25 and 75 km depth.

4.3 Geodynamic Modeling in CitcomS

We use the 3D spherical shell finite-element mantle convection code CitcomS to solve the conservation equations of mass and momentum (Zhong et al., 2000; Tan et al., 2006; Zhong et al., 2008; Moresi et al., 2014). Under the Boussinesq approximation for an incompressible fluid, the conservation equations are:

$$\nabla \cdot \vec{u} = 0 \tag{4.1}$$

$$-\nabla p + \nabla \cdot (\eta \dot{\epsilon}) + (\delta \rho g_0 + \rho_0 \delta g)\hat{e}_r = 0 \tag{4.2}$$

where $\vec{u}$ is the velocity in the non-rotating mantle reference frame; $\dot{\epsilon}$ is the strain-rate; p is the dynamic pressure; η, ρ_0, and g_0 are mantle viscosity, density, and gravitational acceleration, respectively; $\hat{e}_r$ is the unit vector in the radial direction. δg is a perturbation to radial gravitational acceleration that if implemented would represent the effect of self-gravitation (see Chapter 5), and $\delta \rho$ represents perturbations to density, which can arise from both thermal expansion and composition.

$$\delta \rho = \rho_0 \alpha (T - T_r) + \delta \rho_{ch} C \tag{4.3}$$

Here, α is the coefficient of thermal expansion, T is the temperature at a given point, T_r is the radial profile of adiabatic temperature or the mean temperature at a given layer, C is the composition field variable representing compositional and/or rheological heterogeneity and is either 0 or 1, and $\delta \rho_{ch}$ is the density difference between different compositions, which is ultimately implemented non-dimensionally using the buoyancy number (Eq. 4.7). It is these density perturbations that give rise to mantle flow.

The stress field in which we are interested arises from these buoyancy forces and is determined by the first two terms in Eq. 4.2. The stress, σ, is inherently dependent on changes in viscosity, η, and strain-rate, $\dot{\varepsilon}$, through the constitutive relationship

$$\sigma = 2\eta \dot{\varepsilon} \tag{4.4}$$

$$\sigma = 2\eta \left(\frac{\partial v_i}{\partial x_j} + \frac{\partial v_j}{\partial x_i} \right), \tag{4.5}$$

and thus — by the definition of strain rate — on the gradients in the velocity of the flow. A dense mass anomaly at depth (e.g., the Farallon slab) will sink and excite downward flow. The presence of the thick high viscosity cratonic lithosphere can also obstruct horizontal asthenospheric flow, driving it downwards (Paul et al., 2023). Such diversion of the flow amplifies the vertical velocity component, meaning the horizontal gradient of the vertical velocity increases approaching the primary source of the downwelling, be it the Farallon slab or the edge of the continent. The increase in this velocity gradient, and thus strain-rate, would induce high tractions on the lithosphere in these regions, resulting in high stress, particularly when scaled by the high viscosity of the lithosphere. Likewise, the presence of intra-lithospheric weak zones induces velocity gradients between the surrounding rigid high viscosity lithosphere and the faster flowing material within the weak zone, which lead to tractions on the overlying crust. Thus, the presence of lateral gradients in viscosity are key to controlling changes in the strength of the flow that ultimately govern the magnitude and pattern of stress.

Within CitcomS, these equations of motion are solved non-dimensionally and the buoyancy is thus scaled by the Rayleigh number, Ra (Eq. 4.6), which controls the vigor of convection. In CitcomS, the equations are non-dimensionalized using the full planetary radius R instead of the convective layer thickness, so the Rayleigh number is defined using the Earth's radius. η_o is the reference viscosity, κ is the thermal diffusivity, and ΔT is the temperature drop from the surface to the CMB and is the constant used to non-dimensionalize the temperature field. B is the buoyancy ratio (Eq. 4.7), which gives the relative strength between compositional and thermal buoyancy.

$$Ra = \frac{\alpha \rho_0 g_0 \Delta T R^3}{\kappa \eta_0} \tag{4.6}$$

$$B = \frac{\Delta \rho}{\alpha \rho_0 \Delta T} \tag{4.7}$$

CitcomS solves equations 4.1 and 4.2 in a fully global spherical shell geometry with non-dimensional (i.e., scaled by planetary radius) inner and outer radii of $r_b = 0.55$ and $r_t = 1$, respectively. Free-slip boundary conditions and thermal boundary conditions of 0 and 1 (non-dimensional temperature) are applied at the top and bottom boundaries, respectively. Realistic Earth parameters are used for other dimensionalization constants and are given in Table 4.2. To solve the equations of motion, specification of an initial temperature field is required, which we constrain by seismic tomography (Section 4.4.2).

CitcomS has robust solvers that incorporate temperature, pressure, and composition dependent variable viscosity, allowing us to compute temperature dependent viscosity directly from our tomography–constrained thermal input (Zhong et al., 2000). In these models, temperature-dependent viscosity is given in non-dimensional form as:

$$\eta(T, r) = \eta_c \eta_r(r) \exp[E(T_o - T)] \tag{4.8}$$

where $\eta_r(r)$ is the depth-dependent viscosity prefactor, E is the non-dimensional activation energy that controls the strength of the temperature-dependence of the viscosity, T_o is the temperature at which the viscosity equals 1 in the model and is set to be that of the upper mantle, and η_c is an optional spatially dependent prefactor that allows for assigning regions of higher viscosity lithosphere or localized weak zones. The mantle is radially stratified in viscosity, with η_r defining an average lithospheric layer (0-100 km), the asthenosphere (100-300 km), the upper mantle (300-670 km), and the lower mantle (670-2870 km). The actual lithosphere, however, is prescribed using the η_c prefactor in order to accommodate laterally variable lithospheric thickness and only apply excess viscosity to those regions of rigid lithosphere that require it, which allows us to better capture regions of thin and thick lithosphere, such as near mid-ocean ridges or under cratonic roots, respectively.

Dimensional Constants and Model Parameters

Parameters	Symbol	Value
Earth's radius	R	6371 km
Mantle thickness	h	2870 km
Mantle density	ρ_0	3340 kg/m^3
Gravitational acceleration	g	9.81 m/s^2
Thermal expansivity	α	3 x 10^{-5} K^{-1}
Core-Mantle Boundary Temperature	T_{CMB}	4000 K
Upper Mantle Temperature	T_o	0.41
Reference temperature difference	ΔT	3727 K
Thermal diffusivity	κ	10^{-6} m^2/s
Specific heat	C_p	1250 J/(K mol)
Reference viscosity	η_0	10^{21} Pa s
Rayleigh number	Ra	9.4733 x 10^8
Activation energy	E	375; 250 KJ/mol

Table 4.2: Dimensional Constants and Model Parameters. Those values separated by a semi-colon indicate values for the upper mantle and lower mantle, respectively.

Global models allow us to fully capture the effect of Farallon slab–driven mantle flow beneath eastern North America and naturally incorporate far-field stresses associated with plate tectonics via use of the plate cooling model. This also accounts for the effect of subduction and changes in lithospheric thickness and composition associated with the ocean–continent boundary (Humphreys and Coblentz, 2007; Saxena et al., 2023). We can explicitly account for the forces exerted by ridges and slabs by using the thermal plate model of the oceanic lithosphere (Turcotte and Schubert, 2014), as well as a slab thermal structure constrained by the Slab2.0 model (Hayes et al., 2018) and constructed using the age of the plate at the trench and the convergence velocity such that temperatures consistent with the plate cooling model are propagated down the depth of the slab (Rudi et al., 2022; Hu et al., 2022). Plate margins are included as narrow low-viscosity zones, the locations of which are based on the plate margins from Seton et al. (2012). The geometry of the plate boundary weak zones along the subduction interfaces are also constrained by the slab dip and depth from Slab2.0 (Hayes et al., 2018), making them self-consistent with the slab model from Rudi et al. (2022). Using a global model also avoids numerical issues that can arise due to return flow on the artificial bounding walls of a regional domain.

CitcomS makes use of a full multi-grid solver to efficiently solve the discretized matrix equations. The spherical domain is divided into 12 caps, each of which are further divided into $N \times N \times N$ nearly equal area elements (in map view) over the surface of the sphere. The code has excellent strong scaling on parallel computers up to thousands of processors (Zhong et al., 2008). In order to resolve the narrow rift structures that serve as weak-zones, we need spatial resolutions on the order of at least 50 km. We use resolutions of $257 \times 257 \times 257$ elements per cap, which is a $\sim$ 25 km horizontal resolution. With radial grid refinement, we can achieve 1 km vertical resolution in the shallowest layers, which is essential for resolving crustal and lithospheric boundaries and for adequately incorporating the effect of gravitational potential energy differences from the crustal density field. Our calculations are performed on the NSF ACCESS HPC clusters Stampede2 at the Texas Advanced Computing Center (TACC) and Anvil at Purdue University using 16 nodes and 768 processors per run. Typical compute times per simulation are about 8-12 hours and are highly dependent on the viscosity structure, which can span up to six orders of magnitude.

4.4 Data and Methods for Model Input

In order to incorporate realistic mantle and lithospheric thermal structure and the negative buoyancy of the Farallon slab, we use geologically and seismically constrained thermal input in our models. This allows us to naturally incorporate plate driving forces due to the thermal buoyancy of the oceanic lithosphere, as well as the effect of variable lithospheric thickness. We parameterize the Farallon slab in terms of its buoyancy to determine the degree to which the flow induced by the sinking slab contributes to intraplate stress. We explicitly include low viscosity crustal and/or lithospheric weak-zones demarcated by the aulacogens and paleo-rifted structures of eastern North America. Using CitcomS, we compute the instantaneous flow field and associated stress tensor, the S_{Hmax} direction, deviatoric stress, and strain rate in the crust and lithosphere to determine how stress patterns change in the presence of different slab-buoyancies and different weak-zone viscosities. We compare our modeled stresses to those of the WSM (Figure 4.1b) and analyze the stress patterns within specific seismic zones, as well as models with and without the effect of GPE. We assess whether these conditions are likely to favor fault reactivation by calculating the Coulomb stress for known faults in the NMSZ, WQSZ, and LSLSZ/CXSZ.

4.4.1 Lithospheric Thermal Structure

The lithospheric thermal input is constructed from a composite of continental and oceanic models. For the continents, we use the Artemieva (2006) TC1 thermal model of the continental lithosphere, which is constrained primarily by heat flow data, as well as xenolith geotherms and electrical conductivity data, and for which the lithosphere-asthenosphere boundary (LAB) depth is defined as the 1300°C isotherm. For the oceanic lithosphere, we use the global seafloor age grid from Seton et al. (2020) to first calculate the oceanic plate thickness and then to calculate the oceanic lithospheric temperature as a function of depth according to the plate cooling model (Turcotte and Schubert, 2014). The plate cooling calculation is performed using 1300°C as the basal temperature of the plate for consistency with the Artemieva (2006) model. From this we obtain both a combined temperature model for the lithosphere and a combined LAB depth, above which we can apply a rigid lithosphere. Figure 4.2 illustrates the aforementioned data-sets used and the procedure for constructing the lithospheric thermal input.

4.4.2 Seismically Constrained Mantle Thermal Structure

Temperature anomalies create lateral changes in buoyancy that drive mantle flow. The thermal structure of mantle convection models is often constrained by seismic tomography, assuming the seismic anomalies are thermal in origin. It is common to simply scale the velocity to an effective temperature, a method that several studies have used to constrain the temperature and density structure of the mantle beneath eastern North America (Liu et al., 2008; Spasojevic et al., 2009). The more rigorous approach is to use the full anharmonic and anelastic components of the seismic wave-speed equations and the appropriate elastic moduli values constrained by mineral physics experimental data or theoretical values for a given composition (Karato, 1993; Goes et al., 2000; Cammarano et al., 2003; Goes, 2002; Cammarano and Guerri, 2017). The importance of anelasticity — the viscoelastic behaviour at seismic frequency — in the interpretation of seismic velocities was first demonstrated by Karato (1993). Properly accounting for anelasticity is essential because it significantly reduces the sensitivity of shear velocity to temperature, especially

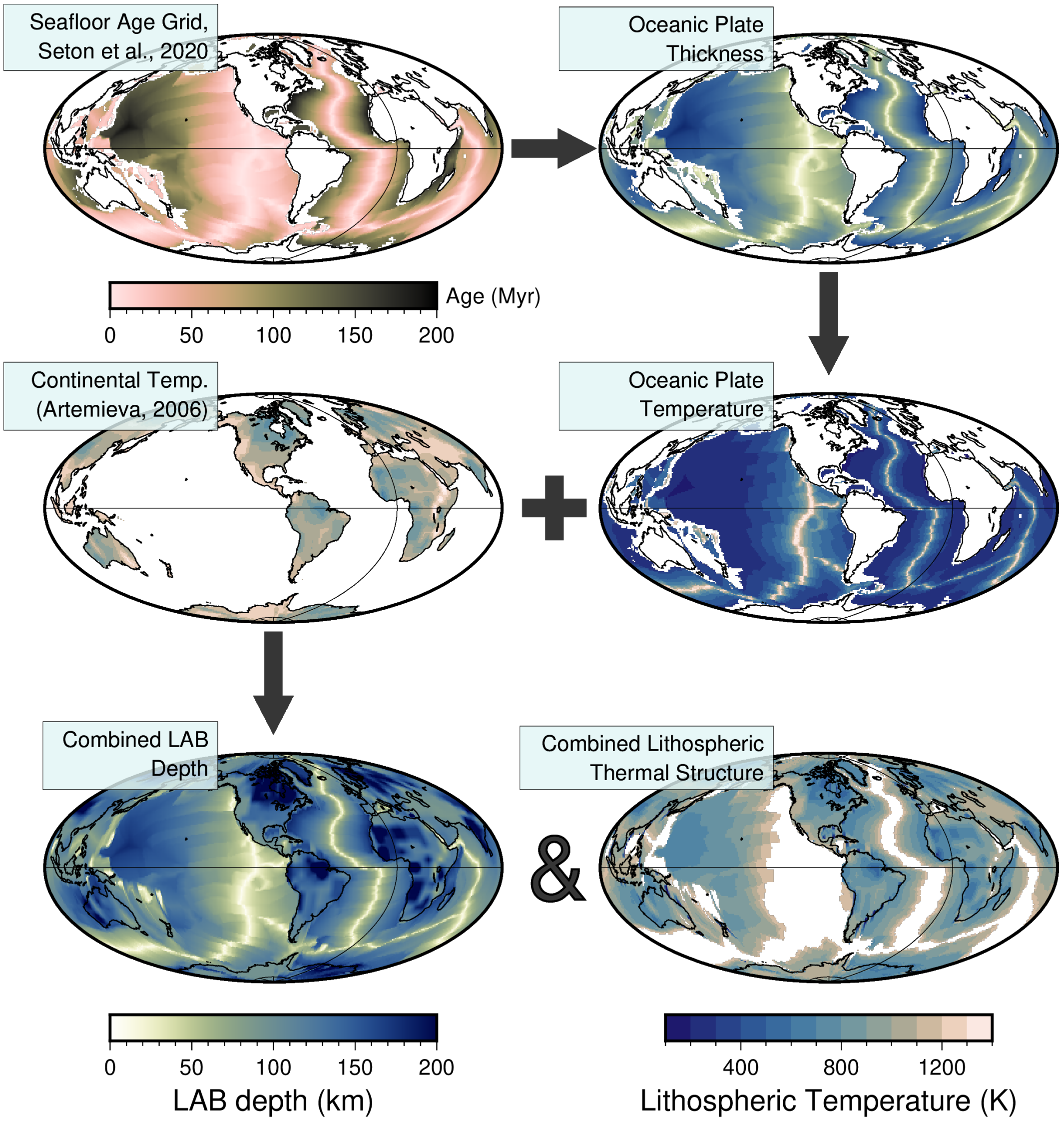

Figure 4.2: Data-sets used to construct the lithospheric thermal structure used in our geodynamic models. We use the seafloor age grid from Seton et al. (2020) (upper left panel) to compute the oceanic plate thickness (upper right panel) and temperature (middle right panel, 20 km depth) according to the plate cooling model. We combine the oceanic plate thermal model with the continental thermal model of Artemieva (2006) (middle left panel, 80 km depth). A slice of the combined temperature model at 80 km depth is shown in the bottom right panel, and the combined LAB depth, which corresponds to the 1300°C isotherm, is shown in the bottom left panel.

in very hot regions near the solidus. This means temperature anomalies associated with low velocity anomalies in the mantle are significantly smaller than they would be if considering anharmonic effects alone (Karato, 1993; Cammarano and Guerri, 2017). Anelasticity also makes the temperature derivative of velocity strongly temperature dependent and hence the conversion of velocity into temperature non-linear (Goes et al., 2000).

With the latter method, compositional effects can largely be neglected in the upper mantle, with uncertainties on estimated temperatures ranging from ±100 K in the upper mantle to ±250 K in the shallow lower mantle (Cammarano et al., 2003). In the upper mantle, many studies (Goes et al., 2000; Goes, 2002; Cammarano et al., 2003) invert the absolute seismic velocity for absolute temperatures. Despite being non-linear, with a single datum (seismic velocity) and a single model parameter (temperature), an inversion scheme can be rather fast and computationally inexpensive. However, due to the limited resolution of seismic tomography, the increase in compositional influence on seismic velocity with depth, and the uncertainty on the physical properties of deep mantle minerals (Cammarano et al., 2003), inversion tends to become unstable for the lower mantle and drastically over-predict temperatures in the deep earth. Because of this, we adopt the approach of scaling the velocities to temperature using a numerically derived depth dependent scaling factor that, like the inversion technique, incorporates the effect of anelasticity.

Seismic velocity including both anharmonic and anelastic terms is given by

$$V(P,T,Z,\omega) = V_{anh}(P,T,X)\left[1 - \frac{Q^{-1}(\omega,T)}{2\tan(\pi a/2)}\right], \tag{4.9}$$

where the anharmonic component, V_{anh}, is V_p or V_s (Eq. 4.10), and the anelastic component is the term in brackets. Q is the seismic quality factor - the inverse of the seismic attenuation. Q is thought to be weakly frequency dependent, where ω^a controls the frequency dependence of attenuation (Eq. 4.11) and a typically ranges from 0.1 to 0.3 (Karato, 1993; Cammarano et al., 2003; Cammarano and Guerri, 2017).

$$\begin{aligned} V_p &= \sqrt{\frac{K + 4\mu/3}{\rho}} \\ Vs &= \sqrt{\frac{\mu}{\rho}} \end{aligned} \tag{4.10}$$

Q is defined differently for p- and s-waves and is primarily dependent on the a parameter and the activation enthalpy, H:

$$Q_\mu = Q_S = A\omega^a \exp(aH/RT) \tag{4.11}$$

$$Q_P = (1 - L)Q_K^{-1} + LQ_\mu^{-1} \tag{4.12}$$

$$L = (4/3)(V_S/V_P)^2. \tag{4.13}$$

The scaling factor of velocity to temperature is typically given as the inverse of the derivative of the natural log of velocity with respect to temperature (Eq. 4.14),

$$\delta T = \left(\frac{\partial \ln V}{\partial T}\right)^{-1} \frac{\delta V}{V}, \tag{4.14}$$

where V is either V_p or V_s. The derivation of $\partial \ln V / \partial T$ is given in Appendix C.1, yielding:

$$\frac{\partial \ln(V)}{\partial T} = \frac{\partial \ln(V_o)}{\partial T} - \left[\frac{aH}{RT^2} \frac{Q^{-1}}{2\tan(\pi a/2)}\right]. \tag{4.15}$$

The first term is the derivative of the anharmonic seismic wave-speed with respect to temperature and is computed as in Eq. 4.16, given that bulk modulus, shear modulus, and density are each a function of temperature (see derivation in Appendix C.1).

$$\frac{\partial \ln(V_o)}{\partial T} = \frac{1}{2 < \rho > V_o^2}\left[\frac{\partial < M >}{\partial T} - V_o^2 \frac{\partial < \rho >}{\partial T}\right], \tag{4.16}$$

where $< M >$ and $< \rho >$ are the Voigt-Reuss-Hill averaged elastic moduli and density, where M is either $K + 4\mu/3$ for P-waves or μ for S-waves, and V_o is either V_S or V_P, as in Eq 4.9.

We use BurnMan (Myhill et al., 2021; Cottaar et al., 2014), a mineral physics toolbox, to calculate the elastic moduli and density at different temperatures and pressures. We use a pyrolitic composition based on that of Frost (2008) consisting of 56% forsterite, 13% pyrope garnet, 14% clinopyroxene, and 17% orthopyroxene in the upper mantle; 28% wadsleyite, 28% ringwoodite, 40% majorite, and 4% ca-perovskite in the transition zone; and 80% Mg-perovskite, 7% Ca-perovskite, and 13% magnesiowustite in the lower mantle. Pressure and density are computed on the basis of PREM (Dziewonski and Anderson, 1981). BurnMan constructs a composite of these minerals for each defined layer, the elastic properties of which are computed using a Voigt-Reuss-Hill averaging scheme and the mineralogical database of Stixrude and Lithgow-Bertelloni (2011), which assumes a Mie-Grueneiesen-Debye equation of state with third order finite strain expansion for the shear modulus. Temperature derivatives of the elastic moduli are numerically calculated at different depths using BurnMan's K, G, and ρ values over a range of temperatures at constant pressure (Figure C.1).

There are a number of different Q models that can be used in the anelastic term in Eq 4.15, either purely seismic Q models (Anderson and Hart, 1978; Dziewonski and Anderson, 1981) or Q calculated from mineral physics experimental data and calibrated to fit seismic observations (Sobolev et al., 1996; Goes et al., 2000; Cammarano et al., 2003). As Q is dependent on a number of factors, calculating Q per Eq. 4.11 requires knowledge of the activation enthalpy and frequency dependence of attenuation. We use the SL8 Q model of Anderson and Hart (1978), a precursor to PREM, as in Steinberger and Calderwood (2006) (Figure C.2b). From this Q model, we calculate the corresponding activation enthalpy profile (Figure C.2) to use in the expansion of the temperature derivative of velocity. We use $a = 0.17$ and $A = 0.056$ in the upper mantle and $a = 0.15$ and $A = 3.6$ in the lower mantle, which yields similar profiles to those used in models Q5 and Q7 in Cammarano et al. (2003) and Steinberger and Calderwood (2006). The SL8 Q-model of Anderson and Hart (1978) also produces temperature estimates from V_p and V_s that correlate well, as shown in the close to 1-to-1 trend in Figure C.3, suggesting a thermal origin to the anomalies and consistent with the finding that temperatures obtained from P and S waves separately agree well when anelasticity is included (Goes et al., 2000).

With Q, H, a, and the derivatives of the moduli computed in BurnMan, we calculate depth dependent scaling factors for converting seismic velocity to temperature (Eq. 4.14) (Figure 4.3b). The computed $\partial \ln(V)/\partial T$ values agree well with those of Steinberger and Calderwood (2006), and the magnitude of the scaling factors is on the order of those used by Spasojevic et al. (2009) and Liu et al. (2008), who find that a scaling of about $2\text{x}10^3\,^\circ$C/km/s produces flow models consistent with plate motions, stratigraphy, and the history of Farallon subduction beneath North America since the Late Cretaceous.

For the global mantle tomography, we use the TX2019 slab model from Lu et al. (2019). By including *a priori* 3D slab structure defined by seismicity, this model addresses shortcomings in using seismic tomography to infer density or thermal anomalies that arise from discrepancies between detailed studies of slabs and global tomography models (Lu et al., 2019). In this model, slab locations are defined a priori by seismicity on a 0.1° x 0.1° grid (Lu et al., 2019). The Farallon slab is identifiable as an elongate high S-wave velocity anomaly in both P and S between 600–2200 km in the mid-lower mantle (Lu et al., 2019; Ren et al., 2007) (Fig. 4.4). P-wave anomalies are determined relative to AK135, and S-wave anomalies are relative to TNA-SNA. We first convert all velocity anomalies to absolute velocity using their respective reference profiles, then recompute $\delta V_{p,s}$ with respect to PREM for consistency with the above derived scaling factors. The velocity anomaly at each

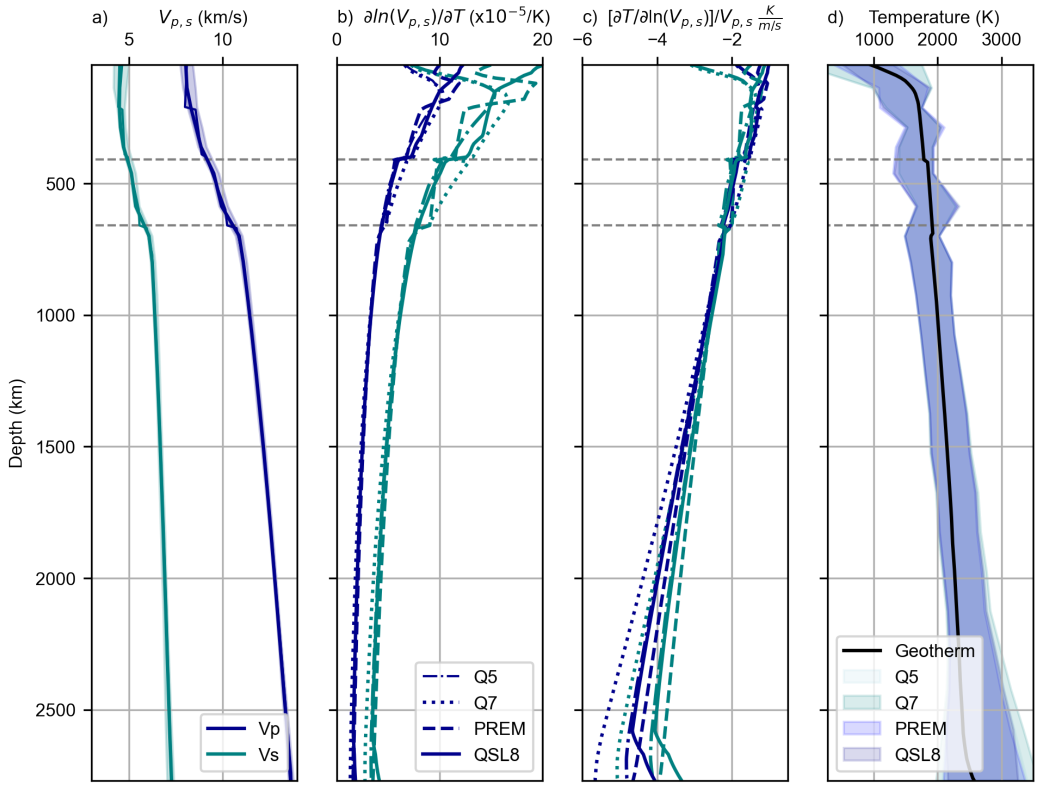

Figure 4.3: Seismic velocity to temperature scaling factors and estimated temperature profiles. a) Vp (dark blue) and Vs (teal) used to construct the scaling factors, predicted from BurnMan for the given composition and consistent with PREM. Shading covers the range of velocities in the TX2019 (Lu et al., 2019) model at a given depth. b) Derivative of the log of viscosity with respect to temperature for the Q models of PREM, QSL8 (Anderson and Hart, 1978), Q5 and Q7 (Cammarano et al., 2003), as discussed in the text. Color for Vp and Vs as in (a). c) The scale factor used to convert the velocity anomalies to temperature anomalies: inverse of the temperature derivative of the natural log of velocity, normalized by the mean radial velocity at that depth. Colors for Vp and Vs as in (a); line-styles as in (b). d) Resulting temperatures from the velocity to temperature conversion. Black line: geotherm (Steinberger and Calderwood, 2006). Colored shading: full range of temperatures predicted from the velocities of the TX2019 model at a given depth after temperature anomalies are added to the geotherm.

point in the model is multiplied by the scaling factor corresponding to its depth to yield a temperature anomaly for that point. Temperatures are determined from V_P and V_S separately and then averaged to get the final temperature anomaly. Absolute temperatures are determined by adding the calculated temperature anomalies to the mantle geotherm (Figure 4.3d). Below tomographic resolution, there is a trade-off between seismic anomaly resolution and grid spacing, which results in a non-unique estimate of absolute seismic velocity and an underestimation of effective temperature (Spasojevic et al., 2009). However, because geodynamic models are driven by thermal gradients and changes in buoyancy, exact knowledge of the absolute temperature is not critical to our set up and the differential temperature computed by scaling the seismic anomalies is sufficient to constrain the thermal buoyancy and flow in the mantle beneath North America.

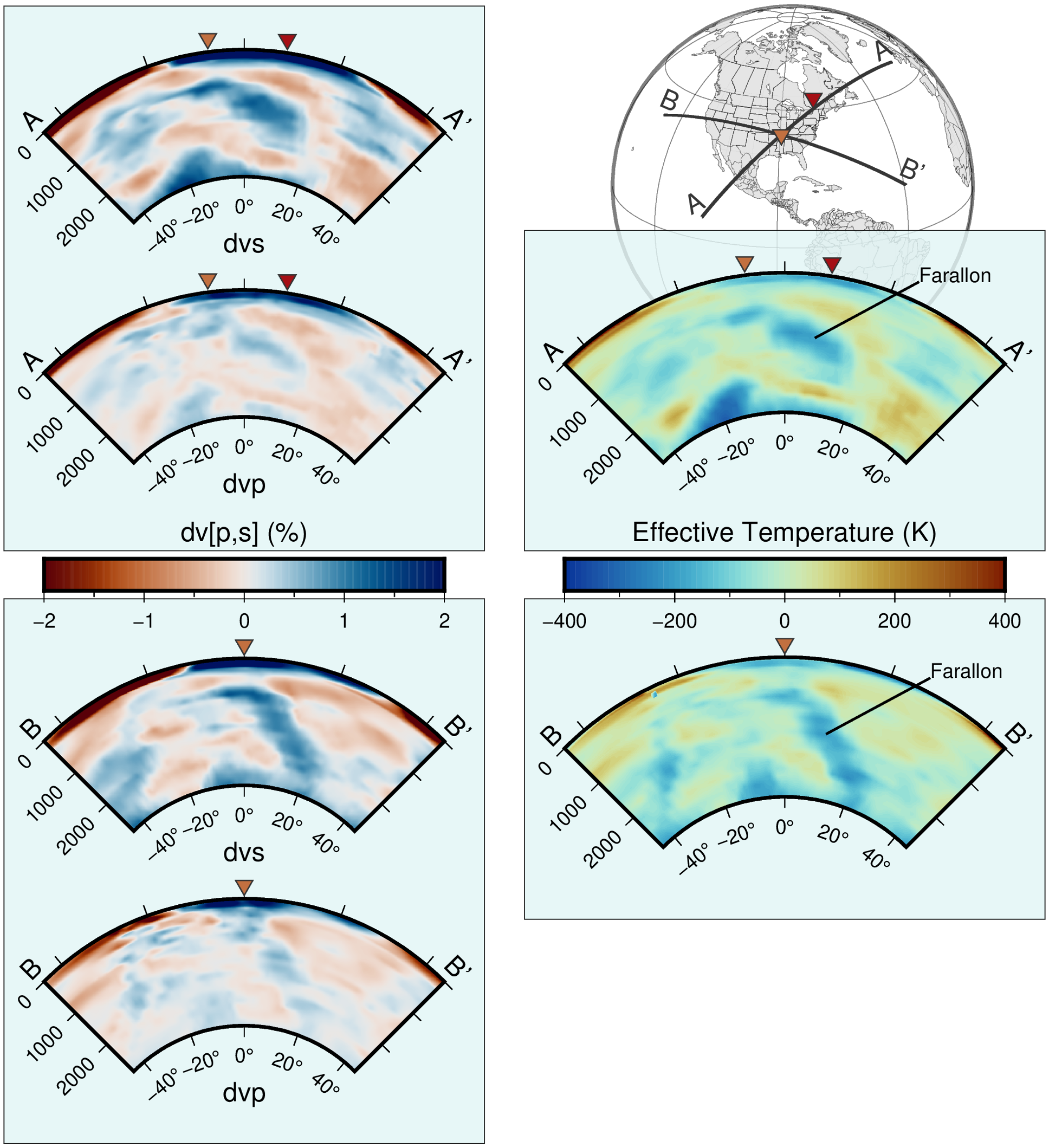

Figure 4.4: Vertical slices of 3D seismic velocity structure and corresponding mantle thermal structure. Left) Vertical slices of the TX2019 (Lu et al., 2019) velocity field for both dV_s and dV_p along two transects. Profile A-A′ trends SW-NE across eastern North America and passes through the New Madrid Seismic Zone (marked by the orange inverted triangle) and the Western Quebec and Charlevoix Seismic Zones (red inverted triangle). Profile B-B′ trends W-E across the US and passes through the New Madrid Seismic Zone. Right) Vertical slices along the same two transects of the effective temperature field (δT) calculated from the velocity anomalies. Locations of the seismic zones are marked as in the velocity plots; the Farallon slab stands out as an elongate cold thermal anomaly.

The central-eastern North American lithosphere is dominated by high velocities, whereas the eastern Appalachians are characterized by largely average to low velocities, including two strong localized low velocity anomalies in the northeast Appalachians at around 100 km depth (Schmandt and Lin, 2014; Boyce et al., 2019). The high velocities of the North American shield terminate abruptly against the Grenville Front to the east, beyond which low velocities dominate in the Grenville Province. Lithospheric thickness is not observed to vary greatly in this region, but there are some abrupt variations from north to south, which are consistent with previous seismic studies of the LAB in eastern North America (Hopper and Fischer, 2018; Artemieva, 2006). These sharp variations could be explained by metasomatic processes that modified the lithospheric mantle composition during subduction along the Laurentian margin (Boyce et al., 2019) and which could have played a role in weakening the crust and lithosphere. This is consistent with the fact that crustal earthquakes in the northern Grenville Province tend to concentrate away from Archean lithosphere and more towards the Appalachian Front and are pervasive throughout the younger altered lithosphere of the Grenville Province in the south (Boyce et al., 2019).

4.4.3 Combined Temperature and Viscosity Input for CitcomS

The lithospheric thermal model (Figure 4.2) is ultimately combined with the temperatures obtained from the tomography. The two models are combined by means of a depth-weighted average following a hyperbolic tangent function in order to ensure a smooth temperature field and eliminate any artefacts that may result from local mismatches in the temperature estimates. The lithosphere is weighted 100% down to 50 km, which is the starting depth of the tomography model. The weight on the lithosphere model then varies smoothly from about 80% at 50 km depth to near 0% at 240 km depth. Below this, the model is based on the tomography. In order to adequately reproduce plate motions, we also superimpose cold slabs over the background tomographic temperature model using the slab geometries from Slab2.0 (Hayes et al., 2018) and slab temperatures from the slab thermal models used in Rudi et al. (2022) and Hu et al. (2022). Temperatures are non-dimensionalized for input to CitcomS assuming a core-mantle boundary (CMB) temperature of 4000 K.

Viscosities are computed directly from the temperature field within CitcomS following Eq. 4.8 and then multiplied by an appropriate pre-factor depending on their radius or their location within the lithosphere, as in the case of applying a high viscosity lithosphere, intraplate weak zones, or weak plate boundaries. The radial profiles of temperature and viscosity are shown in Figure 4.5 along with the full range of temperature and viscosity in each layer and the 2σ spread of the values in that layer. The viscosity profile used in Citcom, with its respective layer-dependent pre-factors, is shown along with other viscosity profiles from the literature commonly used in or derived from GIA analysis for comparison (Figure 4.5b).

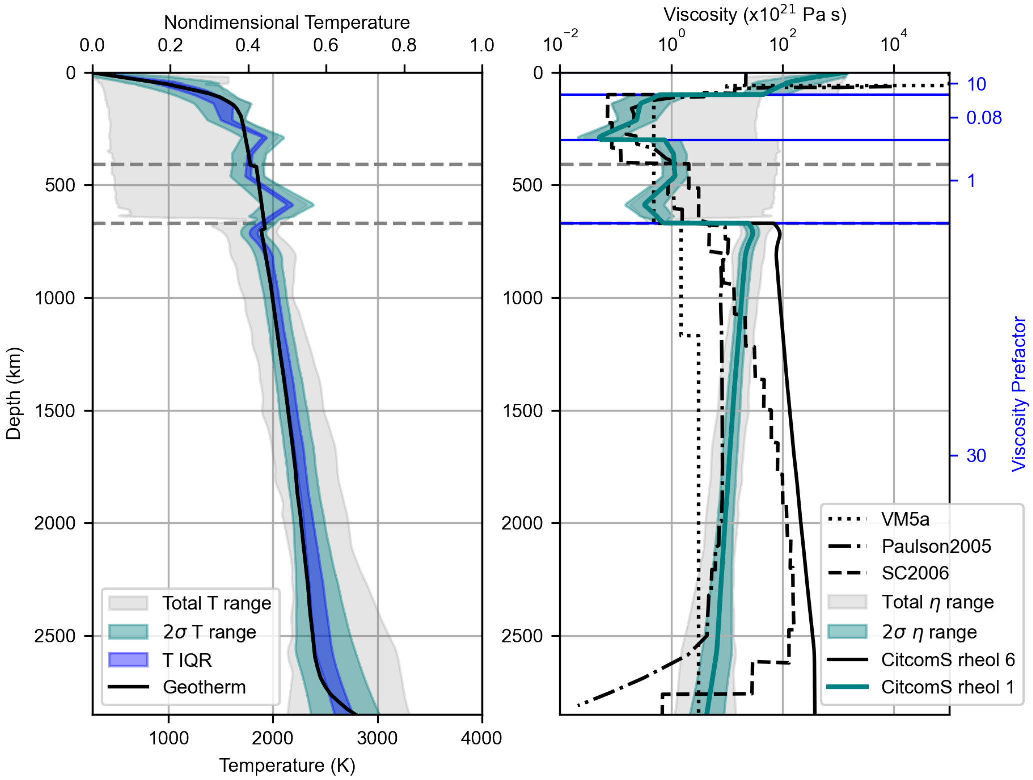

Figure 4.5: Radial temperature and viscosity profiles for models in CitcomS. a) Radial temperature profile for the thermal model used in CitcomS; includes both the seismically derived mantle temperatures and lithospheric temperature from the plate cooling model and Artemieva (2006). Light grey shaded region covers the full range of temperature found at a particular depth. The deep extent of very cold temperatures is due to the presence of cold slabs that penetrate deep into the mantle. The teal green band marks the 2σ spread of the temperatures at a given depth, containing 98% of the values, and the dark blue band marks the inter-quartile range. The black line is the geotherm as used in the velocity to temperature conversion, from Steinberger and Calderwood (2006). b) Radial viscosity profiles for different models. Dark teal line marks the average radial viscosity structure used in CitcomS, as computed from the temperature model on the left. The teal green shading is likewise the 2σ range of viscosity, and the gray shading covers the full range of viscosity values found at a given depth. Solid black line is the radial viscosity structure for an alternative CitcomS rheology. Dotted black line is the VM5a viscosity profile of Peltier et al. (2015); dashed-dotted black line is the seismically derived viscosity profile used in CitcomSVE in the GIA work of Paulson et al. (2005); and the dashed black line is the viscosity profile from Steinberger and Calderwood (2006) that best reproduces observed plate velocities. The right-hand y-axis shows the depth-dependent pre-factors applied to the temperature-dependent viscosity for the 4-layers distinguished by the dark blue lines.

4.4.4 Weak Zones

We emplace weak zones in the crust and/or lithosphere at the locations of the geologically mapped aulacogens or seismically inferred low velocity zones of weakness. This is done by specifying a viscosity pre-factor applied at nodal points that fall within the bounds of the aulacogens. Weak zones are placed at an appropriate depth for each seismic zone, based on local seismic and geologic evidence, the details of which are given in Section 4.2. To summarize, beneath the NMSZ, we emplace a weak zone in the upper mantle between 70 and 150 km along the extent of the Reelfoot Rift as mapped in Figure 4.1a. In the ETSZ, we emplace a 50-100 km wide weak zone along the NY-AL lineament between 15 and 50 km depth. A bit farther north, along the Rome Trough, we emplace an approximately 500 km wide weak zone between 80-200 km depth. Along the entirety of the LSLRS and its associated rift-arms, we emplace a weak zone at the base of the crust between 25 and 75 km depth. While the viscosities of these weak zones likely differ based on their different conditions of formation, we uniformly reduce the viscosity by a factor of 1e4 in all weak zones for simplicity. We also test a case where all weak zones are considered to be shallow and sub-crustal, placed between 25-75 km depth.

4.4.5 Parameterization of Farallon Slab Buoyancy

The Farallon slab is a significant low temperature anomaly in the mantle beneath eastern North America; it lies mostly between 750 and 2200 km depth and is believed to be up to 400 km thick in places (Sun et al., 2017). This structure and its negative buoyancy have the potential to induce strong flow in the mantle beneath eastern North America and exert a significant influence on the intraplate stress field. However, buoyancy from the thermal anomaly alone may be overestimated, as compositional buoyancy within the ancient slab may counteract the thermally derived density. There is reason to suspect the Farallon slab contains some degree of chemical buoyancy. Its long history of flat-slab subduction under western and central North America during the Laramide Orogeny and time frame of the Cretaceous interior Seaway and the passage of the conjugates to the Hess and Shatksy Rises (Sun et al., 2017) — buoyant oceanic plateaus inferred to have been attached to the Farallon plate — indicate the presence of compositional buoyancy. This means the buoyancy of the Farallon slab and its associated effect on the North American lithosphere must be parameterized and explored to better understand the effect this structure and the flow it generates have on intraplate stress and seismicity.

We explore this effect by changing the buoyancy of the slab. The two extremes of the range of scenarios are 1) the case derived entirely from the tomography in which the slab retains its full negative thermal buoyancy (0% of the buoyancy ratio), and 2) the case where the slab anomaly is entirely neutralized by applying a buoyancy ratio that completely counteracts the thermal buoyancy (100 % of the buoyancy ratio). Figure 4.6 shows a representative longitudinal profile through the effective temperature field (temperature minus the radial mean) at 35° N and the corresponding profile of buoyancy ratio derived from these effective temperatures. We identify the slab anomaly as that portion of the slab where the temperature anomaly exceeds the 1σ variation of the temperatures at that depth and apply the neutralizing buoyancy ratio only within that portion (i.e., within the filled portion of the temperature profiles in Figure 4.6a). The second half of this figure likewise shows the buoyancy ratios as applied only to that region for different percentages of the full buoyancy ratio required to neutralize the whole slab anomaly.

Using the same method of calculating the buoyancy ratio from the temperature field, we also apply a neutralizing buoyancy to both the continental lithosphere and the large-low-shear-velocity-provinces (LLSVPs) in the lower mantle. The continental lithosphere, particularly very thick, old cratons and continental keels, are cold and hence thermally dense; however, cratonic stability over geologic time necessitates a chemically buoyant tectosphere depleted in basaltic components that balances the mass increase due to cold temperatures (Jordan, 1988; Shapiro et al., 1999; Forte and Perry, 2000). Indeed, in models without positive buoyancy applied to the continental lithosphere, the keels start to sink, dramatically altering the global flow field. In a similar fashion, the LLSVPs, while hot and hence thermally buoyancy, are believed to be chemically dense and thus neutrally buoyant stable piles at the bottom of the mantle (Ishii and Tromp, 1999; Ballmer et al., 2016; Lau et al., 2017; Vilella et al., 2021). Representative depth slices of the temperature and chemical buoyancy ratio, as applied to the lithosphere, LLSVPs, and Farallon slab, are depicted in Figure 4.7. In all models, we apply the full buoyancy ratio required to neutralize the sinking and rising of the lithosphere and LLSVPs, respectively.

4.4.6 Gravitational Potential Energy from Density and Topography

Gravitational potential energy (GPE) differences arising from lateral variations in density and topography can give rise to variations in deviatoric stress that may help load faults within continental interiors and lead to intraplate seismicity (Ghosh et al., 2009; Ghosh et al., 2013). In order to account for the effect of GPE in our

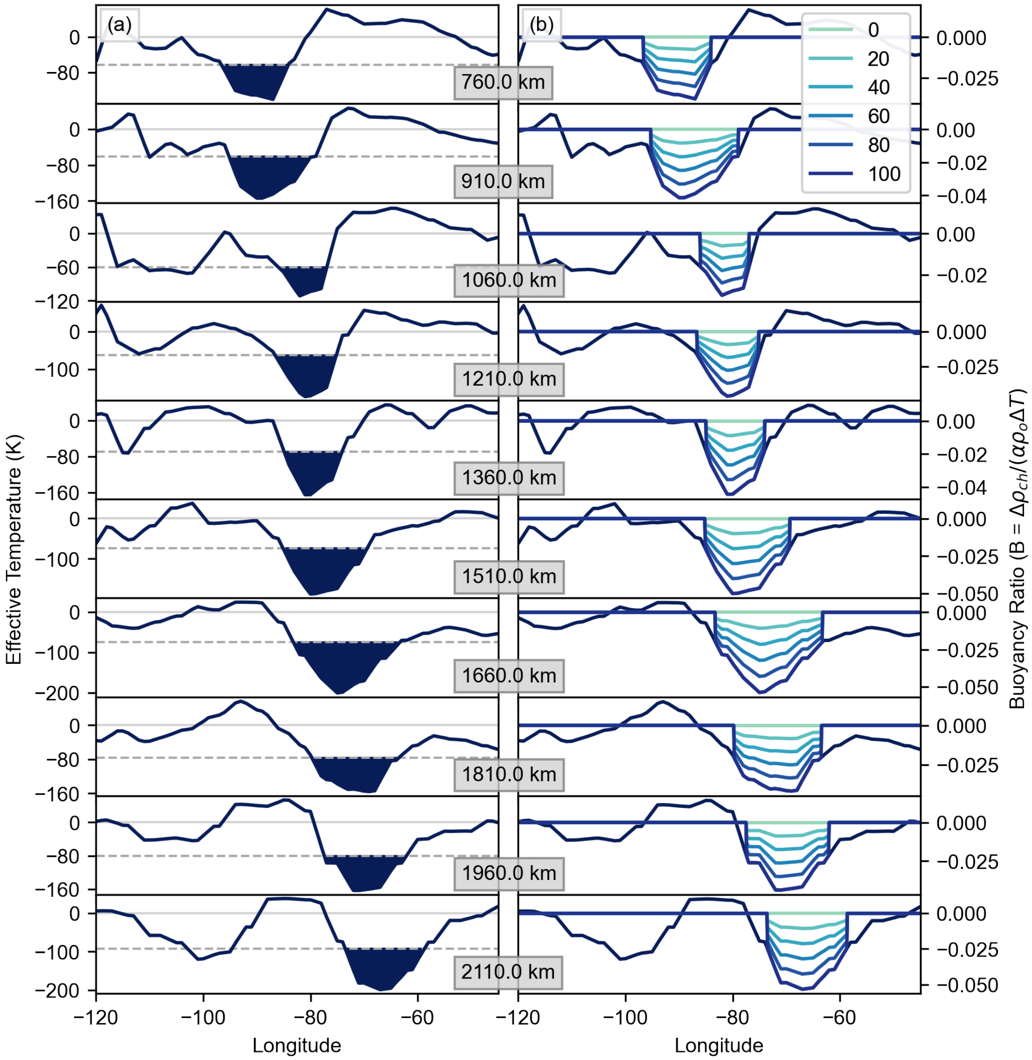

Figure 4.6: Effective temperature and buoyancy ratio profiles across eastern North America. a) (Left) Longitudinal effective temperature profiles in Kelvin at 35° latitude across the United States showing the temperature anomaly associated with the Farallon slab at different depths. Filled dark blue regions indicate the portion of the slab to which we apply the buoyancy ratio and where the negative temperature anomaly exceeds the 1σ variation of temperature at that depth. Dashed gray line marks the 1σ level. Solid gray line marks the zero level (mean effective temperature). b) (Right) Buoyancy ratios computed from the effective temperature field for the same profiles in (a). The darkest line that mirrors the effective temperature profile is the buoyancy ratio that would be needed to completely neutralize the effective temperature shown to the left, for reference. The truncated curves show the buoyancy ratio only where we apply it to the designated slab region as shown by the filled area to the left. Different line colors show the resulting curves for different percentages of the full buoyancy ratio: 0 (no buoyancy ratio applied), 20, 40, 60, 80, and 100 (fully neutralized Farallon slab).

dynamic models, we need to incorporate variable crustal density and topography into CitcomS. The topography requires special consideration. CitcomS uses a flat surface and does not allow the user to input variable topography on a free surface.

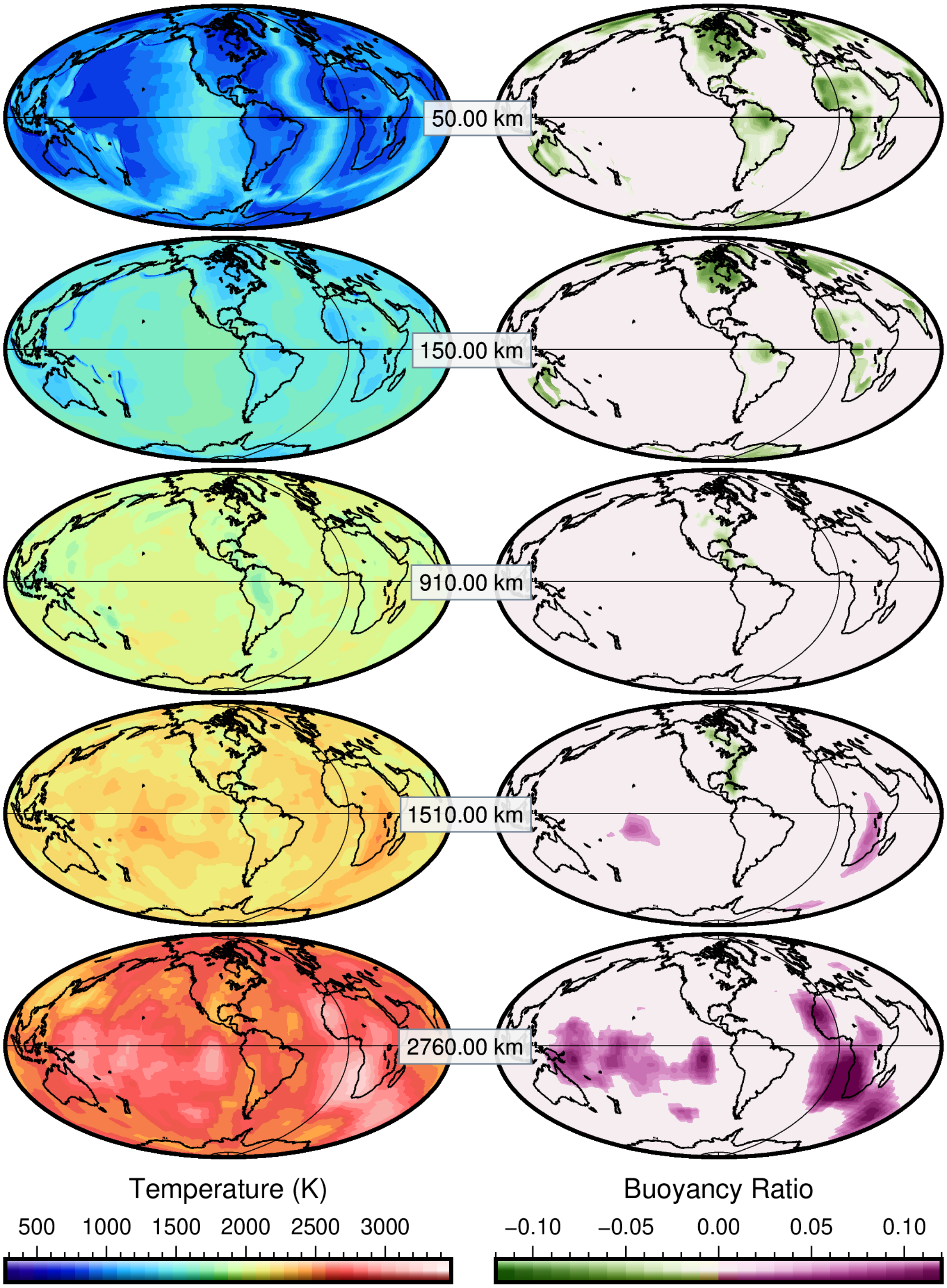

Figure 4.7: Depth slices of the thermal and compositional buoyancy ratio fields input to CitcomS. Left) Representative slices of the temperature field used in CitcomS at 50, 150, 910, 1510, and 2760 km depth. Right) The corresponding buoyancy ratio computed from the temperature anomalies for representative slices of the lithosphere (50 and 150 km depth), the Farallon slab (910 and 1510 km depth), and the LLSVPs (1510 and 2760 km).

We account for the topographic contribution to the stress field by constructing an effective density model that conserves GPE. In doing so, we essentially flatten the topography into a 1 km thick layer at the surface by computing the topography's equivalent density and adding it to that layer; that is, we add a density excess to the top layer such that the GPE computed from the original model with topography is equivalent to the GPE computed from the model with no topography. This effective density can be converted to a buoyancy ratio that can be input into CitcomS.

The GPE is the vertically integrated vertical stress, and takes the form:

$$GPE = \overline{\sigma}_{zz} = \int_{-h}^{L} \rho(z) g (L - z) dz. \tag{4.17}$$

L is a constant reference level and $-h$ is the topographic height, which may vary for each point on the globe. $\rho(z)$ is the density at a given depth z, and g is the gravitational acceleration.

We calculate GPE using the crustal density model CRUST1.0 (Laske et al., 2013), which includes topography and sediments. The CRUST1.0 data-set consists of densities and layer-top depths for different crustal and sedimentary layers, as well as the Moho, which we discretize onto a 3D mesh at 1 km resolution in the vertical direction. We numerically compute GPE from the grid by calculating σ_{zz} for each layer and iteratively summing down to the reference level at $L = 100$ km (Eq. 4.18). Numerically, GPE can be written as:

$$\overline{\sigma}_{zz} = \sum_{i=1}^{n} (L - z_i) \rho_i g \Delta h_i, \tag{4.18}$$

where z_i is taken to be the depth of the midpoint of the layer; ρ_i is the density of that layer as determined from CRUST1.0; Δh_i is the thickness of that layer, which is a constant 1 km for all layers; L is the reference level of 100 km depth; and n is the number of layers ($n = 100$). Below the Moho and down to the reference level, we use a constant mantle density of 3300 kg/m^3. The resulting total GPE is similar to that calculated in Ghosh et al. (2009) and Ghosh et al. (2013).

To create a model with "flattened topography" and crustal density that can be used within CitcomS, we first compute a density grid that accounts for the mass of the topography. From the known topographic contribution to the GPE (GPE_T), we compute the excess density that needs to be added to the top layer of the flattened model (Eq. 4.19), such that the resulting GPE is equivalent to that from a model that includes topography (see derivation in Appendix C.2).

$$\rho_T = \frac{GPE_T}{(L - 0.5 * \Delta h) g \Delta h} \tag{4.19}$$

We can compute GPE_T directly from our density grid, and Δh is the depth to the base of the first layer of elements in our 3D grid (1 km).

4.5 Calculation of S_{Hmax} and Coulomb Stress

CitcomS outputs the viscosity, temperature, and velocity fields, as well as the full stress and strain-rate tensors for each nodal point in the global domain. From the stress tensor, we compute the second invariant of the deviatoric stress (Eq. C.50). With this, we investigate how the stress magnitude changes at the continental scale and within different seismic zones between models with and without influence from the Farallon slab and between models with and without low viscosity weak zones.

From the stress tensor, we also compute the principal stresses, their directions, and the direction of maximum horizontal compressive stress (S_{Hmax}) following Lund and Townend (2007) (Appendix C.3). Since principal stress magnitudes cannot be determined from most stress measurements in typical settings, most stress data consists of only a four-parameter subset of the stress tensor components, which includes the principal directions and relative stress magnitude, a quantity typically defined as $R = (\sigma_1 - \sigma_2)/(\sigma_1 - \sigma_3)$ (Lund and Townend, 2007). Thus, calculation of the S_{Hmax} directions from the modeled stress tensors is necessary for properly comparing our results to stress data. Accurate calculation of S_{Hmax}, as opposed to using the pure principal stress directions, is also important because when none of the three principal stress directions are truly vertical, S_{Hmax} does not simply coincide with the largest subhorizontal stress, though it may be an adequate proxy. However, in our predicted stresses, S_{Hmax}, S_{Hmin}, and S_V almost always coincide with the principal stresses at crustal depths. We compare estimates of the S_{Hmax} direction with those of the World Stress Map (Heidbach et al., 2018) and other focal mechanism stress inversions (Mazzotti and Townend, 2010; Hurd and Zoback, 2012).

Before calculating S_{Hmax} or resolving the stress onto faults, we also add back the lithostatic pressure. In CitcomS, the deviatoric stress tensor is computed from the deviatoric strain rate, to which the *dynamic* pressure is then added. The dynamic pressure, however, is the pressure arising from the flow itself, not the overburden pressure of the overlying rock. Inclusion of the lithostatic pressure is not necessary for the determination of S_{Hmax} and does not affect the orientation of the principal stresses. However, it does affect the magnitude of the principal stresses and the magnitude of the normal stress resolved on any given fault plane. Accurately computing such normal stress is essential for computing the Coulomb failure stress on a fault; without the lithostatic component, Coulomb stresses are greatly overestimated. We compute the lithostatic pressure assuming a mean continental crustal density of 2700 kg/m^3. For consistency with the theory of the critically stressed crust (Townend and Zoback, 2000; Zoback and Townend, 2001; Zoback et al., 2002), the lithostatic pressure is counteracted by the pore-fluid pressure exerted by water and other fluids in the crust such that optimally oriented faults are always on the verge of slipping. Without this reduction in normal stress, lithostatic pressure is such that at seismogenic depths all faults are always completely within the stable regime with respect to the Coulomb failure criterion. To account for the effect of pore fluid, we use a pore fluid factor of 0.6 (see Appendix C.3), which is consistent with intermediate values previously used for conditions of fault slip in intraplate regions like Canada (Zoback, 1992; Rimando and Peace, 2021).

To better clarify the degree to which Farallon slab–induced mantle flow and/or intraplate weak zones impact the potential for fault reactivation in intraplate settings, we must determine whether such stresses are sufficient in both magnitude and orientation to bring intraplate faults closer to failure. The most commonly used criterion for determining whether there will be slip on a fault is the Coulomb Failure Criterion (CFC) (King et al., 1994), defined by the shear and normal stress on the failure plane, the pore pressure, the coefficient of friction, and the cohesion of the rock (Eq. 4.20). The criterion states that when the shear stress on a fault exceeds a certain threshold, failure may occur, possibly initiating an earthquake (King et al., 1994). The Coulomb failure stress (CFS) is the difference between the shear stress on a given fault and the failure threshold (Eq. 4.21), where positive Coulomb failure stresses indicate unstable faults (i.e., likely to slip) and negative Coulomb failure stresses indicate stable faults (i.e., unlikely to slip). As is common practice for preexisting faults, we take the cohesion C to be zero, as it is usually only considered when dealing with newly forming faults where the rock actually needs to break.

$$\mathrm{CFC} \equiv \tau_F = \mu\sigma_n + C \tag{4.20}$$

$$\sigma_{CFS} = \tau - (\mu\sigma_n + C) \tag{4.21}$$

Because CFS is calculated from the shear and normal stress resolved on an actual fault plane, it is highly dependent on the orientation of that fault (e.g., its strike and dip) with respect to the orientation of the stress tensor. Thus, to assess how faults in intraplate settings might respond to the stress states produced by the models, it is essential to analyze the Coulomb failure stress on realistic faults within the different seismic zones. Using fault orientation data and our computed stress tensors, we compute the CFS on faults (Appendix C.3) in the NMSZ, WQSZ, and CXSZ/LSLSZ.

4.6 Results

Two main suites of models were computed to explore the influence of low viscosity weak zones on the intraplate stress field of eastern North America: one with the full expression of the Farallon slab in the thermal field as resolved from seismic tomography and the other with the Farallon slab neutralized by means of the buoyancy ratio. The parameters of these models are summarized in Table 4.3. Within each of these sets, we test a case without weak zones; two cases with weak zones, one with the weak zones at different depths depending on geophysical constraints for their respective locations and one with all weak zones placed at the same depth between 25-75 km; and a case without weak zones but in which we have incorporated the effect of GPE due to crustal density and topography variations. In all cases with weak zones, weak zone viscosity is reduced by a factor of 1e4. Globally, to first order, the velocity field predicted by CitcomS for each of our models is consistent with global plate motions and strain rates match observed values from the Global Strain Rate Map (Kreemer et al., 2014) to within 8-10% error on average. In models with the Farallon slab, strain rate within continental eastern North America are on the order of 1×10^{-9} to 1×10^{-8} yr^{-1}, and the percent error of the log of the second invariant of deviatoric strain rate between the modeled values and those of Kreemer et al. (2018) is generally less than 10% but can be as high as 20% in the central-eastern U.S. (Figure C.4 a,c,e). In models without the Farallon slab, strain rate is slightly lower, with isolate patches in the central-eastern U.S. reaching 15% error, but the majority of error remains broadly less than 10% (Figure C.4 b,d,f). The S_{Hmax} directions derived from the CitcomS stress tensors reproduce first order stress provinces globally, including the general NE S_{Hmax} orientation across eastern North America and the radial pattern of stress orientations in China.

Model Cases

Model No.	Farallon BR %	GPE	WZ η Prefactor	WZ depth
A0	0	N	1	–
A1	0	N	0.0001	variable
A1b	0	N	0.0001	25-75 km
A0G	0	Y	1	–
B0	100	N	1	–
B1	100	N	0.0001	variable
B1b	100	N	0.0001	25-75 km
B0G	100	Y	1	–

Table 4.3: Parameters tested in the different model cases. Models prepended with an A have the full Farallon slab as resolved from seismic tomography. Models prepended with a B have the Farallon slab entirely neutralized by the buoyancy ratio (i.e., Farallon BR 100%). GPE indicates whether the effect of GPE as derived from the Crust1.0 model was included. WZ η prefactor is the viscosity reduction applied to the intraplate weak zones. WZ depth is either variable in accord with the geophysically inferred depths of different structures as discussed in the text or is constant between 25 and 75 km depth.

We begin by comparing the modeled S_{Hmax} orientations to those of the WSM for different cases (Figure 4.8). Panel (a) in Figure 4.8 shows the orientation of the modeled S_{Hmax} for model A0 with the Farallon slab and no weak zones, colored by the absolute misfit to the observed S_{Hmax}, where the maximum misfit is 90°. Across all models, the majority of misfits throughout eastern North America are less than 25° but vary spatially. Misfits are lowest in the central-eastern and north-eastern U.S. in the vicinity of eastern Tennessee and the Rome Trough and up through the Northern Appalachians. Strong fits are also observed in New Madrid and the Canadian seismic zones. The largest misfits are generally isolated to individual points and are not unexpected given the uniformity of the modeled stress field compared to the shorter wavelength spatial variability in the observed S_{Hmax} directions, even across small areas.

The presence or lack of either weak zones or the Farallon slab introduces perturbations to the modeled S_{Hmax} direction and its misfit to the observed data (Figure 4.8 b-d). Including intraplate weak zones only, without the Farallon slab, decreases the misfit by less than one degree on average within the major seismic zones, except in New Madrid where it decreases by about 3° (Figure C.5). On the other hand, the inclusion of the Farallon slab alone, without weak zones, changes the S_{Hmax} misfit by up to ±20° (Figure 4.8 c,d). Specifically, the fit improves by $\sim 11^\circ$ in the NMSZ,

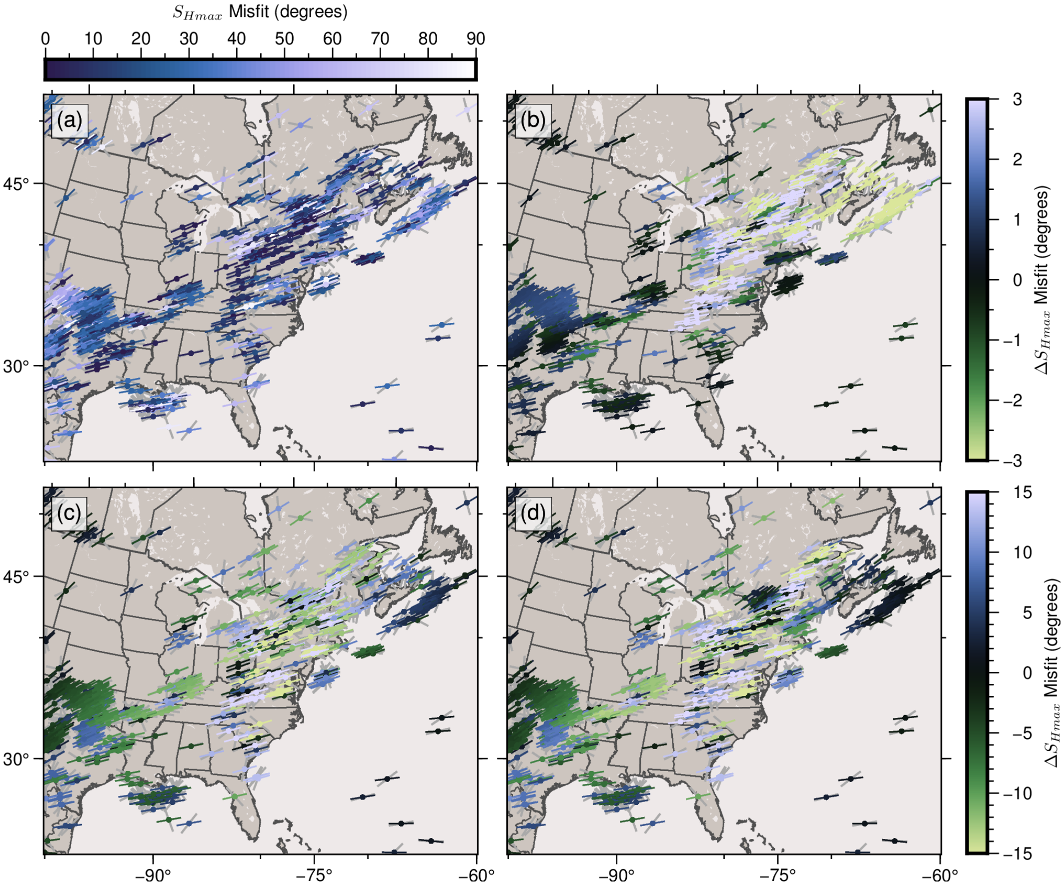

Figure 4.8: Changes in misfit between observed and modeled S_{Hmax} orientations at 10 km depth. a) S_{Hmax} orientations of model A0 colored by misfit (|modeled − observed|) to the observed stress orientations from the WSM of Heidbach et al. (2018) (light gray lines). b) Difference in the S_{Hmax} misfit between model A1 and model A0 (i.e., models with the Farallon slab, but with vs. without weak zones). c) Difference in S_{Hmax} misfit between model A0 and B0 (i.e., models without weak zones, but with vs. without the Farallon slab). d) Difference in S_{Hmax} misfit between model A1 and model B1 (i.e., between the case with both Farallon and weak zones and the case with weak zones but no Farallon.

~ 17° in CVSZ, ~ 13° in the WQSZ, ~ 5° in the CXSZ, and ~ 13° in the LSLSZ. However, fit worsens by about 8° in the ETSZ and South Carolina and by as much as 15° along the Rome Trough (Figure C.5). Inclusion of both weak zones and the Farallon slab results in further misfit reductions in the NMSZ, CVSZ, LSLSZ, and both on and offshore Nova Scotia, but only by up to 8°. It is important to note that while the Farallon slab has a notable impact on S_{Hmax} orientation, the very small change induced by the inclusion of weak zones, generally less than ±5°, is largely insignificant with respect to the local 90% confidence intervals of the WSM data, which for a single seismic zone can often span as much as 25°, with the smallest interval being 8° (Figure C.5).

Overall, the presence of the Farallon slab more accurately reproduces the observed stress field both regionally and in each of the seismic zones, barring the ETSZ. This is not surprising since the Farallon slab is known to exist at depth in the mantle and will therefore have some effect on the stress field. What is more interesting is the direction of rotation induced by the slab effect and the additional small changes induced by weak zones in the presence of the slab's influence. Under only tectonic background forcing, S_{Hmax} directions follow the regional NE-SW trend, but inclusion of the Farallon slab causes a continent wide clockwise rotation of the S_{Hmax} direction of about 10-15° (Figure 4.9 c). This rotation becomes even greater in the presence of weak zones, ranging from an extra couple of degrees in New Madrid to more than 5° along the Appalachian front, from the ETSZ all the way up through the LSLR (Figure 4.9 b,d). However, weak zones induce counterclockwise rotations in the western part of the WQSZ and in northern New England, as well as on and offshore Nova Scotia (Figure 4.9 b). In models with the full Farallon slab, weak zones induce the largest clockwise stress rotations in the Central Virginia, Charlevoix, and Lower Saint Lawrence Seismic Zones (Figure 4.10).

While changes in the S_{Hmax} direction between the different cases are subtle, changes in stress magnitude are substantial. At long-wavelength, the Farallon slab induces a high amplitude stress anomaly across the central-eastern U.S., the peak of which coincides with the vicinity of the NMSZ and the nearby ETSZ. This peak in stress is all but eliminated in the case without the influence of the Farallon slab (dark blue lines in Figure 4.11 a,b). In both cases with and without the Farallon slab, a small peak in stress at around 1300 km from the center of profile B-B' in Figure 4.11a likely reflects the effect of the density and viscosity change at the continent-ocean transition. Without the Farallon slab, mantle flow beneath eastern North America and hence the traction imparted to the base of the lithosphere is greatly reduced (Figure 4.11 e,f), resulting in stress magnitudes on the order of 50 to 100 MPa (dark blue lines in Figure 4.11 a,b) and stress perturbations from the inclusion of weak zones on the order of 5-20 MPa (Figure 4.12). However, when the full expression of the Farallon slab is included (light blue lines in Figure 4.11 a,b and panels c,d), stress magnitudes jump considerably to 200-250 MPa. Most notably, stress perturbations within the WQSZ, LSLSZ, CXSZ, and ETSZ seismic zones due to the inclusion of shallow weak zones in the presence of mantle flow (Figure 4.12) are as much as 70-100 MPa – nearly 50 MPa more than the case of including weak zones alone (Figure 4.12 b).

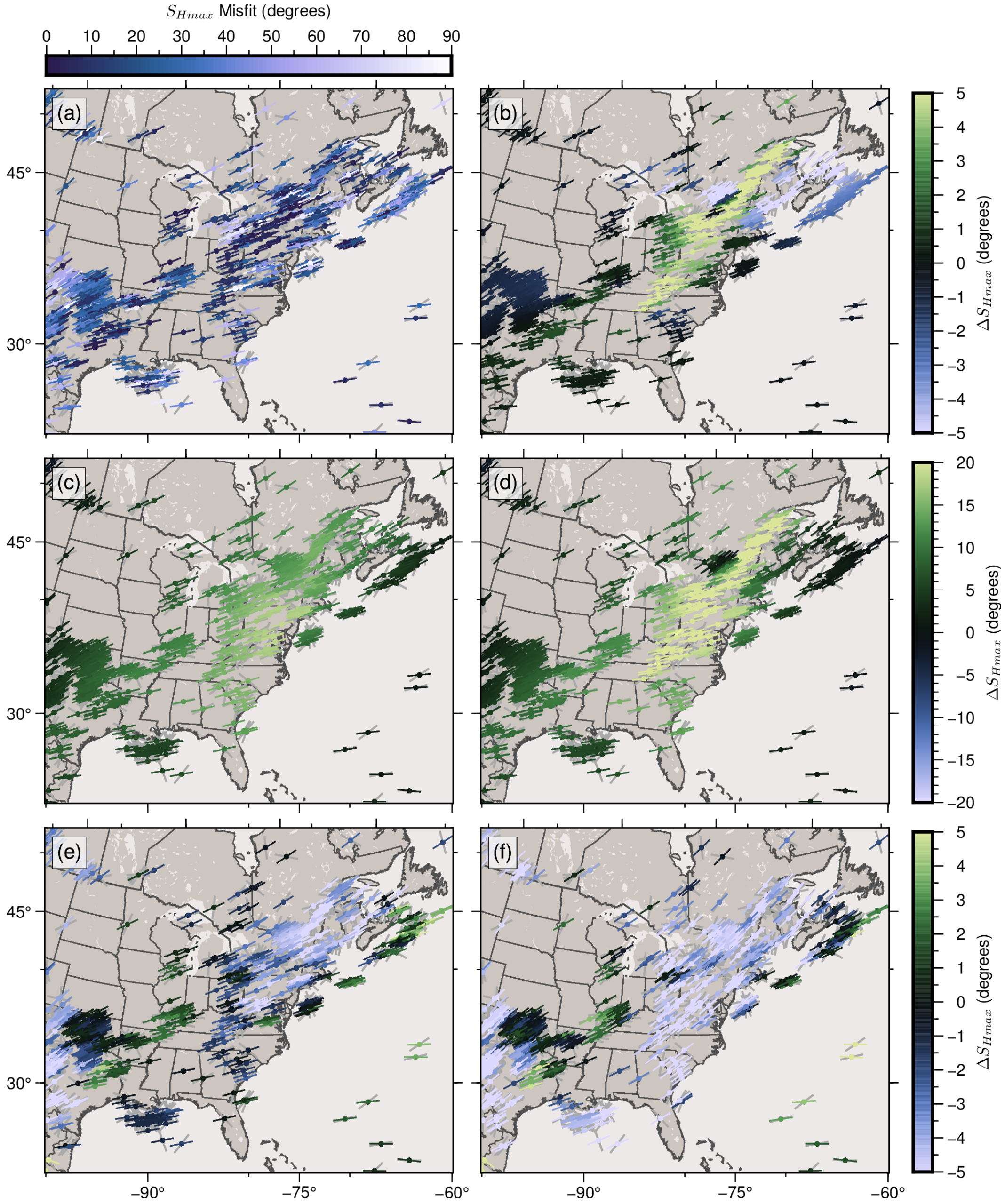

Figure 4.9: Rotation in S_{Hmax} orientation between cases with vs. without weak zones and/or Farallon loading at 10 km depth. a) S_{Hmax} orientations of model A0 colored by misfit as in Figure 4.8. b) S_{Hmax} rotation between models A1 and A0 (i.e., effect of including weak zones in models with the Farallon slab). Positive values indicate clockwise rotation; negative values indicate counterclockwise rotation. c) S_{Hmax} rotation between models A0 and B0 (i.e., effect of including the Farallon alone, without weak zones). d) S_{Hmax} rotation between model A1 and model B0 (i.e., combined effect of including both Farallon and weak zones). e) S_{Hmax} rotation between model A0 and A0G (i.e., effect of including GPE in models with Farallon but no weak zones). f) S_{Hmax} rotation between model B0 and B0G (i.e., effect of including GPE in models with neither Farallon nor weak zones).

Stress magnitudes also exhibit a strong dependence on weak zone depth. Models A1 and B1 contained weak zones emplaced at different depths based on where local

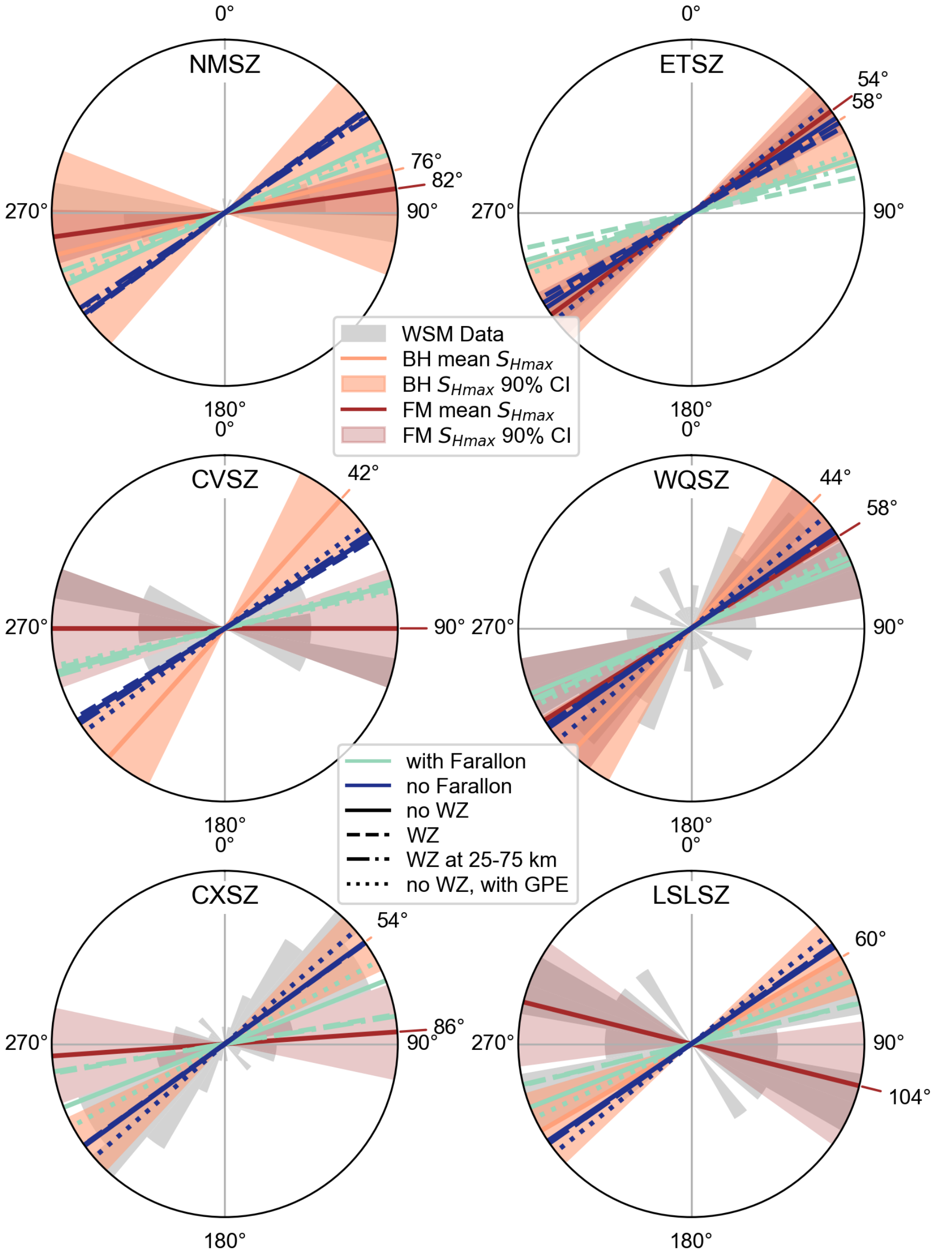

Figure 4.10: S_{Hmax} orientations in different seismic zones. Gray: polar histogram of the local S_{Hmax} orientations from the WSM, binned every 10°. Light orange colors: regional borehole (BH) derived mean S_{Hmax} and 90% CI from Mazzotti and Townend (2010). Reddish colors: local focal mechanism (FM) derived mean S_{Hmax} and 90% CI from Mazzotti and Townend (2010) (see legend). Value of the mean BH and FM S_{Hmax} are labeled on the theta axis for each seismic zone. Light blue lines: local mean S_{Hmax} from models with the Farallon slab (A0, A1, A1b, A0G). Dark blue lines: local mean S_{Hmax} from models with a neutralized slab (B0, B1, B1b, B0G). Line-styles differ for different weak zone cases (see legend). NMSZ: New Madrid Seismic Zone, ETSZ: Eastern Tennessee Seismic Zone, CVSZ: Central Virginia Seismic Zone, WQSZ: Western Quebec Seismic Zones, CXSZ: Charlevoix Seismic Zone, LSLSZ: Lower Saint Lawrence Seismic Zone.

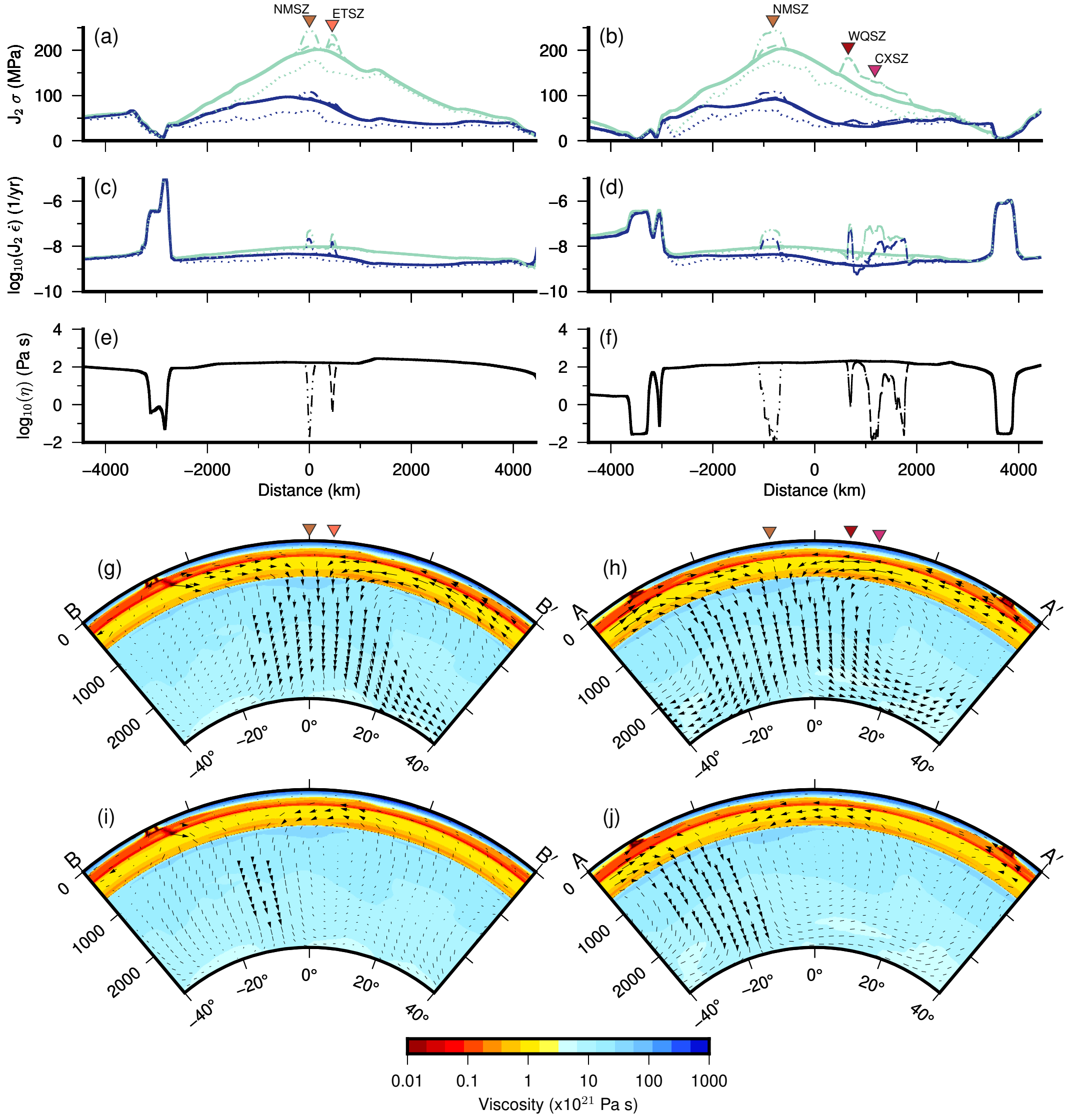

Figure 4.11: Stress, strain, and viscosity profiles. a) 2^{nd} invariant of deviatoric stress at 10 km depth along track B-B′ as in Figure 4.4, traversing W-E across the U.S. and through the NMSZ and ETSZ. Light blue lines: models in set A (i.e., with Farallon slab); dark blue lines: models in set B (i.e., neutralized Farallon slab). Solid lines: no weak zones (models A0 and B0). Thick dashed lines: weak zones at variable depths depending on seismic zone (models A1 and B1). Dashed-dotted lines: weak zones all at 25-75 km depth (models A1b and B1b). Dotted lines: with GPE but no weak zones (models A0G and B0G). b) Stress magnitude as in (a) but along track A-A′ as shown in Figure 4.4, traversing SW-NE across the U.S. and Canada and through the NMSZ, WQSZ, and LSLRS. c, d) 2^{nd} invariant of deviatoric strain rate at 50 km depth along tracks B-B′ and A-A′, respectively. Lines as in (a,b). e, f) Viscosity profiles at 50 km depth along tracks B-B′ and A-A′, respectively. Line-styles as in (a,b). g, h) Vertical slices of the viscosity field along tracks B-B′ and A-A′, respectively, for models with the Farallon slab; black arrows show velocity field. Locations of the seismic zones along the profile are marked as in (a,b). i, j) Viscosity slices and velocity field as in (g,h) but for models with a neutralized Farallon slab.

geophysical data suggests a weak zone may be present (Section 4.2). In this case, the weak zones in the vicinity of New Madrid and the Rome Trough/West Virginia

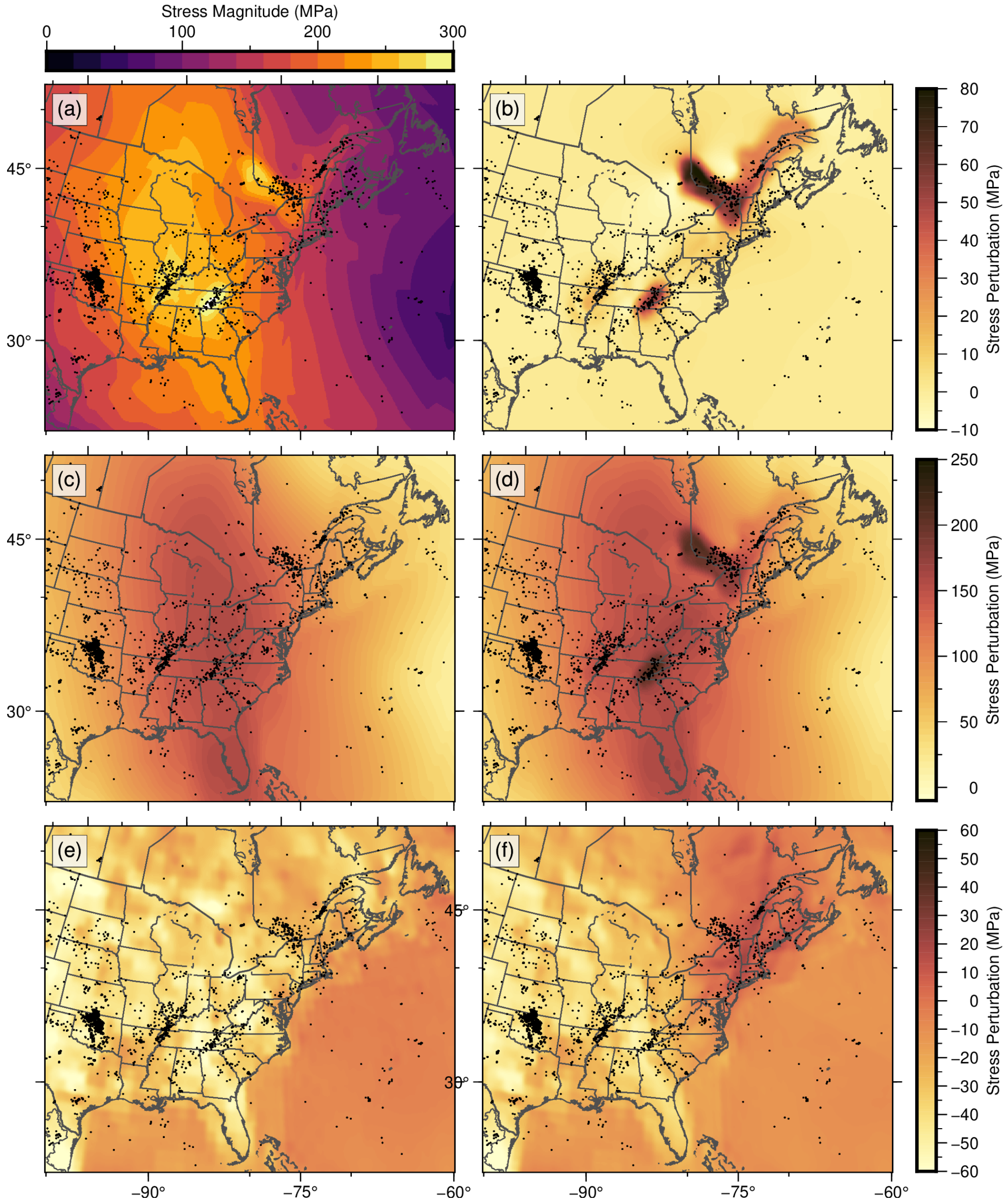

Figure 4.12: Deviatoric stress magnitude for eastern North America for different model cases. a) 2^{nd} Invariant of deviatoric stress for model A1 with both Farallon and weak zones placed at variable depths. b) Stress perturbation from including weak zones in models with the Farallon slab (i.e., between models A1 and A0). c) Stress perturbation from the Farallon slab alone, without weak zones (i.e., between models A0 and B0). d) Combined stress perturbation from including both the Farallon and weak zones (i.e., between models A1 and B0). e) Stress perturbation induced by GPE for models with the Farallon, but no weak zones (i.e., between models A0 and A0G). f) Stress perturbation induced by GPE for models with neither the Farallon nor weak zones (i.e., between models B0 and B0G).

are deeper than those in eastern Tennessee and southeast Canada. As such, they are farther removed from the crustal depths at which we assess the stress magnitudes

(10-15 km) and thus have a weaker and more diffuse effect on loading the overlying crust. In models where all weak zones are assumed to be near the base of the crust and extending into the upper mantle, between 25 and 75 km depth, stress perturbations in New Madrid become the largest of any of the seismic zones (Figure 4.11).

We also assessed the impact of incorporating gravitational potential energy (GPE) differences arising from lateral variations in crustal density and topography (models A0G and B0G). Incorporating GPE actually reduces the overall stress in the continental interior for both cases with and without the Farallon slab (Figure 4.12 e,f and dotted lines in Figure 4.11 a,b) and introduces more high frequency variability in the stress field than we are able to recover from the long-wavelength loading alone. Neither model A0G nor model B0G have weak zones, but interestingly, they both exhibit a small peak in stress at the location of the NMSZ. This peak is equally pronounced in both models with and without the Farallon slab, and is even greater in amplitude than the stress perturbation caused by the inclusion of a deeper upper mantle weak zone. Peaks in stress from the inclusion of GPE are not observed in the WQSZ or CXSZ/LSLSZ (Figure 4.11 b). Inclusion of GPE alone without influence from the Farallon slab also increases S_{Hmax} misfits by on average 5°, except in the NMSZ, where is decreases by a couple degrees. On the other hand, including GPE in the presence of Farallon loading reduces misfits by ∼8° in the Canadian seismic zones, ∼13° in New Madrid, and as much as ∼20° in Central Virginia relative to the WSM data (Figure C.5).

While differences in stress magnitude between the different model cases demonstrate the pronounced influence of the slab and weak zones, whether those stress perturbations are such that they increase the likelihood of seismicity in eastern North America is dependent on the local fault geometry. To assess the likelihood of fault reactivation for each of the different cases, we resolve Coulomb failure stress on actual faults in the NMSZ, WQSZ, and CXSZ/LSLSZ (Figures 4.13, 4.14, and 4.15). Coulomb failure stress is computed for all faults given their strike and dip and the stress tensors along that fault; Mohr circles are drawn relative to the Coulomb failure criteria for specific faults associated with known major historical earthquakes or nearby populated cities.

In the NMSZ, faults are assumed to be vertical unless otherwise indicated. While most faults in the NMSZ are steeply dipping, between 70-90°, yielding low Coulomb stress values and thus stable faults, the Reelfoot Fault dips between 30-44° (Csontos

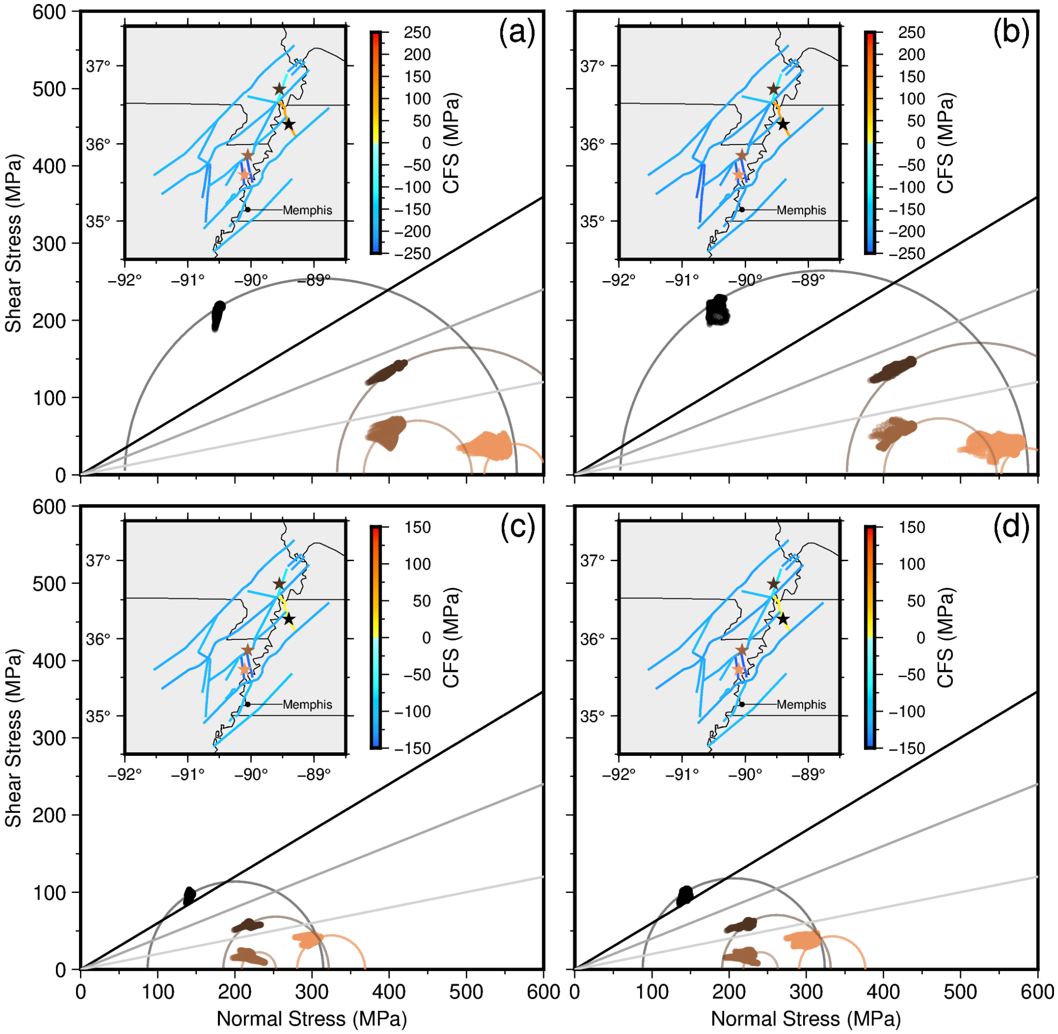

Figure 4.13: Mohr circles (main plot) and Coulomb failure stress (map inset) for faults in the NMSZ calculated using $\mu = 0.6$. Fault locations from Thompson et al. (2020). Fault strike and dip information for the Axial Fault (strike=46°, dip=90°), the New Madrid North Fault (strike=29°, dip=72°), the Risco Fault (strike=92°, dip=82°), and the North Reelfoot Fault (strike=167°, dip=30°) are from Csontos and Van Arsdale (2008). Faults with unknown dip are assumed to have a dip of 90°. Mohr circles are drawn for these New Madrid faults, using the fault's strike and dip and the stress tensor at the location of the corresponding star on the map. Star colors correspond to Mohr circle colors. Star locations for the three northernmost stars correspond to the most likely epicenters of the 1811-1812 earthquake sequence (Delano et al., 2021). The cloud of points on each Mohr circle represent the shear vs. normal stress for all possible stress tensors in the inset region given that fault's geometry. Black straight line is the Mohr-Coulomb failure criterion for $\mu = 0.6$; gray line is for $\mu = 0.4$; and light-gray line is for $\mu = 0.2$. (a) Results from model A0 (with Farallon, no weak zones). (b) Results from model A1 (with Farallon, with weak zones). (c) Results from model B0 (no Farallon, no weak zones). (d) Results from model B1 (no Farallon, with weak zones).

and Van Arsdale, 2008), placing it in an optimal orientation to be reactivated as a thrust fault in the local stress field. This fault indeed happens to be the site of one of the earthquake epicenters in the 1811-1812 earthquake sequence (Delano et al., 2021). The Reelfoot Fault is also the only fault to exhibit positive Coulomb stress values in each of our models (Figure 4.13), indicating a higher likelihood of fault reactivation. Similarly, the New Madrid North Fault also shows higher Coulomb stress, though still in the stable regime, and is also the site of one of the historical earthquakes. The NNW striking Joiner Ridge fault (orange star in Figure 4.13), which intersects the Axial Fault, has an unconstrained dip and thus was assigned a dip of 90°. However, this fault is identified as a thrust fault. If one were to assume a dip between 30-45° as in the case of the Reelfoot Fault, this fault would also exhibit high Coulomb stresses, and is in the vicinity of the remaining historical event just to the north on the Axial Fault (light brown star in Figure 4.13). While the vertical Axial Fault itself is not optimally oriented and exhibits low Coulomb stress, the intersection of a nearby reverse fault on which high Coulomb stress is localized could explain the occurrence of a major earthquake in this location (Talwani, 1988; Talwani, 1999).

The modeled stress state yields results consistent with expectations from the local rupture history, but more interesting are the differences in Coulomb stress we observe between the different models. For non-optimally oriented vertical faults, there is not a pronounced change between different cases, but for the more optimally oriented Reelfoot and New Madrid North Faults, there is an obvious difference. Inclusion of the Farallon slab pushes the Reelfoot Fault farther into the unstable regime by about 75-100 MPa and the New Madrid North Fault by about 10-20 MPa. In both cases with and without the Farallon slab, the inclusion of the weak zone does not have a notable effect, and shifts most faults farther from failure, except for the Reelfoot and New Madrid North Faults, which remain largely unchanged. This smaller effect is likely due to the deeper depth of the weak zone.

Changes between models are much more pronounced in the WQSZ (Figure 4.14). Without the Farallon slab and without weak zones (Figure 4.14 c), all faults are stable with respect to the Mohr-Coulomb failure criterion assuming a coefficient of friction of 0.4 – 0.6 and fault dips of 56°, consistent with steeply dipping rift-bounding normal faults for the region (Bent et al., 2003; Rimando and Peace, 2021). The dips of the Timiskaming fault (black star in Figure 4.14) and nearby parallel faults are 45° based on Bent (1996). Assuming a $\mu = 0.6$, including weak zones without the Farallon slab brings most faults closer to failure (Figure 4.14 d), though still within the stable regime, with the largest changes occurring in and to the northeast of Montreal. If faults are weaker ($\mu \approx 0.4$), many faults would just pass into the unstable regime, including the four plotted as Mohr circles. Similar to the NMSZ, influence of the Farallon slab brings all faults closer to failure by at least 15-25 MPa, but only a few faults exhibit high Coulomb stress above the failure criterion — a change on the order of 75-100 MPa. These faults all have similar orientations and dips and include the fault on which the 1935 M 6.1 Timiskaming earthquake occurred, as well as the nearby Cross Lake, Montreal River, and Latchford Faults. The Mohr circle for this location is solidly within the unstable regime for every stress tensor orientation in the map area. The other plotted Mohr circles, though stable for a μ of 0.6, would likewise fall in the unstable regime for a slightly weaker fault with μ of even just 0.55 (Figure C.6). Inclusion of shallow upper mantle/sub-crustal weak zones noticeably shifts faults in the western half of the WQSZ closer to failure by up to 25 MPa, including some that are less optimally oriented.

The LSLRS, including the CXSZ, is the only region for which we do not recover any positive Coulomb stress values for faults associated with major historical earthquakes if using $\mu = 0.6$. Most faults in the LSLRS strike NE-SW, similar to the regional S_{Hmax} orientation and thus are not optimally oriented for thrust reactivation in such a setting. Interestingly, for $\mu = 0.6$, the inclusion of the Farallon slab by itself pushes faults farther from failure. This is because even though the differential stress on the faults increases (i.e., the radius of the Mohr circle expands), the total normal stress on the fault also increases, pushing the Mohr circle to the right along the abscissa, thus increasing its distance from the failure criterion. Nevertheless, similar to the WQSZ, if one were to assume weaker faults with a μ of 0.4 or less, many of the faults, including those associated with the major historical earthquakes, would be solidly within the unstable regime. With a μ of even 0.5, most faults would be unstable by 5-10 MPa (Figure C.7). The inclusion of weak zones brings faults closer to failure by ~15 MPa in the CXSZ and as much as 20 MPa towards the south near Montreal. For models without the Farallon slab, weak zones increase the Coulomb stress on most faults by ~10-15 MPa.

4.7 Discussion

Using mantle flow models to compute the stress field of eastern North America, we have assessed the influence of Farallon slab buoyancy and weak zones on the likelihood of fault reactivation in intraplate seismic zones. Between end member cases of a fully realized negatively buoyant Farallon slab as inferred from seismic tomography (model set A) and that of a neutrally buoyant Farallon slab (model set B), our models reveal a long-wavelength stress amplification of up to 100-

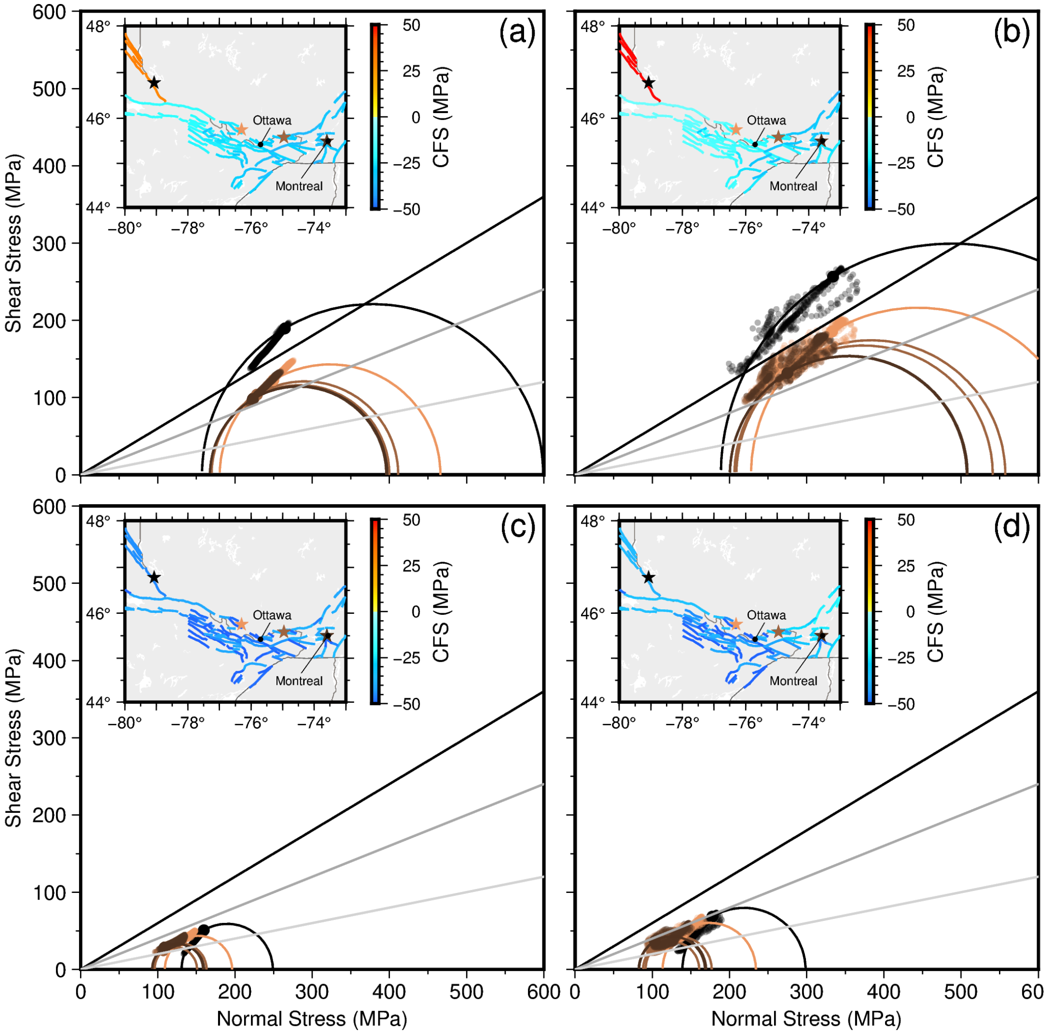

Figure 4.14: Mohr circles (main plot) and Coulomb failure stress (map inset) for faults in the WQSZ calculated using $\mu = 0.6$. Fault locations from Rimando and Peace (2021) and Lamontagne et al. (2020). Fault strikes approximated using the best fitting great circle through the lineation. Unless otherwise specified, fault dips were assumed to be 56° (Bent et al., 2003; Rimando and Peace, 2021). Dip of the fault associated with the Timiskaming 1935 earthquake (black star) and nearby faults are from Bent (1996) (strike=146°, dip=45°). Mohr circles are drawn for four faults, using the stress tensor at the location of the corresponding star on the map: The Timiskaming fault of the M 6.1 1935 earthquake, the Rapide-du-Cheval Blanc Fault near the epicenter of the M 6.3 1732 Montreal earthquake, the Lachute Fault (NE of Ottawa), and the Coulonge Fault (NW of Ottawa). Earthquake locations from Bent (2022) and Bent et al. (2003). Star colors correspond to Mohr circle colors. The cloud of points on each Mohr circle represent all possible stress tensors in the inset region given that fault's geometry. Black straight line is the Mohr-Coulomb failure criterion for $\mu = 0.6$; gray line is for $\mu = 0.4$; and light-gray line is for $\mu = 0.2$. (a) Results from model A0 (with Farallon, no weak zones). (b) Results from model A1 (with Farallon, with weak zones). (c) Results from model B0 (no Farallon, no weak zones). (d) Results from model B1 (no Farallon, with weak zones).

150 MPa induced by the presence of the slab (Figures 4.12, 4.11), as well as a generally compressive stress state within the continent. To understand the origins of this stress pattern, we examine the change in viscosity and strain rate at the

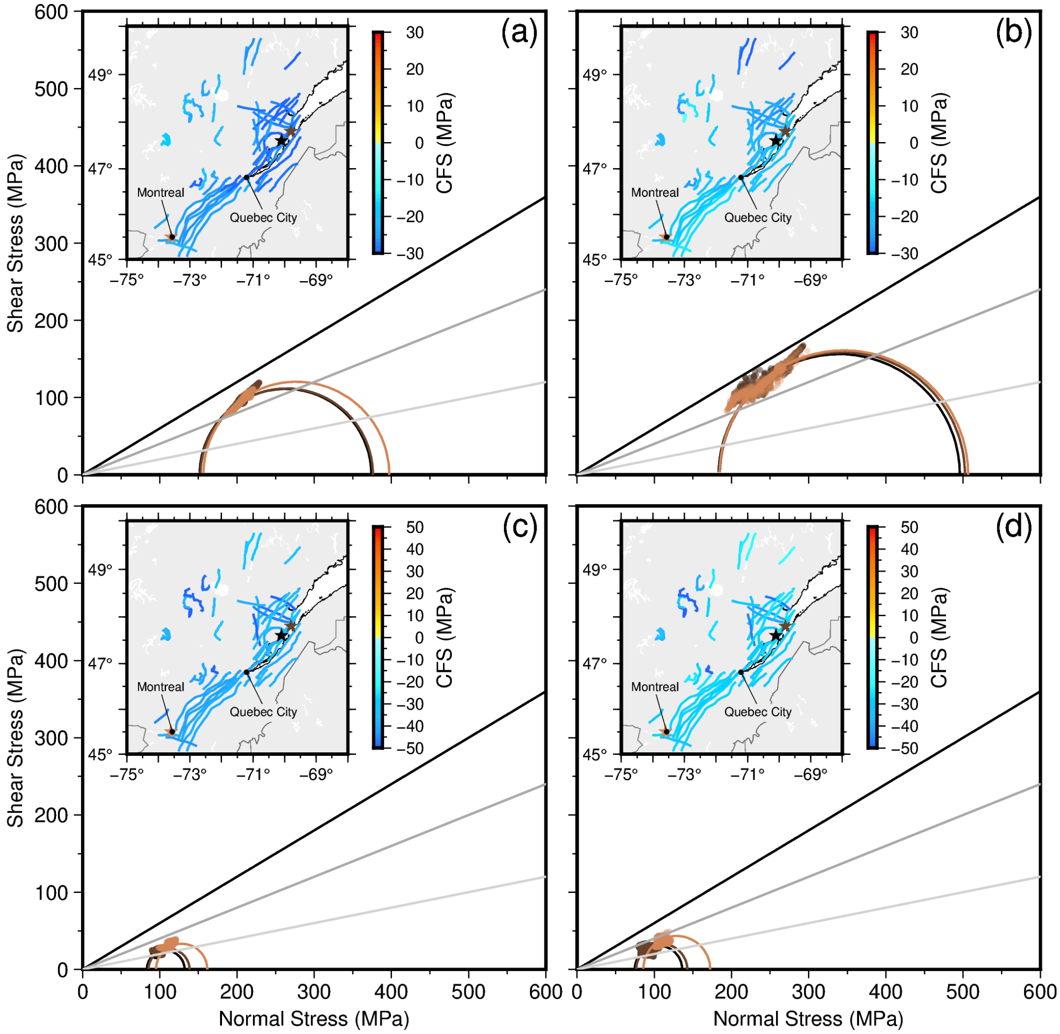

Figure 4.15: Mohr circles (main plot) and Coulomb failure stress (map inset) for faults in the LSLRS, including the CXSZ, calculated using $\mu = 0.6$. Fault strikes approximated for each fault location using the best fitting great circle through the lineation. Fault dips assumed to be 53°, consistent with the values of steeply dipping rift bounding normal faults for the LSLRS as reported by Bent et al. (2003) and Bent (1992). Mohr circles are drawn for the three faults closest to the epicenters of the 1663 M 7.0 and 1925 M 6.2 Charlevoix earthquakes and the M 6.3 1732 Montreal earthquake, using the fault's strike and dip and the stress tensor at the location of the corresponding star on the map. Star colors correspond to Mohr circle colors. Earthquake locations from Bent (2022). The cloud of points on each Mohr circle represent the shear vs. normal stress for all possible stress tensors in the inset region given that fault's geometry. Black straight line is the Mohr-Coulomb failure criterion for $\mu = 0.6$; gray line for $\mu = 0.4$; and light-gray line is for $\mu = 0.2$. (a) Results from model A0 (with Farallon, no weak zones). (b) Results from model A1 (with Farallon, with weak zones). (c) Results from model B0 (no Farallon, no weak zones). (d) Results from model B1 (no Farallon, with weak zones).

depth of the lithospheric weak zones (Figure 4.11 c-f). The buoyancy force of the Farallon slab drives localized mantle flow beneath the central eastern US, consistent with previous findings (Forte et al., 2007). This downward flow (Figure 4.11 g,

h) means an amplified gradient in the vertical velocity in the mantle overlying the downwelling. Because the lithosphere and underlying mantle are viscously coupled, the downward flow in the mantle, excites a downward deflection of the overlying lithosphere. This deflection is small due to the high viscosity of the lithosphere, but even such small horizontal gradients in the vertical velocity are enough to produce a broad low amplitude increase in the strain rate across the continent (Figure 4.11 c, d) compared to the flatter profile in the case with no Farallon slab. While subtle, these higher strain rates, when scaled by the very large viscosity of the lithosphere, result in a strong stress amplification over the central eastern US (Figure 4.11 a, b). The peak of this long-wavelength stress perturbation centers over the New Madrid Seismic Zone. In Western Quebec and the Lower Saint Lawrence Rift, stress perturbations from the presence of the slab are similarly on the order of 100 MPa.

Superimposed on this broad stress high are peaks in stress due to the inclusion of weak zones. The sharp lateral viscosity gradients imposed by such weak zones lead to faster flow and higher strain rates within the weak zones, which likewise are viscously coupled to the surrounding rigid lithosphere and crust and impart tractions in these areas. Scaled by the very low viscosity of the weak zones, this leads to low stresses within the weak zones themselves, but the tractions in the overlying crust, scaled by the higher viscosity of the crustal lithosphere, lead to high stresses localized above the weak zones (Figure 4.11 a,b). The stress perturbations are higher in the models with the Farallon slab because the buoyancy force of the slab excites more flow in these low viscosity regions. Stress perturbations arising from weak zones in the presence of the sinking slab are enhanced by up to 70 MPa more so than in the cases with no slab. Without the Farallon, weak zone stress perturbations are only on the order of 5-15 MPa, suggesting crustal loading from displacements in a mantle low-viscosity zone are relatively small under far-field tectonic stresses alone, consistent with the findings of Zhan et al. (2016).

However, the magnitude of these weak zone stress perturbations is also dependent on the depth of the weak zone. Deeper weak zones such as those beneath New Madrid in models A1 and B1 yield stress perturbations at seismogenic depths of only about 10 MPa compared to sub-crustal weak zones such as those in models A1b and B1b, which yield stress perturbations on the order of 75 MPa. This is because the shallower weak zones impart tractions directly to the base of the crust, but the tractions imparted by the deeper weak zones will decay in magnitude with distance from the weak zone. Thus, we find that for weak zones to exert an appreciable influence on intraplate stress at seismogenic depths, they must be shallow, extending from lower crustal to mid-lithospheric depths and ideally coupled to the crust itself, even when in the presence of full loading from the Farallon slab.

The significance of shallow versus deeper weak zones is even more apparent when including the effect of GPE. While neither model A0G nor B0G have weak zones, both exhibit stress perturbations in the NMSZ on the order of 20-30 MPa. The perturbation is even similar in amplitude or greater than the stress perturbation caused by the deeper-set weak zone of models A1 or B1. This suggests that for the NMSZ, crustal density variations alone could be enough to locally enhance stresses and promote seismicity on pre-existing faults, as has been suggested by other authors (Ghosh et al., 2009; Levandowski et al., 2017). Such a significant density variation could arise from the possible presence of mafic under-plating or high density intrusions originating from the formation of the Reelfoot Rift or the passage of an ancient hotspot (Chu et al., 2013) and is supported in part by the observed seismic structure beneath the NMSZ (Chen et al., 2014; Chen et al., 2016). The small peak in stress at around 1300 km from the center of profile B-B′ in Figure 4.11a is also more prominent in the models with GPE, reflecting the influence of density and lithospheric viscosity changes at the continent-ocean transition. This is also evident in the viscosity profile at 50 km depth (Figure 4.11 e), where a slight increase in the viscosity gradient at that point leads to slightly higher strains and the small peak in the stress magnitude along the passive margin. While small ($\sim$10 MPa), such a stress perturbation in combination with weak zones or structures associated with Mesozoic rift basins along the eastern seaboard could help bring coastal and offshore faults closer to failure. Within the Canadian seismic zones, on the other hand, GPE induces a positive stress perturbation when not loaded by the Farallon slab, in which case the Northern Appalachian and eastern Canadian region show elevated stress magnitudes. GPE combined with low-viscosity weak zones would likely induce even larger stress perturbations. Overall, while the effect of GPE alone is not insignificant, particularly for the NMSZ, the stress perturbations arising from shallow low-viscosity weak zones are more in line with values necessary to reproduce observed stress patterns and enhance stress on faults. In fact, other than in the NMSZ, GPE introduces a counterclockwise rotation of S_{Hmax} in contrast to that observed across eastern North America (Mazzotti and Townend, 2010).

Stress rotations within seismic zones across eastern North America are often considered indicative of long wavelength forcing beyond just tectonic background stress. Mazzotti and Townend (2010) observe 30-50° clockwise rotations of the local focal mechanism derived S_{Hmax} direction from the regional borehole derived S_{Hmax} direction within several seismic zones in eastern North America. They argue that the consistency of such stress rotations observed in seismic zones separated by large distances, such as the LSLRS and parts of the central-eastern U.S, suggests a common mechanism. The borehole and seismically derived S_{Hmax} orientations from Mazzotti and Townend (2010) and their 90% confidence intervals are plotted for six seismic zones in Figure 4.10 along with the mean S_{Hmax} within each seismic zone for each of our models. In all cases except the ETSZ, the clockwise rotation in stress induced by the influence of the Farallon slab shifts the S_{Hmax} direction more in line with the observed seismically inferred S_{Hmax}. This change is even more pronounced for cases with both the slab and weak zones, and in the case of the CVSZ and the CXSZ, shifts the S_{Hmax} direction from the confidence band of the regional borehole value into that of the seismically derived values. The Charlevoix and Lower Saint Lawrence Seismic Zones have the largest weak zone induced S_{Hmax} rotations of ~35° and ~25°, respectively, and the rotation for the CXSZ places S_{Hmax} within a few degrees of the observed value. However, the structural complexities due to the Charlevoix impact crater, as well as variations in S_{Hmax} orientations derived from microseismicity with the CXSZ (Baird et al., 2010), suggest that local stress perturbation may be just as responsible for the anomalous seismicity in this area as is any regional stress perturbation. Nevertheless, the influence of slab loading is shown to induce a clockwise rotation on the intraplate stress field, and the presence of shallow weak zones enhances the magnitude of that stress rotation in line with the observed rotations in some seismic zones.

The New Madrid, Central Virginia, and the Lower Saint Lawrence River Seismic Zones, however, would still require larger rotations to shift S_{Hmax} into the seismically inferred CI band. The observed rotations require stress perturbations on the order of 160-250 MPa, assuming a high friction crust (Mazzotti and Townend, 2010). In our models, the inclusion of zones 1e4 times weaker than the surrounding lithosphere induces stress perturbations on the order of 130 MPa in the presence of slab loading relative to a case with no Farallon loading, yielding total stress magnitudes of 200-250 MPa over the central-eastern U.S. For the NMSZ, only the model with shallow weak zones gets close to the observed S_{Hmax} direction of either the Mazzotti and Townend (2010) or the WSM data, suggesting slightly higher stress perturbations may be required to reach the magnitudes of the observed rotations. This may be achieved by an even shallower or weaker weak zone or by additional sources of stress, such as GIA or local complexities in the faulting that may help further amplify stresses. For example, Wu and Mazzotti (2007) observe clockwise rotation of GIA stresses in the crust above lithospheric weak zones, and GIA induced S_{Hmax} alone is nearly E-W in the central-eastern U.S. (Chapter 5).

The rotations induced by the slab and weak zones are important because they orient the stress tensor into a position more favorable for reactivating faults in some of the seismic zones. In the LSLRS and parts of the WQSZ, the majority of faults strike SW-NE in line with the regional S_{Hmax} direction, making them non-optimally oriented for reactivation. When S_{Hmax} rotates into a more E-W orientation, however, these ancient rift bounding faults become more favorably oriented, potentially promoting slip. Even with the rotations we observe (Figure 4.10) however, Coulomb stresses on these faults are still relatively low (Figure 4.15) assuming a μ of 0.6. However, even a small reduction in the coefficient of friction, as little as 0.1, would promote instability on these faults in the modeled stress field (Figure C.7). A $\mu = 0.5$ in the case of both weak zones and the Farallon loading, for example, pushes the majority of faults in the LSLRS into the unstable regime by about 5-10 MPa. Even without the weak zone, one of the faults closest to the proposed epicenter of the 1732 Montreal earthquake exhibits positive Coulomb stress values. Higher friction values of $\mu \geq 0.6$ are typical of intraplate crust as a whole (Townend and Zoback, 2000; Zoback et al., 2002), but locally within pre-existing crustal weak zones, friction may be much lower. In Charlevoix, for example, relationships between seismicity and geological structures suggest the main rift faults of the LSLRS may have abnormally low friction values, as small $\mu \approx 0.1$, or abnormally high pore fluid pressure (Baird et al., 2010). While such a low value is unlikely, the middle/lower crust in this region is estimated to have a friction coefficient of around 0.5 ± 0.07 based on a joint focal mechanism inversion of events within the CXSZ (Verdecchia et al., 2022). Thus, even just a slightly smaller friction coefficient would allow for faults to reach instability under slab loading without the need for such anomalously weak faults. A reduction by only 0.05 in the coefficient of friction would likewise place many faults in the western half of the WQSZ squarely within the unstable regime relative to the Mohr-Coulomb failure criterion (Figure C.6).

Even with $\mu \geq 0.6$ the likelihood of failure on the Timiskaming fault is clearly resolved in the cases of Farallon loading. Likewise, instability on the Reelfoot Fault associated with the 1811–1812 NMSZ sequence is also apparent in all cases. What these two faults have in common is their optimal orientation for slip within even the background stress field, demonstrating unsurprisingly that the existing fault orientation is a dominant control on its likelihood of reactivation in an intraplate setting. The inclusion of the Farallon slab and/or weak zones, on the other hand, does perturb the magnitudes of stresses in such a way that it brings these faults further into the unstable regime, increasing Coulomb stress on the order of 75-100 MPa (Figures 4.13 and 4.15). More importantly, assuming weak faults, it can also bring non-optimally oriented faults to failure or closer to failure, as in the case of the WQSZ and the CXSZ/LSLSZ (Figures C.6 and C.7). In this case, the southwest portion of the LSLRS is more strongly affected by the Farallon slab than the Charlevoix, reflecting the greater influence of the slab towards the center of eastern North America, where the majority of the Farallon's mass is located beneath the central-eastern U.S. and the NMSZ (Figure 4.11).

Not all seismic zones show improved S_{Hmax} fits or elevated stresses due to the Farallon or weak zones. In the ETSZ and in the vicinity of the Rome Trough and the Northern Appalachians, the inclusion of weak zones actually reduces the fit to the stress data, rotating it too much relative to the observed local S_{Hmax}. This suggests that despite the prominence of a high conductivity and low seismic velocity zone in this region (Evans et al., 2019; Schmandt and Lin, 2014), corresponding low viscosities are not essential for reproducing the observed stress field. On the other hand, the ETSZ is one of the few seismic zones for which GPE actually improved the S_{Hmax} fit. The strong shallow density contrast across the NY-AL lineament evident in magnetic data (Thomas and Powell, 2017) suggests lateral buoyancy effects are likely significant in this region. Another peculiarity worth mentioning is that most of the seismicity in the WQSZ is actually concentrated northeast of the old rift, not within the aulacogen itself, yet most of the known faults, including those for which we perform a CFS analysis (Figure 4.14), are along the Ottawa-Bonnechere Graben. This would either suggest that the most active faults in this area have simply not been mapped or that the weak zone loading the crust is not bounded by the ancient rift faults but instead located slightly to the northeast, along the suggested position of an ancient transform fault (Sykes, 1978) or the passage of the Great Meteor hotspot (Ma and Eaton, 2007). In either case, if we were to shift the sub-crustal weak zone of Western Quebec slightly to the northeast, we would likely see similar patterns and similar stress magnitude perturbations as those of the current results.

While the substantial influence of the Farallon slab and local weak zones on the intraplate stress field is evident, there are still many local sources of stress perturbations and other factors driving intraplate seismicity to consider. One consideration is the actual viscosity of the weak zones. We only test the presence of weak zones by considering the end member cases of no weak zones versus weak zones with a viscosity of 1e–4 relative to the surrounding lithosphere. However, the viscosities of these different weak zones, if present, are likely to vary, possibly by orders of magnitude. There is also likely some trade-off between the impact of the viscosity reduction on the stress perturbations versus the impact of the weak zone depth. Depth is better constrained than viscosity due to the availability of geophysical data, but this trade off still requires further investigation. The other major consideration and one of the most critical is that we do not account for the previous stress history of the fault. In our models, all faults are virtual faults, meaning no physical fault surface is included in the model; rather, the calculated stress tensors at a particular location are applied to a set of faults after the fact to determine there influence on the behavior of a fault of a particular orientation. Were faults present in the model itself, their presence would affect the stress distribution (Wu et al., 2021; Steffen et al., 2014b). Most importantly, the rupture history of the fault, which we do not explicitly model, will affect the local change in CFS and the likelihood and location of future earthquakes (Stein, 1999). This is especially true in light of the long-lived aftershock sequences and temporal clustering that are typical of intraplate settings (Stein and Liu, 2009; Dicaprio et al., 2008). The current models are limited in both the resolutions we are able to obtain and the purely viscous rheological formulation of CitcomS. Future models should seek to incorporate true faults, but would require higher lateral spatial resolutions more suited to a regional scale model and elasticity within the crust to properly capture brittle failure.

4.8 Conclusions

Using the geodynamics code CitcomS, we model the influence of mantle flow induced by the sinking of the Farallon slab on the intraplate stress field of eastern North America. Slab sinking drives localized mantle flow beneath the central-eastern U.S., leading to a stress amplification of 100-150 MPa across the region that peaks over the New Madrid Seismic Zone. This stress amplification introduces a pronounced continent-wide clockwise rotation of the predicted S_{Hmax} direction by as much as ~20° in some places. This rotation is enhanced when lithospheric weak zones are included at the locations of ancient aulacogens and other pre-existing structures and improves the fit to the observed seismic S_{Hmax} direction within most seismic zones. The presence of weak zones loaded by the Farallon slab at depth can also explain the pattern of clockwise rotation of the observed focal mechanism derived S_{Hmax} direction relative to the regional borehole derived S_{Hmax} as reported by Mazzotti and Townend (2010) in the New Madrid, Central Virginia, Charlevoix, and Lower Saint Lawrence Seismic Zones. However, larger stress perturbations are required to fully reproduce the observed degree of stress rotation in most of the seismic zones, except Charlevoix, suggesting the need for weaker weak zones or another source of stress such as glacial isostatic adjustment. The magnitude of the modeled stress perturbations are also dependent on the depth of the weak zones, which have a reduced influence on crustal stresses with greater depth. Thus, in order for pre-existing lithospheric weak zones to exert appreciable control on intraplate stress under the influence of mantle flow, they must be shallow/sub-crustal and in contact with the crust. However, even with shallower weak zones, many of the stress perturbations and rotations between the different models are quite small. Given the many mechanisms giving rise to intraplate stress and the uncertainty on geodynamic model inputs, including the tomography itself, the velocity to temperature conversion, the assumed viscosity law, and the slab parameterization, one may argue that the differences between the models are insignificant, particularly when compared to the spread of the S_{Hmax} data within a single seismic zone. While future work should seek to better quantify the impact of the errors of the inputs, our models nevertheless demonstrate the substantial influence of the Farallon slab on intraplate stress.

Moreover, even small changes in stress are ultimately important because they place S_{Hmax} into a position that may be more favorably oriented to reactivate faults, depending on the fault geometry. Even without weak zones, influence of mantle flow from the Farallon slab is enough to explain fault instability at the locations of some significant historical earthquakes, such as the Reelfoot Fault in New Madrid — the site of one of the 1811-1812 M 7-8 earthquakes — and the Timiskaming Fault in Western Quebec, on which the 1935 M 6.2 earthquake occurred. Across all seismic zones, the inclusion of weak zones brings the majority of faults closer to failure. However, fault orientation and fault weakness remain key controls on their reactivation potential. Weaker faults ($\mu \leq 0.4$) in the NMSZ would not be enough to reactivate them unless optimally oriented, but weak faults ($\mu \leq 0.5$) could explain fault reactivation in the WQSZ and CXSZ in the modeled stress field.

Many previous studies have argued that lithospheric mantle heterogeneity alone is the primary control on intraplate seismicity (Saxena et al., 2021; Levandowski et al., 2017; Zhan et al., 2016). Such heterogeneity in mantle viscosity controls the spatial variability of the velocity gradients by diverting flow to lower viscosity areas, so mantle heterogeneity remains an important factor, but the Farallon slab has the effect of augmenting the magnitude of those gradients, which ultimately helps move many faults closer to failure. Thus, while lithospheric mantle heterogeneity may govern the spatial distribution of intraplate stress, epeirogenic processes are largely responsible for the magnitudes of stress required to reactivate some intraplate faults and to explain continent-wide stress rotations.

Chapter 5

GEODYNAMIC CONTROLS ON INTRAPLATE SEISMICITY IN EASTERN NORTH AMERICA II: THE INFLUENCE OF GLACIAL ISOSTATIC ADJUSTMENT

5.1 Introduction

The continental interior of eastern North America has been host to many major historical earthquakes despite the stability of the craton and the lack of active tectonics (Figure 4.1, Table 4.1). Such intraplate earthquakes occur within defined seismic zones (Figure 4.1) and like other intraplate earthquakes worldwide tend to correlate with Mesozoic or older crustal extensional structures, such as rifted margins, aulacogens, and extensional basins (Johnston et al., 1994; Mazzotti, 2007b), which may act as weak zones in the crust where stress accumulates (Sykes, 1978; Hurd and Zoback, 2012). The New Madrid Seismic Zone (NMSZ) (Reelfoot Rift) and Western Quebec (Ottawa-Bonnecherè Graben) Seismic Zone (WQSZ) are associated with Proterozoic Iapetus failed rift arms (700-550 Ma) (Baird et al., 2010). The Lower St. Lawrence (LSLSZ), Charlevoix (CXSZ), Montreal, and Eastern Tennessee Seismic Zones (ETSZ) are associated with the Iapetus rifted margin itself (Mazzotti and Townend, 2010), and the Northern Appalachian, Central Virginia (CVSZ), and Charleston seismic zones are spatially correlated with Mesozoic rift basins of the extended Atlantic margin (Withjack et al., 1998; Mazzotti and Townend, 2010), as well as other inherited tectonic structures. Earthquakes and modeled stresses also concentrate in zones of thinner lithosphere around the margin of the North American continental lithosphere (Li et al., 2007). While such intraplate seismicity may result from a number of different processes, including far-field tectonic forcing, gravitational potential energy differences, and mantle flow (see Chapter 4), it has long been suggested that stresses induced by glacial isostatic adjustment (GIA) may be responsible for these anomalous earthquakes (Wu and Hasegawa, 1996; Wu and Johnston, 2000; Grollimund and Zoback, 2001; Wu and Mazzotti, 2007; Mazzotti and Townend, 2010).

Glacial isostatic adjustment is the response of the solid earth to the disappearance of major ice sheets following the last glacial maximum (LGM) about 21-26 thousand years ago. At timescales appropriate for post-glacial rebound, the Earth responds to loads viscoelastically (Cathles, 1975; Peltier, 1974), meaning that even after the ice load is gone, there is a time delay of the uplift of the Earth to its pre-glaciation level. GIA continues in the present day, with GPS observable maximum uplift rates of >10 mm/yr (Sella et al., 2007; Lidberg et al., 2010) near the former centers of the Laurentide ice-sheet in North America and the Fennoscandian ice-sheet in northern Europe. During the last glacial maximum, the Laurentide ice sheet covered most of North America, with the thickest ice cover (as much as 3-5 km) positioned at Hudson Bay (Peltier et al., 2015; Lambeck et al., 2017), the site of the largest modern day rebound rates. The southern extent of the former ice-margin during the LGM reached as far south as southern Illinois and as far east as offshore Maine and Nova Scotia (Dyke et al., 2002; Peltier et al., 2015; Dalton et al., 2020). The ice-sheet melted rapidly between 10-12 ka, and deglaciation was nearly complete by ~7-8 ka (Dalton et al., 2020).

During glaciation, the weight of the ice sheet creates an additional vertical stress in the lithosphere, and the flexure of the lithosphere under the load generates horizontal bending stresses. These additional vertical and horizontal stresses increase all three principal stresses. In terms of Mohr Coulomb failure theory (Appendix C.3) for a compressive background stress regime, this stress increase pushes the Mohr circle in the positive direction along the normal stress axis, away from the failure threshold. In other words, during glaciation, the weight of the ice-sheet acts to stabilize faults and suppress fault movement (Johnston, 1987; Wu and Hasegawa, 1996; Steffen et al., 2014a). When the ice-sheet melts, the vertical stress from the load decreases, but the GIA induced horizontal stresses do not decrease as quickly because of the viscoelastic nature of the lithosphere and the upward migration of stress from mantle relaxation. Thus, after deglaciation, the vertical stress disappears but the horizontal stress remains, which increases the differential stress, both expanding the Mohr circle radius and shifting it back in the negative direction along the normal stress axis, bringing it closer to the failure criterion (Steffen et al., 2014a).

The magnitudes of glacial rebound stresses are also dependent on the wavelength of the load relative to the thickness of the lithosphere and are largest for ice sheets with diameters on the order of a couple hundred km rather than continental-scale ice-sheets like the Laurentide (Johnston et al., 1998). However, while the Laurentide itself was of large spatial extent, lobes extending from its southern margin, such as those that covered New York and Massachusetts or extended south of the Great Lakes (Dalton et al., 2020), were of much smaller wavelength and thus may have been more effective at perturbing stress magnitudes in areas of interest regarding the patterns of intraplate seismicity. Nevertheless, the largest confirmed glacially induced fault offset, about 100m, is located in the Canadian Arctic at the Laurentian margin (Dyke et al., 1991). Most glacially reactivated faults, however, are located in the northern Lapland Province of Sweden, Finland, and Norway at the ancient margins of the much smaller Fennoscandian ice sheet (Steffen et al., 2021), consistent with the findings of Johnston et al. (1998). As with many of the faults in eastern North America, especially within the Canadian seismic zones, glacially triggered faults are often steeply dipping normal faults reactivated with a thrust sense of motion, but reactivation under GIA stress perturbations is likely only possible for a coefficient of friction less than 0.4 (Steffen et al., 2014a).

Using a spherical, self-gravitating viscoelastic Earth model, Wu and Johnston (2000) found that GIA is capable of triggering paleo-earthquakes within the Charlevoix Seismic Zone and even in the Wabash Valley, Indiana north of the NMSZ. Within the NMSZ, they find that faults do pass the instability threshold within the last 200 years, consistent with the timing of the 1811-1812 New Madrid earthquakes. However, the magnitude by which the stresses exceed that threshold are very small and are therefore believed unlikely to have triggered the M 7-8 earthquakes of that sequence. This is due to the fact that GIA induced stresses decay rapidly away from the former ice margin (Wu and Johnston, 2000) but also with time after initial deglaciation, as faults are likely to be most unstable immediately following the removal of the load (Steffen et al., 2020; Wu and Hasegawa, 1996), around 8-9 ka. Nevertheless, paleoseismicity in the NMSZ records a Holocene slip rate four orders of magnitude greater than that in the Cretaceous or earlier in the Cenozoic and a slip rate as high as 4.4 mm/yr over the last 2400 years alone, which may be tied to crustal motion from Laurentide deglaciation (Van Arsdale, 2000). Likewise, paleoseismological and geodetic evidence suggestive of recurrence times anywhere between 400 – 1100 years in combination with the lack of accumulated deformation on faults suggests places like the NMSZ became active recently and that the seismic zone itself is only a couple tens of thousands of years old (Schweig and Ellis, 1994), suggesting New Madrid seismicity could be a glacially controlled phenomenon.

However, paleoseismic evidence suggestive of an elevated slip rate on the Reelfoot Fault during the last two major earthquake cycles (Van Arsdale, 2000) is also consistent with idea that the New Madrid sequence was a rare one-off event, and that modern seismicity may be a transient clustering of mainshock earthquake activity in response to viscoelastic relaxation after those major earthquakes (Kenner and Segall, 2000; Kenner and Simons, 2005). Such a prolonged viscoelastic decay of seismicity rate beyond what is expected for a typical aftershock sequence is not unheard of for large earthquakes, such as, for example, the elevated seismicity rates observed after the 2010 El-Mayor Cucapah event in Mexico (Gualandi et al. (2020), e.g., Chapter 3), and long aftershock sequences are more typical of intraplate environments (Stein and Liu, 2009). Nevertheless, such transient seismicity would likely require relaxation of a local lithospheric weak zone that cyclically transfers coseismic stress to the upper crust and triggers slip on faults until the weak zone fully relaxes (Kenner and Segall, 2000). Thus, the presence of a pre-existing weak zone remains a key ingredient to the generation of intraplate earthquakes. This hypothesis begs the question, however, of what loaded the weak zone in the first place. One may consider a mechanism whereby external forcing by GIA gradually loads the weak zone since deglaciation, eventually leading to a large earthquake later on that then continues to load the crust locally due to cyclic stress transfer (Brandes et al., 2015). Such a delay in seismicity is also possible considering that intraplate seismic zones tend to stay in a stress shadow for 100s-1000s of years after large events, owing to the difficulty of full stress restoration due to the strength of the ambient crust and low regional strain rates (Stein, 2007; Stein and Liu, 2009).

Lithospheric weak zones in combination with glacial unloading have also been proposed to explain both the magnitude and orientation of perturbations to the observed stress field. Focal mechanism stress inversion shows some aulacogens in eastern North America exhibit rotational deviation from the regional NE-SW maximum horizontal compressive stress (S_{Hmax}) direction (Hurd and Zoback, 2012; Mazzotti and Townend, 2010). In the Central Virginia, Lower St. Lawrence, and Charlevoix Seismic Zones, there is as much as a 30-50° statistically significant clockwise rotation of the seismically derived S_{Hmax} direction relative to the regional borehole derived S_{Hmax} direction (Mazzotti and Townend, 2010), and depth-dependent stress rotations of up to 40-60° are observed in the Charlevoix seismic zone (Verdecchia et al., 2022). It has been argued that the consistency of these rotations across seismic zones separated by 1000s of kilometers requires a common mechanism, which suggests a long-wavelength source of loading like GIA. GIA stresses show a strong spatial coherence over 1000s of kilometers but are typically only on the order of 10s of MPa (Wu and Hasegawa, 1996; Wu et al., 2021). The observed stress rotations, on the other hand, require perturbations at mid-seismogenic depths on the order of at least 160-250 MPa (Mazzotti and Townend, 2010). However, the presence of a low viscosity lithospheric weak zone may amplify GIA stress magnitudes by a factor of 5-10 compared to homogeneous lithosphere (Grollimund and Zoback, 2001; Wu and Mazzotti, 2007) and could produce clockwise rotations of post-glacial rebound stresses in the crust above the weak zone (Wu and Mazzotti, 2007). Inclusion of such weak zones has also yielded better fits to both modeled stress and strain data in the St. Lawrence River Valley (Mazzotti et al., 2005).

We explore the hypothesis that glacial isostatic adjustment promotes intraplate seismicity in eastern North America via perturbation to the intraplate stress field and reactivation of pre-existing faults. We develop high resolution global models of the solid earth response to glacial loading and unloading with CitcomSVE (Zhong et al., 2022), a spherical finite-element viscoelastic GIA code that implements the sea level equation and ice-loading history of ICE-6G (Peltier et al., 2015) for a fully 3D or 1D Earth viscosity structure. The models use a viscosity structure based on the seismically and geologically constrained thermal structure implemented in the mantle flow models with CitcomS (see Chapter 4). Like in the CitcomS models, we include local-scale, low-viscosity lithospheric weak zones at the locations of the geologically mapped aulacogens (Whitmeyer and Karlstrom, 2007) and other tectonically inherited structures. We calculate the stress tensor, with which we compute the S_{Hmax} direction, the deviatoric stress magnitude, and the Coulomb stress on known faults. We compare our results for the present day to stresses of the World Stress Map (Heidbach et al., 2018) and to those obtained from mantle flow models using the same Earth structure (Chapter 4).

5.2 GIA Modeling with CitcomSVE

The two key components of any GIA model are knowledge of global ice-history change, including ice-volume, its extent, and the shape of the ocean, and the rheology of the solid Earth, which governs how the Earth responds to the weight of the changing ice and ocean load. Studies into the viscosity of the Earth's mantle began with Haskell (1935) and continued with investigations into GIA in the early works of Cathles (1975), Peltier (1974), and Farrell and Clark (1976). Since then GIA modeling has evolved to include the effects of sea-level change (Milne and Mitrovica, 1998; Milne et al., 1999), Earth rotation (Wu and Peltier, 1984; Han and Wahr, 1989; Mitrovica et al., 1994; Milne and Mitrovica, 1998; Mitrovica et al., 2001), and 3D earth viscosity structure (Kaufmann et al., 2005; Wang and Wu, 2006; Paulson et al., 2005; A et al., 2013; Wal et al., 2015; Li et al., 2020; Bagge et al., 2021). GIA models can employ a number of different numerical approaches, including the pseudo-spectral approach (Mitrovica and Peltier, 1991; Mitrovica et al., 1994; Wu and Wal, 2003; Mitrovica and Milne, 2003; Kendall et al., 2005; Spada and Stocchi, 2007), finite element methods (Zhong et al., 2003; Paulson et al., 2005; Lund, 2005; Wang and Wu, 2006; Dal Forno et al., 2012; A et al., 2013; Zhong et al., 2022), spectral-finite element methods (Martinec, 2000; Tanaka et al., 2011), and finite volume methods (Latychev et al., 2005). Numerical methods such as finite-elements have the advantage of being able to incorporate fully 3D Earth structure spanning several orders of magnitude of variation in lateral viscosity (Lund, 2005; Zhong et al., 2015). It is ultimately the lateral gradients in viscosity that give rise to gradients in the velocity field that lead to the stress perturbations in the lithosphere in which we are interested (see Chapter 4). Thus, it is essential to utilize fully 3D viscosity structure, rather than compare the stress fields arising from different local 1D viscosity structures.

With respect to glacially induced faulting, most models to date assume a flat-Earth and thus cannot account for the ocean load by means of the sea level equation (Wu and Hasegawa, 1996; Steffen et al., 2021), or they make use of a spectral approach (Wu and Johnston, 2000) that cannot accommodate 3D viscosity. To our knowledge only one previous study on GIA induced seismicity has been published using a spherical finite-element GIA model formulation (Craig et al., 2016; Steffen et al., 2021). Sphericity of the model is important for large diameter loads, such as the Laurentide, especially when considering areas farther from the ice margin, as in the central-eastern United States (Wu and Johnston, 1998), and it has the advantage of incorporating the effect of ocean loading and the distal effects of Fennoscandian and Antarctic glaciations.

We model the impact of GIA on intraplate stress using the fully spherical finite element code CitcomSVE, which models dynamic deformation of a viscoelastic and incompressible planetary mantle in response to surface loading (Zhong et al., 2003; Zhong et al., 2022). CitcomSVE was built from the widely used purely viscous geodynamics finite-element code CitcomS (Zhong et al., 2003; Zhong et al., 2000; Zhong et al., 2008) by implementing viscoelastic deformation within a Lagrangian formulation compatible with either linear or non-linear viscosity (Kang et al., 2022). The code has been extensively benchmarked for time-dependent loading on the surface of a viscoelastic mantle, using both single harmonic loading and the ICE-6G ice-history model (Bellas et al., 2020; A et al., 2013; Paulson et al., 2005; Zhong et al., 2003; Zhong et al., 2022), as well as tidal loading on either an elastic (Zhong et al., 2012) or viscoelastic (Zhong et al., 2022) mantle. By comparing surface loading, tidal loading, and ice loading model predictions to semi-analytic solutions (A et al., 2013; Han and Wahr, 1995; Paulson et al., 2005), the code has demonstrated successful prediction of deformation rates, displacements, and relative sea level changes (Zhong et al., 2022).

CitcomSVE solves the equations for load induced deformation derived from the laws of conservation of mass and momentum and of gravitation for an incompressible self-gravitating, viscoelastic mantle (Maxwell body) overlying an inviscid fluid core (Zhong et al., 2003; Zhong et al., 2022):

$$\nabla \cdot \bar{u} = 0 \tag{5.1}$$

$$\nabla \cdot \bar{\bar{\sigma}} + \rho_0 \nabla \phi - \nabla(\bar{u} \cdot \rho_0 g \hat{r}) - \rho_1^E g + \rho_0 \nabla V_a = 0 \tag{5.2}$$

$$\nabla^2 \phi = -4\pi G \rho_1^E, \tag{5.3}$$

where $\bar{u}$ is the displacement vector (u_r being displacement in the radial direction); ϕ is the perturbation to the gravitational potential due to deformation; V_a is the applied potential, when applicable; $\bar{\bar{\sigma}}$ is the stress tensor; ρ_0 is the unperturbed mantle density; g is the gravitational acceleration; $\rho_1^E = -\bar{u} \cdot \nabla \rho_0$ is the Eulerian density perturbation for an incompressible medium; and G is the gravitational constant. Poisson's equation (Eq. 5.3) states that the density distribution determines the gravitational potential and acceleration. The notion of a self-gravitating Earth arises from the fact that when deforming stresses are applied, movement of masses alters the local gravity and its potential but such that Poisson's equation remains satisfied (Wu et al., 2021). The applied deformation gives rise to strain ε_{ij} and stress σ_{ij} in addition to the perturbed density, all of which must together satisfy conservation of momentum (Eq. 5.2). The terms of this equation, from left-to-right, are the divergence of the stress, the perturbed gravity field (i.e., self-gravity), the advection of the pre-stress, and the buoyancy force from the local perturbation.

Zero-shear force boundary conditions are applied at the surface and core-mantle boundary (CMB) such that both can deform dynamically. With the incompressibility assumption, the three primary sources of mass anomalies are surface topography (i.e., radial displacement), CMB topography, and the surface loads themselves. The surface boundary condition is

$$\sigma_{ij} n_j = -\sigma_0 n_i, \text{ for } r = r_s, \tag{5.4}$$

representing the pressure loads at the surface (σ_0) from GIA as a function of time and space.

With a Maxwell rheology, the total deformation is the sum of the elastic and viscous strains:

$$\varepsilon_{ij} = \varepsilon^e_{ij} + \varepsilon^v_{ij} = \frac{1}{2}\left(\frac{\partial u_i}{\partial x_j} + \frac{\partial u_j}{\partial x_i}\right). \tag{5.5}$$

ε^e_{ij} and $\dot{\varepsilon}^v_{ij}$ are the elastic strain tensor and viscous strain rate tensor, respectively:

$$\varepsilon^e_{ij} = \frac{1}{2\mu}(\sigma_{ij} + P\delta_{ij}) \tag{5.6}$$

$$\dot{\varepsilon}^v_{ij} = \frac{1}{2\eta}(\sigma_{ij} + P\delta_{ij}). \tag{5.7}$$

P is the dynamic pressure, δ_{ij} is the Kronecker delta, μ is the shear modulus, and η is the viscosity. The resulting rheological equation is the sum of the time derivatives of equations 5.6 and 5.7:

$$\sigma_{ij} + \frac{\eta}{\mu}\dot{\sigma}_{ij} = -\left(P + \frac{\eta}{\mu}\dot{P}\right)\delta_{ij} + 2\eta\dot{\varepsilon}_{ij}. \tag{5.8}$$

Because the deformation is time-dependent due to viscoelasticity, the rheological equations are discretized in time via an incremental displacement formulation (Zhong et al., 2003; Zhong et al., 2022) such that the stress tensor at time t includes a pre-stress term accounting for the stresses at the previous timestep:

$$\sigma^n_{ij} = -P^n\delta_{ij} + 2\tilde{\eta}\Delta\varepsilon^n_{ij} + f\tau^{\text{Pre}}_{ij}. \tag{5.9}$$

The pre-stress is the deviatoric stress at timestep $n-1$ ($\tau^{\text{pre}}_{ij} = \tau^{n-1}_{ij} = \sigma^{n-1}_{ij} + P^{n-1}\delta_{ij}$). $\tilde{\eta} = \eta/(\alpha + \Delta t)$, $f = (\alpha - \Delta t/2)/(\alpha + \Delta t/2)$, and $\alpha = \eta/\mu$ is the Maxwell time. It is this advection of the pre-stress term in Eq. 5.2 that provides the restoring force of isostasy in the fluid that enables post-glacial rebound (Wu, 1992; Wu et al., 2021). The stress tensor at a given timestep can in theory be computed from Equation 5.9 after solving for the incremental displacement and effective pressure. However, to avoid needing to calculate dynamic pressure from the effective pressure, only the deviatoric stress τ_{ij} is computed (Equation 5.10).

$$\tau^n_{ij} = \sigma^n_{ij} + P^n\delta_{ij} = 2\tilde{\eta}\Delta\varepsilon^n_{ij} + f\tau^{\text{pre}}_{ij} \tag{5.10}$$

To accurately model GIA, it is important to account for mass exchange and mass redistribution between continental ice and water in the oceans. As such, CitcomSVE fully implements the sea level equation (Eq. 5.11) (Farrell and Clark, 1976), which gives the change in the height of the ocean load since the onset of glaciation (L_0):

$$L_0(\theta, \phi, t) = [N(\theta, \phi, t) - U(\theta, \phi, t) + c(t)]O(\theta, \phi, t) \tag{5.11}$$

$$c(t) = \frac{1}{A_0}\left[- \frac{M_{\text{ice}}(t)}{\rho_w} - \int (N - U)OdS\right] \tag{5.12}$$

The ocean load is a function of the GIA-related geoid anomaly (N) and radial displacement (U), an ocean function ($O(\theta, \phi, t)$) that describes the distribution of ocean versus land (1 for ocean and 0 for land), and the barystatic sea level ($c(t)$, Eq. 5.12), which is a function of the mass of the ice (M_{ice}), the density of water (ρ_w), and the geoid anomalies and radial displacements integrated over the area of the oceans (A_0). The mass of the ice is calculated for a given ice-history model. While the ocean load is dependent on the incremental displacement and the geoid, it also directly impacts them through the equation of motion and Poisson's equation. CitcomSVE handles this interdependence through an iterative scheme applied at every time-step, which solves for displacements, gravitational potential, and the sea level height changes self-consistently. With self-gravitation, the code also accounts for the contribution from the gravitational attraction of seawater to the mass of the ice (Austermann and Mitrovica, 2015; Zhong et al., 2008).

CitcomSVE takes either a 1D or 3D viscosity structure as input, along with an incrementally defined ice loading history (Eq. 5.9). Poisson's equation for the gravitational potential anomaly is solved in the spherical harmonic domain, while displacements are solved on the finite element grid. Upon solving the GIA problem, the program outputs cumulative topography; incremental radial, latitudinal, and longitudinal displacements; and total and incremental gravitational potential at the surface nodal points of the finite element grid; it outputs the second invariant of deviatoric stress and the viscosity for every nodal point in the 3D domain. We added the ability to output all six components of the deviatoric stress tensor for use in our stress analysis.

The ability to impose 3D viscosity structure in our GIA models is key. Glacial rebound at the margins of formerly glaciated areas tends to be sensitive to variations in lithospheric thickness (Zhong et al., 2003; Latychev et al., 2005), suggesting that the effect of GIA on stress perturbations may be enhanced when coupled with lateral variations in the depth of the lithosphere-asthenosphere boundary (LAB) and lithospheric viscosity. Wu and Mazzotti (2007) have also shown that narrow ductile zones cutting through the full lithosphere have a larger effect on GIA induced deformation than a single mantle weak layer alone. As with our mantle flow models, when assessing the impact of GIA on the intraplate stress field, we likewise consider lateral variations in lithospheric thickness via 3D viscosity structure and how weak-zones may locally amplify stress perturbations (Mazzotti and Townend, 2010; Wu and Mazzotti, 2007). We employ the same geologic and geophysical constraints on the weak-zones as we do using CitcomS (Section 5.3.3).

5.3 Input Ice-Load and Viscosity Structures

5.3.1 Ice Loading History

Several ice-models exist that are often employed in GIA modeling (Peltier et al., 2015; Simon et al., 2016; Lambeck et al., 2017; Simon and Riva, 2020), the most widely used of which and that which we use in our models is the ICE-6G ice history model of Peltier et al. (2015). GIA models essentially seek to solve the Sea Level Equation (Farrell and Clark, 1976; Mitrovica and Milne, 2003), which gives the variations in sea level with respect to the continuously deforming solid Earth through application of glacial isostatic adjustment, given an assumed history of land ice thickness variation and a radial viscoelastic model (Stuhne and Peltier, 2015). ICE-6G solves an inverse problem that predicts the land ice thickness variations and radial viscosity structure based on observations of relative sea level histories and geodetic measurements of the present-day vertical and horizontal motion (Peltier et al., 2015; Stuhne and Peltier, 2015). In ICE-6G, model predictions of the time rate of change of the gravitational field are independently corroborated with time–dependent gravity from GRACE (Peltier et al., 2015). ICE-6G is perhaps the most widely used glaciation model for North America, and CitcomSVE is configured and benchmarked to take the ICE-6G ice thickness history as input (Zhong et al., 2022). However, because the VM5a rheological profile (Peltier et al., 2015) and the predictions of the ICE-6G model are explicitly coupled, one must be careful to maintain reasonable consistency between assumptions on viscosity used in the ice model and in the geodynamic models.

5.3.2 Seismically and Geologically Constrained Thermal Structure

Temperature dependent viscosity is computed within the CitcomS framework of our mantle flow calculations. Within those models, lithospheric thermal structure is constructed from a composite of continental and oceanic models, where for the continents we use the Artemieva (2006) TC1 thermal model, and in the oceans, we use the global seafloor age grid of Seton et al. (2020) and the plate cooling model to calculate oceanic lithospheric temperature (Chapter 4, Section 4.4.2). Mantle temperatures are determined by means of a depth-dependent seismic velocity to temperature scaling of the Lu et al. (2019) global P- and S- wave seismic tomography model that incorporates the effect of anelasticity and mineralogical composition (Chapter 4, Section 4.4.2 and Appendix C.1). Viscosities are computed directly from these temperature fields within CitcomS according to Eq. 4.8 and where appropriate are multiplied by a pre-factor depending on their radius or location within the lithosphere (e.g., for applying low viscosity plate-boundaries or intraplate weak zones). The radial average of the viscosity used in CitcomS, with its respective layer-dependent pre-factors, is shown in Figure 4.5 along with other viscosity profiles from the literature used in or derived from GIA analysis, such as VM5a, for comparison. These thermally derived 3D viscosity structures are then used directly as input to CitcomSVE.

5.3.3 Intraplate weak zones

We emplace low viscosity weak zones in the crust and/or lithosphere at the locations of the geologically mapped aulacogens or seismically inferred low velocity zones of weakness. Weak zones are placed at an appropriate depth for each seismic zone, based on local seismic and geologic evidence, the details of which are given in Section 4.2. Based on the depth of low velocity zones imaged in the upper mantle beneath the New Madrid Seismic Zone (Thomas and Powell, 2017; Chen et al., 2016; Nyamwandha et al., 2016; Chen et al., 2014), we emplace a lithospheric weak zone between 70 and 150 km along the extent of the Reelfoot Rift, as mapped in Figure 4.1a. Based on both seismic (Thomas and Powell, 2017; Powell et al., 2014; Wagner et al., 2012; Long et al., 2016) and magnetotelluric imaging (Murphy and Egbert, 2017; Murphy et al., 2019), in the Eastern Tennessee Seismic Zone we emplace a 50-100 km wide weak zone between 15 and 50 km depth along the NY-AL lineament, which was an ancient sinistral transform fault during the formation of supercontinent Rodinia and which exhibits characteristics of weak sheared crust (Thomas and Powell, 2017; Chen et al., 2016). Likewise, based on magnetotelluric (Evans et al., 2019; Long et al., 2020) and seismic imaging (Schmandt and Lin, 2014), farther to the north along the Rome Trough, we emplace an approximately 500 km wide weak zone between 80-200 km depth. For the Canadian seismic zones, we emplace a weak zone at the base of the crust between 25 and 75 km depth along the entirety of the LSLRS and its associated rift-arms, consistent with the presence of weak ancient rift faults and possible weakening due to the passage of the Great Meteor Hotspot through the WQSZ (Sykes, 1978; Ma and Eaton, 2007) and from the Charlevoix Impact Crater (Baird et al., 2010; Lamontagne and Brouillette, 2022) in the CXSZ. While the viscosities of the intraplate weak zones likely differ based on their different geology and conditions of formation, we impose uniform viscosity reductions for all weak zones for simplicity. We also consider a case where all weak zones are considered to be shallow and sub-crustal and placed at 25-75 km depth.

5.4 Calculation of S_{Hmax} and Coulomb Stress

Several approaches exist for determining whether GIA induced stresses may reactivate faults. These include the commonly used *fault stability margin* (FSM) (Wu and Hasegawa, 1996; Wu and Johnston, 2000) and the *Coulomb failure stress* (CFS) (Steffen et al., 2020; Steffen et al., 2021). As in our mantle flow models, we use the CFS, the advantage of which compared to the FSM is its dependence on the shear and normal stresses, which are functions of the strike and dip of a fault. This allows for the use of realistic fault geometries, either optimally or non-optimally oriented, within a three-dimensional stress setting (Steffen et al., 2021; Steffen et al., 2014a; Steffen et al., 2014c; Steffen et al., 2014b). Within our GIA models, all faults are *virtual faults*, meaning no physical fault surface is included in the model and the fault's presence therefore does not affect the stress distribution (Wu et al., 2021). Rather, the stress tensors calculated by our model are applied to a set of faults after the fact to determine their influence on the behavior of those faults.

The total stress acting on these faults is composed of the GIA induced stresses, the tectonic background stress, and the overburden stress. Thus, before analyzing fault stability, we have to add back both the tectonic background stress and the lithostatic pressure, as well as the weight of the ice that is present for any given timestep. Lithostatic pressure is computed as in Appendix C.3 using an average crustal density of 2700 $\mathrm{kg/m^3}$ and a pore fluid factor of 0.6. Pore fluid pressure is not well studied on glacial timescales (Steffen et al., 2014a) and is thus often neglected in analyses of GIA induced CFS. While there is evidence to suggest pore fluid pressure changes over the course of a glacial cycle (Grollimund and Zoback, 2000; Zhang et al., 2018), for consistency with our mantle flow models, we assume it to be constant and use the same values as in the lithostatic pressures applied to the CitcomS models. Similarly, for the tectonic background stress, which is assumed to be constant over a glacial cycle, we use the stress field predicted from the mantle flow models for the corresponding viscosity fields used in our GIA models. Thus, our tectonic background stress includes both a tectonic and dynamic effect and the modeled GIA stresses can be considered a perturbation to this stress field.

5.5 Results

The set of models testing the influence of GIA on the North American stress field parallel those testing the influence of Farallon slab loading (Chapter 4) and use the same viscosity structures. The first model (GIA-A0) uses the 3D viscosity structure of model A0 in Chapter 4, which does not have any weak zones; the second (GIA-A1) uses the viscosity structure of model A1 in Chapter 4, which has weak zones placed at different depths depending on geophysical constraints for their respective locations; the third (GIA-A1b) uses the viscosity structure of model A1b in Chapter 4, which has weak zones placed at the same depth between 25-75 km; and the fourth (GIA-1D-3Davg) and fifth (GIA-1D-VM5a) models use a 1D viscosity structure from either the radial mean of the 3D viscosity structure of model GIA-A0 or VM5a (Peltier et al., 2015), respectively. Like in the mantle flow models, in all cases with weak zones, weak zone viscosities are a factor of 1000 times less viscous than the surrounding lithosphere.

S_{Hmax} orientations induced solely by GIA stress are shown in Figure 5.1 a,b, which in comparison to Figure 5.1 c,d reveal the importance of including tectonic background stress. The S_{Hmax} directions in eastern North America exhibit a rotational pattern around the margin of the former Laurentide ice-sheet, with near E-W orientations in Texas and the central-eastern U.S. near New Madrid transitioning to N-NE orientations in southeast Canada. The inclusion of weak zones at the locations of the aulacogens or other structures leads to small improvements in the fit of the S_{Hmax} direction in the central eastern U.S. but a reduction in the fit throughout much of the Charlevoix and Lower Saint Lawrence Seismic Zones (Figure 5.1 b). The addition of the tectonic background stress leads to an improvement in the fit throughout most of eastern North America, by as much as 20° in some places. The tectonic stress dominates such that the overall fit of the regional stress field is largely the same as that predicted through mantle flow. But even without the tectonic background stress, the majority of misfits across eastern North American are still less than $\sim 28°$.

There is a progressively counterclockwise stress rotation due to GIA moving northeastwards across eastern North America (Figure 5.2). This gradation is even stronger

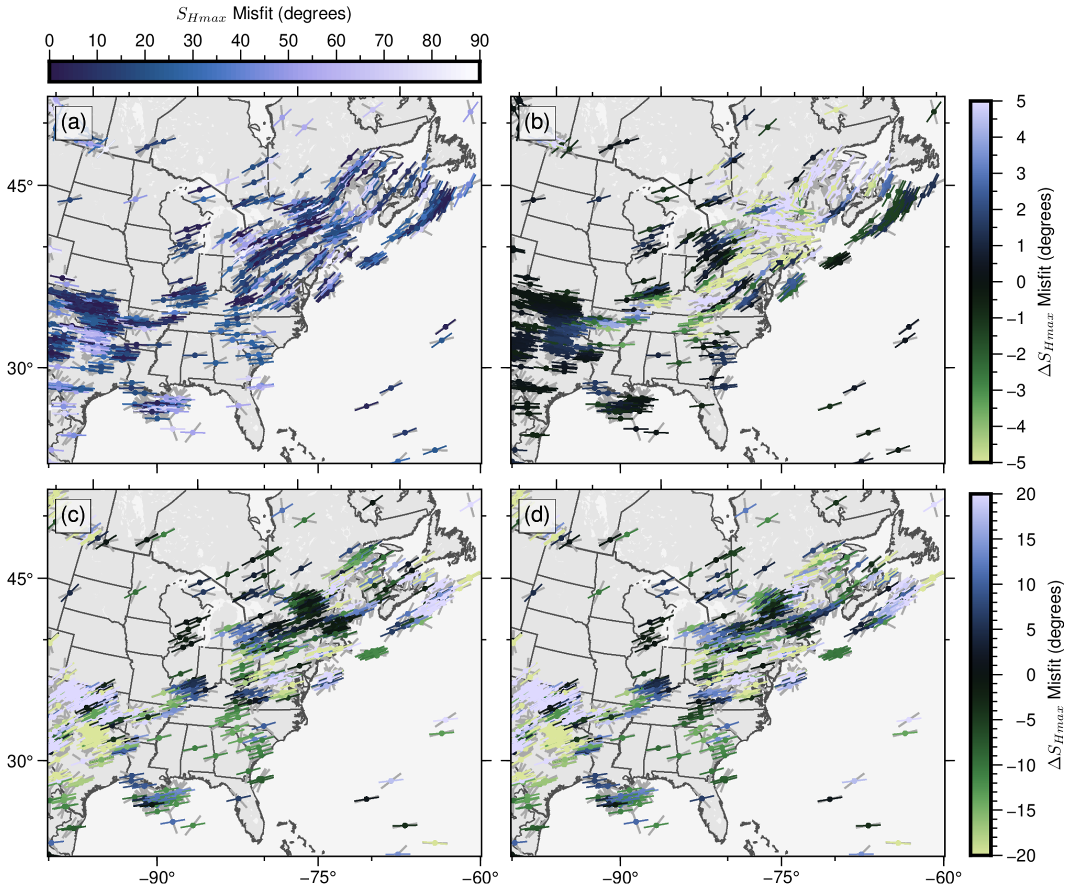

Figure 5.1: Changes in misfit between observed and modeled S_{Hmax} for different GIA models using different viscosity input. a) S_{Hmax} orientations induced by GIA only (i.e., no tectonic background stress) from model GIA-A0 colored by misfit (|modeled - observed|) to the observed stress orientations from the WSM of Heidbach et al. (2018) (light gray lines). b) Difference in the S_{Hmax} misfit between model GIA-A1 and model GIA-A0 (i.e., between models with vs. without weak zones) for GIA only. c) Difference in S_{Hmax} misfit between model GIA-A0 + tectonic background stress and model GIA-A0 with GIA only. d) Difference in S_{Hmax} misfit between model GIA-A1 + tectonic background stress and model GIA-A0 with GIA only.

when assuming a 1D viscosity profile (Figure 5.2 c). In this case, the rotations induced by GIA are mostly dependent on the ice-loading history, as there are no lateral viscosity variations to introduce strength contrasts in the lithosphere. The inclusion of weak zones at either variable depths (Figure 5.2 b) or the constant 25-75 km (Figure 5.2 c) results in subtle clockwise stress rotations in New Madrid and Eastern Tennessee, as well as parts of the Northern Appalachians and Western Quebec, while even stronger counter-clockwise rotations are observed in the LSLSZ. However, the rotations induced by GIA, with or without weak zones, are very small and at most within ±5°. Thus, the spatial variations in stress orientations caused by GIA at the present day are insignificant compared to the observed variation of S_{Hmax} in the WSM, which can often vary by as much as 25° within a single seismic zone. Nevertheless, the subtle transition from clockwise to counterclockwise rotation across eastern North American predicted by the GIA stresses alone produces a style of faulting at the present day that mirrors that observed from focal mechanism stress inversion, transitioning from predominantly strike-slip and normal faulting in the central-eastern U.S. to thrust faulting in southeastern Canada, as measured by the $A\phi$ parameter (Hurd and Zoback, 2012).

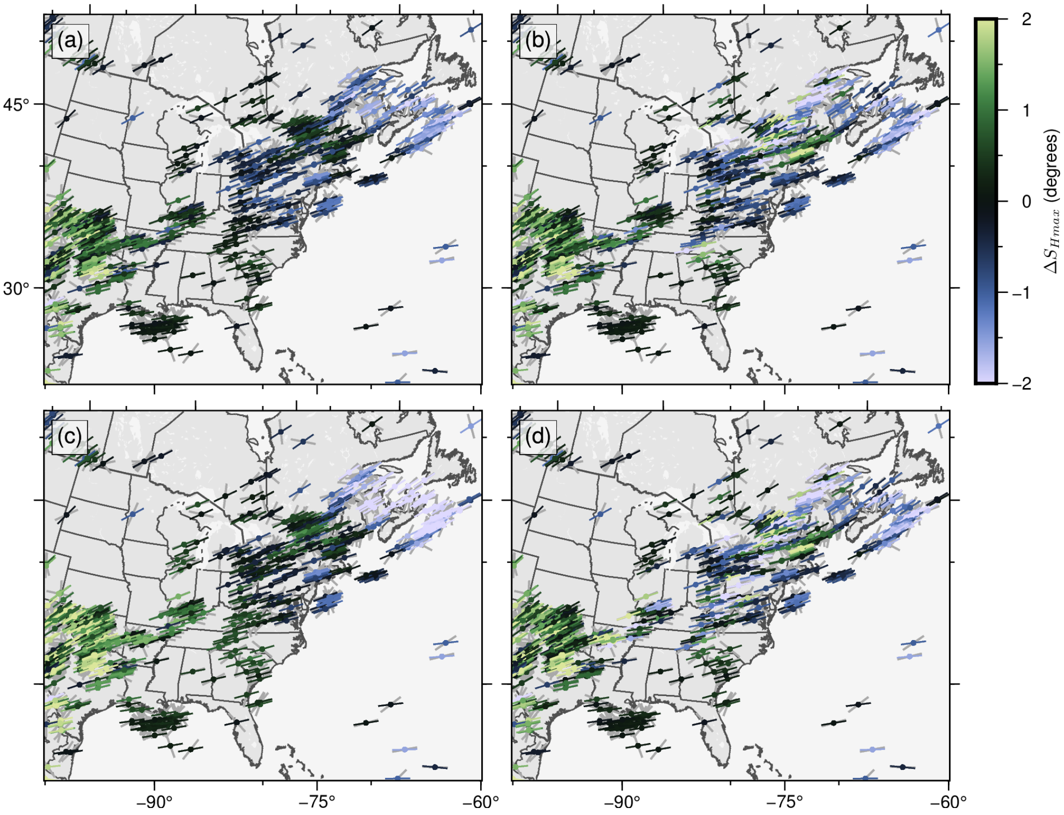

Figure 5.2: Rotation in S_{Hmax} induced by GIA for different viscosity inputs relative to tectonic background stress. a) Rotation in S_{Hmax} orientation induced by GIA using 3D viscosity with no weak zones present (i.e., between model GIA-A0 with tectonic background stress and model A0). Observed stress orientations from the WSM of Heidbach et al. (2018) are shown in the background as light gray lines. b) Rotation in S_{Hmax} induced by GIA in the presence of weak zones (i.e., between model GIA-A1 with tectonic background stress and model A1). c) Rotation in S_{Hmax} induced by GIA assuming a 1D viscosity structure (i.e., between model GIA-1D-3Davg with tectonic background stress and model A0). d) Rotation in S_{Hmax} induced by GIA using 3D viscosity with weak zones all at depths of 25-75 km (i.e., between model GIA-A1b with tectonic background stress and model GIA-A1b.

The magnitudes of the stress perturbations associated with these rotations range from 5-15 MPa, with the highest deviatoric stress magnitudes centered over Hudson Bay, the site of the fastest present day uplift. Two pockets of high stress are situated over northern Virginia and Nova Scotia, separated by a region of little to almost no GIA induced deviatoric stress (Figure 5.3 c). The effect of 3D viscosity versus

1D viscosity is pronounced, however. Lithospheric variability introduces elevated deviatoric stress in Eastern Tennessee, western New York and Pennsylvania, New Hampshire and Vermont, and over the entirety of the LSLR, which exhibits some of the largest stress perturbations (Figure 5.3 e). Within GIA models with 3D viscosity, weak zones introduce an additional stress perturbation of only 2-5 MPa, with the strongest effects on stress magnitude concentrated closer to the former ice-margin. The highest stress perturbations are located along the northwest margin of the LSLR, specifically along the boundary of the weak zone, rather than immediately above the weak zone (Figure 5.3 d,f), which is also where ancient rift-bounding faults are likely to be present. Interestingly, the presence of weak zones actually results in a stress drop in the vicinity of the most seismically active part of the Western Quebec Seismic Zone, though its north-westernmost end does exhibit higher stresses. Stress perturbations in New Madrid and Eastern Tennessee are only on the order of 2 MPa, though are slightly higher in New Madrid when the weak zone is placed at 25-75 km rather than deeper in the mantle lithosphere. Strong peaks in stresses are also present at the PA-NA plate boundary (Figure 5.3 a) due to the inclusion of low viscosity plate boundary weak zones.

While small, the stress rotations and magnitude perturbations that are invoked by GIA still have implications for fault stability in eastern North America. As in Chapter 4, the potential for fault reactivation in the New Madrid, Western Quebec, and Lower Saint Lawrence and Charlevoix Seismic Zones is explored by means of the Coulomb failure stress (CFS) in Figures 5.4, 5.5, and 5.6, respectively. Instead of the absolute CFS, we plot the change in CFS between the GIA models and their corresponding tectonic and dynamic background stress as calculated with CitcomS to highlight the degree to which GIA shifts faults closer to or farther from failure. In this case, a positive change in Coulomb failure stress, like a positive CFS, means a more unstable fault or at least a move towards instability, and a negative change means more stable or a move towards stability. Mohr circles are still plotted at the same fault locations used in Chapter 4 using the full shear and normal stresses resolved on that fault.

In the NMSZ, the pattern of fault stability that GIA affects is opposite to that predicted from the mantle flow models shows in Figure 4.13. The addition of GIA shifts all SW-NE oriented faults within the NMSZ closer to failure. Those oriented NW-SE, including the Reelfoot Fault, actually move farther from failure, in contrast to the results of the mantle flow models, in which the Reelfoot Fault

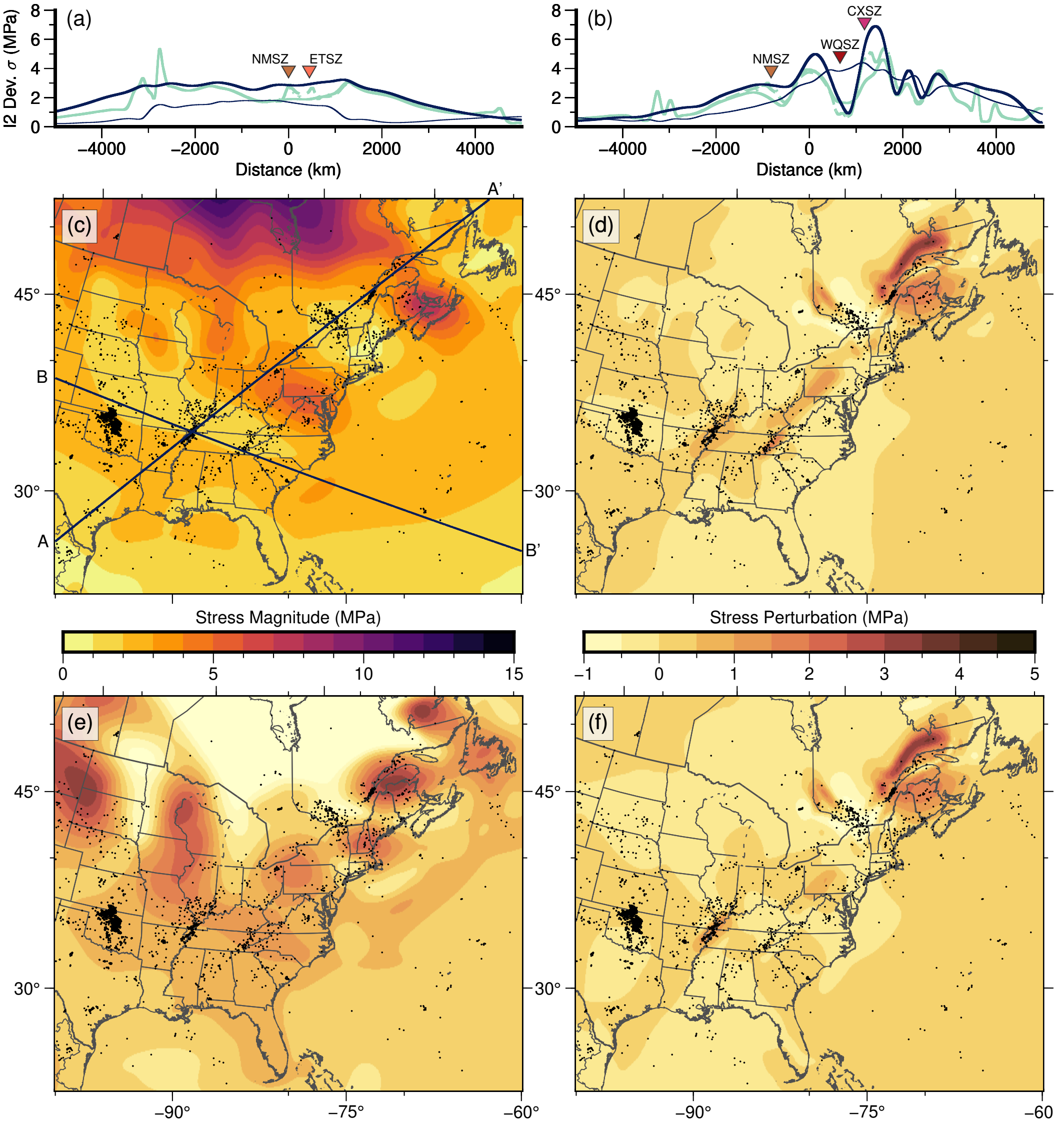

Figure 5.3: GIA induced stress magnitudes. a) Profiles of the second invariant of deviatoric stress from GIA only along line B-B' for 3D viscosity input (light green lines) with no weak zones (solid line), weak zones at different depths (dashed line), weak zones at 25-75 km depth (dashed-dotted line), and 1D viscosity input (dark blue lines) from the radial average of model GIA-A0 (thick line) and from VM5a (thin line). New Madrid Seismic Zone (NMSZ) and Eastern Tennessee Seismic Zone (ETSZ) are labeled accordingly. Profile positions are labeled in panel (c); same transect as in Figures 4.4 and 4.11 in Chapter 4. Note: length of the profile is longer than map area (see Chapter 4, Figure 4.4 orthographic panel). b) Profiles of stress magnitude from GIA along line A-A'. Lines as in (a). New Madrid Seismic Zones (NMSZ), Western Quebec Seismic Zone (WQSZ) and Charlevoix Seismic Zone (CXSZ) are labeled accordingly. c) Map of GIA induced deviatoric stress magnitude for model GIA-A0 (3D viscosity but no weak zones). d) Perturbation to the stress in (c) by including weak zones (i.e., difference between models GIA-A1 and GIA-A0). d) Stress perturbation induced by the inclusion of 3D viscosity (i.e., difference between models GIA-A0 and GIA-1D-3Davg). f) Perturbation to the stress in (c) by placing all weak zones at 25-75 km depth (i.e., difference between models GIA-A1b and GIA-A0).

was the only fault to exhibit positive, and therefore unstable, CFS conditions. This flip in the observed pattern is a direct result of the slight clockwise rotation of the S_{Hmax} direction in the NMSZ towards a more E-W direction under the influence of GIA. Such an orientation places the region's strike-slip faults in a more optimal position to be reactivated. Changes in CFS brought about by GIA are subtle, at most about 5 MPa – not enough to fully stabilize or destabilize a fault in terms of the total Coulomb failure stress, as distances between the resolved shear stress and the failure criterion can still be upwards of ±100 MPa – but the changes do highlight the patterns of relative fault stability promoted by GIA that under different tectonic background stress regimes may bring a fault closer to failure. Changes in CFS are greatest overall in the case of shallower weak zones (Figure 5.4 c), and changes in CFS are both the least pronounced and the most stabilizing in the case of 1D GIA (Figure 5.4 d).

The changes in CFS are more variable in the Western Quebec Seismic Zone, which only exhibits higher stress perturbations towards its northwest end. In the case of 3D GIA without weak zones, GIA stresses lead to an increase in CFS by 0.5 to 1.5 MPa on faults that already breach the instability regime due to loading from the Farallon slab (Figure 4.14 a). Small changes (~ 0.5 MPa) are observed on other WQSZ faults, but only those in the western half come closer to failure. The inclusion of shallow weak zones results in positive changes in CFS, upwards of 3-4 MPa on most faults in the western half, while those in the eastern half move towards stability. The 1D GIA model produces little to no change in the CFS on WQSZ faults, highlighting the role of lateral heterogeneities in governing the stress changes within this seismic zone rather than the ice history alone.

However, within the LSLSZ and CXSZ, even the 1D GIA model leads to notable increases in Coulomb failure stress by as much as 5 MPa (Figure 5.6 d). The lithosphere is thinner in the 1D models, and without lateral variability in the LAB depth, there is no thick craton under North America. Thus, for locations closer to the craton, such as the LSLR, the difference in deformation in response to the ice-load between the 3D and 1D cases will be enhanced, with the 1D model promoting a stronger response. Similar CFS changes are observed in the CXSZ for 3D GIA models with weak zones (Figure 5.6 b,c), which bring almost the entirety of the LSLRS faults closer to failure. The effects, however, are most pronounced specifically within the CXSZ rather than the Montreal Seismic Zone farther to the southwest, consistent with the concentration of seismicity in this part of the LSLRS

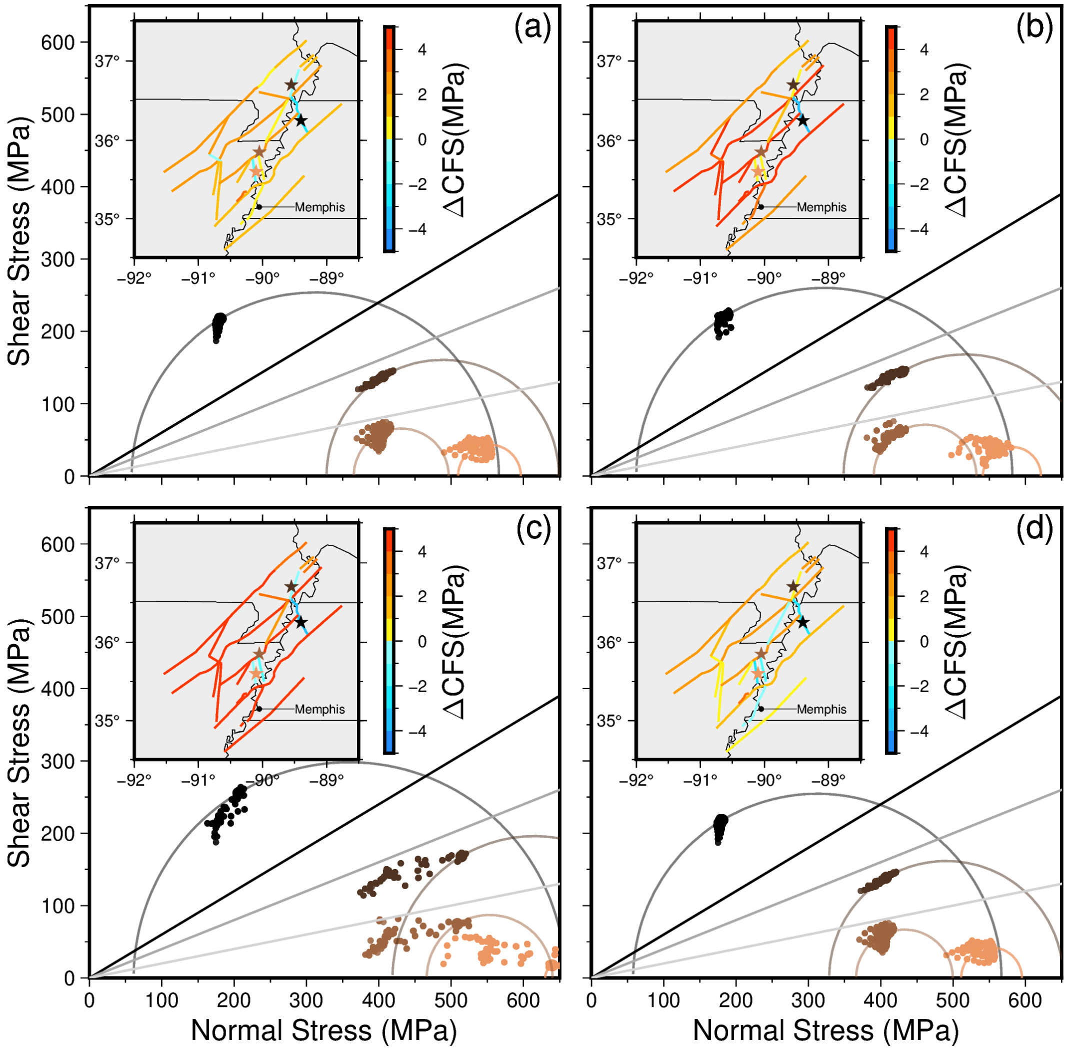

Figure 5.4: Mohr circles (main plot) and change in Coulomb failure stress (map inset) for faults in the NMSZ between models with GIA and the corresponding models without GIA presented in Chapter 4, calculated using $\mu = 0.6$. Fault locations from Thompson et al. (2020). Fault strike and dip information for the Axial Fault (strike=46°, dip=90°), the New Madrid North Fault (strike=29°, dip=72°), the Risco Fault (strike=92°, dip=82°), and the North Reelfoot Fault (strike=167°, dip=30°) are from Csontos and Van Arsdale (2008). Faults with unknown dip are assumed to have a dip of 90°. Mohr circles are drawn for New Madrid faults at the locations of the stars on the map using the fault's strike and dip and the stress tensor at that location. Star colors correspond to Mohr circle colors. Star locations for the three northernmost stars correspond to the most likely epicenters of the 1811-1812 earthquake sequence (Delano et al., 2021). The cloud of points on each Mohr circle represent the shear vs. normal stress for all possible stress tensors in the inset region given that fault's geometry. Black straight line is the Mohr-Coulomb failure criterion for $\mu = 0.6$; gray line is for $\mu = 0.4$; and light-gray line is for $\mu = 0.2$. (a) Results from model GIA-A0 (no weak zones). (b) Results from model GIA-A1 (weak zones at variable depths). (c) Results from model GIA-A1b (weak zones between 25-75 km depth). (d) Results from model GIA-1D-3Davg (radial viscosity, no weak zones).

compared to others. Again, while the changes in CFS are small relative to the absolute CFS plotted in Figure 4.15, for the case of the LSLRS, changes are large

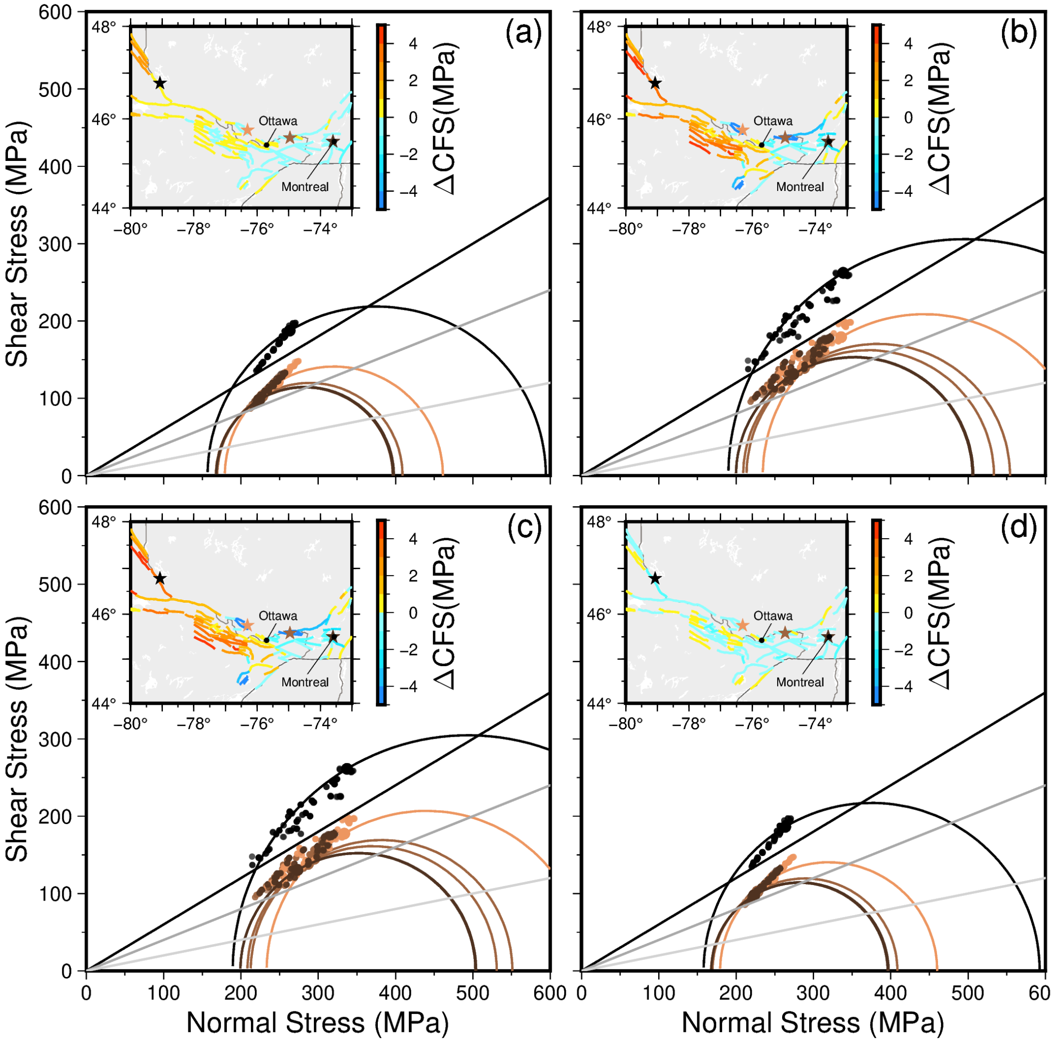

Figure 5.5: Mohr circles (main plot) and change in Coulomb failure stress (map inset) for faults in the WQSZ between models with GIA and the corresponding models without GIA presented in Chapter 4, calculated using $\mu = 0.6$. Fault locations from Rimando and Peace (2021) and Lamontagne et al. (2020). Fault strikes approximated using the best fitting great circle through the lineation. Unless otherwise specified, fault dips were assumed to be 56° (Bent et al., 2003; Rimando and Peace, 2021). Dip of the fault associated with the Timiskaming 1935 earthquake (black star) and nearby faults are from Bent (1996) (strike=146°, dip=45°). Mohr circles are drawn for four faults, using the stress tensor at the location of the corresponding star on the map: The Timiskaming fault of the M 6.1 1935 earthquake, the Rapide-du-Cheval Blanc Fault near the epicenter of the M 6.3 1732 Montreal earthquake, the Lachute Fault (NE of Ottawa), and the Coulonge Fault (NW of Ottawa). Earthquake locations from Bent (2022) and Bent et al. (2003). Star colors correspond to Mohr circle colors. The cloud of points on each Mohr circle represent all possible stress tensors in the inset region given that fault's geometry. Black straight line is the Mohr-Coulomb failure criterion for $\mu = 0.6$; gray line is for $\mu = 0.4$; and light-gray line is for $\mu = 0.2$. (a) Results from model GIA-A0 (no weak zones). (b) Results from model GIA-A1 (weak zones at variable depths). (c) Results from model GIA-A1b (weak zones between 25-75 km depth). (d) Results from model GIA-1D-3Davg (radial viscosity, no weak zones).

enough on some faults that coupled with even a very small reduction in the fault friction, faults that were stable in the case of only the tectonic and mantle flow induced stress would become unstable.

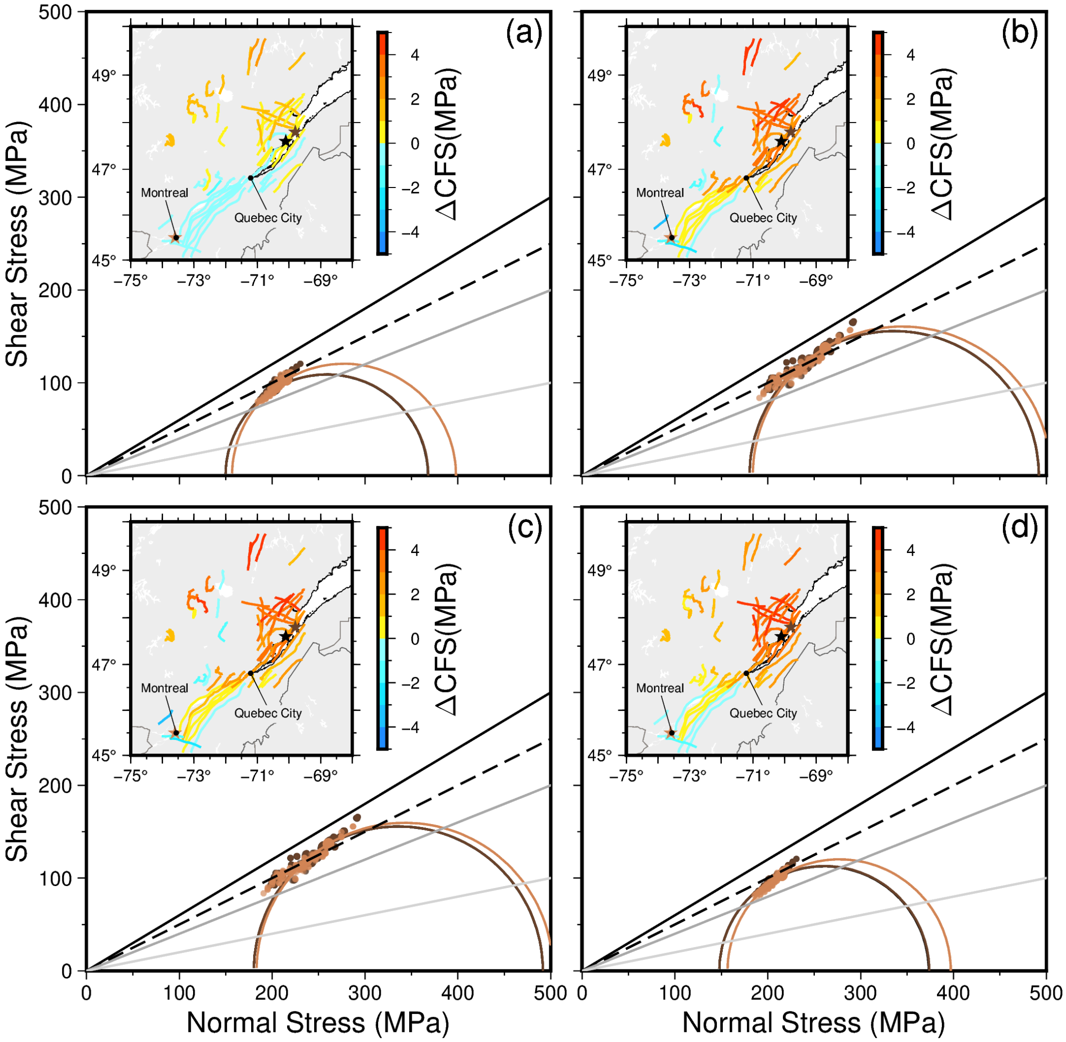

Figure 5.6: Mohr circles (main plot) and change in Coulomb failure stress (map inset) for faults in the LSLRS, including the CXSZ, between models with GIA and those without presented in Chapter 4, calculated using $\mu = 0.6$. Fault strikes approximated for each fault location using the best fitting great circle through the lineation. Fault dips assumed to be 53°, consistent with the values of steeply dipping rift bounding normal faults for the LSLRS as reported by Bent et al. (2003) and Bent (1992). Mohr circles are drawn for the three faults closest to the epicenters of the 1663 M 7.0 and 1925 M 6.2 Charlevoix earthquakes and the M 6.3 1732 Montreal earthquake, using the fault's strike and dip and the stress tensor at the location of the corresponding star on the map. Star colors correspond to Mohr circle colors. Earthquake locations from Bent (2022). The cloud of points on each Mohr circle represent the shear vs. normal stress for all possible stress tensors in the inset region given that fault's geometry. Black straight line is the Mohr-Coulomb failure criterion for $\mu = 0.6$; gray line for $\mu = 0.4$; and light-gray line is for $\mu = 0.2$. (a) Results from model GIA-A0 (no weak zones). (b) Results from model GIA-A1 (weak zones at variable depths). (c) Results from model GIA-A1b (weak zones between 25-75 km depth). (d) Results from model GIA-1D-3Davg (radial viscosity, no weak zones).

5.6 Discussion

While glacially induced faulting is commonly investigated by means of the CFS or FSM, few previous studies have explicitly studied S_{Hmax} orientations resulting from GIA or the CFS resolved onto known faults, rather than assuming optimally oriented faults. The circular pattern of S_{Hmax} orientations predicted by GIA stresses alone (Figure 5.1) is similar to that predicted by Wu (1997) when using a lower mantle viscosity of either 1e22 Pa s or of 1.6e21 Pa s in combination with a reduced upper mantle viscosity. These values are on par with the lower mantle viscosities used in our models. With this pattern, stresses predicted only from GIA do not adequately reproduce the NE-SW uniformity of the eastern North American stress field. When the tectonic background stress, as computed from model A0 (see Chapter 4), is added to the GIA stress, the stress field strongly resembles that predicted by the mantle flow models because the strength of the background stress dominates the stress orientations relative to the GIA induced stresses.

The significance of the tectonic background stress magnitude is unsurprising in light of previous GIA stress analyses, which find that if the tectonic differential stress magnitude is larger than 10 MPa, the temporal stress rotations induced by GIA are quite small, typically less than 10° (Wu, 1997). The tectonic background stress obtained from our mantle flow models is much larger than 10 MPa, and as such dominates the GIA stress field. Wu (1997) argues that in order for GIA to successfully explain the uniformity of the contemporary stress field and the inferred large stress rotations in Canada since post-glacial times, tectonic stress must be in the range of 4-10 MPa. However, the tectonic stress field itself can also explain the uniformity of the observed stress field. In either case, inclusion of tectonic background stress is necessary to accurately calculate the potential for fault reactivation via the Coulomb failure stress. While the magnitude of the tectonic background stress is uncertain and debatable, tectonic stress magnitudes tend to have little effect on the pattern of fault instability so long as they are larger than 20 MPa (Wu and Hasegawa, 1996).

At present day, GIA stresses induced by the former Laurentide deglaciation in the presence of 3D viscosity variations exert a relatively minor influence on stress magnitudes and orientations in eastern North America, relative to the tectonic background stress field. However, the subtle stress rotations within some seismic zones do bring some faults closer to failure by upwards of 5 MPa. Clockwise stress rotations in the central-eastern U.S. heighten stresses on unfavorably oriented strike-slip faults while reducing the likelihood of failure on favorably oriented thrust faults. Slight counter-clockwise rotations of the S_{Hmax} direction in the LSLRS on the other hand help promote higher Coulomb failure stresses on faults in the CXSZ. However, while such stress orientations would increase the likelihood of seismicity in these areas, they do have higher misfits compared to the observed S_{Hmax} direction, in some places by as much as the maximum of 90°. The counterclockwise rotations of GIA stresses observed above weak zones in eastern Canada are also contrary to suggestions from other authors that GIA may be responsible for the clockwise stress rotations observed in the Canadian seismic zones (Mazzotti and Townend, 2010; Verdecchia et al., 2022). Only with the inclusion of the tectonic background stress are clockwise stress rotations observed over all weak zones, an effect of the mantle loading, as demonstrated in Chapter 4, rather than the GIA.

The magnitudes of the GIA stress perturbations correlate with both the geometry of the former ice sheet and the lateral heterogeneities in the lithosphere. Use of 3D viscosity structure causes higher stresses localized over parts of Pennsylvania and Northern Virginia and over New Hampshire and Vermont (Figure 5.3 e). These two stress highs, particularly the northeastern one, correlate with the Central Appalachian Anomaly (CAA) and the Northern Appalachian Anomaly, respectively, as identified in seismic tomography around 200 km depth (Schmandt and Lin, 2014). These low velocity anomalies translate to higher temperatures and therefore lower viscosities that excite higher stresses under loading and unloading from GIA. The higher stresses in the vicinity of the Mid-Continent Rift, on the other hand, are likely associated with the Lake-Michigan, Saginaw, and Huron-Erie Ice Lobes that protruded from the southern margin of the Laurentide Ice Sheet between ~17 and 15 ka (Dalton et al., 2020).

While the ICE-6G model is widely used within the GIA community, care must be taken when interpreting the results of models using ICE-6G and different viscosity structures. The lateral ice extent in the ICE-6G model is primarily constrained by geologic data delineating the location of the ice-margin at different times; what the glaciological evidence cannot tell us on its own, however, is the thickness of the ice over the course of the glacial cycle. The ice-thickness (e.g., the magnitude of the ice-load) in combination with the viscosity of the Earth determines how much the Earth's surface will deflect in response to that load, so the ice-thickness can be determined from how much the Earth has deformed and how much rebound remains at the centers of the former ice-sheet. This is the basis of the classical Haskell constraint (Haskell, 1935), by which we know the viscosity of the upper mantle. The ICE-6G model is built by varying the ice thickness with spatial constraints from glaciology and varying the radial viscosity structure to arrive at a combination of the two that best reproduces the present day uplift rates and gravity signatures of the formerly glaciated regions. This means that the ice-thickness history that we use is intrinsically tied to the viscosity structure used to derive it; deviations from that viscosity structure are not calibrated to this ice-history. By using ICE-6G, we are *assuming* that the ice-history is still valid in spite of those deviations.

This is a large assumption to make and indeed the stress magnitudes and patterns obtained using the radial average of our 3D viscosity model are quite different from those of VM5a, yet for the present study, we use our chosen viscosity profile and/or its 3D equivalent for the sake of consistency and comparison with our mantle flow models. Ideally, one would make use of an ice-history model based only on geological and glacialogical evidence and not tied to any particular Earth structure, but such a history of ice-thickness does not exist for the reasons given above. However, some ice models do try to minimize the assumption of particular viscosity structures. For example, the D1 model of Simon et al. (2017) offers a Bayesian approach where the inversion of geodetic data on vertical motion and gravity change is constrained with *a priori* GIA models, such as those of ICE-5G (Peltier, 2004) or Laur16 (Simon et al., 2016). Because this prior is an average of predictions from over 150 GIA model combinations, it avoids bias towards or dependency on any one underlying earth structure (Simon and Riva, 2020). Ultimately, consideration of alternative ice models (e.g., Lambeck et al. (2017)) would allow for constraining the sensitivity of glacially induced intraplate stress to changes in ice history.

Quantifying the sensitivity of the intraplate stress field to changes in viscosity structure is equally as important. The differences between GIA stresses obtained using VM5a versus our 3D radial average are shown in Figure 4.5 b. Overall, the stress magnitudes resulting from the VM5a Earth structure are lower than those of our 3D averaged viscosity by a couple of MPa. The viscosity of both our lithosphere and asthenosphere is slightly lower than in VM5a, exciting a larger response to the ice loading and larger stress magnitudes. Such lower viscosities also allow the lithosphere to deform more easily at shorter wavelengths in response to local-scale variations in ice-thickness, leading to sharper variability in the stress profile through the Canadian seismic zones versus that of VM5a (Figure 5.3 b). The stress low over the WQSZ may result from changes in the ice margin geometry as it passed through the LSLRS between 11.5 to 10.5 ka, during which time the edge of the ice sheet lingered along the northwestern margin of the Lower Saint Lawrence River but had already retreated from the southeast portion of Western Quebec. The VM5a model on the other hand produces a broad stress high over both the WQSZ and the CXSZ/LSLSZ. As such, use of different viscosity structure has implications for the change in Coulomb stress on the faults in this area.

To develop a clearer picture of just how glaciation changes stress magnitudes and the orientation of S_{Hmax} under different viscosity conditions, it would be prudent to first model the stress field testing only 1D viscosity structures. Wu (1997) has explored such models using several 1D viscosity profiles, finding that contemporary and past GIA stress orientations during the last 9 kyr are sensitive to mantle viscosity and specifically require smaller lower-mantle viscosities on the order of 1e21 rather than 1e22. This contradicts, however, evidence of a jump in viscosity, or at least a gradual increase, in the lower mantle from both other GIA analyses (e.g., Spada et al. (1991), Lambeck et al. (2017), and Caron et al. (2018)) and geodynamics (Mitrovica and Forte, 2004; Steinberger and Calderwood, 2006; Billen, 2008). A higher lower mantle viscosity also means longer rebound times and hence higher present day stresses since the stresses imparted during glaciation remain longer post-glaciation (Spada et al., 1991; Wu, 1997). The models presented in this work have a lower mantle viscosity closer to 1e22 Pa s and thus exhibit larger GIA stresses.

Because there are few studies that actively investigate the S_{Hmax} directions produced by GIA, it would be informative to re-analyze the approach of Wu (1997) with the newer CitcomSVE for the sake of a direct comparison to previous results that assume a flat earth (Wu and Hasegawa, 1996; Wu, 1997). The flat-earth approximation is commonly used for GIA stress and faulting analyses and is argued to be acceptable even for loads as large as the Laurentide owing to the fact that ignoring self-gravitation partially compensates the neglect of sphericity (Amelung and Wolf, 1994; Wu and Johnston, 1998). However, this condition is only valid within the ice margin and does not hold at distances farther from the ice margin, such as New Madrid (Wu and Johnston, 2000; Wu et al., 2021). Thus, sphericity remains important for assessing the impact of GIA on stresses in eastern North America as a whole and also enables implementation of sea level loading via the sea level equation, which the flat-earth model does not. Such work will be the subject of future research, as will a more rigorous examination of the effect of 3D viscosity on intraplate stress. From the differences between the 1D and 3D GIA models presented in Figures

5.3–5.6, it is clear that stress perturbations are controlled by lateral variations in viscosity just as much as or more so than changes in ice-thickness.

Additionally, while of interest as an explanation for intraplate seismicity in eastern North America, GIA also generates stress perturbations elsewhere in North America and globally. Using weak plate boundaries, some of the largest peaks in GIA related deviatoric stress actually occur on the PA-NA plate boundary in California. We also observe heightened stresses along the Queen Charlotte fault in Western Canada and up through Alaska. Unlike the eastern half of Canada and the U.S., these regions lie along active plate boundaries. While tectonics no doubt dominate the stress field and seismicity in these areas, Rollins et al. (2021) demonstrate how GIA can modulate the state of stress on major faults in southeast Alaska, which is actively experiencing rapid uplift rates due to contemporary glacial melting. The role of GIA in perturbing the state of stress even in plate boundary settings thus requires more study. However, to properly assess the role of GIA on faulting in plate-boundary zones one would need to account for the rupture history of individual faults, which are currently not considered with the use of virtual faults in the CitcomSVE models presented here. Some studies have explicitly incorporated faults into finite element GIA models, but these models are usually only regional in scale and again assume a flat Earth (Steffen et al., 2014b; Wu et al., 2021).

5.7 Conclusions

Using the spherical viscoelastic surface loading finite-element code CitcomSVE, we model the influence of glacial isostatic adjustment on the intraplate stress field of eastern North America both with and without the presence of low viscosity intraplate weak zones. While GIA induces a subtle clockwise rotation in central-eastern North America and within the New Madrid Seismic Zone, it actually produces a counterclockwise rotation in the Canadian seismic zones, contrary to suggestions from previous authors that GIA may be responsible for clockwise stress rotations observed between regional borehole and focal mechanism derived S_{Hmax} (Mazzotti and Townend, 2010). Only by including the tectonic background stress do we predict clockwise stress rotations consistent with the observations, suggesting the effect of mantle loading is more important for explaining these observations than is GIA. In the NMSZ, GIA helps promote stability on the Reelfoot Fault, in opposition to mantle flow, while promoting instability on more non-optimally oriented faults. However, the GIA stress perturbations to magnitude and direction do move faults in the Canadian seismic zones closer to failure, including the Timiskaming Fault and other western WQSZ faults. In particular, GIA helps localize higher Coulomb failure stress within the Charlevoix Seismic Zone. In general, weak zones loaded by GIA elevate the change in Coulomb failure stress by several MPa, and in the case of the WQSZ and LSLRS, the perturbations are large enough that even with only a small reduction in the coefficient of friction, faults that are not likely to fail under the background tectonic and geodynamic stresses alone could slip. However, alternate viscosity structures, both radially and laterally, have been shown to impact the orientation and magnitude of GIA induced S_{Hmax} (Spada et al., 1991; Wu, 1997). To fully assess how GIA may rotate S_{Hmax} and elevate CFS in these seismic zones, further investigation into how changes in 1D and 3D viscosity structure affect GIA stresses is warranted. Moreover, modeling the change in stress with time since deglaciation will shed light on how the spatial distribution and character of GIA stress has evolved over the last several thousand years. Such future work will allow for better assessment of the rate of GIA stress relaxation given different viscosity structures and whether the patterns of intraplate seismicity and known instances of glacially induced faulting favor any particular viscosity structure.

Chapter 6

CONCLUSIONS AND FUTURE DIRECTIONS

To better understand the nature and evolution of stress within the lithosphere and crust, this thesis has explored a variety of different geophysical topics, ranging from tectonics and statistical seismology to geodynamics and glacial cycles. In Chapter 2, I used gravity inverse methods to reveal the importance of inherited structures and lateral density contrasts for subduction initiation along the Puysegur Margin, which along with seismic observations helps inform us about the stress changes unfolding during this important tectonic process. In Chapter 3, I transitioned to an exploration of the earthquake interevent time distribution in Southern California, which reveals a significant seasonal periodicity to the annual seismicity rate, demonstrating how surface processes can influence the occurrence of earthquakes on sub-annual to annual timescales. In Chapter 4, I moved from plate boundaries to continental interiors, where I detailed the importance of deep mantle dynamics, in particular the Farallon slab, on controlling the orientation and magnitude of stress within the eastern North American lithosphere and heightening the potential for intraplate fault reactivation. The buoyancy force of the Farallon slab excites significant mantle flow and tractions on the lithosphere that are shown to explain some of the continent wide clockwise rotations in S_{Hmax} observed by previous authors. The force of the slab, in combination with the presence of low viscosity intraplate weakzones shifts some faults in major seismic zones closer to failure or even beyond the failure criterion, including some associated with major historical earthquakes. In Chapter 5, I switched from mantle loading to surface loading and demonstrated the influence of glacial isostatic adjustment (GIA) on perturbing stress in the intraplate lithosphere. The influence of GIA is small compared to that of the mantle loading, but GIA stress perturbations do help shift some faults closer to failure, particularly within the Charlevoix Seismic Zone, while helping to stabilize others.

Ultimately, this research highlights the important role of mantle dynamics on crustal processes, connecting the deep Earth to the shallow, and has implications for our understanding of intraplate seismicity elsewhere on Earth as well. A similar study, using the same methods and input data, with only minor modifications, could be performed for Central Europe or Central China, both of which experience significant intraplate earthquakes (Brandes et al., 2015; Mazzotti et al., 2020; Qingyun et al., 2021). GIA's role in promoting intraplate seismicity is also particularly relevant for Northern Europe due to the Fennoscandian deglaciation and is the subject of much active research (Brandes et al., 2015). The study of GIA overall is a rapidly developing field with many facets and important implications for both the solid Earth and the hydro- and cryospheres. These include not just glacially induced faulting but also more general considerations of land uplift, ice-sheet-solid-Earth coupling and the role GIA plays in contemporary ice mass loss due to climate change, the signal GIA imposes in geodetic data, and the influence of GIA on surface water mass balance and the spatial variability of future sea level rise. As such, future research will involve a continuation of the GIA component of this work.

6.1 Crustal Loading from GIA and Sea Level Change

The GIA results presented in this thesis focus predominantly on the present day for the sake of comparison with the results obtained from the mantle loading in Chapter 4. However, the likelihood of glacially induced faulting is predicted to be at a maximum soon after the end of deglaciation (Wu and Hasegawa, 1996; Steffen et al., 2020). To better assess how GIA impacts fault reactivation within the seismic zones of eastern North America over the course of a glacial cycle, we require higher temporal resolutions of the CitcomSVE output. Such models will be computed to explore the change in Coulomb failure stress with time at specific locations, as is commonly pursued in studies of glacially induced faulting (Steffen et al., 2020; Wu et al., 2021). While not the focus of the current work, stress and seismicity in response to GIA elsewhere in North America are worth exploring as well. The models presented here reveal elevated GIA stresses in the vicinity of the Queen Charlotte Fault in western Canada and Alaska and even along the San Andreas plate boundary. While tectonics no doubt dominate the stress field and seismicity in these areas, Rollins et al. (2021) demonstrate how GIA can modulate the state of stress on major faults in southeast Alaska, which is experiencing rapid uplift rates due to contemporary melting of glaciers. The role of GIA in perturbing the state of stress even in plate boundary settings thus requires more study. A similar case may be made for other regions experiencing modern day ice loss and ensuing rebound, such as Greenland and Antarctica. While these areas are not heavily populated, glacially induced faulting remains a seismic hazard, and fault offset, when coastal, can even impact relative sea level (RSL) change and RSL data (Steffen et al., 2020).

Sea level change itself also represents a possible source of crustal stress perturbation via changes in ocean loading, which has the potential to impact many highly populated coastal areas. Like with GIA modeling, we can use CitcomSVE to investigate ocean loading along continental margins. Luttrell and Sandwell (2010) demonstrate that sea level rise since the last glacial maximum (LGM) has induced bending stresses on global coastlines and can effectively reduce the magnitude of normal stress and perceptibly weaken onshore coastal faults, promoting failure. Specifically, onshore coastal transform faults will tend to be weaker during periods of high sea level, leading to a more rapid seismic cycle. While changes in the Coulomb stress accumulation rate were found to be about 100 times smaller than tectonic loading on plate boundary faults, the influence of plate bending on coastal stresses is likely observable in regions with a lower tectonic loading rate, implying the effect of sea level loading in tectonically quiescent settings, such as passive continental margins like eastern North America, may be more pronounced (Luttrell and Sandwell, 2010; Neves et al., 2015). Existing studies focus predominantly on the impact of sea level rise on active plate boundaries and assume a constant thickness elastic plate over a fluid low viscosity viscoelastic half-space. A more focused examination of the effect of sea level loading on passive margins, incorporating more realistic lithospheric thickness and mantle viscosity variations, will further clarify the extent to which sea level rise perturbs crustal stresses along coastlines. This is critical because the strongest sea level loading occurs were the gradients in lithospheric strength are greatest, and the flexural response to ocean loading is principally determined by the elastic plate thickness at the edge of the load, i.e., the coastline (Neves et al., 2015).

Previous work on sea level induced stresses off the coast of the Carolinas indeed predicts an increase in the maximum shear stress at seismogenic depths following 120 m of sea level rise since the LGM, with failure promoted on nearshore faults (Brothers et al., 2013; Neves et al., 2015). Similar patterns are observed along the entirety of the mid-Atlantic margin and the Iberian margin, where the narrow continental shelf and relatively low elastic plate thickness promote rupture of basement faults within 80-100 km of the coast (Brothers et al., 2013). While anthropogenic sea level rise is projected to be only about a meter by 2100 and 5-6 meters by 2300 (Oppenheimer et al., 2019), certain regions may be particularly prone to inundation depending on the local coastline morphology. Locally enhanced inundation may sufficiently perturb crustal stresses in the near future. Nearshore fault rupture can also trigger large submarine landslides, which in turn may pose a tsunami hazard to the eastern seaboard (Brothers et al., 2013; Brink et al., 2009). However, many existing studies (Luttrell and Sandwell, 2010; Brothers et al., 2013) do not account for ice mass unloading. Simultaneously modeling the coupled effect of GIA and loading from sea-level rise in the presence of lithospheric weak zones is critical to accurately predicting the resulting change in Coulomb stress at continental margins. Glacial removal in addition to sea level high-stand is expected to increase activity on onshore faults even more so than sea level loading alone (Luttrell and Sandwell, 2010). With a better understanding of the contributions from different drivers of intraplate and coastal stress changes and how those changes impact fault reactivation, we may begin to construct predictive models of the stress changes induced by future accelerating sea level rise.

Even the combined effect of slab loading and GIA on lithospheric deformation is potentially a very relevant problem for contemporary ice mass loss and GIA in Antarctica. Between 117 and 30 Ma, the Phoenix Plate subducted beneath the coast of what is today the Antarctic Peninsula, resulting in a back-arc rift system that today makes up the West Antarctic lithosphere (Artemieva and Thybo, 2020; Lloyd et al., 2019). Extensive lithospheric thinning and mantle hydration resulting from past subduction is thought to have lowered the viscosity of the West Antarctic mantle by as much as three orders of magnitude (Ivins et al., 2023; Wiens et al., 2023). This alone has implications for the relaxation times of GIA in the region, but the possible presence of the Phoenix slab in the mantle beneath West Antarctica and the Antarctic Peninsula (Lloyd et al., 2019) may also have considerable influence on present day Antarctic topography and mantle flow that could feedback into the GIA response. Any dynamic subsidence attributed to the pull of a relict slab counteracting the uplift induced by GIA has implications for the response of the West-Antarctic lithosphere, and in turn, the stability of the ice that sits upon it. Just as one considers the balance between slab pull and plate resistive forces that govern plate motions and subduction initiation, one might consider the balance of forces between GIA and long-wavelength continental subsidence driven by mantle dynamics.

6.2 Influence of 3D Earth Viscosity Structure on GIA and Implications for GRACE Estimates of Global Water Mass Balance

The displacement of the solid Earth due to GIA is essentially a change in the Earths' mass distribution, resulting in a change in gravitational potential and thus in the observed gravity field. Temporal changes in the Earth's gravity field, as measured by the Gravity Recovery and Climate Experiment (GRACE) satellites, are one of the primary means by which one can determine changes in surface water mass balance due to both seasonal cycles and long-term climate change, including cryospheric evolution and sea-level rise, but these data record a combination of hydro- and cryospheric mass changes as well as solid-Earth deformation arising from past and present surface loading. GIA has long been problematic for GRACE interpretation due to the large time-varying signal that post-glacial rebound introduces to gravity data (Wahr et al., 1998). Isolating the signal of surface mass balance (SMB) change from that of the solid Earth requires data constrained models of GIA.

GIA models used for gravity corrections typically use a viscoelastic Earth model with 1D radially symmetric viscosity. However, as discussed in Chapters 4 and 5, Earth's viscosity varies laterally as a function of temperature and composition, and the assumption of 1D viscosity has been acknowledged as an oversimplification since the advent of the GRACE mission (Wahr et al., 1998; Wang and Wu, 2006). In fact, the primary factor causing significant differences in ocean mass inferred from GRACE is the choice of GIA model (Chambers et al., 2010). Differences in radial 1D Earth structure and uncertainties in ice sheet history can yield a spread of up to 1.4 mm/yr in the estimates of the GIA contribution (Tamisiea, 2011), and uncertainty on lower mantle viscosity alone is large enough to undermine the inference of secular changes in oceanography and hydrology at long wavelengths (Wahr et al., 1998; Métivier et al., 2016). An uncertainty of even 1 mm/yr in GIA models can significantly limit the usefulness of GRACE for inferring ocean mass trends (Chambers et al., 2010). Additionally, the solid-Earth response to *contemporary* mass loss is rarely considered in the determination of surface mass changes from GRACE (Ivins et al., 2011), but may be significant for both the interpretation of gravity data and the dynamics and stabilization of ice sheets (Larour et al., 2019). Isolating this contemporary GIA signal in time-variable gravity data is increasingly important as the GRACE(-FO) mission extends beyond 20 years.

Differences between GIA models and GIA model misfits can arise from the viscosity model used, uncertainties in the ice loading history (Spada et al., 2006), and the treatment of polar wander (Adhikari et al., 2018; Chambers et al., 2010). However, the most significant differences arise from the solid-Earth model, especially between models using 1D radial viscosity with constant lithospheric thickness and those using 3D viscosity and variable lithospheric thickness (Li et al., 2020; Wal et al., 2015; Latychev et al., 2005; Spada et al., 2006). Studies of GIA model sensitivity to 3D Earth structure reveal 1D models have difficulty reproducing the rebound and relative sea level (RSL) predictions of 3D models to better than 10%, namely because GIA is sensitive to both local viscosity at the observation point and the viscosity under the load itself (Paulson et al., 2005; A et al., 2013; Bagge et al., 2021). Because 1D viscosity profiles derived from GNSS observations of glacial rebound most closely resemble the viscosity beneath the load instead of a global average, such viscosity structure is not appropriate for corrections to global GRACE data (Paulson et al., 2005; Powell et al., 2022). Lithospheric thickness and lower-mantle viscosity alone may have a larger effect on GIA misfits than a heterogeneous upper mantle due to mutual cancellation of the effect of lateral variations globally (Spada et al., 2006). However, lateral heterogeneity is more influential on regional scales (Kaufmann et al., 2005; Li et al., 2020), particularly in Antarctica, where upper mantle viscosities can vary by 2-3 orders of magnitude (Wal et al., 2015; Powell et al., 2022). Using a 1D earth model in such regions does not adequately capture fast relaxing deformation, resulting in an overall underestimation of GIA uncertainties (Caron et al., 2018).

GIA impacts GRACE more so than other means of measuring the global oceans (e.g., altimetry) because the mass change associated with GIA results from radial flow in the solid Earth. Despite the small magnitude of GIA uplift, the larger density of rock means the size of the GIA contribution is equivalent to the expected gravitational variation due to water fluxes in the ocean; even small solid-Earth height variations will produce significantly larger apparent changes in equivalent water thickness (EWT) (Tamisiea, 2011). Before present-day ice-mass and sea-level changes can be inferred, GRACE gravity measurements, which are obtained from the satellite motion by solving for the difference in gravity from an initial model in a non-linear least squares sense, must be corrected for GIA. The *a priori* model against which the gravitational potential anomalies are measured includes the gravitational effects of the solid Earth and GIA. Thus, the residual differences reflect not only the processes of interest that are not modeled in the background, such as hydrology or ice sheet mass changes, but also processes erroneously modeled in the background (Zlotnicki et al., 2012). It is furthermore assumed in the interpretation of GRACE data that monthly changes in gravitational attraction are produced primarily by lateral movement of water within and among the hydrosphere and cryosphere (Zlotnicki et al., 2012). Thus, it is paramount that GIA corrections used in the background model are as accurately constrained as possible to avoid propagation of error into the quantities of interest (Caron et al., 2018). Ultimately, these GIA corrections directly affect the ability to properly quantify and understand climatic processes such as contemporary ice mass loss and sea-level rise, coastal subsidence, ocean and surface mass transport, and Earth's energy budget.

The GIA correction is produced either by forward modeling the GIA contribution (A et al., 2013; Wal et al., 2015) or by inverting for the GIA signal from GRACE, GPS, and satellite altimetry data (Rietbroek et al., 2016; Wu et al., 2020). The latter approach remains very uncertain because of reference frame drift, limited knowledge of glacier ice compaction, striping error in the reduced level-2 and level-3 GRACE data, and inhomogeneous spatiotemporal coverage of altimetry data (Wal et al., 2015). GIA forward models constrained by a host of independently determined data sets, such as historic sea-level indicators; geomorphological, geological, and glaciological constraints on ice history; and knowledge of Earth structure are the most straightforward and standard way of accounting for the GIA signal (Ivins et al., 2023). The level-3 GRACE mass grids distributed to the scientific community are also corrected with such forward GIA models. However, the corrections applied in standard GRACE processing still assume a 1D viscosity structure, yielding secular global values of around -1.17 mm/yr (A et al., 2013; Uebbing et al., 2019). The GIA correction is of particular concern for Antarctica, where the estimated mean GIA contribution to mass change is on the order of 56 Gt/yr – as large as the error in the overall ice mass trend for the continent (-109 ± 56 Gt/yr) (IMBIE, 2018). The magnitude of the GIA contribution also differs by as much as 44 Gt/yr between models with 3D structure and those without (IMBIE, 2018) and greatly affects the SMB trend of glaciated regions. GIA model uncertainties propagate directly into uncertainties of the estimated ice loss (Caron et al., 2018), which has major implications for the accuracy of future sea level rise estimates.

In my post-graduate research, I will work to quantify the impact of 3D lateral variations in Earth's rheology on 1) the GIA signal in time-variable gravity as measured by GRACE, 2) contemporary solid-Earth uplift generated by ice mass loss in Greenland and Antarctica, and 3) projections of sea level rise associated with these processes, with the ultimate goal of providing updated GIA corrections for GRACE that account for 3D viscosity. With insights from geodynamic models such as those presented in Chapter 4 and knowledge of mantle rheology, we will parameterize 3D viscosity structures constrained by modern high resolution seismic tomography models.

We can explore four main controls on the Earth model: 1) the tomography model itself, 2) the conversion of seismic velocities to temperature, 3) the form of the Arrhenius law controlling the temperature dependence of viscosity, and 4) the viscosity of the lithosphere and asthenosphere and presence, or lack, of weak plate boundaries. Globally, the choice of tomography model is likely to have relatively little impact, but regionally, high resolution tomography can image fine scale structure that may influence both long-term GIA and contemporary elastic response to ice-loss from specific glaciers or ice-shelves. Uncertainty on the conversion of seismic velocities to temperature will require exploration and optimization of mineralogical assumptions on mantle composition. The temperature to viscosity conversion is key, in particular the form of the viscosity law, the activation energy, and the viscosity pre-factor. In addition, plate boundaries on the order of $1/10^{th}$ the viscosity of the upper mantle are rarely included in GIA models but can perturb horizontal rates by up to 1-2 mm/yr and strengthen the signal of Laurentide deglaciation in Europe (Latychev et al., 2005; Klemann et al., 2008). We will test the impact of such weak zones, as well as the impact of non-Newtonian viscosity through the role of stress-dependence (Kang et al., 2022; Ivins et al., 2023). Through my work in this thesis using both CitcomS and CitcomSVE, I have established a workflow for both the inversion and scaling of seismic velocities to temperature, as well as the viscosity calculations (e.g., Chapter 4) that can be used for this research.

Using CitcomSVE (Zhong et al., 2022) (see Chapter 5), we will model the impact of such 3D heterogeneous viscosity structure on the GIA response. In addition to stress, CitcomSVE self-consistently computes displacements, gravitational potential, and sea level height changes and accounts for both the effect of polar wander on the degree-2, order-1 harmonics (Zhong et al., 2022) and the effect of any hemispherically asymmetric load distribution on degree-1 displacement (Paulson et al., 2005; A et al., 2013). Outputs also include spherical harmonic expansions of displacements and gravitational potential up to a specified degree and order (Zhong et al., 2022). With its applications to GIA and integration with ICE-6G (Peltier et al., 2015), CitcomSVE can be considered a continuation of the GIA community's ongoing benchmark effort (Spada et al., 2011; Martinec et al., 2018). In its earlier form, 3D GIA models from CitcomSVE (Paulson et al., 2005) have been used to provide reconciled monthly time series of global mean ocean mass (A et al., 2013; Uebbing et al., 2019). With recent updates to handle more complicated 3D heterogeneous viscosity structure and scalability to massively parallel computers with greater than 6000 CPUs (Zhong et al., 2022), CitcomSVE has the potential to provide improved, more geophysically constrained and higher resolution solutions of the GIA correction needed for GRACE. Consideration of compressibility in GIA models is also currently of great interest to the GIA community and a benchmark effort on this front is beginning to take shape (Erik Ivins, personal communication, via Rebekka Steffen). The compressible version of CitcomSVE (A et al., 2013) is also currently being updated for greater parallelization and should be available within the time frame of this work (Zhong, personal communication).

We will test the sensitivity of GIA model predictions to both 3D and 1D viscosity structure using the aforementioned models by building upon the Bayesian approach in Caron et al. (2018), which quantified the uncertainty of 1D GIA models through an exploration of the parameters controlling GIA using GPS and RSL data (Caron et al., 2018). This will allow us to statistically characterize the plausible range of 3D Earth models appropriate for GRACE corrections as well as their uncertainties. These models with be parameterized by the seismic velocity to temperature scaling; the activation energy and prefactor of the Arrhenius relation; the lithospheric viscosity; the viscosity contrasts between the upper mantle, transition zone, and lower mantle; and the viscosity of plate boundaries, as well as the ice loading history. Modeled uplift rates, RSL, and gravitational potential can be directly compared with GIA observables such as GPS uplift rates, paleo-sea-level indicators, and gravity change from GRACE. From the modeled incremental gravitational potential, combinations of the Stokes coefficients, and the time increment used in the model, we can compute changes in geoid height and rates of gravity anomaly change. We will quantify the spatial patterns and amplitudes at which spatial heterogeneity in viscosity affects the gravity signals. We can difference the apparent GIA surface mass equivalent between different models to assess the sensitivity of the inferred hydro- and cryospheric surface mass rates in GRACE data to any particular viscosity structure. This is especially important for Antarctica, where the spatial pattern of gravity rates is markedly different between 3D and 1D models (Wal et al., 2015). Likewise, preliminary runs with CitcomSVE comparing simple models with 1D versus 3D mantle viscosity reveal notable differences at the global scale. Uplift and geoid rates predicted using a 3D mantle viscosity are much larger (upwards of 14 mm/yr at Hudson Bay) than those using a 1D viscosity profile (~ 8 mm/yr). Geoid rates differ mostly over West Antarctica, Patagonia, and Fennoscandia.

Rigorous statistical treatment of the GIA impact on GRACE allows for identifying and rooting out the sources and scales of biases in the SMB trends of both Greenland and Antarctica. For example, the amplitude of the SMB trend on the vast East Antarctic Ice Sheet (EAIS) is small and positive (+5 Gt/yr) but has the largest spread in both GRACE and altimetry data. Consequently, because the GIA signal is relatively large, if the GIA correction is even slightly off, it can bias the entire

SMB of the ice-sheet in the wrong direction (IMBIE, 2018). However, use of 3D structure may reduce the residuals on SMB as measured by GRACE and altimetry, and no one has yet modeled the effect of low viscosity zones on the EAIS. Moreover, GIA can bias mass trend estimates if it includes a transient signal associated with recent ice-sheet change within the past few millennia – a problem we can address with higher temporal resolution in GIA models.

Surface loading affects time scales ranging from those of GIA (10,000s of years) to Anthropocene ice mass and sea-level change (100s of years). This work will focus on GIA solutions stemming from both loading since the last inter-glacial and over the past 170 years, including the satellite era. As such, we will explore decadal time scale computations in CitcomSVE. CitcomSVE currently performs best in terms of computational speed and accuracy with time-steps of 100 to 250 years, though errors between semi-analytic solutions (Han and Wahr, 1995; A et al., 2013) and predicted displacements and rates are generally insensitive to temporal resolution (Zhong et al., 2022). Errors are, however, smaller for cases with higher spatial resolution (less than 0.2% for spherical harmonic degree $l < 10$ and less than 2% for $l < 23$) and mostly originate from relatively short wavelengths ($l > 15$) (Zhong et al., 2022). Resolutions in CitcomSVE, up to about 25 km laterally, are adequate to resolve the GIA process globally and provide corrections for GRACE data, which at most achieves resolutions of $\sim$ 300 km (Zlotnicki et al., 2012; Tapley et al., 2019). Nevertheless, 1 km-scale resolution is required to accurately capture the coupling of solid-Earth deformation and ice in fast ungrounding regions of marine-terminating ice-sheets (Cuzzone et al., 2019). Additionally, since different ocean kernels can introduce differences of up to 0.3 mm/yr equivalent sea level change (Chambers et al., 2010), higher resolutions are needed to fully capture the geometry of ocean basins and coastlines. Assessing convergence methods for higher resolutions in CitcomSVE is essential for modeling contemporary solid-Earth response to mass changes, but even at lower resolutions, this work can still inform the implementation of 3D structure in km-scale coupled ice-solid-Earth models in ISSM.

While many 3D GIA models are constrained by seismic data and include laterally variable lithospheric thickness, heterogeneous viscosity (Paulson et al., 2005; A et al., 2013; Wal et al., 2015; Li et al., 2020; Bagge et al., 2021; Powell et al., 2022), and plate boundary weak zones (Latychev et al., 2005; Klemann et al., 2008), *these characteristics of a 3D Earth have not yet been integrated with any fidelity into GIA corrections for GRACE estimates of surface mass change on a global scale.*

This work will focus on providing GRACE science analyses with improved GIA predictions based on fully-3D Earth models using multi-disciplinary data, including paleo-sea-level indicators, tide-gauge data, GPS crustal motions, and gravimetry and altimetry. We will use newer higher resolution regional seismic models, particularly for North America and Antarctica, in concert with global tomography to parameterize 3D Earth structure and analyze its influence on gravity, equivalent water height, and RSL estimates using CitcomSVE. We anticipate 3D and 1D GIA solutions and their impact on gravity and SMB as inferred from GRACE to differ substantially, especially at regional scales in places like the Western Antarctic Ice Sheet and Patagonia. This research will result in three primary scientific products that are useful to both NASA and the geoscience and hydro/cryoscience communities. 1) We will develop new GIA corrections for constructing level-3 GRACE products using 3D Earth rheology. 2) Our results will benefit the joint inversion of altimetry and GRACE data for the computation of well constrained mascons, particularly in areas with low SMB signal amplitude like the EAIS. 3) With modeled GIA uplift, we can deliver maps of vertical land motion time series that can directly support GNSS time series analysis. The improvements derived from rigorously constrained 3D GIA corrections will lead to more robust capability for all future gravity missions and inform reassessment of global water mass balance and sea level rise projections for the 21st century as inferred from GRACE.

Building upon the work presented in this thesis, the above proposed GIA modeling is an integral part of the framework with which we can determine the past, present, and future viscoelastic time-varying response of the solid Earth and has implications for climate relevant mass changes, sea level rise, and associated hazards, such as coastal subsidence (Larour et al., 2017), flooding, and perturbation to crustal stresses (Brothers et al., 2013). Likewise, geodynamic modeling more broadly can help constrain seismic hazard models via a more realistic understanding of intraplate seismicity, especially in light of how modern day climatic and sea level changes may regionally impact crustal stresses, earthquake hazard, and liquefaction risk in highly populated coastal areas. Ultimately, a refined understanding of the driving mechanisms of intraplate seismic events will enhance earthquake engineering and preparedness initiatives.

BIBLIOGRAPHY

A, G., J. Wahr, and S. Zhong (2013). “Computations of the viscoelastic response of a 3-D compressible earth to surface loading: An application to glacial isostatic adjustment in Antarctica and Canada”. In: *Geophys. J. Int.* 192.2, pp. 557–572. DOI: 10.1093/gji/ggs030.

Abers, G. A. and Hacker (2016). “A MATLAB toolbox and Excel workbook for calculating the densities, seismic wave speeds, and major element composition of minerals and rocks at pressure and temperature”. In: *Geochemistry, Geophys. Geosystems* 17.11, pp. 616–624. DOI: 10.1002/2015GC006171.Received.

Adams, J. and S. Halchuk (2003). “Fourth generation seismic hazard maps of Canada: Values for over 650 Canadian localities intended for the 2005 National Building Code of Canada”. In: *Geol. Surv. Canada Open File Rep.* 4459, p. 156.

Adams, J. (2019). “A 65-year history of seismic hazard estimates in Canada”. In: *12th Can. Conf. Earthq. Eng.* Quebec City, p. 8.

Ader, T. J. and J. P. Avouac (2013). “Detecting periodicities and declustering in earthquake catalogs using the Schuster spectrum, application to Himalayan seismicity”. In: *Earth Planet. Sci. Lett.* 377-378, pp. 97–105. DOI: 10.1016/j.epsl.2013.06.032.

Adhikari, S., L. Caron, B. Steinberger, J. T. Reager, K. K. Kjeldsen, B. Marzeion, E. Larour, and E. R. Ivins (2018). “What drives 20th century polar motion?” In: *Earth Planet. Sci. Lett.* 502, pp. 126–132. DOI: 10.1016/j.epsl.2018.08.059.

Amelung, F. and D. Wolf (1994). “Viscoelastic perturbations of the earth: significance of the incremental gravitational force in models of glacial isostasy”. In: *Geophys. J. Int.* 117, pp. 864–879. DOI: 10.1111/j.1365-246X.1994.tb02476.x.

Amos, C. B., P. Audet, W. C. Hammond, R. Bürgmann, I. A. Johanson, and G. Blewitt (2014). “Uplift and seismicity driven by groundwater depletion in central California”. In: *Nature* 509.7501, pp. 483–486. DOI: 10.1038/nature13275.

Anderson, D. L. and R. S. Hart (1978). “Q of the Earth”. In: *J. Geophys. Res.* 83.B12, pp. 5869–5882.

Artemieva, I. M. (2006). “Global 1° × 1° thermal model TC1 for the continental lithosphere: Implications for lithosphere secular evolution”. In: *Tectonophysics* 416.1-2, pp. 245–277. DOI: 10.1016/j.tecto.2005.11.022.

Artemieva, I. M. and H. Thybo (2020). “Continent size revisited: Geophysical evidence for West Antarctica as a back-arc system”. In: *Earth-Science Rev.* 202.103106. DOI: 10.1016/j.earscirev.2020.103106.

Aster, R. C., B. Borchers, and C. H. Thurber (2013). *Parameter Estimation and Inverse Problems*. 2nd. Waltham: Elsevier Inc., p. 360.

Austermann, J. and J. X. Mitrovica (2015). “Calculating gravitationally self-consistent sea level changes driven by dynamic topography”. In: *Geophys. J. Int.* 203.3, pp. 1909–1922. DOI: 10.1093/gji/ggv371.

Bagge, M., V. Klemann, B. Steinberger, M. Latinović, and M. Thomas (2021). “Glacial-Isostatic Adjustment Models Using Geodynamically Constrained 3D Earth Structures”. In: *Geochemistry, Geophys. Geosystems* 22.11. DOI: 10.1029/2021GC009853.

Bai, Y., S. E. Williams, R. Dietmar Müller, Z. Liu, and M. Hosseinpour (2014). “Mapping crustal thickness using marine gravity data: Methods and uncertainties”. In: *Geophysics* 79.2, G27–G36. DOI: 10.1190/geo2013-0270.1.

Baiesi, M. and M. Paczuski (2004). “Scale-free networks of earthquakes and aftershocks”. In: *Phys. Rev. E - Stat. Physics, Plasmas, Fluids, Relat. Interdiscip. Top.* 69.6, p. 8. DOI: 10.1103/PhysRevE.69.066106.

Baird, A. F., S. D. McKinnon, and L. Godin (2010). “Relationship between structures, stress and seismicity in the Charlevoix seismic zone revealed by 3-D geomechanical models: Implications for the seismotectonics of continental interiors”. In: *J. Geophys. Res.* 115.B11402, pp. 1–16. DOI: 10.1029/2010JB007521.

Ballmer, M. D., L. Schumacher, V. Lekic, C. Thomas, and G. Ito (2016). “Compositional layering within the large low shear-wave velocity provinces in the lower mantle”. In: *Geochemistry Geophys. Geosystems* 17, pp. 5056–5077. DOI: 10.1002/2015GC006205.Received.

Barnoud, A., O. Coutant, C. Bouligand, H. Gunawan, and S. Deroussi (2016). “3-D linear inversion of gravity data: Method and application to Basse-Terre volcanic island, Guadeloupe, Lesser Antilles”. In: *Geophys. J. Int.* 205.1, pp. 562–574. DOI: 10.1093/gji/ggw030.

Barton, P. J. (1986). “The relationship between seismic velocity and density in the continental crust — a useful constraint?” In: *Geophys. J. R. Astron. Soc.* 87.1, pp. 195–208. DOI: 10.1111/j.1365-246X.1986.tb04553.x.

Bear, G. W., H. J. Al-shukri, and A. J. Rudman (1995). “Linear inversion of gravity data for 3-D density distributions”. In: *Geophysics* 60.5, pp. 1354–1364.

Bellas, A., S. Zhong, and A. Watts (2020). “Constraints on the Rheology of the Lithosphere From Flexure of the Pacific Plate at the Hawaiian Islands”. In: *Geochemistry, Geophys. Geosystems* 21.2, pp. 1–19. DOI: 10.1029/2019GC008819.

Ben-Zion, Y. and I. Zaliapin (2020). “Localization and coalescence of seismicity before large earthquakes”. In: *Geophys. J. Int.* 223.1, pp. 561–583. DOI: 10.1093/gji/ggaa315.

Bendick, R. and D. Mencin (2020). “Evidence for Synchronization in the Global Earthquake Catalog”. In: *Geophys. Res. Lett.* 47.15, pp. 1–8. DOI: 10.1029/2020GL087129.

Bent, A. (1992). “A re-examination of the 1925 Charlevoix, Quebec, Earthquake”. In: *Bull. Seismol. Soc. Am.* 82.5, pp. 2097–2113.

Bent, A. (2022). “A revised moment magnitude catalog of Eastern Canada’s largest earthquakes”. In: *Geol. Surv. Canada Open File* 8862, p. 36.

Bent, A. L. (1996). “An improved source mechanism for the 1935 Timiskaming, Quebec earthquake from regional waveforms”. In: *Pure Appl. Geophys.* 146.1, pp. 5–20. DOI: 10.1007/bf00876667.

Bent, A. L., J. Drysdale, and H. K. Perry (2003). “Focal mechanisms for Eastern Canadian Earthquakes, 1994-2000”. In: *Seismol. Res. Lett.* 74.4, pp. 452–468. DOI: 10.1785/gssrl.74.4.452.

Bettinelli, P., J. P. Avouac, M. Flouzat, L. Bollinger, G. Ramillien, S. Rajaure, and S. Sapkota (2008). “Seasonal variations of seismicity and geodetic strain in the Himalaya induced by surface hydrology”. In: *Earth Planet. Sci. Lett.* 266.3-4, pp. 332–344. DOI: 10.1016/j.epsl.2007.11.021.

Billen, M. I. (2008). “Modeling the dynamics of subducting slabs”. In: *Annu. Rev. Earth Planet. Sci.* 36, pp. 325–356. DOI: 10.1146/annurev.earth.36.031207.124129.

Boyce, A., I. D. Bastow, E. M. Golos, S. Rondenay, S. Burdick, and R. D. van der Hilst (2019). “Variable modification of continental lithosphere during the Proterozoic Grenville orogeny: Evidence from teleseismic P-wave tomography”. In: *Earth Planet. Sci. Lett.* 525.115763.

Bradshaw, J. Y. (1990). “Geology of crystalline rocks of northern fiordland: Details of the granulite facies western fiordland orthogneiss and associated rock units”. In: *New Zeal. J. Geol. Geophys.* 33.3, pp. 465–484. DOI: 10.1080/00288306.1990.10425702.

Brandes, C., H. Steffen, R. Steffen, and P. Wu (2015). “Intraplate seismicity in northern Central Europe is induced by the last glaciation”. In: *Geology* 43.7, pp. 611–614. DOI: 10.1130/G36710.1.

Brink, U. S. ten, H. J. Lee, E. L. Geist, and D. Twichell (2009). “Assessment of tsunami hazard to the U.S. East Coast using relationships between submarine landslides and earthquakes”. In: *Mar. Geol.* 264, pp. 65–73. DOI: 10.1016/j.margeo.2008.05.011.

Brocher, T. M. (2005). “Empirical relations between elastic wavespeeds and density in the Earth’s crust”. In: *Bull. Seismol. Soc. Am.* 95.6, pp. 2081–2092. DOI: 10.1785/0120050077.

Brothers, D. S., K. M. Luttrell, and J. D. Chaytor (2013). “Sea-level-induced seismicity and submarine landslide occurrence”. In: *Geology* 41.9, pp. 979–982. DOI: 10.1130/G34410.1.

Calais, E., A. M. Freed, R. Van Arsdale, and S. Stein (2010). "Triggering of New Madrid seismicity by late-Pleistocene erosion". In: *Nature* 466.7306, pp. 608–611. doi: 10.1038/nature09258.

Calais, E., J. Y. Han, C. DeMets, and J. M. Nocquet (2006). "Deformation of the North American plate interior from a decade of continuous GPS measurements". In: *J. Geophys. Res. Solid Earth* 111.B06402, pp. 1–23. doi: 10.1029/2005JB004253.

Calvetti, D. and E. Somersalo (2018). "Inverse problems: From regularization to Bayesian inference". In: *Wiley Interdiscip. Rev. Comput. Stat.* 10.3. doi: 10.1002/wics.1427.

Camacho, A. G., J. Fernández, and J. Gottsmann (2011). "A new gravity inversion method for multiple subhorizontal discontinuity interfaces and shallow basins". In: *J. Geophys. Res.* 116.B02413, pp. 1–13. doi: 10.1029/2010JB008023.

Cammarano, F., S. Goes, P. Vacher, and D. Giardini (2003). "Inferring upper-mantle temperatures from seismic velocities". In: *Phys. Earth Planet. Inter.* 138.3-4, pp. 197–222. doi: 10.1016/S0031-9201(03)00156-0.

Cammarano, F. and M. Guerri (2017). "Global thermal models of the lithosphere". In: *Geophys. J. Int.* 210.1, pp. 56–72. doi: 10.1093/gji/ggx144.

Caron, L., E. R. Ivins, E. Larour, S. Adhikari, J. Nilsson, and G. Blewitt (2018). "GIA Model Statistics for GRACE Hydrology, Cryosphere, and Ocean Science". In: *Geophys. Res. Lett.* 45.5, pp. 2203–2212. doi: 10.1002/2017GL076644.

Castonguay, S., J. Dietrich, D. Lavoie, and J. Y. Laliberté (2010). "Structure and petroleum plays of the St. Lawrence Platform and Appalachians in southern Quebec: Insights from interpretation of MRNQ seismic reflection data". In: *Bull. Can. Pet. Geol.* 58.3, pp. 219–234. doi: 10.2113/gscpgbull.58.3.219.

Cathles, L. M. (1975). *Viscosity of the Earth's Mantle*. Princeton University Press, p. 371.

Chambers, D. P., J. Wahr, M. E. Tamisiea, and R. S. Nerem (2010). "Ocean mass from GRACE and glacial isostatic adjustment". In: *J. Geophys. Res. Solid Earth* 115.11, pp. 1–9. doi: 10.1029/2010JB007530.

Chappell, A. R. and N. J. Kusznir (2008). "Three-dimensional gravity inversion for Moho depth at rifted continental margins incorporating a lithosphere thermal gravity anomaly correction". In: *Geophys. J. Int.* 174, pp. 1–13. doi: 10.1111/j.1365-246X.2008.03803.x.

Chen, C., H. Gilbert, C. Andronicos, M. W. Hamburger, T. Larson, S. Marshak, G. L. Pavlis, and X. Yang (2016). "Shear velocity structure beneath the central United States: implications for the origin of the Illinois Basin and intraplate seismicity". In: *Geochemistry Geophys. Geosystems* 17, pp. 1020–1041. doi: 10.1002/2015GC006206.

Chen, C., D. Zhao, and S. Wu (2014). "Crust and upper mantle structure of the New Madrid Seismic Zone: Insight into intraplate earthquakes". In: *Phys. Earth Planet. Inter.* 230, pp. 1–14. DOI: 10.1016/j.pepi.2014.01.016.

Christensen, U. R. and D. A. Yuen (1984). "The Interaction of a Subducting Lithospheric Slab With a Chemical or Phase Boundary". In: *J. Geophys. Res.* 89.B6, pp. 4389–4402. DOI: 10.1029/JB089iB06p04389.

Chu, R., W. Leng, D. V. Helmberger, and M. Gurnis (2013). "Hidden hotspot track beneath the eastern United States". In: *Nat. Geosci.* 6.11, pp. 963–966. DOI: 10.1038/ngeo1949.

Collot, J.-Y., G. Lamarche, R. A. Wood, J. Delteil, M. Sosson, J.-F. Lebrun, and M. F. Coffin (1995). "Morphostructure of an incipient subduction zone along a transform plate boundary: Puysegur Ridge and Trench". In: *Geology* 23.6, pp. 519–522.

Cornell, C. A. (1968). "Engineering Seismic Risk Analysis". In: *Bull. Seismol. Soc. Am.* 58.5, pp. 1583–1606.

Corral, Á. (2004). "Long-Term Clustering , Scaling , and Universality in the Temporal Occurrence of Earthquakes". In: *Phys. Rev. Lett.* 92.10, pp. 1–4. DOI: 10.1103/PhysRevLett.92.108501.

Cottaar, S., T. Heister, I. Rose, and C. Unterborn (2014). "BurnMan: A lower mantle mineral physics toolkit". In: *Geochemistry Geophys. Geosystems* 15, pp. 1164–1179. DOI: 10.1002/2013GC005122.

Cowie, L. and N. Kusznir (2012). "Mapping crustal thickness and oceanic lithosphere distribution in the Eastern Mediterranean using gravity inversion". In: *Pet. Geosci.* 18, pp. 373–380. DOI: 10.1144/petgeo2011-071.1354-0793/12/.

Craig, T. J., E. Calais, L. Fleitout, L. Bollinger, and O. Scotti (2016). "Evidence for the release of long-term tectonic strain stored in continental interiors through intraplate earthquakes". In: *Geophys. Res. Lett.* 43.13, pp. 6826–6836. DOI: 10.1002/2016GL069359.

Craig, T. J., K. Chanard, and E. Calais (2017). "Hydrologically-driven crustal stresses and seismicity in the New Madrid Seismic Zone". In: *Nat. Commun.* 8.1. DOI: 10.1038/s41467-017-01696-w.

Csontos, R. and R. Van Arsdale (2008). "New Madrid seismic zone fault geometry". In: *Geosphere* 4.5, pp. 802–813. DOI: 10.1130/GES00141.1.

Culotta, R. C., T. Pratt, and J. Oliver (1990). "A tale of two sutures: COCORP's deep seismic surveys of the Grenville province in the eastern U.S. midcontinent". In: *Geology* 18.7, pp. 646–649. DOI: 10.1130/0091-7613(1990)018<0646:ATOTSC>2.3.CO;2.

Cuzzone, J. K., N. J. Schlegel, M. Morlighem, E. Larour, J. P. Briner, H. Seroussi, and L. Caron (2019). "The impact of model resolution on the simulated Holocene retreat of the southwestern Greenland ice sheet using the Ice Sheet System Model (ISSM)". In: *Cryosphere* 13.3, pp. 879–893. DOI: 10.5194/tc-13-879-2019.

Dal Forno, G., P. Gasperini, and G. Spada (2012). "Implementation of the Complete Sea Level Equation in a 3D Finite Elements Scheme: A Validation Study". In: *VII Hotine-Marussi Symp. Math. Geod.* Vol. 137. July 6-10. Rome, Italy: International Association of Geodesy Symposia. DOI: 10.1007/978-3-642-22078-4.

Daley, D. and D. Vere-Jones (2003). *An introduction to the theory of points processes, Volume I: Elementary Theory and Methods*. 2nd ed. New York: Springer-Verlag, p. 471. DOI: https://doi.org/10.1007/b97277.

Dalton, A. S., M. Margold, C. R. Stokes, L. Tarasov, A. S. Dyke, R. S. Adams, S. Allard, H. E. Arends, N. Atkinson, J. W. Attig, P. J. Barnett, R. L. Barnett, M. Batterson, P. Bernatchez, H. W. Borns, et al. (2020). "An updated radiocarbon-based ice margin chronology for the last deglaciation of the North American Ice Sheet Complex". In: *Quat. Sci. Rev.* 234. DOI: 10.1016/j.quascirev.2020.106223.

Davidsen, J. and G. Kwiatek (2013). "Earthquake interevent time distribution for induced micro-, nano-, and picoseismicity". In: *Phys. Rev. Lett.* 110.6, pp. 1–5. DOI: 10.1103/PhysRevLett.110.068501.

De La Varga, M. and J. F. Wellmann (2016). "Structural geologic modeling as an inference problem: A Bayesian perspective". In: *Interpretation* 4.3, SM1–SM16. DOI: 10.1190/INT-2015-0188.1.

Delano, J. E., R. W. Briggs, J. Thompson Jobe, R. D. Gold, and S. E. Engelhart (2021). "Quaternary Reelfoot Fault Deformation in the Obion River Valley, Tennessee, USA". In: *Tectonics* 40.8. DOI: 10.1029/2019TC005990.

DeMets, C., R. G. Gordon, and D. F. Argus (2010). "Geologically current plate motions". In: *Geophys. J. Int.* 181.1, pp. 1–80. DOI: 10.1111/j.1365-246X.2009.04491.x.

Dicaprio, C. J., M. Simons, S. J. Kenner, and C. A. Williams (2008). "Post-seismic reloading and temporal clustering on a single fault". In: *Geophys. J. Int.* 172.2, pp. 581–592. DOI: 10.1111/j.1365-246X.2007.03622.x.

Dyke, A. S., J. T. Andrews, P. U. Clark, J. H. England, G. H. Miller, J. Shaw, and J. J. Veillette (2002). "The Laurentide and Innuitian ice sheets during the Last Glacial Maximum". In: *Quat. Sci. Rev.* 21.1-3, pp. 9–31. DOI: 10.1016/S0277-3791(01)00095-6.

Dyke, A. S., T. F. Morris, and D. E. Green (1991). "Postglacial tectonic and sea level history of the central Canadian Artic". In: *Geol. Surv. Canada Bull.* 397, p. 63. DOI: 10.1038/075149c0.

Dziewonski, A. M. and D. L. Anderson (1981). "Preliminary reference Earth model". In: *Phys. Earth Planet. Inter.* 25.4, pp. 297–356. doi: 10.1016/0031-9201(81)90046-7.

Eberhart-Phillips, D. and M. Reyners (2001). "A complex, young subduction zone imaged by three-dimensional seismic velocity, Fiordland , New Zealand". In: *Geophys. J. Int.* 146, pp. 731–746.

Ende, M. P. van den and J. P. Ampuero (2020). "On the Statistical Significance of Foreshock Sequences in Southern California". In: *Geophys. Res. Lett.* 47.3, pp. 1–9. doi: 10.1029/2019GL086224.

Evans, R. L., M. H. Benoit, M. D. Long, J. Elsenbeck, H. A. Ford, J. Zhu, and X. Garcia (2019). "Thin lithosphere beneath the central Appalachian Mountains: A combined seismic and magnetotelluric study". In: *Earth Planet. Sci. Lett.* 519, pp. 308–316. doi: 10.1016/j.epsl.2019.04.046.

Farquharson, C. G. (2008). "Constructing piecewise-constant models in multidimensional minimum-structure inversions". In: *Geophysics* 73.1, K1–K9.

Farrell, W. E. and J. A. Clark (1976). "On Postglacial Sea Level". In: *Geophys. J. R. Astron. Soc.* 46.3, pp. 647–667. doi: 10.1111/j.1365-246X.1976.tb01252.x.

Field, E. H., K. R. Milner, J. L. Hardebeck, M. T. Page, N. van der Elst, T. H. Jordan, A. J. Michael, B. E. Shaw, and M. J. Werner (2017). "A spatiotemporal clustering model for the third uniform California earthquake rupture forecast (UCERF3-ETAS): Toward an operational earthquake forecast". In: *Bull. Seismol. Soc. Am.* 107.3, pp. 1049–1081. doi: 10.1785/0120160173.

Forte, A. M., J. X. Mitrovica, R. Moucha, N. A. Simmons, and S. P. Grand (2007). "Descent of the ancient Farallon slab drives localized mantle flow below the New Madrid seismic zone". In: *Geophys. Res. Lett.* 34.L04308, pp. 1–5. doi: 10.1029/2006GL027895.

Forte, A. M., R. Moucha, N. A. Simmons, S. P. Grand, and J. X. Mitrovica (2010). "Deep-mantle contributions to the surface dynamics of the North American continent". In: *Tectonophysics* 481.1-4, pp. 3–15. doi: 10.1016/j.tecto.2009.06.010.

Forte, A. M. and H. K. Perry (2000). "Geodynamic evidence for a chemically depleted continental tectosphere". In: *Science* 290.5498, pp. 1940–1944. doi: 10.1126/science.290.5498.1940.

Frost, D. J. (2008). "The Upper Mantle and Transition Zone". In: *Elements* 4, pp. 171–176.

Gangopadhyay, A. and P. Talwani (2007). "Two-dimensional numerical modeling suggests preferred geometry of intersecting seismogenic faults". In: *Spec. Pap. Geol. Soc. Am.* 425.07, pp. 87–99. doi: 10.1130/2007.2425(07).

Gardner, J. and L. Knopoff (1974). "Is The Sequence of Earthquakes in Southern California, with Aftershocks Removed, Poissonian?" In: *Bull. Seismol. Soc. Am.* 64.5, pp. 1363–1367.

Geng, M., J. K. Welford, C. G. Farquharson, and X. Hu (2019). “Gravity modeling for crustal-scale models of rifted continental margins using a constrained 3D inversion method”. In: *Geophysics* 84.4, G25–G39. DOI: 10.1190/geo2018-0134.1.

Gephart, J. W. and D. W. Forsyth (1984). “An improved method for determining the regional stress tensor using earthquake focal mechanism data: application to the San Fernando earthquake sequence.” In: *J. Geophys. Res.* 89.B11, pp. 9305–9320. DOI: 10.1029/JB089iB11p09305.

Ghosh, A., W. E. Holt, and L. Wen (2013). “Predicting the lithospheric stress field and plate motions by joint modeling of lithosphere and mantle dynamics”. In: *J. Geophys. Res. Solid Earth* 118.1, pp. 346–368. DOI: 10.1029/2012JB009516.

Ghosh, A., W. E. Holt, and L. M. Flesch (2009). “Contribution of gravitational potential energy differences to the global stress field”. In: *Geophys. J. Int.* 179.2, pp. 787–812. DOI: 10.1111/j.1365-246X.2009.04326.x.

Goes, S., R. Govers, and P. Vacher (2000). “Shallow mantle temperatures under Europe from P and S wave tomography”. In: *J. Geophys. Res. Solid Earth* 105.B5, pp. 11153–11169. DOI: 10.1029/1999jb900300.

Goes, S. (2002). “Thermal structure of the North American uppermost mantle inferred from seismic tomography”. In: *J. Geophys. Res.* 107.B3. DOI: 10.1029/2000jb000049.

Griffin, J. D., M. W. Stirling, and T. Wang (2020). “Periodicity and Clustering in the Long-Term Earthquake Record”. In: *Geophys. Res. Lett.* 47.22. DOI: 10.1029/2020GL089272.

Grollimund, B. and M. D. Zoback (2000). “Post glacial lithospheric flexure and induced stresses and pore pressure changes in the northern North Sea”. In: *Tectonophysics* 327.1-2, pp. 61–81. DOI: 10.1016/S0040-1951(00)00162-1.

Grollimund, B. and M. D. Zoback (2001). “Did deglaciation trigger intraplate seismicity in the New Madrid seismic zone?” In: *Geology* 29.2, pp. 175–178. DOI: 10.1130/0091-7613(2001)029<0175:DDTISI>2.0.CO;2.

Gualandi, A., Z. Liu, and C. Rollins (2020). “Post-large earthquake seismic activities mediated by aseismic deformation processes”. In: *Earth Planet. Sci. Lett.* 530. DOI: 10.1016/j.epsl.2019.115870.

Gurnis, M. (1992). “Long-term Controls on Eusatic and Epeirogenic Motions by Mantle Convection”. In: *GSA Today* 2.7, pp. 144–157.

Gurnis, M., C. Hall, and L. Lavier (2004). “Evolving force balance during incipient subduction”. In: *Geochemistry, Geophys. Geosystems* 5.7, pp. 1–31. DOI: 10.1029/2003GC000681.

Gurnis, M., H. Van Avendonk, S. P. Gulick, J. Stock, R. Sutherland, E. Hightower, B. Shuck, J. Patel, E. Williams, D. Kardell, E. Herzig, B. Idini, K. Graham, J. Estep, and L. Carrington (2019). “Incipient subduction at the contact with stretched continental crust: The Puysegur Trench”. In: *Earth Planet. Sci. Lett.* 520.1, pp. 212–219. doi: 10.1016/j.epsl.2019.05.044.

Hacker, B. R., G. A. Abers, and S. M. Peacock (2003). “Subduction factory 1. Theoretical mineralogy, densities, seismic wave speeds, and H2O contents”. In: *J. Geophys. Res. Solid Earth* 108.B1, pp. 1–26. doi: 10.1029/2001jb001127.

Hager, B. H. (1984). “Subducted Slabs and the Geoid: Constraints on Mantle Rheology and Flow”. In: *J. Geophys. Res.* 89.B7, pp. 6003–6015.

Hainzl, S., F. Scherbaum, and C. Beauval (2006). “Estimating Background Activity Based on Interevent-Time Distribution”. In: *Bull. Seismol. Soc. Am.* 96.1, pp. 313–320. doi: 10.1785/0120050053.

Han, D. and J. Wahr (1989). “Post-Glacial Rebound Analysis for a Rotating Earth”. In: *Slow Deform. Transm. Stress Earth*. Ed. by S. Cohen and P. VanííEk. American Geophysical Union.

Han, D. and J. Wahr (1995). “The viscoelastic relaxation of a realistically stratified earth, and a further analysis of postglacial rebound”. In: *Geophys. J. Int.* 120, pp. 287–311.

Haskell, N. (1935). “The motion of a viscous fluid under a surface load”. In: *J. Appl. Phys.* 6, pp. 265–269. doi: 10.1016/j.ijnonlinmec.2013.12.006.

Hauksson, E., W. Yang, and P. M. Shearer (2012). “Waveform relocated earthquake catalog for Southern California (1981 to June 2011)”. In: *Bull. Seismol. Soc. Am.* 102.5, pp. 2239–2244. doi: 10.1785/0120120010.

Hayes, G. P., G. L. Moore, D. E. Portner, M. Hearne, H. Flamme, M. Furtney, and G. M. Smoczyk (2018). “Slab2, a comprehensive subduction zone geometry model”. In: *Science* 362, pp. 58–61.

Heaton, T. H. (1975). “Tidal Triggering of Earthquakes”. In: *Geophys. J. R. Astron. Soc.* 43.2, pp. 307–326. doi: 10.1111/j.1365-246X.1975.tb00637.x.

Heidbach, O., M. Rajabi, X. Cui, K. Fuchs, B. Müller, J. Reinecker, K. Reiter, M. Tingay, F. Wenzel, F. Xie, M. O. Ziegler, M. L. Zoback, and M. Zoback (2018). “The World Stress Map database release 2016: Crustal stress pattern across scales”. In: *Tectonophysics* 744.September, pp. 484–498. doi: 10.1016/j.tecto.2018.07.007.

Hightower, E., M. Gurnis, and H. van Avendonk (2020). “A Bayesian 3D Linear Gravity Inversion for Complex Density Distributions: Application to the Puysegur Subduction System”. In: *Geophys. J. Int.* 223, pp. 1899–1918. doi: 10.1093/gji/ggaa425.

Hopper, E. and K. M. Fischer (2018). “The Changing Face of the Lithosphere-Asthenosphere Boundary: Imaging Continental Scale Patterns in Upper Mantle Structure Across the Contiguous U.S. With Sp Converted Waves”. In: *Geochemistry, Geophys. Geosystems* 19.8, pp. 2593–2614. DOI: 10.1029/2018GC007476.

Hough, S. E., J. G. Armbruster, L. Seeber, and J. F. Hough (2000). “On the modified Mercalli intensities and magnitudes of the 1811-1812 New Madrid earthquakes”. In: *J. Geophys. Res. Solid Earth* 105.B10, pp. 23839–23864. DOI: 10.1029/2000jb900110.

Hu, J., M. Gurnis, J. Rudi, G. Stadler, and R. D. Müller (2022). “Dynamics of the abrupt change in Pacific Plate motion around 50 million years ago”. In: *Nat. Geosci.* 15.1, pp. 74–78. DOI: 10.1038/s41561-021-00862-6.

Humphreys, E. D. and D. D. Coblentz (2007). “North American dynamics and western U.S. tectonics”. In: *Rev. Geophys.* 45.3, pp. 1–30. DOI: 10.1029/2005RG000181.

Hurd, O. and M. D. Zoback (2012). “Intraplate earthquakes, regional stress and fault mechanics in the Central and Eastern U.S. and Southeastern Canada”. In: *Tectonophysics* 581, pp. 182–192. DOI: 10.1016/j.tecto.2012.04.002.

IMBIE (2018). “Mass balance of the Antarctic Ice Sheet from 1992 to 2017”. In: *Nature* 558, pp. 219–222. DOI: 10.1017/cbo9780511535659.014.

Ishii, M. and J. Tromp (1999). “Normal-mode and free-air gravity constraints on lateral variations in velocity and density of earth’s mantle”. In: *Science* 285, pp. 1231–1236. DOI: 10.1126/science.285.5431.1231.

Ivins, E. R., W. van der Wal, D. A. Wiens, A. J. Lloyd, and L. Caron (2023). “Antarctic upper mantle rheology”. In: *Geochemistry Geophys. Antarct. Mantle*. Ed. by A. Martin and W. van der Wal. Vol. 56. Geological Society of London, Memoirs, pp. 267–294. DOI: 10.1144/m56-2020-19.

Ivins, E. R., M. M. Watkins, D. N. Yuan, R. Dietrich, G. Casassa, and A. Rülke (2011). “On-land ice loss and glacial isostatic adjustment at the Drake Passage: 2003-2009”. In: *J. Geophys. Res. Solid Earth* 116.2, pp. 2003–2009. DOI: 10.1029/2010JB007607.

James, T. S. and A. L. Bent (1994). “A comparison of eastern North American seismic strain-rates to glacial rebound strain-rates”. In: *Geophys. Res. Lett.* 21.19, pp. 2127–2130.

Johnson, C. W., Y. Fu, and R. Bürgmann (2017a). “Seasonal water storage, stress modulation, and California seismicity”. In: *Science* 356.6343, pp. 1161–1164. DOI: 10.1126/science.aak9547.

Johnson, C. W., Y. Fu, and R. Bürgmann (2017b). “Stress Models of the Annual Hydrospheric, Atmospheric, Thermal, and Tidal Loading Cycles on California Faults: Perturbation of Background Stress and Changes in Seismicity”. In: *J. Geophys. Res. Solid Earth* 122, pp. 10605–10625.

Johnson, C. W., Y. Fu, and R. Bürgmann (2020). “Hydrospheric modulation of stress and seismicity on shallow faults in southern Alaska”. In: *Earth Planet. Sci. Lett.* 530. DOI: 10.1016/j.epsl.2019.115904.

Johnston, A. C. (1987). “Suppression of earthquakes by large continental ice sheets”. In: *Nature* 330, pp. 467–469.

Johnston, A. C., K. Coppersmith, L. Kanter, and C. Cornell (1994). “The earthquakes of stable continental regions: Assessment of large earthquake potential”. In: *Electr. Power Res. Inst. Rep. TR-102261*. Ed. by J. Schneider. Palo Alto, California: Electric Power Research Institute, p. 309.

Johnston, A. C. and E. S. Schweig (1996). “The Enigma of the New Madrid Earthquakes of 1811-1812”. In: *Annu. Rev. Earth Planet. Sci.* 24, pp. 339–384.

Johnston, P., P. Wu, and K. Lambeck (1998). “Dependence of horizontal stress magnitude on load dimension in glacial rebound models”. In: *Geophys. J. Int.* 132.1, pp. 41–60. DOI: 10.1046/j.1365-246x.1998.00387.x.

Jordan, T. H. (1988). “Structure and formation of the continental tectosphere”. In: *J. Petrol.* Special Li.1, pp. 11–37. DOI: 10.1093/petrology/Special_Volume.1.11.

Kang, K., S. Zhong, A. Geruo, and W. Mao (2022). “The effects of non-Newtonian rheology in the upper mantle on relative sea level change and geodetic observables induced by glacial isostatic adjustment process”. In: *Geophys. J. Int.* 228.3, pp. 1887–1906. DOI: 10.1093/gji/ggab428.

Karato, S.-i. (1993). “Importance of Anelasticity in the Interpretation of Seismic Tomography”. In: *Geophys. Res. Lett.* 20.15, pp. 1623–1626.

Kaufmann, G., P. Wu, and E. R. Ivins (2005). “Lateral viscosity variations beneath Antarctica and their implications on regional rebound motions and seismotectonics”. In: *J. Geodyn.* 39.2, pp. 165–181. DOI: 10.1016/j.jog.2004.08.009.

Kendall, R. A., J. X. Mitrovica, and G. A. Milne (2005). “On post-glacial sea level - II. Numerical formulation and comparative results on spherically symmetric models”. In: *Geophys. J. Int.* 161.3, pp. 679–706. DOI: 10.1111/j.1365-246X.2005.02553.x.

Kenner, S. J. and P. Segall (2000). “A mechanical model for intraplate earthquakes: Application to the New Madrid Seismic Zone”. In: *Science* 289.5488, pp. 2329–2332. DOI: 10.1126/science.289.5488.2329.

Kenner, S. J. and M. Simons (2005). “Temporal clustering of major earthquakes along individual faults due to post-seismic reloading”. In: *Geophys. J. Int.* 160.1, pp. 179–194. DOI: 10.1111/j.1365-246X.2005.02460.x.

King, G. C. P., R. S. Stein, and J. Lin (1994). “Static Stress Changes and the Triggering of Earthquakes”. In: *Bull. Seismol. Soc. Am.* 84.3, pp. 935–953.

Klemann, V., Z. Martinec, and E. R. Ivins (2008). “Glacial isostasy and plate motion”. In: *J. Geodyn.* 46, pp. 95–103. DOI: 10.1016/j.jog.2008.04.005.

Kreemer, C., G. Blewitt, and E. C. Klein (2014). “A geodetic plate motion and Global Strain Rate Model”. In: *Geochemistry Geophys. Geosystems* 15, pp. 3849–3889. DOI: 10.1002/2014GC005407.Received.

Kreemer, C., W. C. Hammond, and G. Blewitt (2018). “A Robust Estimation of the 3-D Intraplate Deformation of the North American Plate From GPS”. In: *J. Geophys. Res. Solid Earth* 123.5, pp. 4388–4412. DOI: 10.1029/2017JB015257.

Kreemer, C. and I. Zaliapin (2018). “Spatiotemporal Correlation Between Seasonal Variations in Seismicity and Horizontal Dilatational Strain in California”. In: *Geophys. Res. Lett.* 45.18, pp. 9559–9568. DOI: 10.1029/2018GL079536.

Krien, Y. and L. Fleitout (2008). “Gravity above subduction zones and forces controlling plate motions”. In: *J. Geophys. Res. Solid Earth* 113.B09407, pp. 1–20. DOI: 10.1029/2007JB005270.

Kuehn, N. M., S. Hainzl, and F. Scherbaum (2008). “Non-Poissonian earthquake occurrence in coupled stress release models and its effect on seismic hazard”. In: *Geophys. J. Int.* 174, pp. 649–658. DOI: 10.1111/j.1365-246X.2008.03835.x.

Lambeck, K., A. Purcell, and S. Zhao (2017). “The North American Late Wisconsin ice sheet and mantle viscosity from glacial rebound analyses”. In: *Quat. Sci. Rev.* 158, pp. 172–210. DOI: 10.1016/j.quascirev.2016.11.033.

Lamontagne, M. and P. Brouillette (2022). “Faults and lineaments of the Quebec City , Charlevoix and Saguenay – Lac-St-Jean regions , Québec”. In: *Geol. Surv. Canada Open File* 8826.

Lamontagne, M., P. Brouillette, S. Grégoire, M. Bédard, and W. Bleeker (2020). “Faults and lineaments of the Western Quebec seismic zone, Quebec, and Ontario”. In: *Geol. Surv. Canada Open File* 8361, p. 28. DOI: 10.4095/321900.

Lamontagne, M. and G. Ranalli (1996). “Thermal and rheological constraints on the earthquake depth distribution in the Charlevoix, Canada, intraplate seismic zone”. In: *Tectonophysics* 257, pp. 55–69. DOI: 10.1016/0040-1951(95)00120-4.

Lamontagne, M. and G. Ranalli (2014). “Earthquakes and geological structures of the St. Lawrence Rift System”. In: *Intraplate Earthquakes*. Ed. by P. Talwani. Cambridge University Press, pp. 72–96. DOI: 10.1017/CBO9781139628921.005.

Larour, E., H. Seroussi, S. Adhikari, E. Ivins, L. Caron, M. Morlighem, and N. Schlegel (2019). “Slowdown in Antarctic mass loss from solid Earth and sea-level feedbacks”. In: *Science* 364.969. DOI: 10.1126/science..aav7908.

Larour, E., E. R. Ivins, and S. Adhikari (2017). “Should coastal planners have concern over where land ice is melting?” In: *Sci. Adv.* 3.11, pp. 1–9. DOI: 10.1126/sciadv.1700537.

Laske, G., G. Masters, Z. Ma, and M. E. Pasyanos (2013). “Update on CRUST1.0: A 1-degree Global Model of Earth’s Crust”. In: *Eur. Geosci. Union*. Vienna, Abstract EGU2013–2658.

Last, B. J. and K. Kubik (1983). “Compact gravity inversion.” In: *Geophysics* 48.6, pp. 713–721. DOI: 10.1190/1.1441501.

Latychev, K., J. X. Mitrovica, M. E. Tamisiea, J. Tromp, and R. Moucha (2005). “Influence of lithospheric thickness variations on 3-D crustal velocities due to glacial isostatic adjustment”. In: *Geophys. Res. Lett.* 32.1, pp. 1–4. DOI: 10.1029/2004GL021454.

Lau, H. C., J. X. Mitrovica, J. L. Davis, J. Tromp, H. Y. Yang, and D. Al-Attar (2017). “Tidal tomography constrains Earth’s deep-mantle buoyancy”. In: *Nature* 551, pp. 321–326. DOI: 10.1038/nature24452.

Lebrun, J.-F., G. Lamarche, and J.-Y. Collot (2003). “Subduction initiation at a strike-slip plate boundary: The Cenozoic Pacific-Australian plate boundary, south of New Zealand”. In: *J. Geophys. Res.* 108.B9 2453, pp. 1–18. DOI: 10.1029/2002JB002041.

Leng, W. and M. Gurnis (2015). “Subduction initiation at relic arcs”. In: *Geophys. Res. Lett.* 42, pp. 7014–7021. DOI: 10.1002/2015GL064985.Received.

Levandowski, W., R. B. Herrmann, R. Briggs, O. Boyd, and R. Gold (2018). “An updated stress map of the continental United States reveals heterogeneous intraplate stress”. In: *Nat. Geosci.* 11, pp. 433–437. DOI: 10.1038/s41561-018-0120-x.

Levandowski, W., M. Zellman, and R. Briggs (2017). “Gravitational body forces focus North American intraplate earthquakes”. In: *Nat. Commun.* 8.14314, pp. 1–9. DOI: 10.1038/ncomms14314.

Li, Q., M. Liu, Q. Zhang, and E. Sandvol (2007). “Stress evolution and seismicity in the central-eastern United States: Insights from geodynamic modeling”. In: *Cont. Intraplate Earthquakes Sci. Hazard, Policy*. Ed. by S. Stein and S. Mazzotti. 425th ed. Geological Society of America.

Li, T., P. Wu, H. Wang, H. Steffen, N. S. Khan, S. E. Engelhart, M. Vacchi, T. A. Shaw, W. R. Peltier, and B. P. Horton (2020). “Uncertainties of Glacial Isostatic Adjustment Model Predictions in North America Associated With 3D Structure”. In: *Geophys. Res. Lett.* 47.10, pp. 1–10. DOI: 10.1029/2020GL087944.

Li, Y. H. and J. E. Schoonmaker (2003). “Chemical Composition and Mineralogy of Marine Sediments”. In: *Treatise on Geochemistry* 7-9, pp. 1–35. DOI: 10.1016/B0-08-043751-6/07088-2.

Li, Y. and D. W. Oldenburg (1998). “3-D inversion of gravity data”. In: *Geophysics* 63.1, pp. 109–119.

Lidberg, M., J. M. Johansson, H. G. Scherneck, and G. A. Milne (2010). “Recent results based on continuous GPS observations of the GIA process in Fennoscandia from BIFROST”. In: *J. Geodyn.* 50.1, pp. 8–18. DOI: 10.1016/j.jog.2009.11.010.

Lin, G., P. M. Shearer, and E. Hauksson (2007). “Applying a three-dimensional velocity model, waveform cross correlation, and cluster analysis to locate southern California seismicity from 1981 to 2005”. In: *J. Geophys. Res.* 112.B12309, pp. 1–14.

Liu, L., S. Spasojević, and M. Gurnis (2008). “Reconstructing Farallon plate subduction beneath North America back to the Late Cretaceous”. In: *Science* 322.5903, pp. 934–938. DOI: 10.1126/science.1162921.

Lloyd, A. J., D. A. Wiens, H. Zhu, J. Tromp, A. A. Nyblade, R. C. Aster, S. E. Hansen, I. W. Dalziel, T. J. Wilson, E. R. Ivins, and J. P. O’Donnell (2019). “Seismic Structure of the Antarctic Upper Mantle Imaged with Adjoint Tomography”. In: *J. Geophys. Res. Solid Earth* 124, pp. 1–33. DOI: 10.1029/2019JB017823.

Long, M. D., M. H. Benoit, R. L. Evans, J. C. Aragon, and J. Elsenbeck (2020). “The MAGIC experiment: A combined seismic and magnetotelluric deployment to investigate the structure, dynamics, and evolution of the central appalachians”. In: *Seismol. Res. Lett.* 91, pp. 2960–2975. DOI: 10.1785/0220200150.

Long, M. D., K. G. Jackson, and J. F. McNamara (2016). “SKS splitting beneath Transportable Array stations in eastern North America and the signature of past lithospheric deformation”. In: *Geochemistry Geophys. Geosystems* 17, pp. 2–15. DOI: 10.1002/2015GC006088.Received.

Lu, C., S. P. Grand, H. Lai, and E. J. Garnero (2019). “TX2019slab: A New P and S Tomography Model Incorporating Subducting Slabs”. In: *J. Geophys. Res. Solid Earth* 124.11, pp. 11549–11567. DOI: 10.1029/2019JB017448.

Ludwig, W., J. Nafe, and C. Drake (1970). “Seismic Refraction”. In: *Sea*. Vol. 4. New York: Wiley-Interscience, pp. 53–84.

Luen, B. and P. B. Stark (2012). “Poisson tests of declustered catalogues”. In: *Geophys. J. Int.* 189.1, pp. 691–700. DOI: 10.1111/j.1365-246X.2012.05400.x.

Lund, B. (2005). “Effects of deglaciation on the crustal stress field and implications for endglacial faulting: A parametric study of simple Earth and ice models”. In: *Swedish Nucl. Fuel Waste Manag. Co Tech. Rep.* TR-05-04, p. 66.

Lund, B. and J. Townend (2007). “Calculating horizontal stress orientations with full or partial knowledge of the tectonic stress tensor”. In: *Geophys. J. Int.* 170.3, pp. 1328–1335. DOI: 10.1111/j.1365-246X.2007.03468.x.

Luttrell, K. and D. Sandwell (2010). “Ocean loading effects on stress at near shore plate boundary fault systems”. In: *J. Geophys. Res. Solid Earth* 115.8, pp. 1–14. DOI: 10.1029/2009JB006541.

Ma, S. and D. W. Eaton (2007). “Western Quebec seismic zone (Canada): Clustered, midcrustal seismicity along a Mesozoic hot spot track”. In: *J. Geophys. Res. Solid Earth* 112.6, pp. 1–16. DOI: 10.1029/2006JB004827.

Marsan, D. and O. Lengliné (2008). “Extending Earthquakes’ Reach Through Cascading”. In: *Science* 319.2008, pp. 1076–1079. DOI: 10.1126/science.1148783.

Martinec, Z., V. Klemann, W. van der Wal, R. E. Riva, G. Spada, Y. Sun, D. Melini, S. B. Kachuck, V. Barletta, K. Simon, G. A, and T. S. James (2018). “A benchmark study of numerical implementations of the sea level equation in GIA modelling”. In: *Geophys. J. Int.* 215.1, pp. 389–414. DOI: 10.1093/gji/ggy280.

Martinec, Z. (2000). “Spectral-finite element approach to three-dimensional viscoelastic relaxation in a spherical earth”. In: *Geophys. J. Int.* 142, pp. 117–141. DOI: 10.1046/j.1365-246X.2000.00138.x.

Matthews, M. V., W. L. Ellsworth, and P. A. Reasenberg (2002). “A Brownian Model for Recurrent Earthquakes”. In: *Bull. Seismol. Soc. Am.* 92.6, pp. 2233–2250.

Maurer, J., D. Kane, M. Nyst, and J. Velasquez (2020). “Risk from oklahoma’s induced earthquakes: The cost of declustering”. In: *Bull. Seismol. Soc. Am.* 110.5, pp. 2454–2465. DOI: 10.1785/0120190268.

Mazzotti, S. (2007a). “Geodynamic models for earthquake studies in intraplate North America”. In: *Spec. Pap. Geol. Soc. Am.* 425.02, pp. 17–33. DOI: 10.1130/2007.2425(02).

Mazzotti, S. (2007b). “Geodynamic models for earthquake studies in intraplate North America”. In: *Spec. Pap. Geol. Soc. Am.* 425.02, pp. 17–33. DOI: 10.1130/2007.2425(02).

Mazzotti, S. and J. Townend (2010). “State of stress in central and eastern North American seismic zones”. In: *Lithosphere* 2.2, pp. 76–83. DOI: 10.1130/L65.1.

Mazzotti, S. and J. Adams (2005). “Rates and uncertainties on seismic moment and deformation in eastern Canada”. In: *J. Geophys. Res.* 110.B09301, pp. 1–16. DOI: 10.1029/2004JB003510.

Mazzotti, S., T. S. James, J. Henton, and J. Adams (2005). “GPS crustal strain, postglacial rebound, and seismic hazard in eastern North America: The Saint Lawrence valley example”. In: *J. Geophys. Res. Solid Earth* 110.B11301, pp. 1–16. DOI: 10.1029/2004JB003590.

Mazzotti, S., H. Jomard, and F. Masson (2020). “Processes and deformation rates generating seismicity in metropolitan France and conterminous Western Europe”. In: *BSGF - Earth Sci. Bull.* 191.19, pp. 1–20. DOI: 10.1051/bsgf/2020019.

Medeiros, W. E. and J. B. C. Silva (1996). “Geophysical inversion using approximate equality constraints”. In: *Geophysics* 61.6, pp. 1678–1688.

Métivier, L., L. Caron, M. Greff-Lefftz, G. Pajot-Métivier, L. Fleitout, and H. Rouby (2016). “Evidence for postglacial signatures in gravity gradients: A clue in lower mantle viscosity”. In: *Earth Planet. Sci. Lett.* 452, pp. 146–156. DOI: 10.1016/j.epsl.2016.07.034.

Michael, A. J. (1987). “Use of Focal Mechanisms to Determine Stress: A Control Study.” In: *J. Geophys. Res.* 92.B1, pp. 357–368. DOI: 10.1029/JB092iB01p00357.

Milne, G. A. and J. X. Mitrovica (1998). “Postglacial sea-level change on a rotating Earth”. In: *Geophys. J. Int.* 133.1, pp. 1–19. doi: 10.1046/j.1365-246x.1998.1331455.x.

Milne, G. A., J. X. Mitrovica, and J. L. Davis (1999). “Near-field hydro-isostasy: The implementation of a revised sea-level equation”. In: *Geophys. J. Int.* 139, pp. 464–482. doi: 10.1046/j.1365-246X.1999.00971.x.

Mitchell, J., K. Mackay, H. Neil, E. Mackay, A. Pallentin, and P. Notman (2012). *Undersea New Zealand, 1:5,000,000*.

Mitrovica, J. X. and W. R. Peltier (1991). “On Postglacial Geoid Subsidence Over the Equatorial Oceans”. In: *J. Geophys. Res.* 96.B12, pp. 20053–20071.

Mitrovica, J. X., C. Beaumont, and G. Jarvis (1989). “Tilting of Continental Interiors by the Dynamical Effects of Subduction”. In: *Tectonics* 8.5, pp. 1079–1094.

Mitrovica, J. X. and A. M. Forte (2004). “A new inference of mantle viscosity based upon joint inversion of convection and glacial isostatic adjustment data”. In: *Earth Planet. Sci. Lett.* 225.1-2, pp. 177–189. doi: 10.1016/j.epsl.2004.06.005.

Mitrovica, J., J. Davis, and I. Shapiro (1994). “A spectral formalism for computing three-dimensional deformations due to surface loads 2: Present-day glacial isostatic adjustment”. In: *J. Geophys. Res.* 99.B4, pp. 7075–7101.

Mitrovica, J. X. and G. A. Milne (2003). “On post-glacial sea level: I. General theory”. In: *Geophys. J. Int.* 154.2, pp. 253–267. doi: 10.1046/j.1365-246X.2003.01942.x.

Mitrovica, J. X., G. A. Milne, and J. L. Davis (2001). “Glacial isostatic adjustment on a rotating earth”. In: *Geophys. J. Int.* 147, pp. 562–578. doi: 10.1046/j.1365-246x.2001.01550.x.

Molchan, G. (2005). “Interevent time distribution in seismicity: A theoretical approach”. In: *Pure Appl. Geophys.* 162.6-7, pp. 1135–1150. doi: 10.1007/s00024-004-2664-5.

Moresi, L., S. Zhong, L. Han, C. Conrad, E. Tan, M. Gurnis, E. Choi, P. Thoutireddy, V. Manea, A. McNamara, T. Becker, W. Leng, and L. Armendariz (2014). *CitcomS v3.3.1*. doi: 10.5281/zenodo.7271920.

Murphy, B. S. and G. D. Egbert (2017). “Electrical conductivity structure of southeastern North America: Implications for lithospheric architecture and Appalachian topographic rejuvenation”. In: *Earth Planet. Sci. Lett.* 462, pp. 66–75. doi: 10.1016/j.epsl.2017.01.009.

Murphy, B. S., L. Liu, and G. D. Egbert (2019). “Insights Into Intraplate Stresses and Geomorphology in the Southeastern United States”. In: *Geophys. Res. Lett.* 46, pp. 8711–8720. doi: 10.1029/2019GL083755.

Myhill, R., S. Cottaar, T. Heister, I. Rose, and C. Unterborn (2021). *BurnMan v1.0.1*. doi: 10.5281/zenodo.5552756.

Neves, M. C., J. Cabral, K. Luttrell, P. Figueiredo, T. Rockwell, and D. Sandwell (2015). “The effect of sea level changes on fault reactivation potential in Portugal”. In: *Tectonophysics* 658, pp. 206–220. doi: 10.1016/j.tecto.2015.07.023.

Newman, A., S. Stein, J. Weber, J. Engeln, A. Mao, and T. Dixon (1999). “Slow deformation and lower seismic hazard at the New Madrid seismic zone”. In: *Science* 284, pp. 619–621. doi: 10.1126/science.284.5414.619.

Nyamwandha, C. A., C. A. Powell, and C. A. Langston (2016). “A joint local and teleseismic tomography study of the Mississippi Embayment and New Madrid Seismic Zone”. In: *J. Geophys. Res. Solid Earth* 121, pp. 3570–3585. doi: 10.1002/2015JB012761.

Ogata, Y. (1999). “Seismicity analysis through point-process modeling: A review”. In: *Pure Appl. Geophys.* 155.2-4, pp. 471–507. doi: 10.1007/s000240050275.

Oldenburg, D. W. (1974). “The inversion and interpretation of gravity anomalies”. In: *Geophysics* 39.4, pp. 526–536.

Oppenheimer, M., B. Glavovic, J. Hinkel, R. van de Wal, A. Magnan, A. Abd-Elgawad, R. Cai, M. Cifuentes-Jara, R. DeConto, T. Ghosh, J. Hay, F. Isla, B. Marzeion, B. Meyssignac, and Z. Sebesvari (2019). “Sea Level Rise and Implications for Low-Lying Islands, Coasts, and Communities”. In: *IPCC Spec. Rep. Ocean Cryosph. a Chang. Clim.* Ed. by H.-O. Pörtner, D. Roberts, V. Masson-Delmotte, P. Zhai, M. Tignor, E. Poloczanska, K. Mintenbeck, A. Alegría, M. Nicolai, A. Okem, J. Petzold, B. Rama, and N. Weyer. IPCC, pp. 321–445. doi: 10.1126/science.aam6284.

Parker, R. L. (1972). “The Rapid Calculation of Potential Anomalies”. In: *Geophys. J. R. Astron. Soc.* 31, pp. 447–455.

Parker, R. L. (1995). “Improved Fourier terrain correction, Part I”. In: *Geophysics* 60.4, pp. 1007–1017.

Patel, J., R. Sutherland, M. Gurnis, H. Van Avendonk, S. P. Gulick, B. Shuck, J. Stock, and E. Hightower (2020). “Stratigraphic architecture of Solander Basin records Southern Ocean currents and subduction initiation beneath southwest New Zealand”. In: *Basin Res.* 00.April, pp. 1–24. doi: 10.1111/bre.12473.

Paul, J., C. P. Conrad, T. W. Becker, and A. Ghosh (2023). “Convective Self-Compression of Cratons and the Stabilization of Old Lithosphere”. In: *Geophys. Res. Lett.* 50.4, pp. 1–10. doi: 10.1029/2022GL101842.

Paulson, A., S. Zhong, and J. Wahr (2005). “Modelling post-glacial rebound with lateral viscosity variations”. In: *Geophys. J. Int.* 163.1, pp. 357–371. doi: 10.1111/j.1365-246X.2005.02645.x.

Peltier, W. R. (1974). “The impulse response of a Maxwell Earth”. In: *Rev. Geophys.* 12.4, pp. 649–669. doi: 10.1029/RG012i004p00649.

Peltier, W. R. (2004). "Global glacial isostasy and the surface of the ice-age earth: The ICE-5G (VM2) model and GRACE". In: *Annu. Rev. Earth Planet. Sci.* 32, pp. 111–149. DOI: 10.1146/annurev.earth.32.082503.144359.

Peltier, W. R., D. F. Argus, and R. Drummond (2015). "Space geodesy constrains ice age terminal deglaciation: The global ICE-6G (VM5a) model". In: *J. Geophys. Res. Solid Earth* 120, pp. 450–487. DOI: 10.1002/2014JB011176.

Petersen, M. D., A. M. Shumway, P. M. Powers, C. S. Mueller, M. P. Moschetti, A. D. Frankel, S. Rezaeian, D. E. McNamara, N. Luco, O. S. Boyd, K. S. Rukstales, K. S. Jaiswal, E. M. Thompson, S. M. Hoover, B. S. Clayton, et al. (2020). "The 2018 update of the US National Seismic Hazard Model: Overview of model and implications". In: *Earthq. Spectra* 36.1, pp. 5–41. DOI: 10.1177/8755293019878199.

Pollitz, F. F. and C. Cattania (2017). "Connecting crustal seismicity and earthquake-driven stress evolution in Southern California". In: *J. Geophys. Res. Solid Earth* 122, pp. 6473–6490.

Portniaguine, O. and M. S. Zhdanov (1999). "Focusing geophysical inversion images". In: *Geophysics* 64.3, pp. 874–887. DOI: 10.1190/1.1444596.

Powell, C. A., M. M. Withers, R. T. Cox, G. Vlahovic, and P. Arroucau (2014). "Crustal velocity structure associated with theeastern Tennessee seismic zone: Vp and Vs images based upon local earthquake tomography". In: *J. Geophys. Res. Solid Earth* 119, pp. 464–489. DOI: 10.1002/2013JB010433.Received.

Powell, E., K. Latychev, N. Gomez, and J. X. Mitrovica (2022). "The robustness of geodetically derived 1-D Antarctic viscosity models in the presence of complex 3-D viscoelastic Earth structure". In: *Geophys. J. Int.* 231.1, pp. 118–128. DOI: 10.1093/gji/ggac129.

Prutkin, I. and U. Casten (2009). "Efficient gravity data inversion for 3D topography of a contact surface with application to the Hellenic subduction zone". In: *Comput. Geosci.* 35.2, pp. 225–233. DOI: 10.1016/j.cageo.2008.02.036.

Qingyun, D., T. Fei, S. Yanhui, G. Rui, L. Sanzhong, F. Changmin, W. Guangzeng, L. Feng, and T. Yuyang (2021). "Linkage of deep lithospheric structures to intraplate earthquakes: A perspective from multi-source and multi-scale geophysical data in the South China Block". In: *Earth-Science Rev.* 214.October 2020, p. 103504. DOI: 10.1016/j.earscirev.2021.103504.

Ren, Y., E. Stutzmann, R. D. van der Hilst, and J. Besse (2007). "Understanding seismic heterogeneities in the lower mantle beneath the Americas from seismic tomography and plate tectonic history". In: *J. Geophys. Res.* 112.B01302, pp. 1–15. DOI: 10.1029/2005JB004154.

Richards-Dinger, K. and J. H. Dieterich (2012). "RSQSim earthquake simulator". In: *Seismol. Res. Lett.* 83.6, pp. 983–990. DOI: 10.1785/0220120105.

Rietbroek, R., S. E. Brunnabend, J. Kusche, J. Schröter, and C. Dahle (2016). "Revisiting the contemporary sea-level budget on global and regional scales". In: *Proc. Natl. Acad. Sci. U. S. A.* 113.6, pp. 1504–1509. DOI: 10.1073/pnas.1519132113.

Rimando, J. M. and A. L. Peace (2021). "Reactivation Potential of Intraplate Faults in the Western Quebec Seismic Zone, Eastern Canada". In: *Earth Sp. Sci.* 8.8. DOI: 10.1029/2021EA001825.

Rollins, C., J. T. Freymueller, and J. M. Sauber (2021). "Stress Promotion of the 1958 Mw7.8 Fairweather Fault Earthquake and Others in Southeast Alaska by Glacial Isostatic Adjustment and Inter-earthquake Stress Transfer". In: *J. Geophys. Res. Solid Earth* 126.1. DOI: 10.1029/2020JB020411.

Ross, Z. E., D. T. Trugman, E. Hauksson, and P. M. Shearer (2019). "Searching for hidden earthquakes in Southern California". In: *Science* 364, pp. 767–771.

Rudi, J., M. Gurnis, and G. Stadler (2022). "Simultaneous inference of plate boundary stresses and mantle rheology using adjoints: Large-scale 2-D models". In: *Geophys. J. Int.* 231.1, pp. 597–614. DOI: 10.1093/gji/ggac207.

Sandwell, D., E. Garcia, K. Soofi, P. Wessel, M. Chandler, and W. H. Smith (2013). "Toward 1-mGal accuracy in global marine gravity from CryoSat-2, Envisat, and Jason-1". In: *Lead. Edge* 32.8, pp. 892–899. DOI: 10.1190/tle32080892.1.

Sandwell, D. T., H. Harper, B. Tozer, and W. H. Smith (2019). "Gravity field recovery from geodetic altimeter missions". In: *Adv. Sp. Res.* DOI: 10.1016/j.asr.2019.09.011.

Sandwell, D. T., R. D. Müller, W. H. Smith, E. Garcia, and R. Francis (2014). "New global marine gravity model from CryoSat-2 and Jason-1 reveals buried tectonic structure". In: *Science* 346.6205, pp. 65–67. DOI: 10.1126/science.1258213.

Saxena, A., E. Choi, C. A. Powell, and K. S. Aslam (2021). "Seismicity in the central and southeastern United States due to upper mantle heterogeneities". In: *Geophys. J. Int.* 225.3, pp. 1624–1636. DOI: 10.1093/gji/ggab051.

Saxena, A., J. Dannberg, R. Gassmöller, M. Fraters, T. Heister, and R. Styron (2023). "High-Resolution Mantle Flow Models Reveal Importance of Plate Boundary Geometry and Slab Pull Forces on Generating Tectonic Plate Motions". In: *J. Geophys. Res. Solid Earth* 128.8, pp. 1–25. DOI: 10.1029/2022JB025877.

Schmandt, B. and F.-C. Lin (2014). "P and S wave tomography of the mantle beneath the United States". In: *Geophys. Res. Lett.* 41, pp. 1–8. DOI: 10.1002/2014GL061231.Received.

Schuster, A. (1897). "On lunar and solar periodicities of earthquakes". In: *Proc. R. Soc. London* 61.369-377, pp. 455–465. DOI: 10.1038/056321a0.

Schweig, E. S. and M. A. Ellis (1994). "Reconciling short recurrence intervals with minor deformation in the New Madrid seismic zone". In: *Science* 264, pp. 1308–1311. DOI: 10.1126/science.264.5163.1308.

Sella, G. F., S. Stein, T. H. Dixon, M. Craymer, T. S. James, S. Mazzotti, and R. K. Dokka (2007). “Observation of glacial isostatic adjustment in "stable" North America with GPS”. In: *Geophys. Res. Lett.* 34.2, pp. 1–6. DOI: 10.1029/2006GL027081.

Seton, M., R. D. Müller, S. Zahirovic, C. Gaina, T. Torsvik, G. Shephard, A. Talsma, M. Gurnis, M. Turner, S. Maus, and M. Chandler (2012). “Global continental and ocean basin reconstructions since 200Ma”. In: *Earth-Science Rev.* 113.3-4, pp. 212–270. DOI: 10.1016/j.earscirev.2012.03.002.

Seton, M., R. D. Müller, S. Zahirovic, S. Williams, N. M. Wright, J. Cannon, J. M. Whittaker, K. J. Matthews, and R. McGirr (2020). “A Global Data Set of Present-Day Oceanic Crustal Age and Seafloor Spreading Parameters”. In: *Geochemistry, Geophys. Geosystems* 21.10, pp. 1–15. DOI: 10.1029/2020GC009214.

Shapiro, S. S., B. H. Hager, and T. H. Jordan (1999). “Stability and Dynamics of the Continental Tectosphere”. In: *Dev. Geotecton.* 24, pp. 115–133.

Shaw, B. E., K. R. Milner, E. H. Field, K. Richards-Dinger, J. J. Gilchrist, J. H. Dieterich, and T. H. Jordan (2018). “A physics-based earthquake simulator replicates seismic hazard statistics across California”. In: *Sci. Adv.* 4.8, pp. 1–10. DOI: 10.1126/sciadv.aau0688.

Shuck, B., S. P. Gulick, H. J. Van Avendonk, M. Gurnis, R. Sutherland, J. Stock, and E. Hightower (2022). “Stress transition from horizontal to vertical forces during subduction initiation”. In: *Nat. Geosci.* 15.2, pp. 149–155. DOI: 10.1038/s41561-021-00880-4.

Shuck, B., H. Van Avendonk, S. P. Gulick, M. Gurnis, R. Sutherland, J. Stock, J. Patel, E. Hightower, S. Saustrup, and T. Hess (2021). “Strike-Slip Enables Subduction Initiation Beneath a Failed Rift: New Seismic Constraints From Puysegur Margin, New Zealand”. In: *Tectonics* 40.5, pp. 1–33. DOI: 10.1029/2020TC006436.

Silva, J., W. E. Medeiros, and V. Barbosa (2001). “Potential-field inversion: Choosing the appropriate technique to solve a geologic problem”. In: *Geophysics* 66.2, pp. 511–520.

Silva Dias, F. J. S., V. C. F. Barbosa, and J. B. C. Silva (2009). “3D gravity inversion through an adaptive-learning procedure”. In: *Geophysics* 74.3, pp. I9–I21. DOI: 10.1190/1.3092775.

Simon, K. M., T. S. James, J. A. Henton, and A. S. Dyke (2016). “A glacial isostatic adjustment model for the central and northern Laurentide ice sheet based on relative sea level and GPS measurements”. In: *Geophys. J. Int.* 205.3, pp. 1618–1636. DOI: 10.1093/gji/ggw103.

Simon, K. M. and R. E. Riva (2020). “Uncertainty Estimation in Regional Models of Long-Term GIA Uplift and Sea Level Change: An Overview”. In: *J. Geophys. Res. Solid Earth* 125.8. DOI: 10.1029/2019JB018983.

Simon, K. M., R. E. Riva, M. Kleinherenbrink, and N. Tangdamrongsub (2017). “A data-driven model for constraint of present-day glacial isostatic adjustment in North America”. In: *Earth Planet. Sci. Lett.* 474, pp. 322–333. doi: 10.1016/j.epsl.2017.06.046.

Sobolev, S. V., H. Zeyen, G. Stoll, F. Werling, R. Altherr, and K. Fuchs (1996). “Upper mantle temperatures from teleseismic tomography of French Massif Central including effects of composition, mineral reactions, anharmonicity, anelasticity and partial melt”. In: *Earth Planet. Sci. Lett.* 139, pp. 147–163.

Sowers, T. and O. Boyd (2019). “Petrologic and Mineral Physics Database for Use with the U.S. Geological Survey National Crustal Model”. In: *USGS Open-File Rep. 2019-1035*.

Spada, G., A. Antonioli, S. Cianetti, and C. Giunchi (2006). “Glacial isostatic adjustment and relative sea-level changes: The role of lithospheric and upper mantle heterogeneities in a 3-D spherical Earth”. In: *Geophys. J. Int.* 165.2, pp. 692–702. doi: 10.1111/j.1365-246X.2006.02969.x.

Spada, G., V. R. Barletta, V. Klemann, R. E. Riva, Z. Martinec, P. Gasperini, B. Lund, D. Wolf, L. L. Vermeersen, and M. A. King (2011). “A benchmark study for glacial isostatic adjustment codes”. In: *Geophys. J. Int.* 185.1, pp. 106–132. doi: 10.1111/j.1365-246X.2011.04952.x.

Spada, G. and P. Stocchi (2007). “SELEN: A Fortran 90 program for solving the "sea-level equation"”. In: *Comput. Geosci.* 33.4, pp. 538–562. doi: 10.1016/j.cageo.2006.08.006.

Spada, G., D. A. Yuen, R. Sabadini, and E. Boschi (1991). “Lower-mantle viscosity constrained by seismicity around deglaciated regions”. In: *Nature* 351.6321, pp. 53–55. doi: 10.1038/351053a0.

Spasojevic, S., L. Liu, and M. Gurnis (2009). “Adjoint models of mantle convection with seismic, plate motion, and stratigraphic constraints: North America since the Late Cretaceous”. In: *Geochemistry, Geophys. Geosystems* 10.5. doi: 10.1029/2008GC002345.

Spasojevic, S., L. Liu, M. Gurnis, and R. D. Müller (2008). “The case for dynamic subsidence of the U.S. east coast since the Eocene”. In: *Geophys. Res. Lett.* 35.L08305, pp. 1–6. doi: 10.1029/2008GL033511.

Steffen, H., O. Olesen, and R. Sutinen, eds. (2021). *Glacially-Triggered Faulting*. Cambridge University Press. doi: https://doi.org/10.1017/9781108779906.

Steffen, R., H. Steffen, R. Weiss, B. S. Lecavalier, G. A. Milne, S. A. Woodroffe, and O. Bennike (2020). “Early Holocene Greenland-ice mass loss likely triggered earthquakes and tsunami”. In: *Earth Planet. Sci. Lett.* 546. doi: 10.1016/j.epsl.2020.116443.

Steffen, R., H. Steffen, P. Wu, and D. W. Eaton (2014a). “Stress and fault parameters affecting fault slip magnitude and activation during a glacial cycle”. In: *Tectonics* 33, pp. 1461–1476. doi: 10.1002/2015TC003992.

Steffen, R., P. Wu, H. Steffen, and D. W. Eaton (2014b). “On the implementation of faults in finite-element glacial isostatic adjustment models”. In: *Comput. Geosci.* 62, pp. 150–159. doi: 10.1016/j.cageo.2013.06.012.

Steffen, R., P. Wu, H. Steffen, and D. W. Eaton (2014c). “The effect of earth rheology and ice-sheet size on fault slip and magnitude of postglacial earthquakes”. In: *Earth Planet. Sci. Lett.* 388, pp. 71–80. doi: 10.1016/j.epsl.2013.11.058.

Stein, R. S. (1999). “The role of stress transfer in earthquake occurrence”. In: *Nature* 402.December, pp. 605–609.

Stein, S. (2007). “Approaches to continental intraplate earthquake issues”. In: *Spec. Pap. Geol. Soc. Am.* 425.01, pp. 1–16. doi: 10.1130/2007.2425(01).

Stein, S., S. Cloetingh, N. H. Sleep, and R. Wortel (1989). “Passive Margin Earthquakes, Stresses, and Rheology”. In: *Earthquakes North-Atlantic Passiv. Margins Neotectonics Postglacial Rebound*. Ed. by S. Gregersen and P. W. Basham. Kluwer Academic Publishers, pp. 231–259. doi: 10.1007/978-94-009-2311-9.

Stein, S. and M. Liu (2009). “Long aftershock sequences within continents and implications for earthquake hazard assessment”. In: *Nature* 462.7269, pp. 87–89. doi: 10.1038/nature08502.

Stein, S. and G. F. Sella (2002). “Plate Boundary Zones: Concepts and Approaches”. In: *Plate Bound. Zo.* Ed. by S. Stein and J. T. Freymueller.

Steinberger, B. and A. R. Calderwood (2006). “Models of large-scale viscous flow in the Earth’s mantle with constraints from mineral physics and surface observations”. In: *Geophys. J. Int.* 167.3, pp. 1461–1481. doi: 10.1111/j.1365-246X.2006.03131.x.

Stern, R. J. and S. H. Bloomer (1992). “Subduction zone infancy: examples from the Eocene Izu-Bonin-Mariana and Jurassic California arcs”. In: *Geol. Soc. Am. Bull.* 104.12, pp. 1621–1636. doi: 10.1130/0016-7606(1992)104<1621:SZIEFT>2.3.CO;2.

Stevens, V. L. and J.-P. Avouac (2021). “On the relationship between strain rate and seismicity in the India–Asia collision zone: implications for probabilistic seismic hazard”. In: *Geophys. J. Int.* 226.1, pp. 220–245. doi: 10.1093/gji/ggab098.

Stixrude, L. and C. Lithgow-Bertelloni (2011). “Thermodynamics of mantle minerals – II. Phase equilibria”. In: *Geophys. J. Int.* 184.3, pp. 1180–1213. doi: 10.1111/j.1365-246X.2010.04890.x.

Straume, E. O., C. Gaina, S. Medvedev, K. Hochmuth, K. Gohl, J. M. Whittaker, R. Abdul Fattah, J. C. Doornenbal, and J. R. Hopper (2019). “GlobSed: Updated Total Sediment Thickness in the World’s Oceans”. In: *Geochemistry, Geophys. Geosystems* 20.4, pp. 1756–1772. doi: 10.1029/2018GC008115.

Stuhne, G. R. and W. R. Peltier (2015). "Reconciling the ICE-6G-C reconstruction of glacial chronology with ice sheet dynamics: The cases of Greenland and Antarctica". In: *J. Geophys. Res. Earth Surf.* 120.9, pp. 1841–1865. DOI: 10.1002/2015JF003580.

Sun, D., M. Gurnis, J. Saleeby, and D. Helmberger (2017). "A dipping, thick segment of the Farallon Slab beneath central U.S." In: *J. Geophys. Res. Solid Earth* 122.4, pp. 2911–2928. DOI: 10.1002/2016JB013915.

Sutherland, R., G. R. Dickens, P. Blum, C. Agnini, L. Alegret, G. Asatryan, J. Bhattacharya, A. Bordenave, L. Chang, J. Collot, M. J. Cramwinckel, E. Dallanave, M. K. Drake, S. J. Etienne, M. Giorgioni, et al. (2020). "Continental-scale geographic change across zealandia during Paleogene subduction initiation". In: *Geology* 48.5, pp. 419–424. DOI: 10.1130/G47008.1.

Sutherland, R. (1995). "The Australia-Pacific boundary and Cenozoic plate motions in the SW Pacific: Some constraints from Geosat data". In: *Tectonics* 14.4, pp. 819–831.

Sutherland, R., P. Barnes, and C. Uruski (2006). "Miocene-Recent deformation, surface elevation, and volcanic intrusion of the overriding plate during subduction initiation, offshore southern Fiordland, Puysegur margin, southwest New Zealand". In: *New Zeal. J. Geol. Geophys.* 49.1, pp. 131–149.

Sutherland, R., J. Collot, Y. Lafoy, G. A. Logan, R. Hackney, V. Stagpoole, C. Uruski, T. Hashimoto, K. Higgins, R. H. Herzer, R. Wood, N. Mortimer, and N. Rollet (2010). "Lithosphere delamination with foundering of lower crust and mantle caused permanent subsidence of New Caledonia Trough and transient uplift of Lord Howe Rise during Eocene and Oligocene initiation of Tonga-Kermadec subduction, western Pacific". In: *Tectonics* 29.2, p. 16. DOI: 10.1029/2009TC002476.

Sykes, L. R. (1978). "Intraplate Seismicity Reactivation of Preexisting Zones of Weakness, Alkaline Magmatism, and Other Tectonism Postdating Continental Fragmentation". In: *Rev. Geophys. Sp. Phys.* 16.4, pp. 621–688.

Tackley, P. J., D. J. Stevenson, G. A. Glatzmaier, and G. Schubert (1993). "Effects of an endothermic phase transition at 670 km depth in a spherical model of convection in the Earth's mantle". In: *Nature* 361, pp. 699–704. DOI: 10.1038/361699a0.

Talwani, P. (1988). "The intersection model for intraplate earthquakes". In: *Seismol. Res. Lett.* 59.4, pp. 305–310. DOI: 10.1785/gssrl.59.4.305.

Talwani, P. (1999). "Fault geometry and earthquakes in continental interiors". In: *Tectonophysics* 305, pp. 371–379.

Tamisiea, M. E. (2011). "Ongoing glacial isostatic contributions to observations of sea level change". In: *Geophys. J. Int.* 186.3, pp. 1036–1044. DOI: 10.1111/j.1365-246X.2011.05116.x.

Tan, E., E. Choi, P. Thoutireddy, M. Gurnis, and M. Aivazis (2006). "GeoFramework: Coupling multiple models of mantle convection within a computational framework". In: *Geochemistry, Geophys. Geosystems* 7.6, pp. 1–14. DOI: 10.1029/2005GC001155.

Tanaka, Y., V. Klemann, Z. Martinec, and R. E. Riva (2011). "Spectral-finite element approach to viscoelastic relaxation in a spherical compressible Earth: Application to GIA modelling". In: *Geophys. J. Int.* 184, pp. 220–234. DOI: 10.1111/j.1365-246X.2010.04854.x.

Tapley, B. D., M. M. Watkins, F. Flechtner, C. Reigber, S. Bettadpur, M. Rodell, I. Sasgen, J. S. Famiglietti, F. W. Landerer, D. P. Chambers, J. T. Reager, A. S. Gardner, H. Save, E. R. Ivins, S. C. Swenson, et al. (2019). "Contributions of GRACE to understanding climate change". In: *Nat. Clim. Chang.* 9.5, pp. 358–369. DOI: 10.1038/s41558-019-0456-2.

Tarantola, A. (2005). *Inverse Problem Theory and Methods for Model Parameter Estimation*. Philadelphia: Society for Industrial and Applied Mathematics, p. 342.

Thomas, W. A. and C. A. Powell (2017). "Necessary Conditions for Intraplate Seismic Zones in North America". In: *Tectonics* 36.12, pp. 2903–2917. DOI: 10.1002/2017TC004502.

Thompson, J. J., R. Gold, R. Briggs, R. Williams, W. Stephenson, J. Delano, A. Shah, and B. Minsley (2020). *Digital datasets documenting subsurface data locations, topographic metrics, fault scarp mapping, and revised fault network for Crowley's Ridge, New Madrid Seismic Zone: U.S. Geological Survey data release*. DOI: 10.5066/P9TFRP5D.

Toth, J. and M. Gurnis (1998). "Dynamics of subduction initiation at preexisting fault zones". In: *J. Geophys. Res.* 103.B8, pp. 18053–18067.

Townend, J. and M. D. Zoback (2000). "How faulting keeps the crust strong". In: *Geology* 28.5, pp. 399–402. DOI: 10.1130/0091-7613(2000)028<0399:HFKTCS>2.3.CO;2.

Trugman, D. T. and Z. E. Ross (2019). "Pervasive Foreshock Activity Across Southern California". In: *Geophys. Res. Lett.* 46.15, pp. 8772–8781. DOI: 10.1029/2019GL083725.

Turcotte, D. and G. Schubert (2014). *Geodynamics*. 3rd. Cambridge: Cambridge University Press, p. 623.

Uebbing, B., J. Kusche, R. Rietbroek, and F. W. Landerer (2019). "Processing Choices Affect Ocean Mass Estimates From GRACE". In: *J. Geophys. Res. Ocean.* 124.2, pp. 1029–1044. DOI: 10.1029/2018JC014341.

Van Arsdale, R. (2000). "Displacement history and slip rate on the Reelfoot fault of the New Madrid seismic zone". In: *Eng. Geol.* 55, pp. 219–226. DOI: 10.1016/S0013-7952(99)00093-9.

Van Avendonk, H. J., D. J. Shillington, W. S. Holbrook, and M. J. Hornbach (2004). “Inferring crustal structure in the Aleutian island arc from a sparse wide-angle seismic data set”. In: *Geochemistry, Geophys. Geosystems* 5.8. DOI: 10.1029/2003GC000664.

Verdecchia, A., J. Onwuemeka, Y. Liu, and R. M. Harrington (2022). “Depth-Dependent Crustal Stress Rotation and Strength Variation in the Charlevoix Seismic Zone (CSZ), Québec, Canada”. In: *Geophys. Res. Lett.* 49. DOI: 10.1029/2022gl100276.

Vere-Jones, D. (1995). “Forecasting earthquakes and earthquake risk”. In: *Int. J. Forecast.* 11, pp. 503–538.

Vilella, K., T. Bodin, C. E. Boukaré, F. Deschamps, J. Badro, M. D. Ballmer, and Y. Li (2021). “Constraints on the composition and temperature of LLSVPs from seismic properties of lower mantle minerals”. In: *Earth Planet. Sci. Lett.* 554, p. 116685. DOI: 10.1016/j.epsl.2020.116685. arXiv: 2004.10932.

Wagner, L. S., M. D. Long, M. D. Johnston, and M. H. Benoit (2012). “Lithospheric and asthenospheric contributions to shear-wave splitting observations in the southeastern United States”. In: *Earth Planet. Sci. Lett.* 341-344, pp. 128–138. DOI: 10.1016/j.epsl.2012.06.020.

Wahr, J., M. Molenaar, and F. Bryan (1998). “Time variability of the Earth’s gravity field: Hydrological and oceanic effects and their possible detection using GRACE”. In: *J. Geophys. Res.* 103.B12, pp. 30, 205–30, 229.

Wal, W. van der, P. L. Whitehouse, and E. J. Schrama (2015). “Effect of GIA models with 3D composite mantle viscosity on GRACE mass balance estimates for Antarctica”. In: *Earth Planet. Sci. Lett.* 414, pp. 134–143. DOI: 10.1016/j.epsl.2015.01.001.

Wang, H. and P. Wu (2006). “Effects of lateral variations in lithospheric thickness and mantle viscosity on glacially induced relative sea levels and long wavelength gravity field in a spherical, self-gravitating Maxwell Earth”. In: *Earth Planet. Sci. Lett.* 249.3-4, pp. 368–383. DOI: 10.1016/j.epsl.2006.07.011.

Welford, J. K., P. M. Shannon, B. M. O’Reilly, and J. Hall (2010). “Lithospheric density variations and Moho structure of the Irish Atlantic continental margin from constrained 3-D gravity inversion”. In: *Geophys. J. Int.* 183.1, pp. 79–95. DOI: 10.1111/j.1365-246X.2010.04735.x.

Welford, J. K., A. L. Peace, M. Geng, S. A. Dehler, and K. Dickie (2018). “Crustal structure of Baffin Bay from constrained three-dimensional gravity inversion and deformable plate tectonic models”. In: *Geophys. J. Int.* 214.2, pp. 1281–1300. DOI: 10.1093/GJI/GGY193.

Wellmann, J. F., M. De La Varga, R. E. Murdie, K. Gessner, and M. Jessell (2018). “Uncertainty estimation for a geological model of the Sandstone greenstone belt, Western Australia - insights from integrated geological and geophysical inversion in a Bayesian inference framework". In: *Charact. Ore-Forming Syst. from Geol. Geochemical Geophys. Stud.* Ed. by K. Gessner, T. Blenkinsop, and P. Sorjonen-Ward. 453rd ed. London: Geological Society of London, pp. 41–56.

Whitmeyer, S. J. and K. E. Karlstrom (2007). "Tectonic model for the Proterozoic growth of North America". In: *Geosphere* 3.4, pp. 220–259. DOI: 10.1130/GES00055.1.

Wiens, D. A., W. Shen, and A. J. Lloyd (2023). "The seismic structure of the Antarctic upper mantle". In: *Geol. Soc. London, Mem.* 56.1, pp. 195–212. DOI: 10.1144/m56-2020-18.

Withjack, M. O., R. Schlische, and P. Olsen (1998). "Diachronous rifting, drifting, and inversion on the passive margin of central eastern North America: An analog for other passive margins". In: *Am. Assoc. Pet. Geol. Bull.* 82, pp. 817–835.

Wu, P. and P. Johnston (2000). "Can deglaciation trigger earthquakes in N. America?" In: *Geophys. Res. Lett.* 27.9, pp. 1323–1326. DOI: 10.1029/1999GL011070.

Wu, P. (1992). "Viscoelastic versus viscous deformation and the advection of pre-stress". In: *Geophys. J. Int.* 108, pp. 136–142. DOI: 10.1111/j.1365-246X.1992.tb00844.x.

Wu, P. (1997). "Effect of viscosity structure on fault potential and stress orientations in eastern Canada". In: *Geophys. J. Int.* 130.2, pp. 365–382. DOI: 10.1111/j.1365-246X.1997.tb05653.x.

Wu, P. and H. S. Hasegawa (1996). "Induced stresses and fault potential in eastern Canada due to a realistic load: A preliminary analysis". In: *Geophys. J. Int.* 127.1, pp. 215–229. DOI: 10.1111/j.1365-246X.1996.tb01546.x.

Wu, P. and P. Johnston (1998). "Validity of using Flat-Earth Finite Element Models in the study of Postglacial Rebound". In: *Dyn. Ice Age Earth A Mod. Perspect.* Ed. by P. Wu. Switzerland: Trans Tech Publications, pp. 191–202.

Wu, P. and S. Mazzotti (2007). "Effects of a lithospheric weak zone on postglacial seismotectonics in eastern Canada and the northeastern United States". In: *Spec. Pap. Geol. Soc. Am.* 425.09, pp. 113–128. DOI: 10.1130/2007.2425(09).

Wu, P. and W. R. Peltier (1984). "Pleistocene deglaciation and the Earth's rotation: a new analysis". In: *Geophys. J. R. Astron. Soc.* 76, pp. 753–791. DOI: 10.1111/j.1365-246X.1984.tb01920.x.

Wu, P., R. Steffen, H. Steffen, and B. Lund (2021). "Glacial Isostatic Adjustment Models for Earthquake Triggering". In: *Glacially-Triggered Faulting*, pp. 383–401. DOI: 10.1017/9781108779906.029.

Wu, P. and W. van der Wal (2003). "Postglacial sealevels on a spherical, self-gravitating viscoelastic earth: Effects of lateral viscosity variations in the upper mantle on the inference of viscosity contrasts in the lower mantle". In: *Earth Planet. Sci. Lett.* 211, pp. 57–68. DOI: 10.1016/S0012-821X(03)00199-7.

Wu, X., B. J. Haines, M. B. Heflin, and F. W. Landerer (2020). “Improved Global Nonlinear Surface Mass Variation Estimates From Geodetic Displacements and Reconciliation With GRACE Data”. In: *J. Geophys. Res. Solid Earth* 125.2. DOI: 10.1029/2019JB018355.

Yang, T. and M. Gurnis (2016). “Dynamic topography, gravity and the role of lateral viscosity variations from inversion of global mantle flow”. In: *Geophys. J. Int.* 207.2, pp. 1186–1202. DOI: 10.1093/gji/ggw335.

Yang, T., M. Gurnis, and S. Zahirovic (2016). “Mantle-induced subsidence and compression in SE Asia since the early Miocene”. In: *Geophys. Res. Lett.* 43.16, pp. 1901–1909. DOI: 10.1002/2016GL068050.Received.

Yang, T., M. Gurnis, and S. Zahirovic (2018). “Slab avalanche-induced tectonics in self-consistent dynamic models”. In: *Tectonophysics* 746, pp. 251–265. DOI: 10.1016/j.tecto.2016.12.007.

Zaliapin, I. and Y. Ben-Zion (2013). “Earthquake clusters in southern California II: Classification and relation to physical properties of the crust”. In: *J. Geophys. Res. Solid Earth* 118.March, pp. 2865–2877. DOI: 10.1002/jgrb.50178.

Zaliapin, I. and Y. Ben-Zion (2015). “Artefacts of earthquake location errors and short-term incompleteness on seismicity clusters in southern California”. In: *Geophys. J. Int.* 202.3, pp. 1949–1968. DOI: 10.1093/gji/ggv259.

Zaliapin, I., A. Gabrielov, V. Keilis-Borok, and H. Wong (2008). “Clustering Analysis of Seismicity and Aftershock Identification”. In: *Phys. Rev. Lett.* 101.018501, pp. 1–4. DOI: 10.1103/PhysRevLett.101.018501.

Zhan, Y., G. Hou, T. Kusky, and P. M. Gregg (2016). “Stress development in heterogenetic lithosphere: Insights into earthquake processes in the New Madrid Seismic Zone”. In: *Tectonophysics* 671, pp. 56–62. DOI: 10.1016/j.tecto.2016.01.016.

Zhang, Y., M. Person, V. Voller, D. Cohen, J. McIntosh, and R. Grapenthin (2018). “Hydromechanical Impacts of Pleistocene Glaciations on Pore Fluid Pressure Evolution, Rock Failure, and Brine Migration Within Sedimentary Basins and the Crystalline Basement”. In: *Water Resour. Res.* 54, pp. 7577–7602. DOI: 10.1029/2017WR022464.

Zhong, S. J., D. A. Yuen, L. N. Moresi, and M. G. Knepley (2015). *Numerical Methods for Mantle Convection*. Vol. 7. Elsevier B.V., pp. 197–222. DOI: 10.1016/B978-0-444-53802-4.00130-5.

Zhong, S., K. Kang, G. A, and C. Qin (2022). “CitcomSVE: A Three-Dimensional Finite Element Software Package for Modeling Planetary Mantle’s Viscoelastic Deformation in Response to Surface and Tidal Loads”. In: *Geochemistry, Geophys. Geosystems* 23.10, pp. 1–28. DOI: 10.1029/2022gc010359.

Zhong, S., A. McNamara, E. Tan, L. Moresi, and M. Gurnis (2008). “A benchmark study on mantle convection in a 3-D spherical shell using CitcomS”. In: *Geochemistry, Geophys. Geosystems* 9.10, pp. 1–32. DOI: 10.1029/2008GC002048.

Zhong, S., A. Paulson, and J. Wahr (2003). “Three-dimensional finite-element modelling of Earth’s viscoelastic deformation: Effects of lateral variations in lithospheric thickness”. In: *Geophys. J. Int.* 155.2, pp. 679–695. DOI: 10.1046/j.1365-246X.2003.02084.x.

Zhong, S., C. Qin, G. Geruo, and J. Wahr (2012). “Can tidal tomography be used to unravel the long-wavelength structure of the lunar interior?” In: *Geophys. Res. Lett.* 39.L15201, pp. 1–5. DOI: 10.1029/2012GL052362.

Zhong, S., M. T. Zuber, L. Moresi, and M. Gurnis (2000). “Role of temperature-dependent viscosity and surface plates in spherical shell models of mantle convection”. In: *J. Geophys. Res.* 105.B5, pp. 11063–11082.

Zlotnicki, V., S. Bettadpur, and F. W. Landerer (2012). “Gravity Recovery and Climate Experiment (GRACE): Detection of Ice Mass Loss, Terrestrial Mass Changes, and Ocean Mass Gains”. In: *Encycl. Sustain. Sci. Technol.* Ed. by R. A. Meyers. Chap. Chapter 7, pp. 123–152. DOI: 10.1007/978-1-4419-0851-3.

Zoback, M. L. (1992). “Stress field constraints on intraplate seismicity in eastern North America”. In: *J. Geophys. Res.* 97.B8, pp. 11761–11782. DOI: 10.1029/92jb00221.

Zoback, M. D. and J. Townend (2001). “Implications of hydrostatic pore pressures and high crustal strength for the deformation of intraplate lithosphere”. In: *Tectonophysics* 336, pp. 19–30. DOI: 10.1016/S0040-1951(01)00091-9.

Zoback, M. D., J. Townend, and B. Grollimund (2002). “Steady-state failure equilibrium and deformation of intraplate lithosphere”. In: *Int. Geol. Rev.* 44, pp. 383–401. DOI: 10.2747/0020-6814.44.5.383.

Zoback, M. L. and M. D. Zoback (2007). “Lithosphere Stress and Deformation”. In: *Treatise Geophys.* 6, pp. 253–273.

Zöller, G. (2018). “A Statistical Model for Earthquake Recurrence Based on the Assimilation of Paleoseismicity, Historic Seismicity, and Instrumental Seismicity”. In: *J. Geophys. Res. Solid Earth* 123, pp. 4906–4921.

Appendix A

SUPPLEMENTARY MATERIAL FOR CHAPTER 2

A.1 Tikhonov Regularization

Tikhonov regularization is implemented using different regularization matrices for each of the x, y, and z directions. For first order Tikhonov regularization and the one-dimensional case, the finite difference approximation to the first derivative is

$$\frac{\partial m_k}{\partial x} = \frac{1}{\Delta x}(-m_k + m_{k+1}), \tag{A.1}$$

which can be represented in the form of an upper bi-diagonal matrix operator **L1** acting on a vector of the spatially discretized model parameters. The result is an *M-1* x *M* matrix.

$$\frac{\partial m_k}{\partial x} = \frac{1}{\Delta x}\begin{bmatrix} -1 & 1 & 0 & \cdots & 0 \\ 0 & -1 & 1 & \cdots & 0 \\ \vdots & \ddots & \ddots & \ddots & 0 \\ 0 & \cdots & 0 & -1 & 1 \end{bmatrix}\begin{bmatrix} m_1 \\ m_2 \\ \vdots \\ m_k \end{bmatrix} \tag{A.2}$$

Because the discretization can vary within the x, y, and z directions, the **L** matrices are unique for each of those directions and Δx, Δy, or Δz may vary for each adjacent pair of model parameters being regularized. When this is the case, the $1/\Delta x$ term is brought inside **L**.

For second order Tikhonov regularization and for the one-dimensional case, the finite difference approximation to the second derivative is

$$\frac{\partial^2 m_k}{\partial x^2} = \frac{1}{\Delta x^2}(m_{k-1} - 2m_k + m_{k+1}), \tag{A.3}$$

which can likewise be represented in the form of an upper tri-diagonal matrix operator **L2** acting on a vector of the model parameters, where **L2** is an *M-2* x *M* matrix.

$$\frac{\partial^2 m_k}{\partial x^2} = \frac{1}{\Delta x^2}\begin{bmatrix} 1 & -2 & 1 & 0 & \cdots & 0 \\ 0 & 1 & -2 & 1 & \cdots & 0 \\ \vdots & \ddots & \ddots & \ddots & \ddots & 0 \\ 0 & \cdots & 0 & 1 & -2 & 1 \end{bmatrix}\begin{bmatrix} m_1 \\ m_2 \\ \vdots \\ m_k \end{bmatrix} \tag{A.4}$$

The second derivative finite difference operator can be written in terms of the first derivative finite difference approximation as

$$\begin{aligned}\frac{\partial^2 m_k}{\partial x^2} &= \frac{1}{\delta x_j}\left(\frac{\partial m_{k+1}}{\partial x_{i+1}} - \frac{\partial m_k}{\partial x_i}\right)\\ &= \frac{1}{\delta x_j}\left(\frac{-m_k + m_{k+1}}{\Delta x_{i+1}} - \left(\frac{-m_{k-1} + m_k}{\Delta x_i}\right)\right).\end{aligned} \tag{A.5}$$

The **L2** matrix is thus calculated from the **L1** matrix for the x and y directions. For the z-direction, we use only first order Tikhonov regularization.

A.2 Synthetic Tests for BayGrav3D Inversion of a Subduction Zone

Here we present the results from each of the synthetic tests. For each metric shown in Figures A.1-A.4, the combinations of Tikhonov order and priors tested are organized into panels. Rows correspond to the order(s) of Tikhonov tested and columns to the combination of priors used. Each of the figures also shows the α, ζ combination that gives the lowest mean absolute error on the gravity and the lowest mean absolute error on the model parameters as compared to the true model for comparison. Discussion of these results is provided in the main text of the paper. We also show additional cross-sections of the model results for different combinations of α and ζ and different orientations to illustrate how the quality of the final model changes with different regularization strengths across the different tests and how the model changes lateral in both the x and y directions.

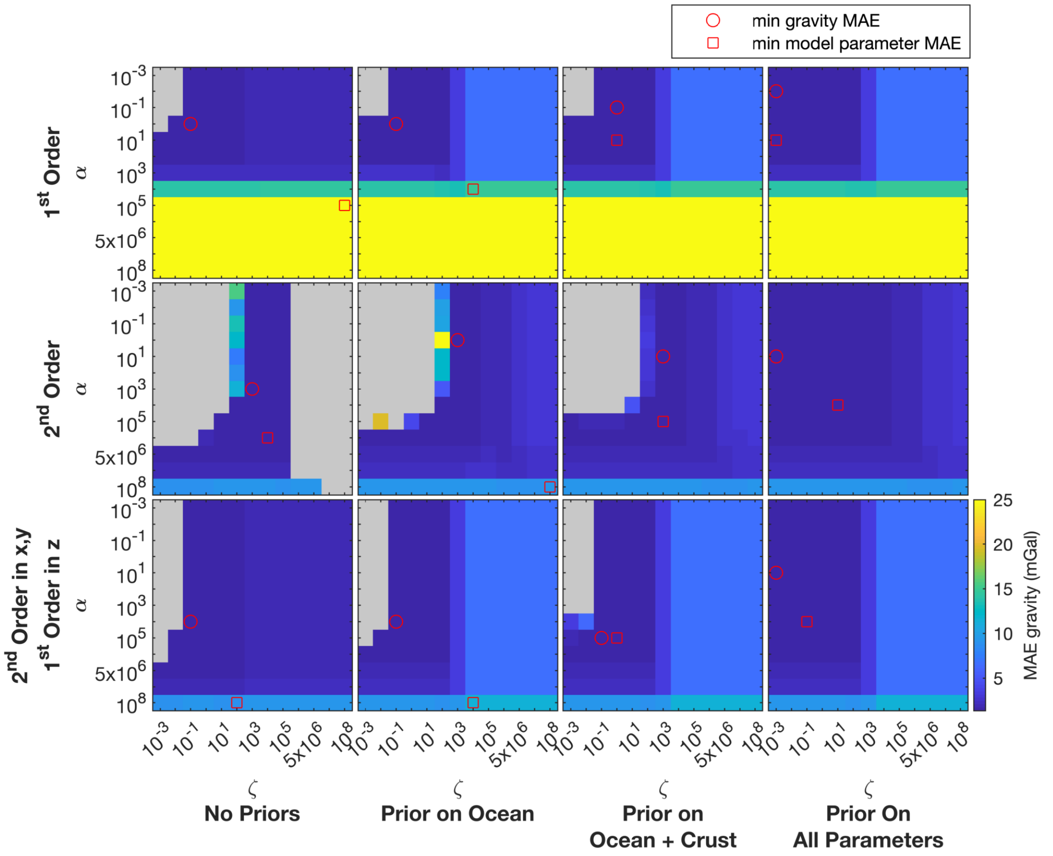

Figure A.1: Mean absolute error between the gravity from the true density model and that predicted by the inversion for each combination of α and ζ, which are labeled for every other value. Panel rows represent either first or second order Tikhonov regularization or a combination of the two. Panel columns represent, from left to right, inversion with no priors, inversion with priors only on prisms that fall within the ocean, inversion with priors on prisms in the ocean and crustal rocks, and inversion with priors on all prisms, including the mantle. Red circles mark the α,ζ combination corresponding to the minimum MAE on the gravity; red squares mark the α,ζ combination corresponding to the minimum MAE on the model parameters relative to the true model. Colorbar is saturated at 25 mGal. Gray regions correspond to α,ζ combinations that yield unstable or unreasonable results.

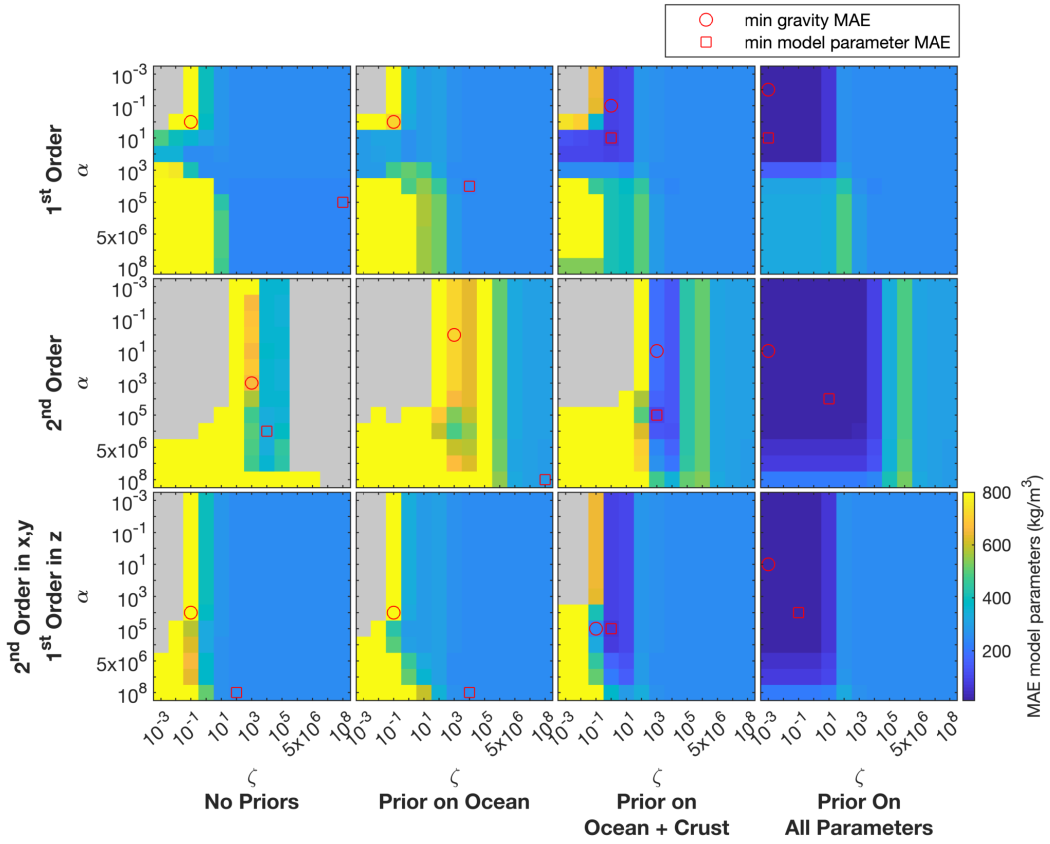

Figure A.2: Mean absolute error between the predicted model parameter values and the known model parameter values from the synthetic model for each combination of α and ζ, which are labeled for every other value. Panel rows represent either first or second order Tikhonov regularization or a combination of the two. Panel columns represent, from left to right, inversion with no priors, inversion with priors only on prisms that fall within the ocean, inversion with priors on prisms in the ocean and crustal rocks, and inversion with priors on all prisms, including the mantle. Red circles mark the α,ζ combination corresponding to the minimum MAE on the gravity; red squares mark the α,ζ combination corresponding to the minimum MAE on the model parameters relative to the true model. Colorbar is saturated at 800 kg/m^3. Gray regions correspond to α,ζ combinations that yield unstable or unreasonable results.

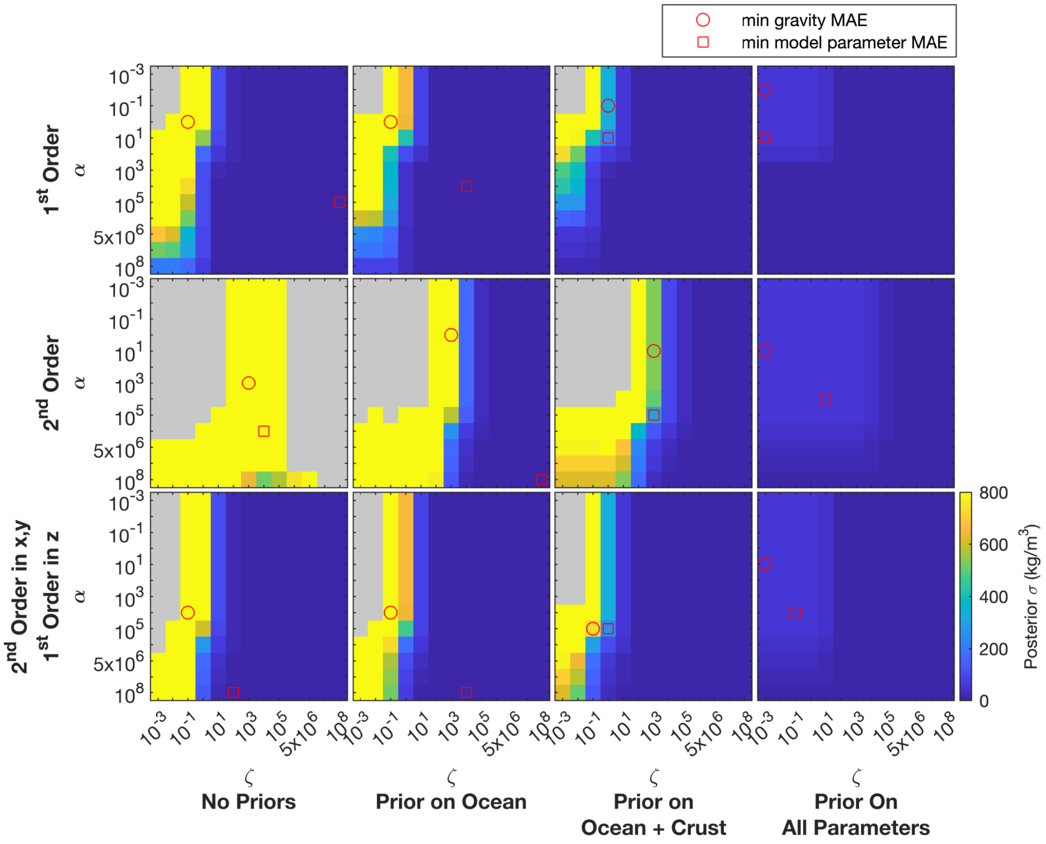

Figure A.3: Mean standard deviation on the model parameters as determined from the diagonal of the covariance matrix **C** for each combination of α and ζ, which are labeled for every other value. Panel rows represent either first or second order Tikhonov regularization or a combination of the two. Panel columns represent, from left to right, inversion with no priors, inversion with priors only on prisms that fall within the ocean, inversion with priors on prisms in the ocean and crustal rocks, and inversion with priors on all prisms, including the mantle. Red circles mark the α,ζ combination corresponding to the minimum MAE on the gravity; red squares mark the α,ζ combination corresponding to the minimum MAE on the model parameters relative to the true model. Colorbar is saturated at 800 kg/m^3. Gray regions correspond to α,ζ combinations that yield unstable or unreasonable results.

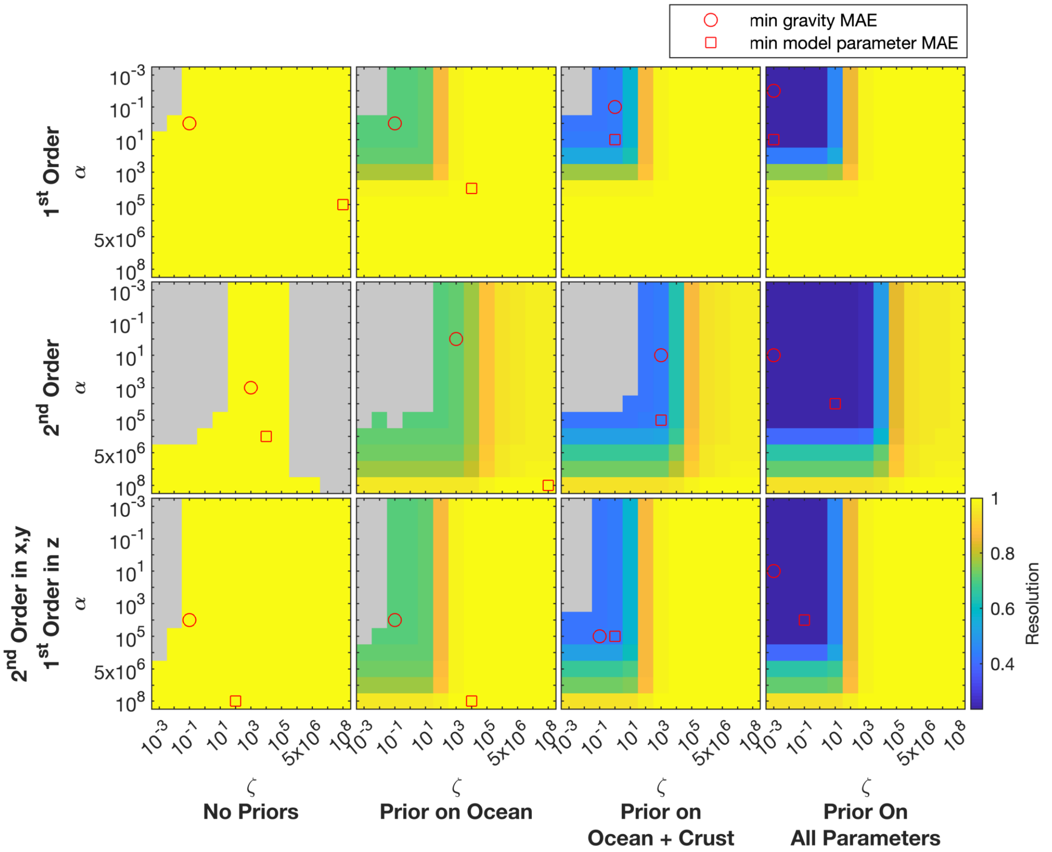

Figure A.4: Mean resolution of the model parameters as determined from the diagonal of the resolution matrix **R** for each combination of α and ζ, which are labeled for every other value. Panel rows represent either first or second order Tikhonov regularization or a combination of the two. Panel columns represent, from left to right, inversion with no priors, inversion with priors only on prisms that fall within the ocean, inversion with priors on prisms in the ocean and crustal rocks, and inversion with priors on all prisms, including the mantle. Red circles mark the α,ζ combination corresponding to the minimum MAE on the gravity; red squares mark the α,ζ combination corresponding to the minimum MAE on the model parameters relative to the true model. Gray regions correspond to α,ζ combinations that yield unstable or unreasonable results. Lower resolution means that model parameters are determined more by the prior than they are the gravity data itself. Resolution values of 1 or near 1 mean model parameter values are resolved more by the gravity data than the prior.

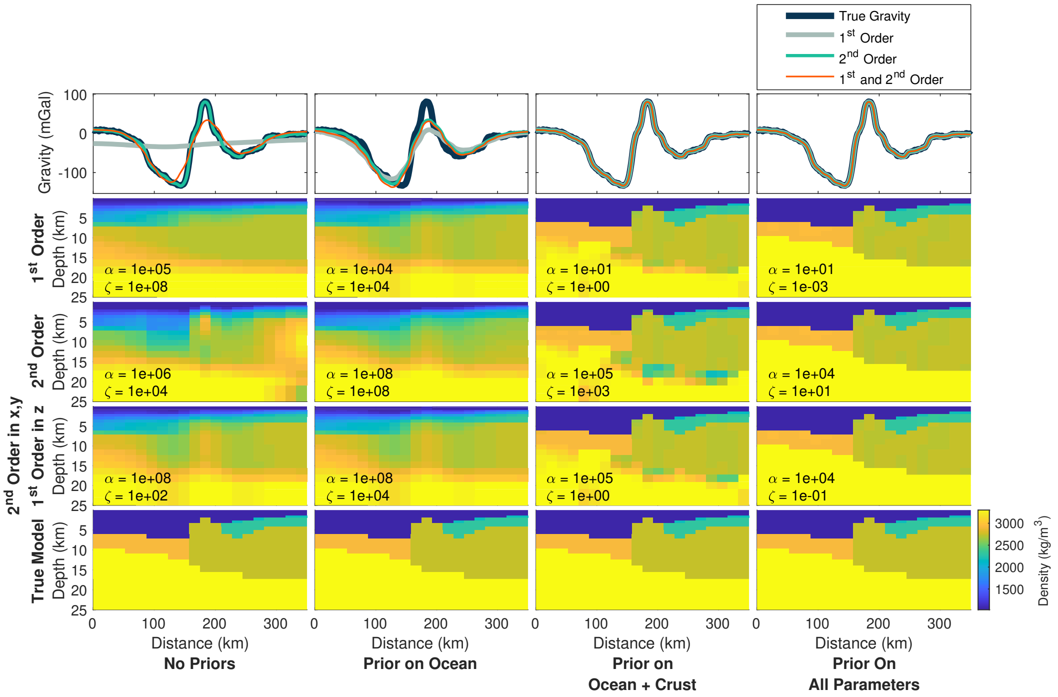

Figure A.5: Representative cross section in the x-direction of the 3D inversion results for the α and ζ combinations that produced the minimum MAE on the model parameters for each of the regularization order and prior combinations, as determined from the test results depicted in Figs. A.1-A.4. **Row 1**: gravity profiles for each of the three cases depicted in the panels below. Dark blue line: true gravity produced by the synthetic model, with noise; gray line: gravity from inversion using only first order Tikhonov; light blue line: gravity from inversion using only second order Tikhonov; orange line: gravity from inversion using second order Tikhonov in the horizontal and first order in the vertical. **Row 2**: cross-sections of the density model recovered from using only first order Tikhonov for the cases of no priors, priors only on the ocean water parameters, priors on the ocean and crustal parameters, and priors on all parameters, each with their respective minimum model parameter MAE α, ζ combinations. **Row 3**: cross-sections of the density model recovered from using only second order Tikhonov for each of the different prior cases. **Row 4**: cross-sections of the density model recovered from using a combination of first and second order Tikhonov for each of the different prior cases. **Row 5**: cross-section of true synthetic density model for comparison.

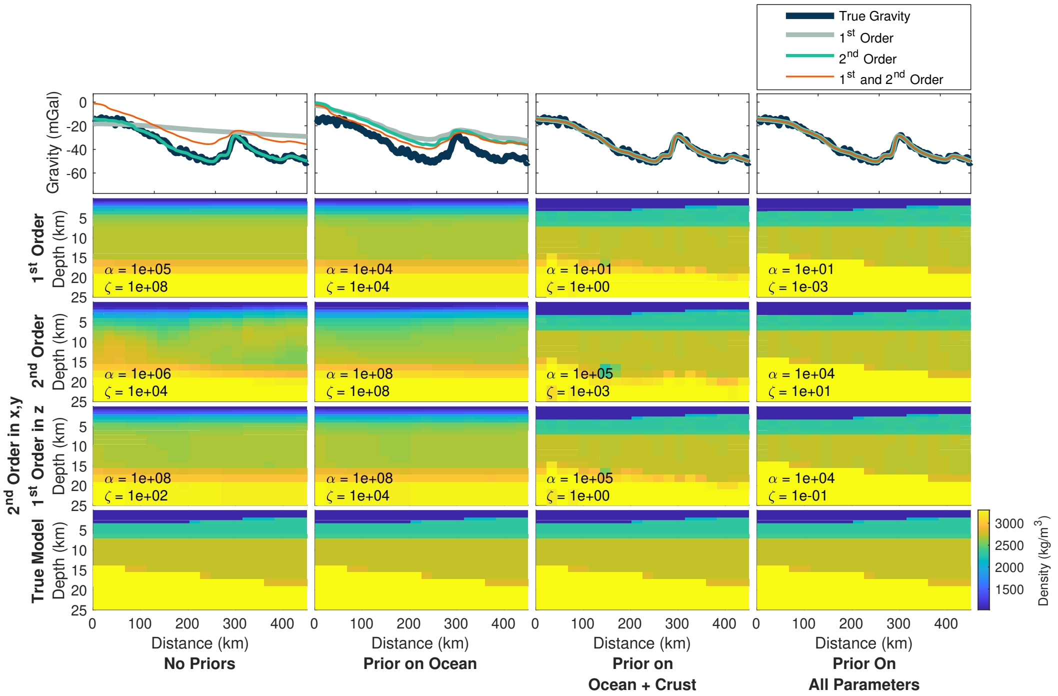

Figure A.6: Representative cross-section in the y-direction of the inversion results for α and ζ combinations that produced the minimum MAE on the model parameters for each of the regularization order and prior combinations, as determined by comparing the test results depicted in Figures A.1-A.4. **Row 1**: gravity profiles for each of the three cases depicted in the panels below. Dark blue line: true gravity produced by the synthetic model, with noise; gray line: gravity from inversion using only first order Tikhonov; light blue line: gravity from inversion using only second order Tikhonov; orange line: gravity from inversion using second order Tikhonov in the horizontal and first order in the vertical. **Row 2**: cross-sections of the density model recovered from using only first order Tikhonov for the cases of no priors, priors only on the ocean water parameters, priors on the ocean and crustal parameters, and priors on all parameters, each with their respective minimum model parameter MAE α, ζ combinations. **Row 3**: cross-sections of the density model recovered from using only second order Tikhonov for each of the different prior cases. **Row 4**: cross-sections of the density model recovered from using a combination of first and second order Tikhonov for each of the different prior cases. **Row 5**: cross-section of true synthetic density model for comparison.

Appendix B

SUPPLEMENTARY MATERIAL FOR CHAPTER 3

B.1 Probability Distributions for Earthquake Interevent Times

The Poisson probability distribution gives the probability of observing n events in a period of time t and is given by:

$$P_n(t) = \frac{(\lambda t)^n}{n!} e^{-\lambda t}. \tag{B.1}$$

The distribution of the interevent times is the probability that the waiting time, or interval time, is less than some t, and follows the exponential distribution. This probability is the cumulative distribution function (CDF) of the interevent times: $P(\leq t) = 1 - P(> t) = CDF(t)$. The probability that t is greater than T, on the other hand, is equivalent to the probability that there are no events in time T: $P(t > T) = P(n = 0)$. This is just the Poisson distribution for n = 0,

$$P(> t) = P_0(t) = \frac{(\lambda t)^0}{0!} e^{-\lambda t} = e^{-\lambda t}. \tag{B.2}$$

Thus, the CDF of the interevent times is simply:

$$\begin{aligned} CDF(t) = P(\leq t) &= 1 - e^{-\lambda t} \\ &= 1 - e^{-t/t_o}. \end{aligned} \tag{B.3}$$

λ is the mean occurrence rate (i.e., the Poisson parameter) and can also be written as $1/t_o$, where t_o is the mean interevent time.

The derivative of the CDF gives the probability distribution of obtaining a particular interevent time for randomly distributed independent events with a given rate:

$$\begin{aligned} PDF = P(t) &= \lambda e^{-\lambda t} \\ &= \frac{e^{-t/t_o}}{t_o}. \end{aligned} \tag{B.4}$$

The Gamma distribution, as used in Figure 3.2, has a probability density function defined as:

$$P(\tau) = \frac{\beta^{-\gamma} \tau^{\gamma - 1} e^{-\tau/\beta}}{\Gamma(\gamma)}, \tag{B.5}$$

where τ is the normalized interevent time (obtained by multiplying the interevent time with the earthquake rate), γ is the shape parameter, β is the mean interevent time (or $1/\lambda$, the background earthquake rate), and $\Gamma(\gamma)$ is the gamma function. The ratio of independent events over the total number of events, i.e., the mainshock fraction, is often represented by the shape parameter γ, which in the case of normalizing the interevent times, is equivalent to $1/\beta$ (Hainzl et al., 2006; Molchan, 2005).

$$\beta = \sigma_\tau^2/\bar{\tau} = \sigma_\tau^2 \tag{B.6}$$

$$\gamma = \bar{\tau}/\beta = 1/\beta \tag{B.7}$$

B.2 Equations Used in Declustering of Earthquake Catalogs

The following equations are taken from Zaliapin and Ben-Zion (2013) and are used in the declustering algorithm to classify events as either foreshocks, mainshocks, or aftershocks. The distance between earthquake i (the parent earthquake) and j (the event being considered) is given by:

$$\eta_{ij} = \begin{cases} t_{ij}(r_{ij})^{d_f}10^{-bm}, & t_{ij} > 0 \\ \infty, & t_{ij} \leq 0 \end{cases} \tag{B.8}$$

where $t_{ij} = t_j - t_i$ is the inter-occurrence time in years; $r_{ij} \geq 0$ is the spatial distance between earthquake hypocenters (or epicenters when depth is ignored) in km; d_f is the fractal dimension of the earthquake hypocenter distribution, which is often taken to be around 1.6; b is the b-value of the catalog being declustered; and m_i is the magnitude of the parent event.

The scalar distance η is best represented in terms of its space and time components, normalized by the magnitude of the parent event (Zaliapin and Ben-Zion, 2013; Zaliapin et al., 2008):

$$T_{ij} = t_{ij}10^{-qbm} \tag{B.9}$$

$$R_{ij} = (r_{ij})^{d}_{f}10^{-(1-q)bm}$$

$$\eta_{ij} = T_{ij}R_{ij} \tag{B.10}$$

$$\log_{10}\eta_{ij} = \log_{10}T_{ij} + \log_{10}R_{ij}.$$

The nearest neighbor distance for a given event j is then defined as the minimal distance among η_{ij} for all earlier events i in the catalog, and the event i that corresponds to that nearest-neighbor distance is the *nearest neighbor*, i.e., the parent, of event j. Further details of the declustering based on these equations are given in Zaliapin et al. (2008) and Zaliapin and Ben-Zion (2013).

B.3 Generation of Synthetic Earthquake Catalogs

The following material provides details on the generation of the synthetic catalogs and figures illustrating the Gutenberg-Richter distributions, aftershock sequences, and declustering results for the synthetic catalogs discussed in Chapter 3, Section 3.5.2.

Earthquake magnitudes are randomly generated according to the Gutenberg-Richter distribution, using the inverse transform method, which takes uniformly sampled random numbers and transforms them such that they take on the desired probability distribution given a known cumulative distribution function. The CDF of the Gutenberg-Richter distribution (i.e., the probability that an earthquake has a magnitude less than or equal to a given value) is:

$$F(m) = 1 - 10^{-b(m-M_c)}, \tag{B.11}$$

where M_c is the magnitude of completeness, b is the slope of the GR distribution, and m is the magnitude, here treated as a random variable. To perform the inverse transform sampling, we set m equal to $F^{-1}(u)$ and $F(F^{-1}(u))$ equal to u, where u is a vector of uniformly distributed random numbers between 0 and 1. Solving for $F^{-1}(u)$ then gives us a sequence of magnitudes distributed according to the GR law:

$$m = F^{-1}(u) = M_c - \frac{1}{b} log_{10}(1-u). \tag{B.12}$$

Earthquake magnitudes are generated using a minimum magnitude of 2 and a b-value of 1. Figures B.1 – B.10 panels (a) and (b) show the GR distribution and the earthquake sequence with time for each of the synthetic catalogs with at least one M > 7 earthquake.

The locations of the mainshocks are randomly generated according to a uniform distribution and depth is ignored, as we are only interesting in the timing of the events. Thus, we do not account for spatial details like fault geometry in the locations of the earthquakes, although a joint space-time analysis accounting for spatial non-homogeneity of real seismicity may shed light on other peculiarities of the interevent time distribution.

The interevent times of the mainshock events in the synthetic catalog are generated according to an exponential distribution for the non-stationary case with t_0 equal to the yearly varying mean interevent times for either the QTM or HYS catalogs. In the case of the QTM-based synthetics, the t_0 values are scaled up by a factor of

10. This scales down the overall earthquake rate and reduces the total number of mainshocks in order to make the synthetic catalogs a more reasonable size to work with. The timings of the events are then calculated from the cumulative sum of the interevent times. The cumulative number of mainshocks with time is shown by the gray line in Figures B.1 – B.10 panel (b). The cumulative distribution of the synthetic mainshock interevent times is determined as described previously, in the main text and in the appendix.

From these mainshocks, aftershocks are simulated using a simple-type aftershock sequence model (STAS), where each earthquake in the mainshock catalog generates its own aftershock sequence, as opposed to an epidemic-type aftershock sequence model, which allows every earthquake, including aftershocks, to generate their own aftershocks (Hainzl et al., 2006). The timing of aftershocks follows a non-stationary Poisson function, where the aftershock rate induced by an earthquake of magnitude M_i that occurred at time t_i is given by the modified Omori's law, (Hainzl et al., 2006) (Eq. B.13). K, α, c, and p are constant for all earthquakes of a given area, and are chosen in accordance with the values in Hainzl et al. (2006) and Hainzl et al. (2008). K is calculated as a function of $(n, \alpha, b, c, p, M_{min}, M_{max})$ (Eq. B.14).

$$\lambda_i(t) = \frac{K}{(c + t - t_i)^p} 10^{\alpha(M_i - M_c)} \tag{B.13}$$

$$K = \frac{n(b_a - \alpha)(p - 1)(1 - 10^{-b_a(M_{max} - M_{min})})}{b_a c^{(1-p)}(1 - 10^{\alpha(M_i - M_{min}})} \tag{B.14}$$

n, the branching parameter of the ETAS model, is set to 0.95. α is the aftershock productivity, which is set to the higher end value of 1.1. b_a is the slope of the GR distribution for a particular aftershock sequence and is set to 1 for simplicity. c is the onset time of aftershock activity and usually ranges from 1 minute to 1 hour. p is the decay rate and is set to 1.1. M_{min} is set to 2, though in reality aftershock magnitudes may be a lot smaller. We limit it to 2 to reduce the number of aftershocks and make the catalog a more reasonable size to work with. M_{max} is the mainshock magnitude, so that no aftershock can have a magnitude greater than that of the mainshock.

Aftershock magnitudes are assigned according to the Gutenberg-Richter distribution, since aftershocks, like mainshocks, are known to follow the GR law. Aftershock locations are randomly generated according to a Cauchy distribution, as aftershock locations are often modeled according to an isotropic power law or the Cauchy distribution (Hainzl et al., 2006), which simulates a similar dispersion of aftershock locations. The simulation produces a reasonable aftershock sequence, as seen in Figures B.1 – B.10 panel (c), which shows earthquake magnitudes with time and the characteristic aftershock decay in magnitude after the largest events. Figures B.1 – B.10 panel (b) likewise show the strong jump in earthquake activity following the larger mainshocks, compared to the mostly straight line that only the mainshock sequence produces.

We simulate 50 synthetic catalogs using the time-varying t_0 from the HYS catalog and 50 synthetic catalogs using the time-varying t_0 from the QTM catalog (Figure 10). Of the 50 synthetic catalogs for each case, we decluster those that have at least one M > 7 earthquake: 4 catalogs for the QTM based synthetics (Figure B.1–B.4) and 6 catalogs for the HYS based synthetics (Figures B.5–B.10). In the synthetic catalogs there are consistently more mainshocks than there are aftershocks, mostly due to the limitations on aftershock productivity in the setup of the synthetic catalogs and the use of only a STAS instead of a full ETAS model. The bi-modal nature of the clustered modes that sometimes shows up in the space-time density and histograms of the declustering is a result of there being only a few, usually no more than two, if any, larger events in the catalog, whose aftershock sequences dominate. In a real earthquake catalog, on the other hand, there would likely be many more aftershocks, due to aftershocks of aftershocks, and more complex behavior that would act to fill in the space between the two main clustered peaks, eliminating the bi-modal appearance. This is not of concern to our study, however, since we are only interested in the extraction of the mainshocks and not in the nature of the aftershock distributions themselves. Sharp edges that may appear on the clustered modes in the space-time density plots are the results of there being hard boundaries on the edges of the area in which we uniformly generate aftershock locations and at the end of the synthetic catalog in time. The interevent time distributions of the synthetic catalogs, both before and after declustering, are presented and discussed in the main text.

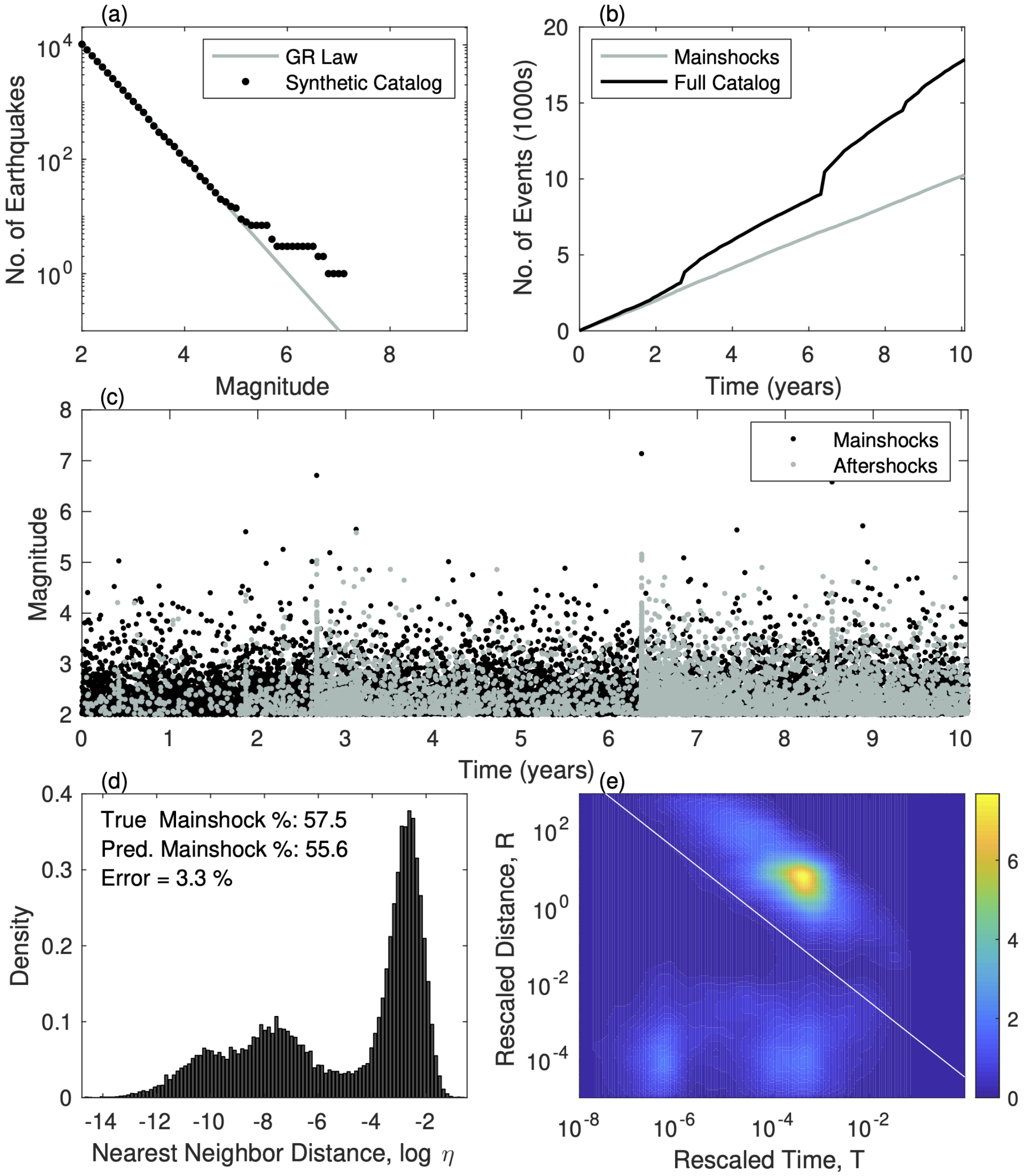

Figure B.1: 1^{st} full synthetic catalog with mainshock times based on the non-stationary t_0 of the QTM catalog and at least one M > 7 earthquake. (a) GR distribution for synthetic mainshocks. (b) Cumulative number of events with time, in 1000s, for mainshocks (light grey line) and the full catalog with aftershocks (black line). (c) Magnitudes with time, showing characteristic aftershock decay after large events. Black dots are mainshocks and grey dots are aftershocks. (d-e) Histogram and space-time density plot of the background and clustered modes obtained from the Zaliapin and Ben-Zion declustering, which predicts the correct proportion of mainshock events relative to the known mainshock fraction, with 3.3% error.

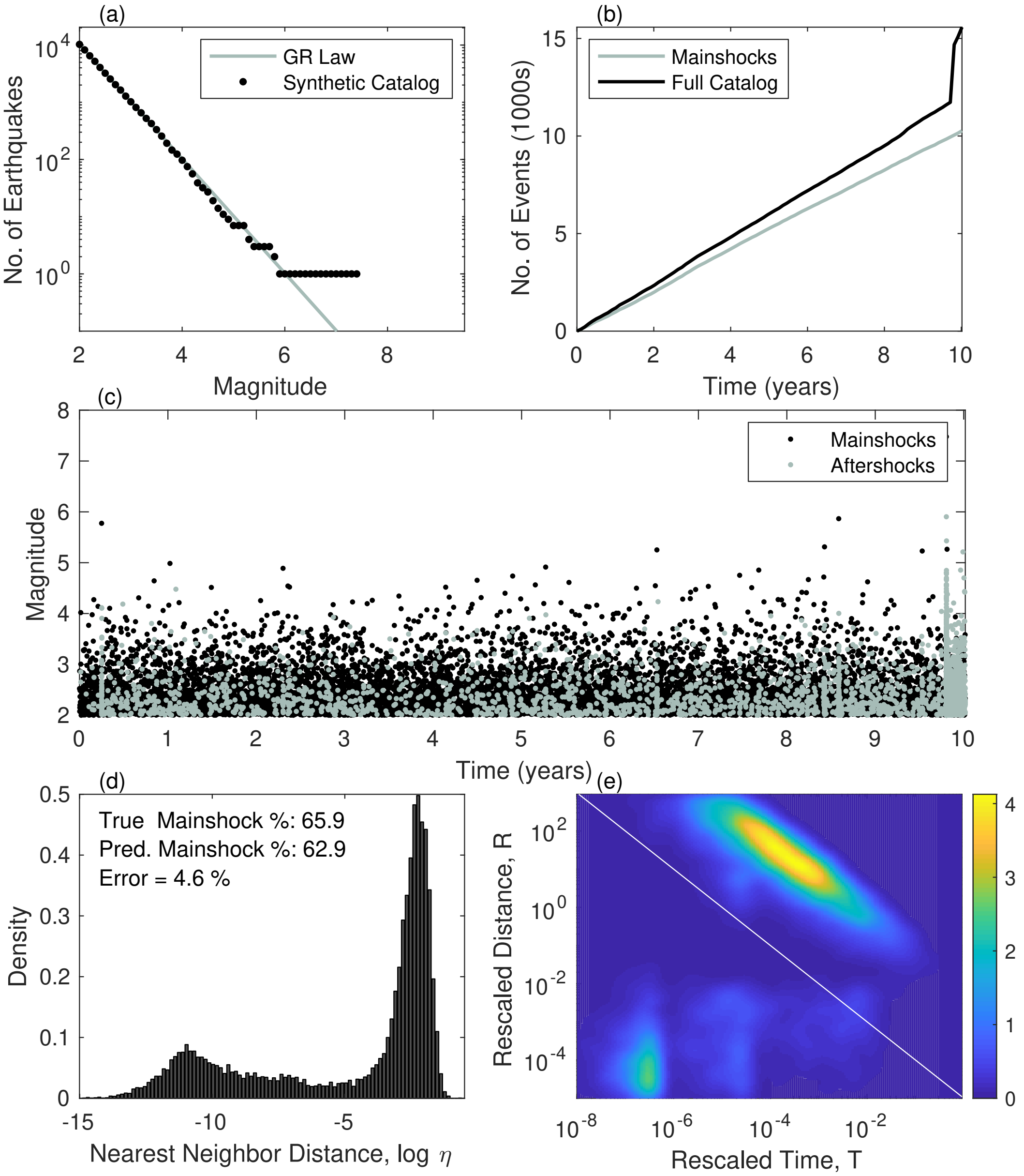

Figure B.2: 2nd full synthetic catalog with mainshock times based on the non-stationary t_0 of the QTM catalog and at least one M > 7 earthquake. (a) GR distribution for synthetic mainshocks. (b) Cumulative number of events with time, in 1000s, for mainshocks (light grey line) and the full catalog with aftershocks (black line). (c) Magnitudes with time, showing characteristic aftershock decay after large events. Black dots are mainshocks and grey dots are aftershocks. (d-e) Histogram and space-time density plot of the background and clustered modes obtained from the Zaliapin and Ben-Zion declustering, which predicts the correct proportion of mainshock events relative to the known mainshock fraction, with 4.6% error.

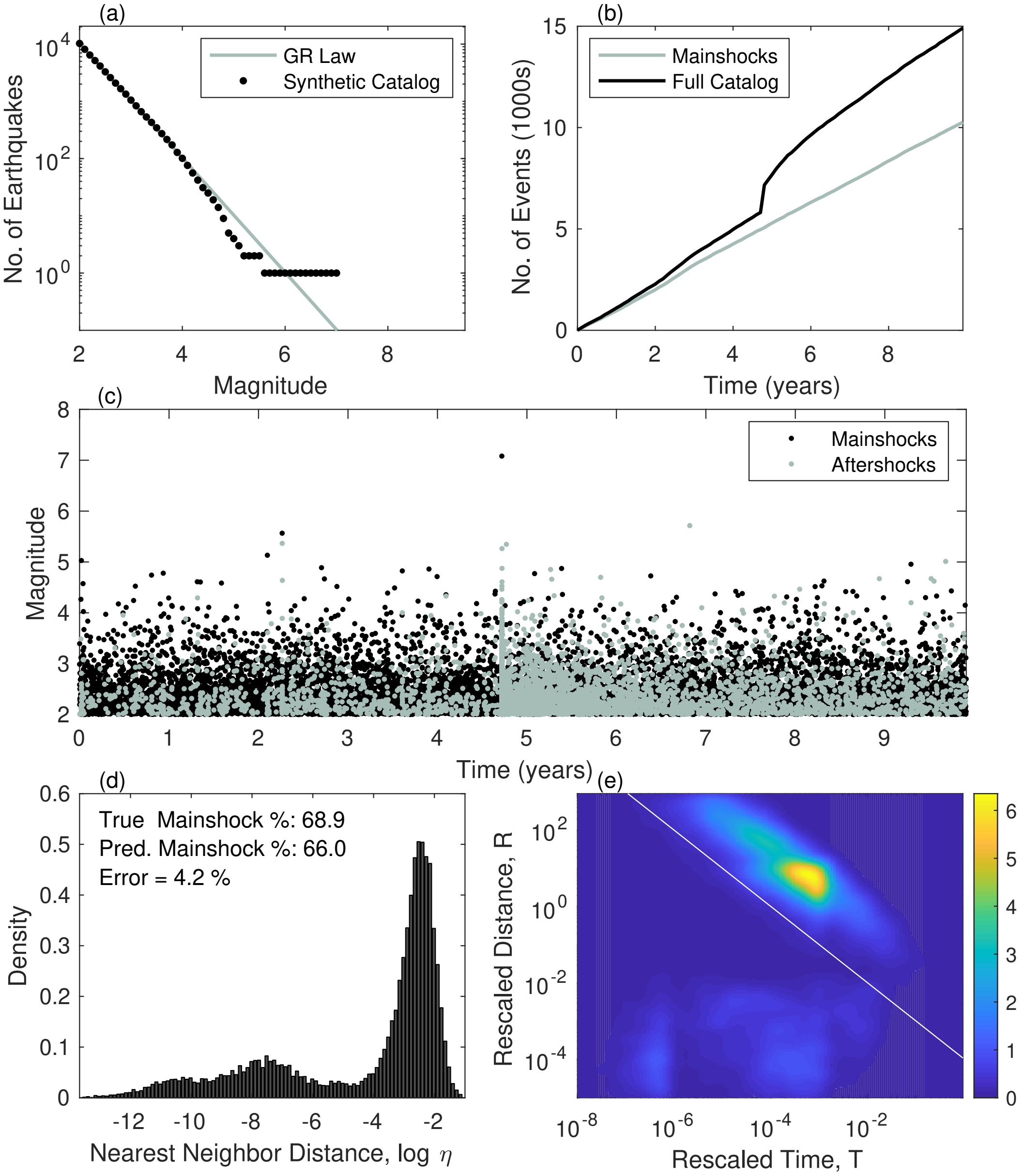

Figure B.3: 3rd full synthetic catalog with mainshock times based on the non-stationary t_0 of the QTM catalog and at least one M > 7 earthquake. (a) GR distribution for synthetic mainshocks. (b) Cumulative number of events with time, in 1000s, for mainshocks (light grey line) and the full catalog with aftershocks (black line). (c) Magnitudes with time, showing characteristic aftershock decay after large events. Black dots are mainshocks and grey dots are aftershocks. (d-e) Histogram and space-time density plot of the background and clustered modes obtained from the Zaliapin and Ben-Zion declustering, which predicts the correct proportion of mainshock events relative to the known mainshock fraction, with 4.2% error.

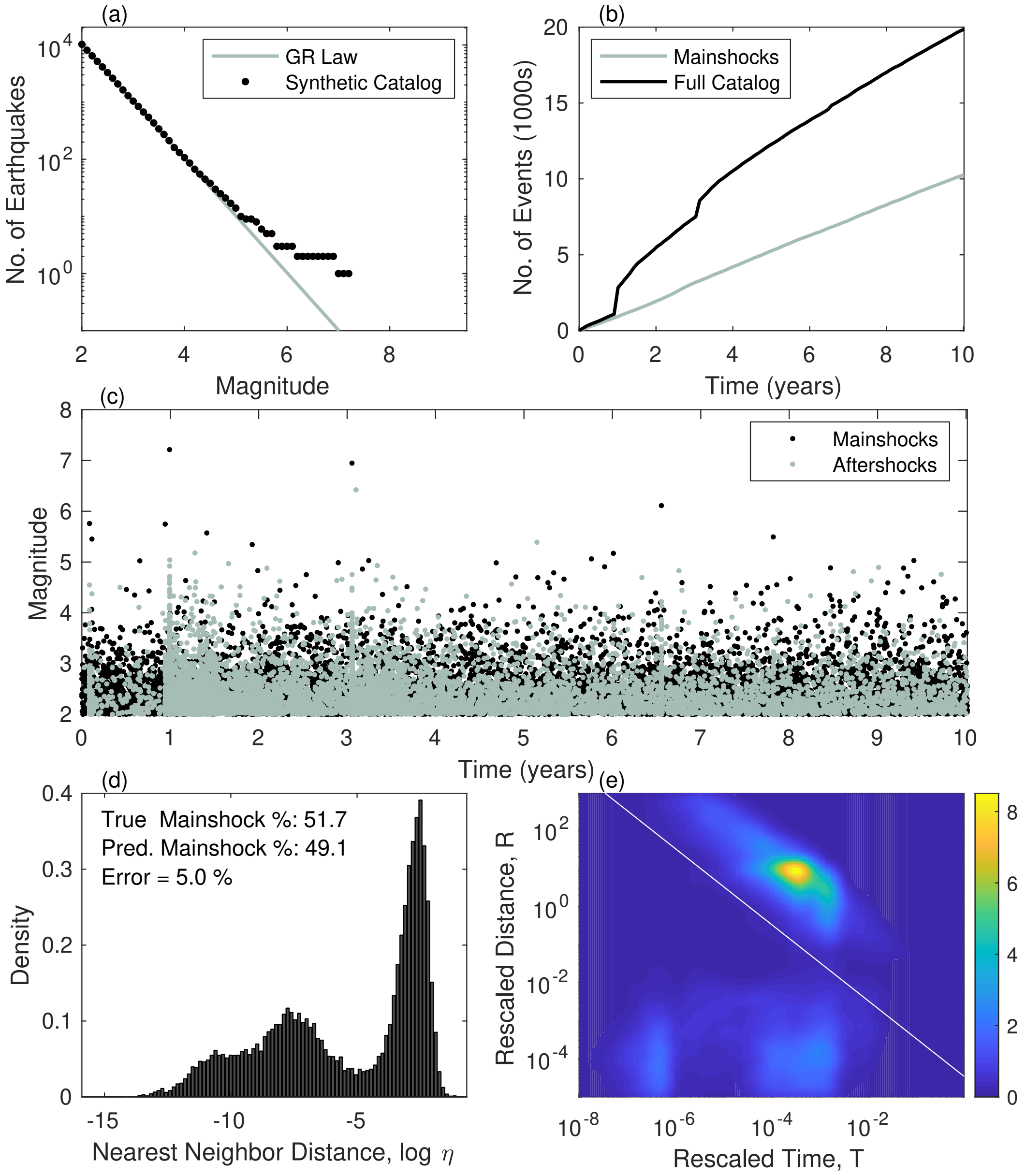

Figure B.4: 4th full synthetic catalog with mainshock times based on the non-stationary t_0 of the QTM catalog and at least one M > 7 earthquake. (a) GR distribution for synthetic mainshocks. (b) Cumulative number of events with time, in 1000s, for mainshocks (light grey line) and the full catalog with aftershocks (black line). (c) Magnitudes with time, showing characteristic aftershock decay after large events. Black dots are mainshocks and grey dots are aftershocks. (d-e) Histogram and space-time density plot of the background and clustered modes obtained from the Zaliapin and Ben-Zion declustering, which predicts the correct proportion of mainshock events relative to the known mainshock fraction, with 5% error.

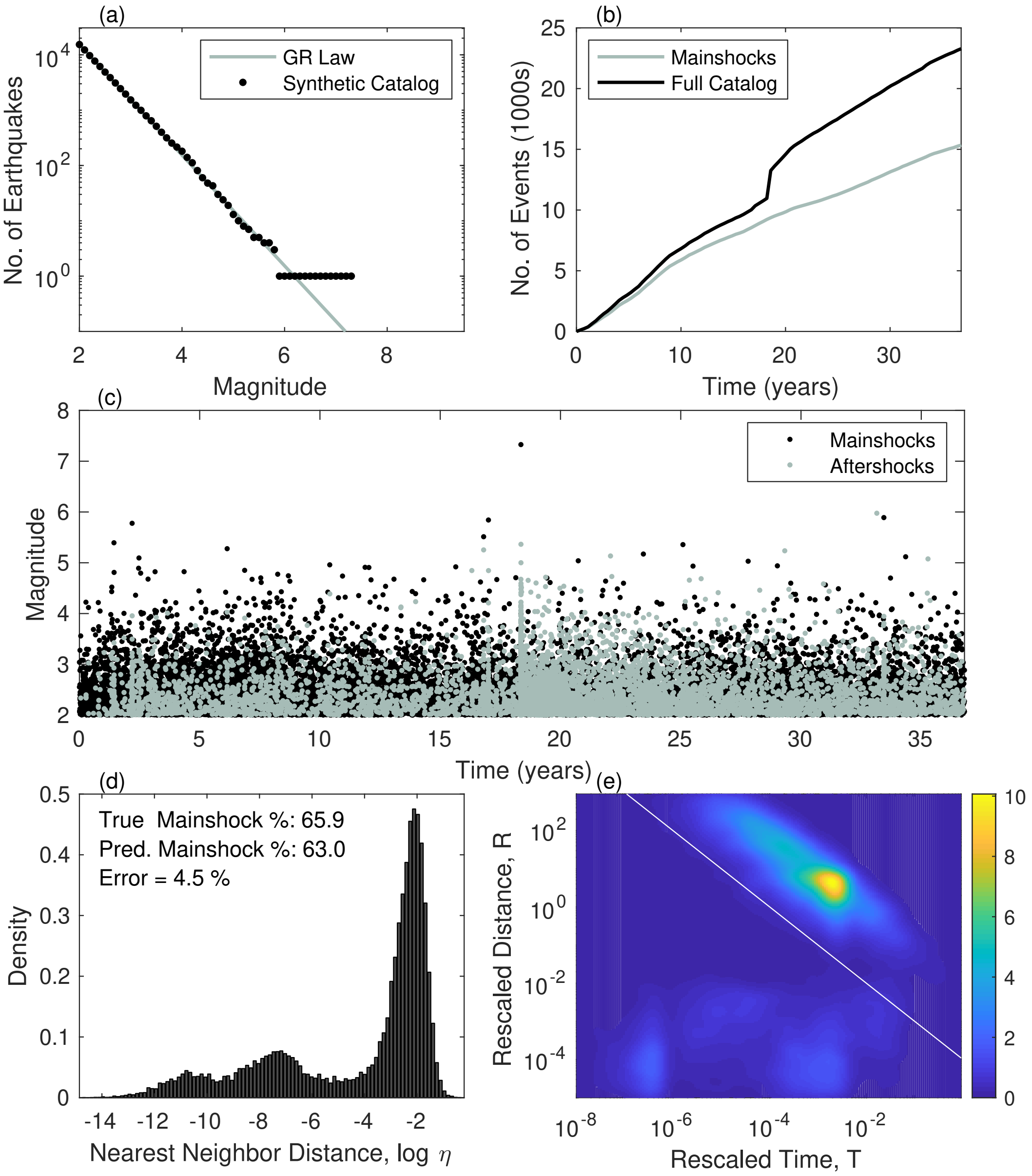

Figure B.5: 1st full synthetic catalog with mainshock times based on the non-stationary t_0 of the QTM catalog and at least one M > 7 earthquake. (a) GR distribution for synthetic mainshocks. (b) Cumulative number of events with time, in 1000s, for mainshocks (light grey line) and the full catalog with aftershocks (black line). (c) Magnitudes with time, showing characteristic aftershock decay after large events. Black dots are mainshocks and grey dots are aftershocks. (d-e) Histogram and space-time density plot of the background and clustered modes obtained from the Zaliapin and Ben-Zion declustering, which predicts the correct proportion of mainshock events relative to the known mainshock fraction, with 4.5% error.

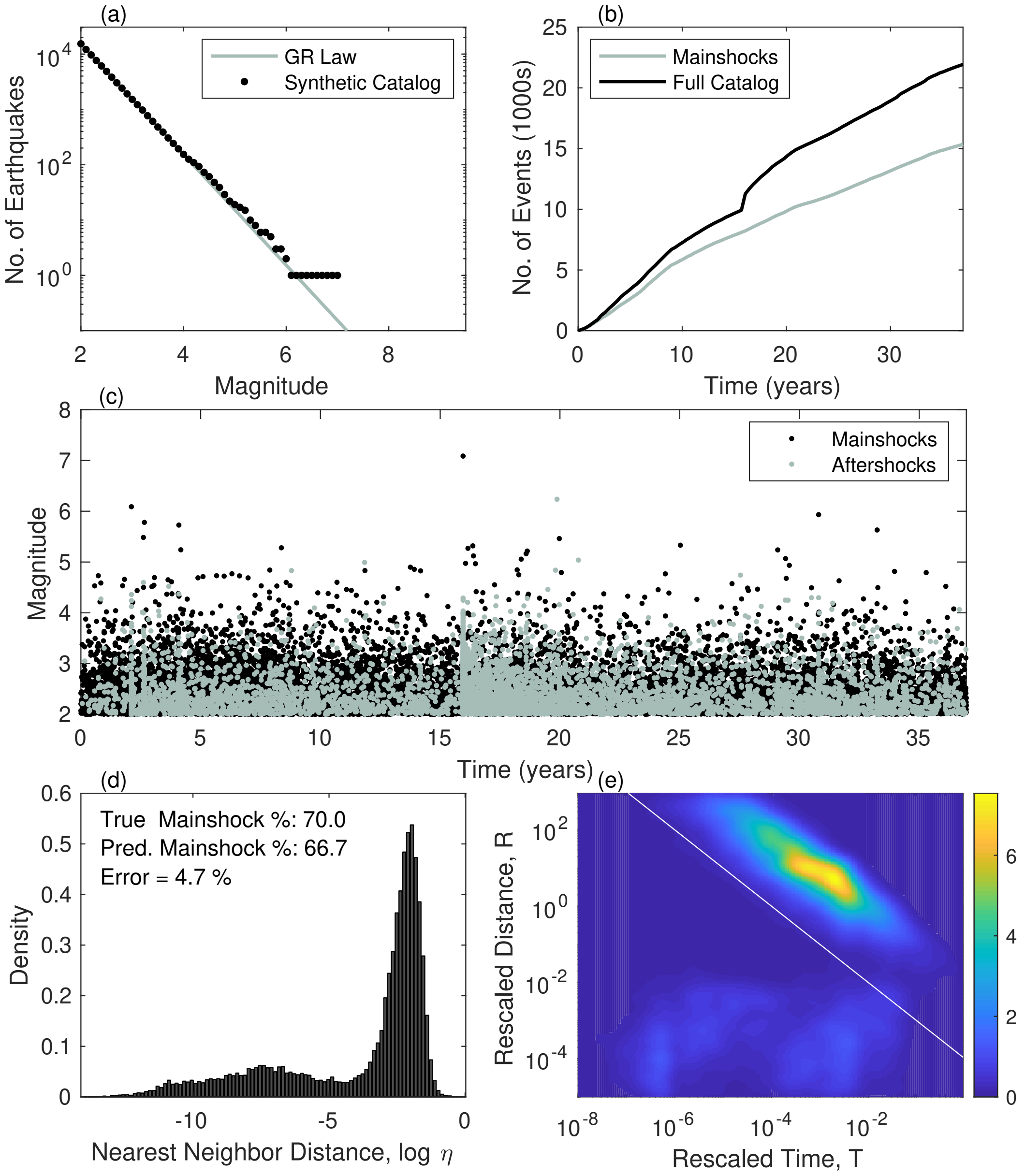

Figure B.6: 2^{nd} full synthetic catalog with mainshock times based on the non-stationary t_0 of the QTM catalog and at least one M > 7 earthquake. (a) GR distribution for synthetic mainshocks. (b) Cumulative number of events with time, in 1000s, for mainshocks (light grey line) and the full catalog with aftershocks (black line). (c) Magnitudes with time, showing characteristic aftershock decay after large events. Black dots are mainshocks and grey dots are aftershocks. (d-e) Histogram and space-time density plot of the background and clustered modes obtained from the Zaliapin and Ben-Zion declustering, which predicts the correct proportion of mainshock events relative to the known mainshock fraction, with 4.7% error.

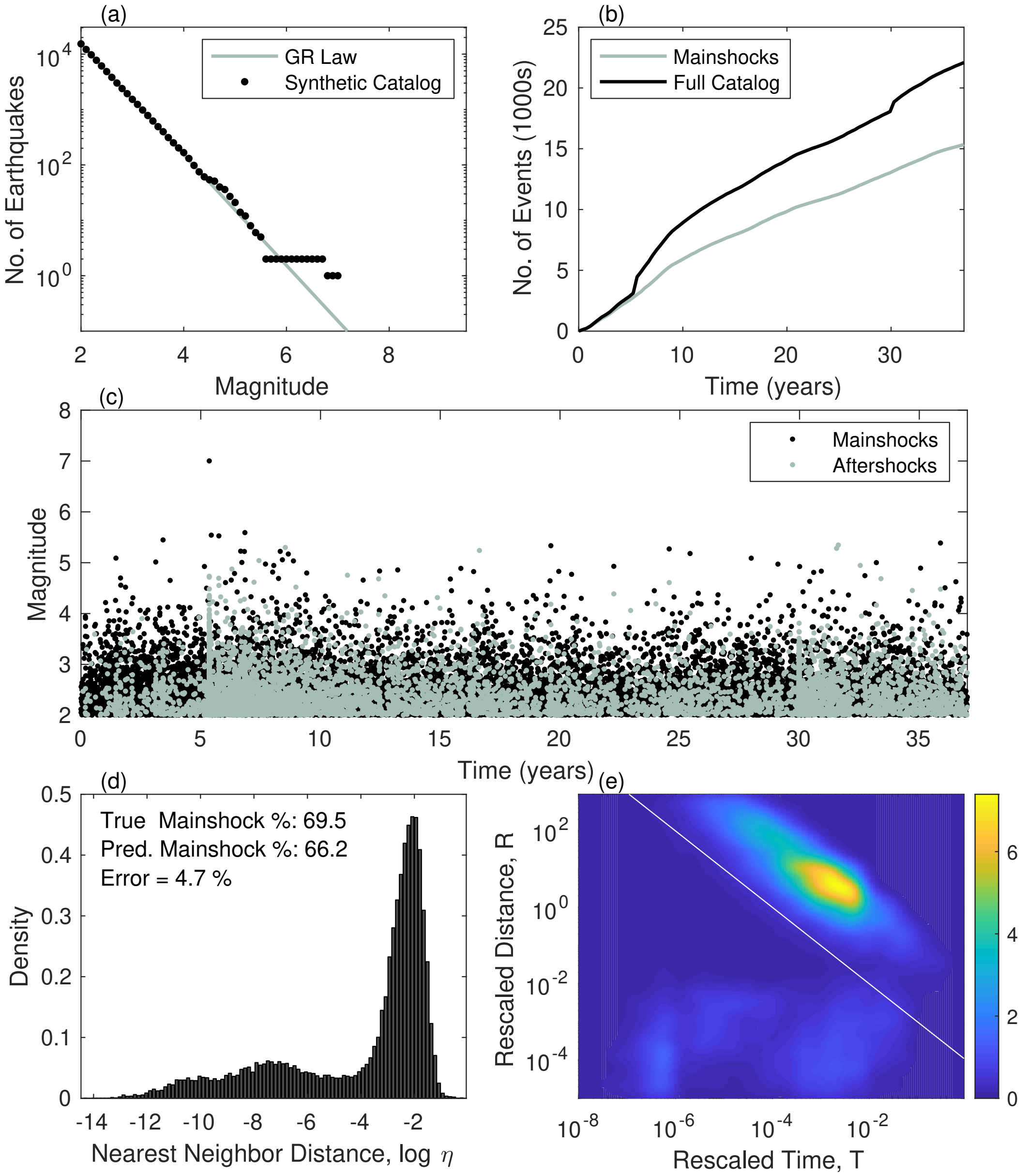

Figure B.7: 3^{rd} full synthetic catalog with mainshock times based on the non-stationary t_0 of the QTM catalog and at least one $M > 7$ earthquake. (a) GR distribution for synthetic mainshocks. (b) Cumulative number of events with time, in 1000s, for mainshocks (light grey line) and the full catalog with aftershocks (black line). (c) Magnitudes with time, showing characteristic aftershock decay after large events. Black dots are mainshocks and grey dots are aftershocks. (d-e) Histogram and space-time density plot of the background and clustered modes obtained from the Zaliapin and Ben-Zion declustering, which predicts the correct proportion of mainshock events relative to the known mainshock fraction, with 4.7% error.

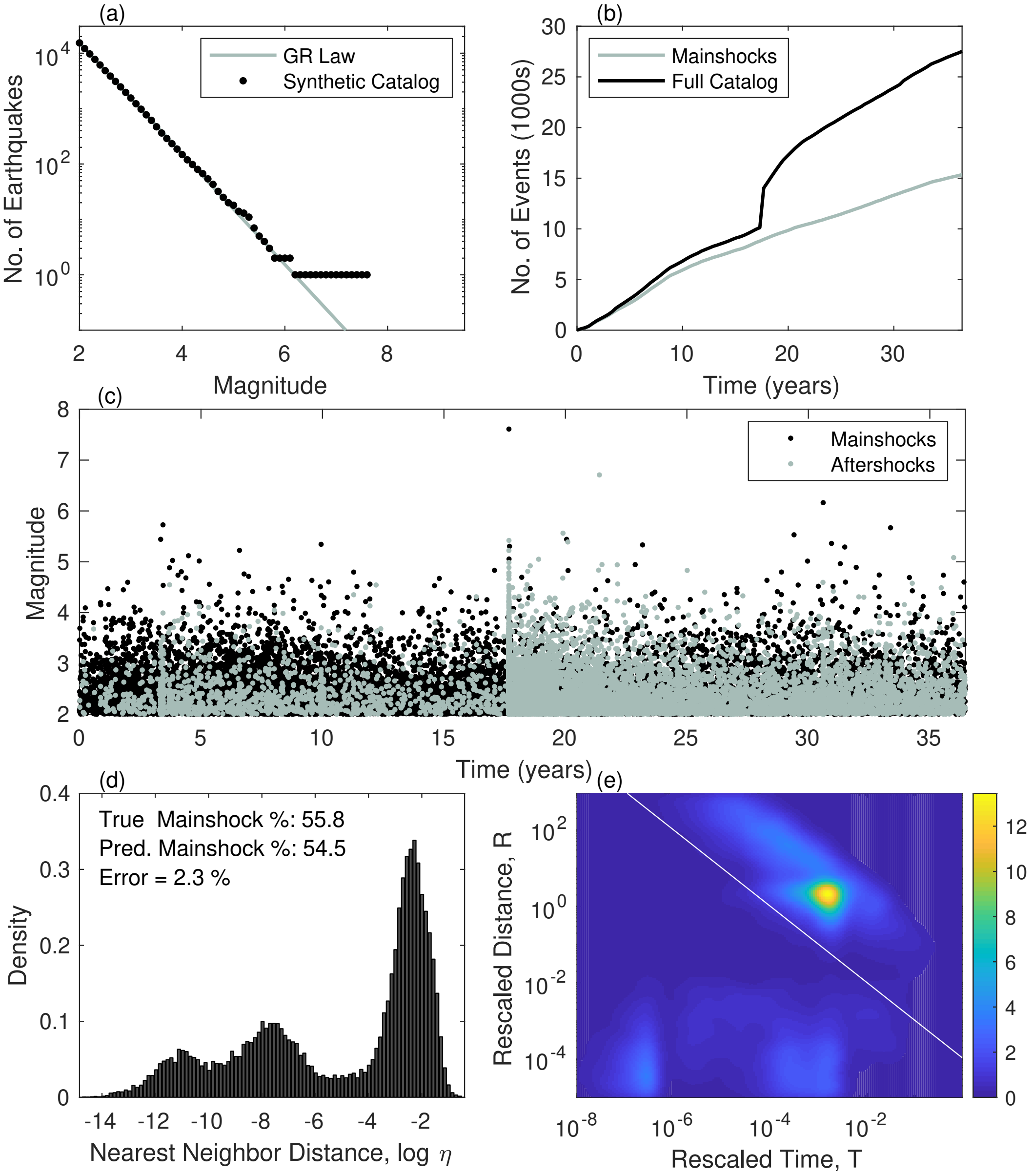

Figure B.8: 4th full synthetic catalog with mainshock times based on the non-stationary t_0 of the QTM catalog and at least one M > 7 earthquake. (a) GR distribution for synthetic mainshocks. (b) Cumulative number of events with time, in 1000s, for mainshocks (light grey line) and the full catalog with aftershocks (black line). (c) Magnitudes with time, showing characteristic aftershock decay after large events. Black dots are mainshocks and grey dots are aftershocks. (d-e) Histogram and space-time density plot of the background and clustered modes obtained from the Zaliapin and Ben-Zion declustering, which predicts the correct proportion of mainshock events relative to the known mainshock fraction, with 2.3% error.

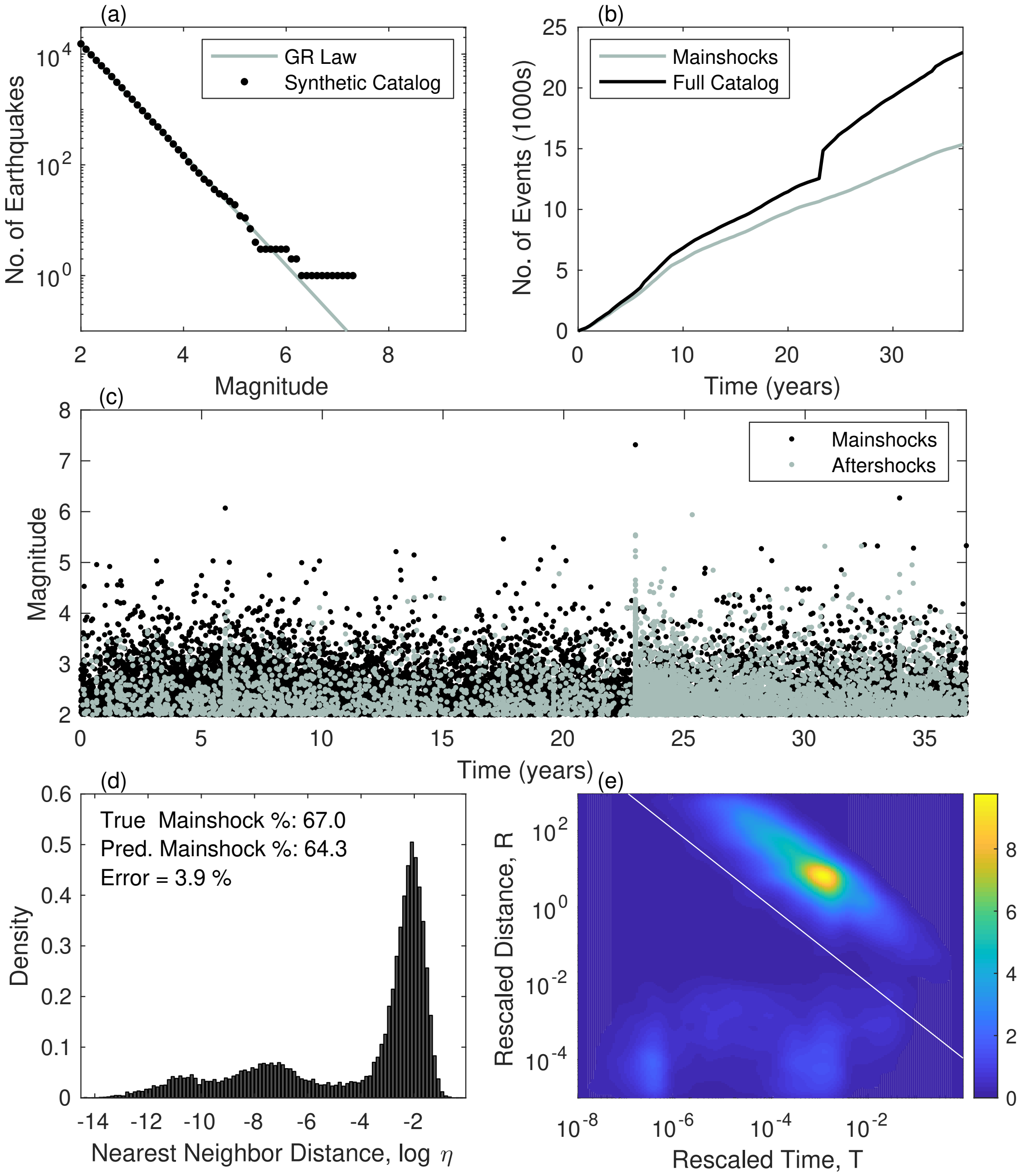

Figure B.9: 5th full synthetic catalog with mainshock times based on the non-stationary t_0 of the QTM catalog and at least one M > 7 earthquake. (a) GR distribution for synthetic mainshocks. (b) Cumulative number of events with time, in 1000s, for mainshocks (light grey line) and the full catalog with aftershocks (black line). (c) Magnitudes with time, showing characteristic aftershock decay after large events. Black dots are mainshocks and grey dots are aftershocks. (d-e) Histogram and space-time density plot of the background and clustered modes obtained from the Zaliapin and Ben-Zion declustering, which predicts the correct proportion of mainshock events relative to the known mainshock fraction, with 3.9% error.

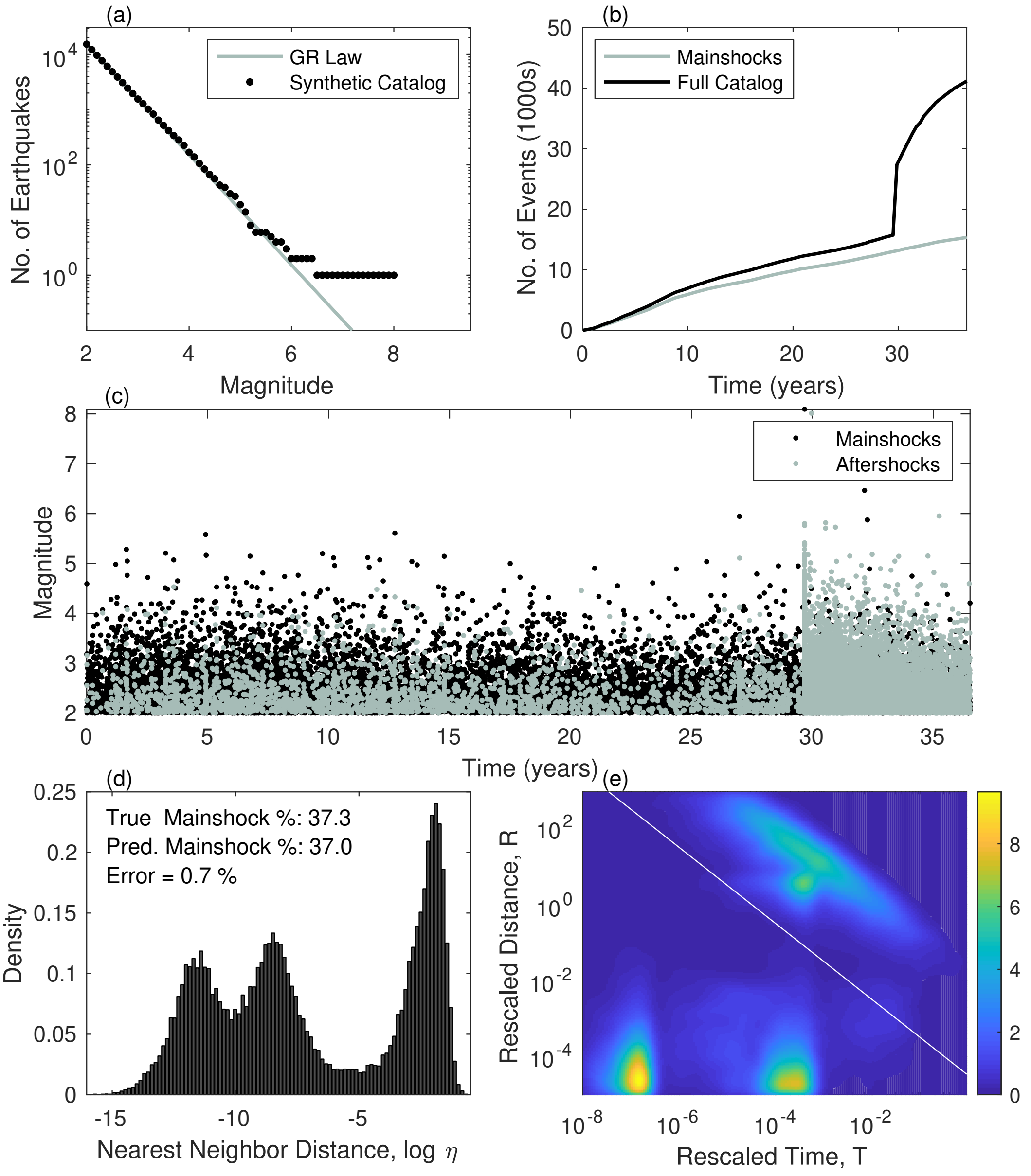

Figure B.10: 6th full synthetic catalog with mainshock times based on the non-stationary t_0 of the QTM catalog and at least one M > 7 earthquake. (a) GR distribution for synthetic mainshocks. (b) Cumulative number of events with time, in 1000s, for mainshocks (light grey line) and the full catalog with aftershocks (black line). (c) Magnitudes with time, showing characteristic aftershock decay after large events. Black dots are mainshocks and grey dots are aftershocks. (d-e) Histogram and space-time density plot of the background and clustered modes obtained from the Zaliapin and Ben-Zion declustering, which predicts the correct proportion of mainshock events relative to the known mainshock fraction, with 0.7% error.

Appendix C

SUPPLEMENTARY MATERIAL FOR CHAPTERS 4 AND 5

C.1 Derivation of the Scaling Factor of Seismic Velocity to Temperature

Seismic velocity including both anharmonic and anelastic terms is given by

$$V(P,T,Z,\omega) = V_{anh}(P,T,X)\left[1 - \frac{Q^{-1}(\omega,T)}{2\tan(\pi a/2)}\right], \tag{C.1}$$

where the anharmonic component, V_{anh}, is V_p or V_s (Eq. C.2), and the anelastic component is the term in brackets. Q is the seismic quality factor - the inverse of the seismic attenuation. Q is thought to be weakly frequency dependent, where ω^a controls the frequency dependence of attenuation and a typically ranges from 0.1 to 0.3 (Karato, 1993; Cammarano et al., 2003; Cammarano and Guerri, 2017).

$$\begin{aligned} V_p &= \sqrt{\frac{K + 4\mu/3}{\rho}} \\ Vs &= \sqrt{\frac{\mu}{\rho}} \end{aligned} \tag{C.2}$$

Q is defined differently for P- and S-waves and is primarily dependent on the a parameter and the activation enthalpy, H:

$$Q_\mu = Q_S = A\omega^a \exp(aH/RT) \tag{C.3}$$

$$Q_P = (1 - L)Q_K^{-1} + LQ_\mu^{-1} \tag{C.4}$$

$$L = (4/3)(V_S/V_P)^2. \tag{C.5}$$

The scaling factor of velocity to temperature is typically given as the inverse of the natural log of velocity with respect to temperature (Eq. C.6),

$$\delta T = \left(\frac{\partial \mathrm{ln} V}{\partial T}\right)^{-1} \frac{\delta V}{V}, \tag{C.6}$$

where V is either V_p or V_s. The derivation of $\partial \ln V/\partial T$ is as follows.

$$\begin{aligned}
\ln(V) &= \ln(V_o) + \ln\left[1 - \frac{Q^{-1}}{2\tan(\pi a/2}\right] \\
\frac{\partial \ln(V)}{\partial T} &= \frac{\partial \ln(V_o)}{\partial T} - \left[1 - \frac{(A\omega^a \exp(aH/RT))^{-1}}{2\tan(\pi a/2)}\right]^{-1}\left[\frac{aHA\omega^a \exp(aH/RT)}{(A\omega^a \exp(aH/RT))^2 2\tan(\pi a/2)RT^2}\right] \\
&= \frac{\partial \ln(V_o)}{\partial T} - \left[1 - \frac{Q^{-1}}{2\tan(\pi a/2)}\right]^{-1}\left[\frac{aHQ^{-1}}{2\tan(\pi a/2)RT^2}\right] \\
&= \frac{\partial \ln(V_o)}{\partial T} - \left[\frac{2\tan(\pi a/2) - Q^{-1}}{2\tan(\pi a/2)}\right]^{-1}\left[\frac{aHQ^{-1}}{2\tan(\pi a/2)RT^2}\right] \\
&= \frac{\partial \ln(V_o)}{\partial T} - \left[\frac{2\tan(\pi a/2)}{2\tan(\pi a/2) - Q^{-1}}\right]\left[\frac{aHQ^{-1}}{2\tan(\pi a/2)RT^2}\right] \\
&= \frac{\partial \ln(V_o)}{\partial T} - \left[\frac{aH}{RT^2}\frac{Q^{-1}}{2\tan(\pi a/2) - Q^{-1}}\right] \\
&= \frac{\partial \ln(V_o)}{\partial T} - \left[\frac{aH}{RT^2}\frac{1}{\left(\frac{2\tan(\pi a/2)}{Q^{-1}} - 1\right)}\right]
\end{aligned}$$

Assuming $Q^{-1} << 1$ as in Karato (1993), the first term in the denominator will be $>> 1$, so we drop the 1 for simplicity, which leaves us with:

$$\frac{\partial \ln(V)}{\partial T} = \frac{\partial \ln(V_o)}{\partial T} - \left[\frac{aH}{RT^2}\frac{Q^{-1}}{2\tan(\pi a/2)}\right]. \tag{C.7}$$

The first term is the derivative of the anharmonic seismic wave-speed with respect to temperature and is computed as follows, given that the bulk modulus, shear modulus, and density are each a function of temperature.

$$\begin{aligned}
\frac{\partial \ln(V_p)}{\partial T} &= \frac{\partial}{\partial T}\left[\ln\left(\frac{K + 4\mu/3}{\rho}\right)^{\frac{1}{2}}\right] \\
&= \frac{\partial}{\partial T}\left[\frac{1}{2}\left(\ln(K + 4\mu/3) - \ln(\rho)\right)\right] \\
&= \frac{1}{2}\left[\frac{1}{K + 4\mu/3}\left(\frac{\partial K}{\partial T} + \frac{4}{3}\frac{\partial \mu}{\partial T}\right) - \frac{1}{\rho}\frac{\partial \rho}{\partial T}\right] \\
&= \frac{1}{2}\frac{1}{K + 4\mu/3}\left[\frac{\partial K}{\partial T} + \frac{4}{3}\frac{\partial \mu}{\partial T} - \frac{K + 4\mu/3}{\rho}\frac{\partial \rho}{\partial T}\right] \\
&= \frac{1}{2\rho V_p^2}\left[\frac{\partial K}{\partial T} + \frac{4}{3}\frac{\partial \mu}{\partial T} - V_p^2\frac{\partial \rho}{\partial T}\right]
\end{aligned}$$

$$
\begin{aligned}
\frac{\partial \ln(V_s)}{\partial T} &= \frac{\partial}{\partial T}\left[\ln\left(\frac{\mu}{\rho}\right)^{\frac{1}{2}}\right] \\
&= \frac{\partial}{\partial T}\left[\frac{1}{2}\left(\ln(\mu) - \ln(\rho)\right)\right] \\
&= \frac{1}{2}\left[\frac{1}{\mu}\left(\frac{\partial \mu}{\partial T}\right) - \frac{1}{\rho}\frac{\partial \rho}{\partial T}\right] \\
&= \frac{1}{2\mu}\left[\frac{\partial \mu}{\partial T} - \frac{\mu}{\rho}\frac{\partial \rho}{\partial T}\right] \\
&= \frac{1}{2\rho V_s^2}\left[\frac{\partial \mu}{\partial T} - V_s^2\frac{\partial \rho}{\partial T}\right]
\end{aligned}
$$

We can summarize these two derivatives as

$$
\frac{\partial \ln(V_o)}{\partial T} = \frac{1}{2 < \rho > V_o^2}\left[\frac{\partial < M >}{\partial T} - V_o^2\frac{\partial < \rho >}{\partial T}\right], \tag{C.8}
$$

where $< M >$ and $< \rho >$ are the Voigt-Reuss-Hill averaged elastic moduli and density, where M is either $K + 4\mu/3$ for P-waves or μ for S-waves, and V_o is either V_S or V_P.

Converting V_p and V_s to temperature separately allows for independently comparing the temperature estimates from the two wave types and hence verifying the thermal origin of the velocity anomalies. A significant lack of correlation between the estimates obtained from P- and S-waves would indicate a non-thermal origin of the anomalies, but temperatures obtained from P- and S- wave velocity models tend to agree well when anelasticity it included (Goes et al., 2000). The SL8 Q-model of Anderson and Hart (1978) produces temperature estimates from Vp and Vs that agree well, as shown in the close to 1-to-1 trend in Figure C.3.

C.2 Gravitational Potential Energy from Density and Topography

C.2.1 Deriving Gravitational Potential Energy

Gravitational potential energy (GPE) differences arising from lateral variations in density and topography can give rise to variations in deviatoric stress that may help load faults within continental interiors and lead to intraplate seismicity (Ghosh et al., 2009; Ghosh et al., 2013). In order to account for the effect of GPE in our dynamic models, we need to incorporate variable crustal density and topography into CitcomS. The crustal density field will come from CRUST1.0 (Laske et al., 2013). The topography, on the other hand, requires special consideration. CitcomS uses a

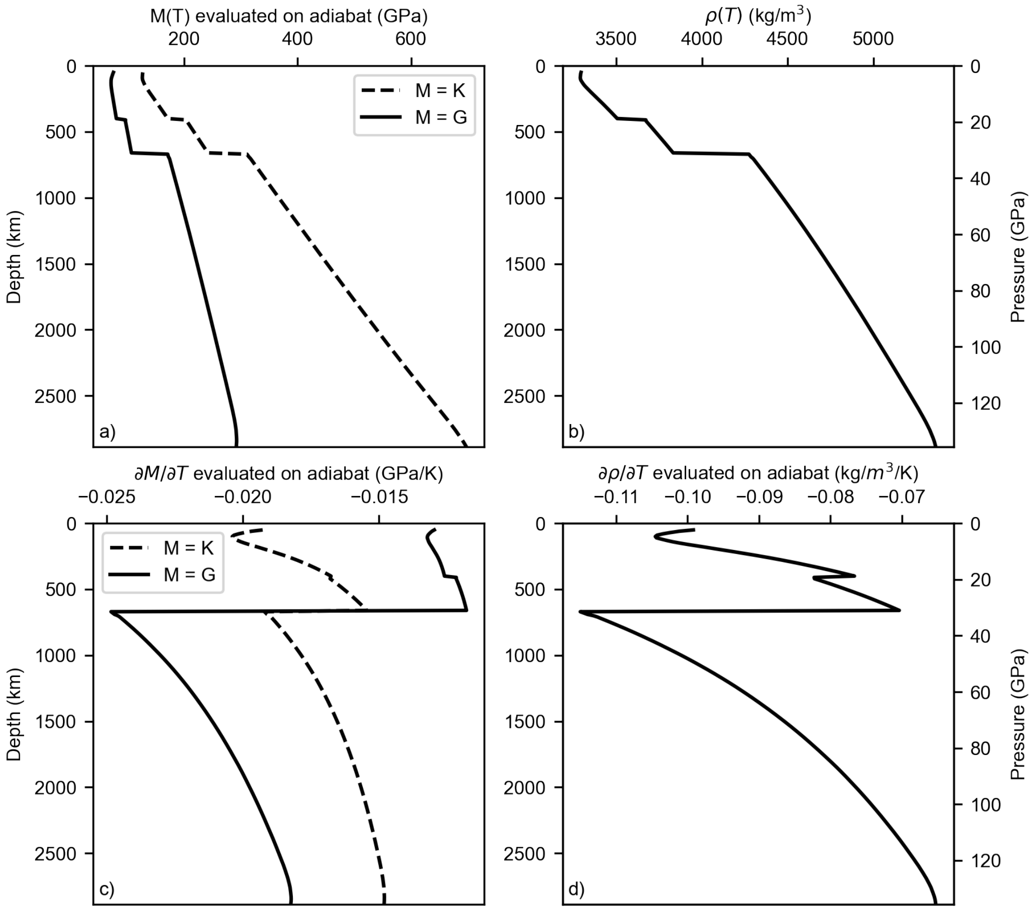

Figure C.1: Depth-dependent bulk and shear moduli and their temperature derivatives used in the velocity to temperature conversion. a) Bulk and shear moduli as a function of depth computed using BurnMan for pressures from PREM and the mineral composition given in the text. b) Density as a function of depth. c) Temperature derivatives of bulk and shear moduli with depth used in the calculation of the velocity temperature derivative. d) Temperature derivative of density with depth used in the calculation of the velocity temperature derivative.

flat surface and does not allow the user to input variable topography on a free surface. Thus, we account for the topographic contribution to the stress field by constructing an effective density model that conserves GPE. In doing so, we essentially flatten the topography into a 1 km thick layer at the surface by computing the topography's equivalent density and adding it to that layer; that is, we add a density excess to the top layer such that the GPE computed from the original model with topography is equivalent to the GPE computed from the model with no topography. This effective density can be converted to a buoyancy ratio that can be input into CitcomS.

We begin by explaining the concept of GPE and deriving its equation. GPE is the vertically integrated vertical stress down to some reference level, usually 100 km

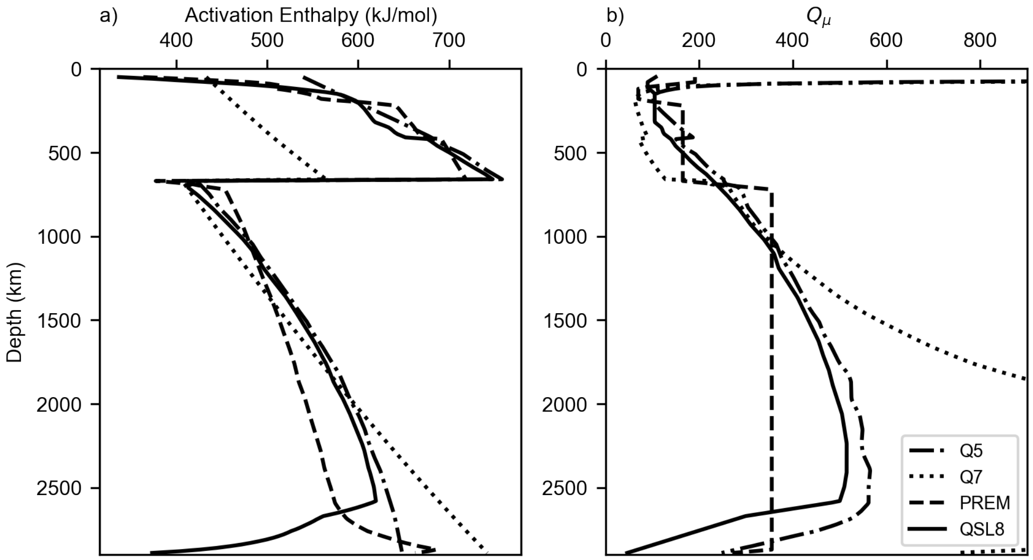

Figure C.2: Depth dependent activation enthalpy and Q models used in the velocity to temperature conversion. a) Activation enthalpy with depth for PREM (Dziewonski and Anderson, 1981) and QSL8 (Anderson and Hart, 1978), assuming $a = 0.17$ and $A = 0.056$ in the upper mantle and $a = 0.15$ and $A = 3.6$ in the lower mantle, and models Q5 and Q7 from Cammarano et al. (2003), except the latter uses a as in the curves for PREM and QSL8. In Cammarano et al. (2003) and Cammarano and Guerri (2017), $a = 0.2$. We use slightly lower values as they yeild a better fit to the seismic Q models; our prefactor A is the same as in Cammarano et al. (2003). b) Seismic quality factor Q for shear waves as a function of depth for PREM and QSL8 and Q calculated from the models Q5 and Q7.

depth, an average depth for the base of the lithosphere (Ghosh et al., 2009). To derive GPE, we can start with a simplified momentum equation

$$\nabla \cdot \boldsymbol{\sigma} + \rho \mathbf{f} = 0. \tag{C.9}$$

With GPE, we are only interested in the vertical gravitational force, so instead of the full divergence of the stress tensor and the full 3-component force vector, we can write:

$$\frac{\partial \sigma_{ij}}{\partial x_j} + \rho g_i = 0 \tag{C.10}$$

$$\frac{\partial \sigma_{zx}}{\partial x} + \frac{\partial \sigma_{zy}}{\partial y} + \frac{\partial \sigma_{zz}}{\partial z} = -\rho g_z. \tag{C.11}$$

This equation states that the gradients in the vertical stress are balanced by the force of gravity per unit volume. The GPE is the depth integrated vertical stress from a surface of variable topography down to a common-depth reference level L. Thus,

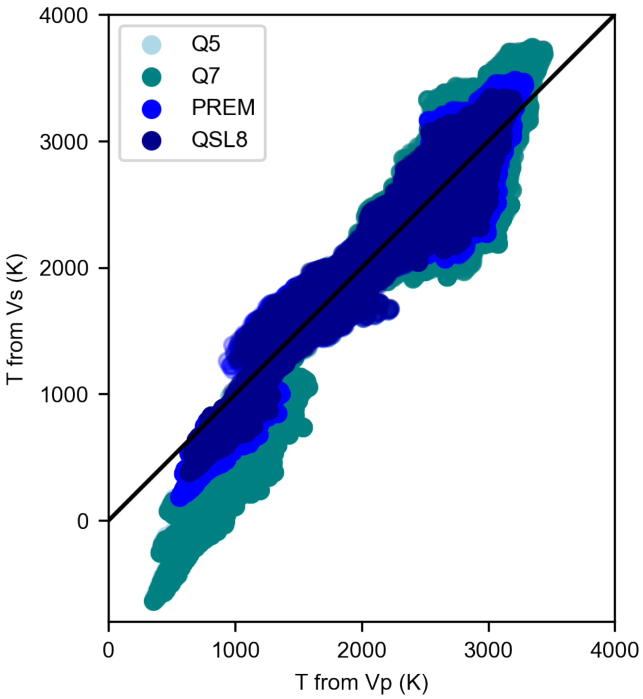

Figure C.3: Temperature computed from Vp versus temperature computed from Vs. The black line shows the 1-to-1 linear relation expected for velocity anomalies of thermal origin and for which temperature estimates include anelasticity. Of the models explored, the QSL8 model of Anderson and Hart (1978) (orange dots) shows the best agreement between Vs and Vp based temperature estimates.

we can compute depth integrals of the force balance equations down to L.

$$\int_{-h}^{L}\left[\frac{\partial\sigma_{zx}}{\partial x}+\frac{\partial\sigma_{zy}}{\partial y}+\frac{\partial\sigma_{zz}}{\partial z}\right]dz=-\int_{-h}^{L}\rho g_z dz \tag{C.12}$$

$$\underbrace{\int_{-h}^{L}\frac{\partial\sigma_{zx}}{\partial x}dz}_{\text{x term}}+\underbrace{\int_{-h}^{L}\frac{\partial\sigma_{zy}}{\partial y}dz}_{\text{y term}}+\underbrace{\int_{-h}^{L}\frac{\partial\sigma_{zz}}{\partial z}dz}_{\text{z term}}=-\int_{-h}^{L}\rho g_z dz \tag{C.13}$$

Here, we will use the thin sheet approximation to simplify the equations. This approximation states that because the horizontal dimensions over which deformation is occurring far exceed the thickness of the lithosphere, we can consider the lithosphere as a thin viscous sheet and solve for the depth averaged deviatoric stresses. This assumes that the gradients in the shear tractions (i.e., the gradients in σ_{xz} and σ_{yz} at the base of the plate are negligibly small compared to the force of gravity acting on density. Thus, the x- and y-term in Eq. C.13 drop out, leaving us with an expression in terms of only the vertical stresses and forces:

$$\int_{-h}^{L}\frac{\partial\sigma_{zz}}{\partial z}dz=\frac{\partial}{\partial z}\int_{-h}^{L}\sigma_{zz}dz=-\int_{-h}^{L}\rho g_z dz. \tag{C.14}$$

For the arbitrary case where L is just any depth z, we can write this by replacing z with a dummy variable z'.

$$\sigma_{zz}(z) = -\int_{-h}^{z} \rho(z')g dz' \tag{C.15}$$

To check our intuition, if ρ is constant, then we have

$$\sigma_{zz} = -\int_{-h}^{z} \rho(z')g dz' = -\rho g z'|_{-h}^{z} = -\rho g(z+h) = -\rho g H$$

giving $\sigma_{zz} = P = -\rho g H$, where H is the thickness of a column of crust. This is the same basic equation we use for isostasy.

The GPE is the vertically integrated vertical stress, so we have an equation of the form:

$$GPE = \overline{\sigma}_{zz} = \int_{-h}^{L} \sigma_{zz} dz = -\int_{-h}^{L}\int_{-h}^{z} \rho(z')g dz' dz. \tag{C.16}$$

To solve for GPE, we need to integrate downwards to the reference level L from each depth z. To do this, we need to flip the order of integration, which means the bounds of integration change as follows:

$$\text{For } dz': \; -h \le z' \le z \to -h \le z' \le L$$
$$\text{For } dz: \; -h \le z \le L \to z' \le z \le L.$$

This yields:

$$GPE = \overline{\sigma}_{zz} = -\int_{-h}^{L}\int_{z'}^{L} \rho(z) g dz dz'. \tag{C.17}$$

We can integrate the inner integral to get GPE as a function of depth z' and reference level L. ρ is a function of z, but because this will be solved numerically and z is just a dummy variable for depth that is physically identical to z', the integral of $\rho(z)$ is likewise a density that is function of z', $\rho(z')$:

$$\begin{aligned}\overline{\sigma}_{zz} &= \int_{-h}^{L} [\rho(z)gz]_{z'}^{L} \, dz' \\ \overline{\sigma}_{zz} &= \int_{-h}^{L} \rho(z')g(L - z')dz'.\end{aligned} \tag{C.18}$$

z' is just depth, anywhere down to L, so we can drop the primes for clarity to get our final GPE equation.

$$GPE = \overline{\sigma}_{zz} = \int_{-h}^{L} \rho(z)g(L - z)dz \tag{C.19}$$

In this final equation, L is a constant reference level, and $-h$ is the topographic height, which may vary for each point on the globe. $\rho(z)$ is the density at a given depth z, and g is the gravitational acceleration.

C.2.2 Calculating GPE, Effective Density, and Buoyancy from CRUST1.0

We calculate GPE using the crustal density model CRUST1.0 (Laske et al., 2013), a 1-degree density model of the Earth's crust including topography and sediments. The CRUST1.0 data-set consists of densities and layer-top depths for different crustal and sedimentary layers, as well as the Moho, which we discretize onto a 3D mesh at 1 km resolution in the vertical direction. We numerically compute GPE from the grid by calculating σ_{zz} for each layer and iteratively summing down to the reference level at $L = 100$ km (Eq. C.20). Numerically, GPE can be written as:

$$\overline{\sigma}_{zz} = \sum_{i=1}^{n} (L - z_i)\rho_i g \Delta h_i, \tag{C.20}$$

where z_i is taken to be the depth of the midpoint of the layer; ρ_i is the density of that layer as determined from CRUST1.0; Δh_i is the thickness of that layer, which is a constant 1 km for all layers; L is the reference level of 100 km depth; and n is the number of layers ($n = 100$). Below the Moho and down to the reference level, we use a constant mantle density of 3300 kg/m^3. The resulting total GPE is similar to that calculated in Ghosh et al. (2009) and Ghosh et al. (2013).

To create a model with "flattened topography" and crustal density that can be used within CitcomS, we must first compute a density grid that accounts for the mass of the topography. From the known topographic contribution to the GPE, we can compute the excess density that needs to be added to the top layer of the flattened model, such that the resulting GPE is equivalent to that from a model that includes topography. The GPE can be split up to compute this, such that

$$GPE = \int_{-h}^{L} (L - z)\rho(z) g dz = \int_{-h}^{0} (L - z)\rho(z) g dz + \int_{0}^{L} (L - z)\rho(z) g dz, \tag{C.21}$$

where the contribution from topography can be defined as

$$GPE_T = \int_{-h}^{0} (L - z)\rho(z) g dz. \tag{C.22}$$

We wish to account for GPE$_T$ in the first layer of our density model. This means finding a density adjustment that we add to the current density model, such that the resulting total GPE when integrated from 0 to L is the same as previously when integrated from -h to L. Thus we must solve an equation of the following form for ρ_T.

$$GPE_T = \int_{-h}^{0} (L - z)\rho(z) g dz = \int_{0}^{\Delta h} (L - z)\rho_T g dz, \tag{C.23}$$

where Δh is the depth to the base of the first layer of elements in our 3D grid. Since we are only adding the density adjustment to the first layer in our 3D grid, this numerically becomes:

$$GPE_T = \int_{-h}^{0} (L - z)\rho(z) g dz = (L - 0.5 * \Delta h)\rho_T g \Delta h, \tag{C.24}$$

where ρ_T is the excess density that we need in order conserve GPE.

$$\rho_T = \frac{GPE_T}{(L - 0.5 * \Delta h) g \Delta h}. \tag{C.25}$$

We can compute GPE_T directly from our density grid and Δh is a constant 1 km. Adding ρ_T to the top layer of the density model and recomputing GPE as before yields the equivalent GPE.

C.3 Calculation of Principal Stresses and S_{Hmax}

C.3.1 Conventions and Coordinate Systems for the CitcomS Stress Output

CitcomS outputs the components $\sigma_{\theta\theta}$, $\sigma_{\phi\phi}$, σ_{rr}, $\sigma_{\theta\phi}$, $\sigma_{\theta r}$, and $\sigma_{\phi r}$, which form the symmetric Cauchy Stress Tensor.

$$\boldsymbol{\sigma} = \begin{bmatrix} \sigma_{\theta\theta} & \sigma_{\theta\phi} & \sigma_{\theta r} \\ \sigma_{\theta\phi} & \sigma_{\phi\phi} & \sigma_{\phi r} \\ \sigma_{\theta r} & \sigma_{\phi r} & \sigma_{rr} \end{bmatrix} \tag{C.26}$$

This stress tensor is for a specific point on the Earth's surface, which serves as the origin point for a geographical coordinate system about that point. We will call this initial coordinate system $\mathbb{C}$ for Citcom. CitcomS is a spherical code and thus defines its mesh coordinates in terms of colatitude θ (x), longitude ϕ (y), and radius r (z). That is, the stress tensors are output in a south-east-up-positive (SEU) right-handed coordinate system. Thus, before we compute the principal stresses and S_{Hmax} we need to transform the stress tensor into a north-east-down-positive (NED) coordinate system for consistency with traditional methods. This can be achieved by simply rotating the stress tensor about the y (or easterly) axis using the rotation matrix (Eq. C.27).

$$\boldsymbol{T} = \begin{bmatrix} \cos\Theta & 0 & \sin\Theta \\ 0 & 1 & 0 \\ -\sin\Theta & 0 & \cos\Theta \end{bmatrix} \tag{C.27}$$

To switch north to positive x and down to positive z, we simply rotate the stress tensor by $\Theta = \pi$.

$$\hat{\boldsymbol{\sigma}} = \boldsymbol{T}\boldsymbol{\sigma}\boldsymbol{T}^T = \begin{bmatrix} \sigma_{\theta\theta} & -\sigma_{\theta\phi} & \sigma_{\theta r} \\ -\sigma_{\theta\phi} & \sigma_{\phi\phi} & -\sigma_{\phi r} \\ \sigma_{\theta r} & -\sigma_{\phi r} & \sigma_{rr} \end{bmatrix} \tag{C.28}$$

$\hat{\boldsymbol{\sigma}}$ is now the stress tensor for a point on Earth's surface (or at some given depth) that serves as the origin point for the traditional geographical coordinate system $\mathbb{G}$ with basis vectors $\hat{\boldsymbol{g}}_1 = (1, 0, 0)$, $\hat{\boldsymbol{g}}_2 = (0, 1, 0)$, and $\hat{\boldsymbol{g}}_3 = (0, 0, 1)$.

Before continuing, we must also add back the lithostatic pressure. In CitcomS, the deviatoric stress tensor is computed from the deviatoric strain rate; the *dynamic* pressure is then added back. The dynamic pressure, however, is the pressure arising from the flow itself, not the overburden pressure of the overlying rock. Inclusion of the lithostatic pressure is not necessary for the determination of S_{Hmax} and does not affect the orientation of S_{Hmax}. However, it does affect the magnitude of the principal stresses and hence affects the magnitude of the normal stress resolved on any given fault plane. Accurately computing such normal stress is essential for computing the Coulomb failure stress on a fault; without the lithostatic component, Coulomb stresses are greatly overestimated. We compute the lithostatic pressure assuming a mean continental crustal density of 2700 kg/m^3. For consistency with the theory of the critically stressed crust (Townend and Zoback, 2000; Zoback et al., 2002), the lithostatic pressure is counteracted by the pore-fluid pressure exerted by water and other fluids in the crust so that differential stress values are such that optimally oriented faults are on the verge of slipping. Without this reduction in normal stress, lithostatic pressure is high enough that at seismogenic depths all faults are completely within the stable regime with respect to the Coulomb failure criterion. Thus, we calculate our lithostatic pressure as

$$P_{lith} = (1 - \lambda)\rho g z, \tag{C.29}$$

where λ is the pore-fluid factor and z is the depth of the nodal layer. We use a λ of 0.6, which is consistent with values previously used for conditions of fault slip in intraplate regions like Canada (Zoback, 1992; Rimando and Peace, 2021). The full stress tensor then becomes

$$\hat{\boldsymbol{\sigma}}_T = \hat{\boldsymbol{\sigma}} - P_{lith}\delta_{ij}. \tag{C.30}$$

Note that we subtract the lithostatic pressure. This is in keeping with the negative-in-compression convention assumed by CitcomS, which is consistent with the fluid mechanics convention and therefore appropriate for a mantle convection code. However, for calculating S_{Hmax} and analyzing the Coulomb stress on faults, we want to use the rock mechanics convention of positive-in-compression. To do so, we multiply the stress tensor by -1. Thus, our final stress tensor with which we perform the following calculations is

$$\hat{\boldsymbol{\sigma}}_T^+ = \begin{bmatrix} -\sigma_{\theta\theta} + P_{lith} & \sigma_{\theta\phi} & -\sigma_{\theta r} \\ \sigma_{\theta\phi} & -\sigma_{\phi\phi} + P_{lith} & \sigma_{\phi r} \\ -\sigma_{\theta r} & \sigma_{\phi r} & -\sigma_{rr} + P_{lith} \end{bmatrix}. \tag{C.31}$$

C.3.2 Computing S_{Hmax}

To compute S_{Hmax}, we first solve the eigenvalue problem to get the principal stresses $(\sigma_1, \sigma_2, \sigma_3)$ and their directions $(\hat{s}_1 = (s_{1N}, s_{1E}, s_{1Z})$, $\hat{s}_2 = (s_{2N}, s_{2E}, s_{2Z})$, and $\hat{s}_3 = (s_{3N}, s_{3E}, s_{3Z})$. This is done for each of our stress tensors using the standard python Numpy linear algebra eigenvalue solver. Let $\mathbb{S}$ be the principal stress coordinate system where the shear stresses vanish and the stress tensor is diagonal with the eigenvalues on the diagonal. We get such a representation by diagonalizing the stress tensor using the eigenvectors as a transformation matrix:

$$\boldsymbol{A} = \begin{bmatrix} \hat{s}_1 \cdot \hat{\boldsymbol{g}}_1 & \hat{s}_1 \cdot \hat{\boldsymbol{g}}_2 & \hat{s}_1 \cdot \hat{\boldsymbol{g}}_3 \\ \hat{s}_2 \cdot \hat{\boldsymbol{g}}_1 & \hat{s}_2 \cdot \hat{\boldsymbol{g}}_2 & \hat{s}_2 \cdot \hat{\boldsymbol{g}}_3 \\ \hat{s}_3 \cdot \hat{\boldsymbol{g}}_1 & \hat{s}_3 \cdot \hat{\boldsymbol{g}}_2 & \hat{s}_3 \cdot \hat{\boldsymbol{g}}_3 \end{bmatrix} = \begin{bmatrix} s_{1N} & s_{1E} & s_{1Z} \\ s_{2N} & s_{2E} & s_{2Z} \\ s_{3N} & s_{3E} & s_{3Z} \end{bmatrix}, \tag{C.32}$$

leading to the stress tensor in the principal stress coordinate system

$$\boldsymbol{S} = (\boldsymbol{A}^T)^{-1}\hat{\boldsymbol{\sigma}}_T^+\boldsymbol{A}^T = \begin{bmatrix} \sigma_1 & 0 & 0 \\ 0 & \sigma_2 & 0 \\ 0 & 0 & \sigma_3 \end{bmatrix}. \tag{C.33}$$

To determine S_{Hmax}, we first define an arbitrary vertical plane in the geographic coordinate system $\mathbb{G}$ using its unit normal vector: $\hat{\boldsymbol{n}}_{\mathbb{G}} = (n_N, n_E, n_Z) = (\cos\alpha, \sin\alpha, 0)$, where α is the normal's azimuthal angle measured clockwise from north. $\hat{\boldsymbol{n}}_{\mathbb{G}}$ is the direction of horizontal stress and its azimuth α is the S_{Hmax} orientation that we seek to find. $\hat{\boldsymbol{n}}_{\mathbb{G}}$ must first be represented in the principal stress coordinate system by means of the transformation matrix $\boldsymbol{A}$:

$$\hat{\boldsymbol{n}}_{\mathbb{S}} = \boldsymbol{A}\hat{\boldsymbol{n}}_{\mathbb{G}} = \begin{bmatrix} s_{1N}n_N + s_{1E}n_E \\ s_{2N}n_N + s_{2E}n_E \\ s_{3N}n_N + s_{3E}n_E \end{bmatrix}. \tag{C.34}$$

Thus, with both the normal vector and the stress tensor now in the principal stress coordinate system, the normal stress acting on the arbitrary vertical plane of interest is

$$\begin{aligned} \boldsymbol{s}_n &= (\hat{\boldsymbol{n}}_{\mathbb{S}}^T \boldsymbol{S} \hat{\boldsymbol{n}}_{\mathbb{S}})\hat{\boldsymbol{n}}_{\mathbb{S}} \\ &= [\sigma_1(s_{1N}n_N + s_{1E}n_E)^2 + \sigma_2(s_{2N}n_N + s_{2E}n_E)^2 + \sigma_3(s_{3N}n_N + s_{3E}n_E)^2]\hat{\boldsymbol{n}}_{\mathbb{S}} \\ &= S_n \hat{\boldsymbol{n}}_{\mathbb{S}}, \end{aligned} \tag{C.35}$$

where S_n is the S_{Hmax} magnitude.

To find the direction of the maximum horizontal stress, we differentiate the magnitude S_n with respect to α, and setting equal to zero, solve for α. This gives us

$$\begin{aligned} \frac{\partial S_n}{\partial \alpha} &= [\sigma_1(s_{1E}^2 - s_{1N}^2) + \sigma_2(s_{2E}^2 - s_{2N}^2) + \sigma_3(s_{3E}^2 - s_{3N}^2)]\sin 2\alpha \\ &\quad + 2[\sigma_1 s_{1N}s_{1E} + \sigma_2 s_{2N}s_{2E} + \sigma_3 s_{3N}s_{3E}]\cos 2\alpha \end{aligned} \tag{C.36}$$

$$\tan 2\alpha = \frac{2(\sigma_1 s_{1N}s_{1E} + \sigma_2 s_{2N}s_{2E} + \sigma_3 s_{3N}s_{3E})}{\sigma_1(s_{1N}^2 - s_{1E}^2) + \sigma_2(s_{2N}^2 - s_{2E}^2) + \sigma_3(s_{3N}^2 - s_{3E}^2)}. \tag{C.37}$$

The second derivative determines whether α yields the minimum or maximum horizontal stress.

$$\begin{aligned} \frac{\partial^2 S_n}{\partial \alpha^2} &= 2[\sigma_1(s_{1E}^2 - s_{1N}^2) + \sigma_2(s_{2E}^2 - s_{2N}^2) + \sigma_3(s_{3E}^2 - s_{3N}^2)]\cos 2\alpha \\ &\quad - 4[\sigma_1 s_{1N}s_{1E} + \sigma_2 s_{2N}s_{2E} + \sigma_3 s_{3N}s_{3E}]\sin 2\alpha \end{aligned} \tag{C.38}$$

$$S_H = \begin{cases} \alpha & \text{if } S_n(\alpha) \text{ is a max} \\ \alpha + \frac{\pi}{2} & \text{if } S_n(\alpha) \text{ is a min} \end{cases} \tag{C.39}$$

With S_{Hmax} computed from our modeled stress tensors, we compare our results directly to those of the World Stress Map database (Heidbach et al., 2018) both across eastern North America (Figure 4.8) and for specific seismic zones (Figure C.5).

C.3.3 Coulomb Failure Stress

In order to assess how faults in intraplate settings might respond to these stresses, and in particular how those responses differ between cases with full Farallon negative-buoyancy and cases with reduced Farallon negative-buoyancy and between cases with and without low viscosity weakzones, we analyze the Coulomb failure stress on realistic faults within the different seismic zones. The Coulomb Failure Criterion states that when the shear stress on a fault exceeds a certain threshold, failure may occur, possibly initiating an earthquake. The Coulomb failure stress is defined as the shear stress minus the normal stress scaled by the friction coefficient (Eq. C.40). The normal stress here also assumes a certain pore fluid pressure that we have already accounted for in the stress tensor. The cohesion C is usually taken to be zero for pre-existing faults, as it is usually only considered when dealing with newly forming faults where the rock actually needs to break.

$$\sigma_{CFS} = \tau - (\mu\sigma_n + C) \tag{C.40}$$

One can calculate Coulomb failure stress in 2-dimensions by using the principal stresses σ_1 and σ_3 and assuming a fault oriented at some angle θ to σ_1 (Eq. C.41). For the case of optimally oriented faults, which maximize the Coulomb stress on the failure plane and which are oriented at $\beta = \tan^{-1}(1/\mu)/2$, the Coulomb failure stress is

$$\begin{aligned} \sigma_{CFS} &= \tau_\beta - \mu(\sigma_\beta - p) \\ \sigma_{CFS} &= \frac{1}{2}(\sigma_1 - \sigma_3)(\sin 2\beta - \mu\cos 2\beta) - \frac{1}{2}\mu(\sigma_1 + \sigma_3) + \mu p, \end{aligned} \tag{C.41}$$

where τ_β is the shear stress on the optimal failure plane, σ_β is the normal stress on that plane, p is the pore fluid pressure, μ is the coefficient of friction, and σ_1 and σ_3 are the maximum and minimum principal stresses, respectively.

However, a more thorough treatment is to simply resolve the full stress tensor on a fault of known orientation rather than assuming an optimally oriented one. Knowing the strike and dip of a fault plane, one can compute the shear and normal stress on that plane from the full stress tensor. To do so, one must first define the strike, dip, and normal vectors of the fault, each of which are functions of only the known strike and dip:

$$f_s = \begin{bmatrix} cos(s) \\ sin(s) \\ 0 \end{bmatrix}, \; f_d = \begin{bmatrix} -sin(s)cos(d) \\ cos(s)cos(d) \\ sin(d) \end{bmatrix}, \; f_n = \begin{bmatrix} -sin(s)sin(d) \\ cos(s)sin(d) \\ -cos(d) \end{bmatrix}. \tag{C.42}$$

With these vectors, we can compute the traction vector acting on the fault plane:

$$\boldsymbol{t} = \hat{\boldsymbol{\sigma}}_T^+ \boldsymbol{f}_n. \tag{C.43}$$

The total normal stress on the plane of the fault is then:

$$\sigma_n = \boldsymbol{t} \cdot \boldsymbol{f}_n. \tag{C.44}$$

The shear stress on the plane of the fault can be decomposed in the dip and strike directions:

$$\tau_d = \boldsymbol{t} \cdot \boldsymbol{f}_d \tag{C.45}$$

$$\tau_s = \boldsymbol{t} \cdot \boldsymbol{n}_s. \tag{C.46}$$

The total shear stress is then:

$$\tau = \sqrt{\tau_d^2 + \tau_s^2}. \tag{C.47}$$

The Coulomb Failure Criterion (CFC) is given by

$$CFC = \mu\sigma_n + C, \tag{C.48}$$

where we will set $C = 0$ as we are concerned only with the potential for seismicity on pre-existing faults.

In addition to assessing S_{Hmax} and Coulomb stress on faults, we also compute the 2nd invariant of the deviatoric stress (Eq. C.50) and deviatoric strain rate (Eq. C.49) to assess the magnitudes of these quantities and in particular how the stress magnitude changes between models with and without the Farallon slab and models with and without low viscosity weakzones.

$$\dot{\epsilon}_{II} = \sqrt{\frac{1}{2}\dot{\epsilon}_{ij}^2} = \sqrt{\frac{1}{2}(\dot{\epsilon}_{xx}^2 + \dot{\epsilon}_{yy}^2 + \dot{\epsilon}_{zz}^2) + \dot{\epsilon}_{xy}^2 + \dot{\epsilon}_{xz}^2 + \dot{\epsilon}_{yz}^2} \tag{C.49}$$

$$\sigma_{II} = \sqrt{\frac{1}{2}\sigma_{ij}^2} = \sqrt{\frac{1}{2}(\sigma_{xx}^2 + \sigma_{yy}^2 + \sigma_{zz}^2) + \sigma_{xy}^2 + \sigma_{xz}^2 + \sigma_{yz}^2} \tag{C.50}$$

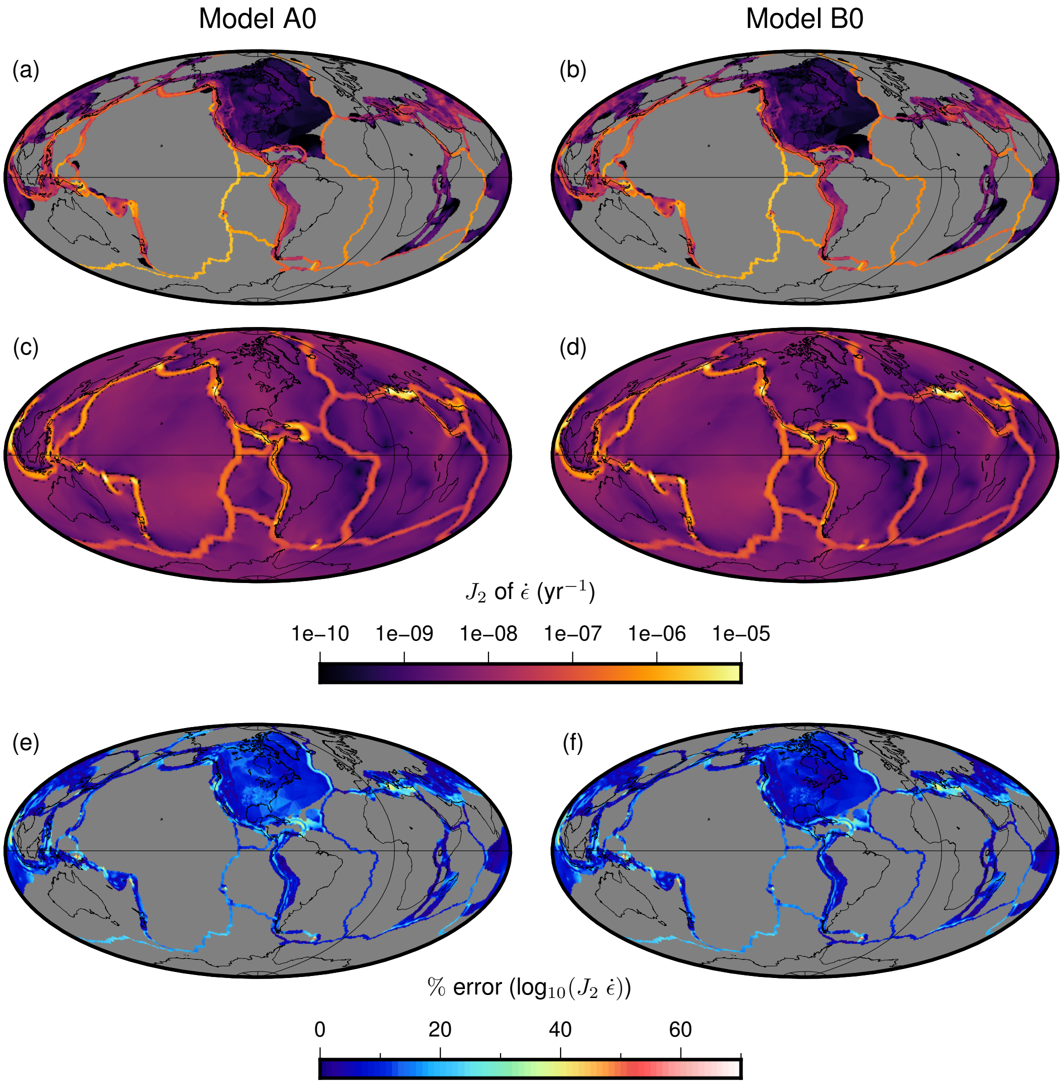

Figure C.4: Observed vs. modeled strain rates. a, b) Geodetic 2^{nd} invariant of the deviatoric strain rate from Kreemer et al. (2014) for plate boundary regions and Kreemer et al. (2018) for intraplate North America. c) 2^{nd} invariant of the deviatoric strain rate from Model A0 with the full expression of the negative buoyancy of the Farallon slab. d) 2^{nd} invariant of the deviatoric strain rate from Model B0 with the neutralized Farallon slab. e) Percent error of the log of the 2^{nd} invariant of the deviatoric strain rate between Model A0 and the geodetic strain rates (e.g., the percent error on the order of magnitude of the strain rate). f) Same as in (e) but for Model B0.

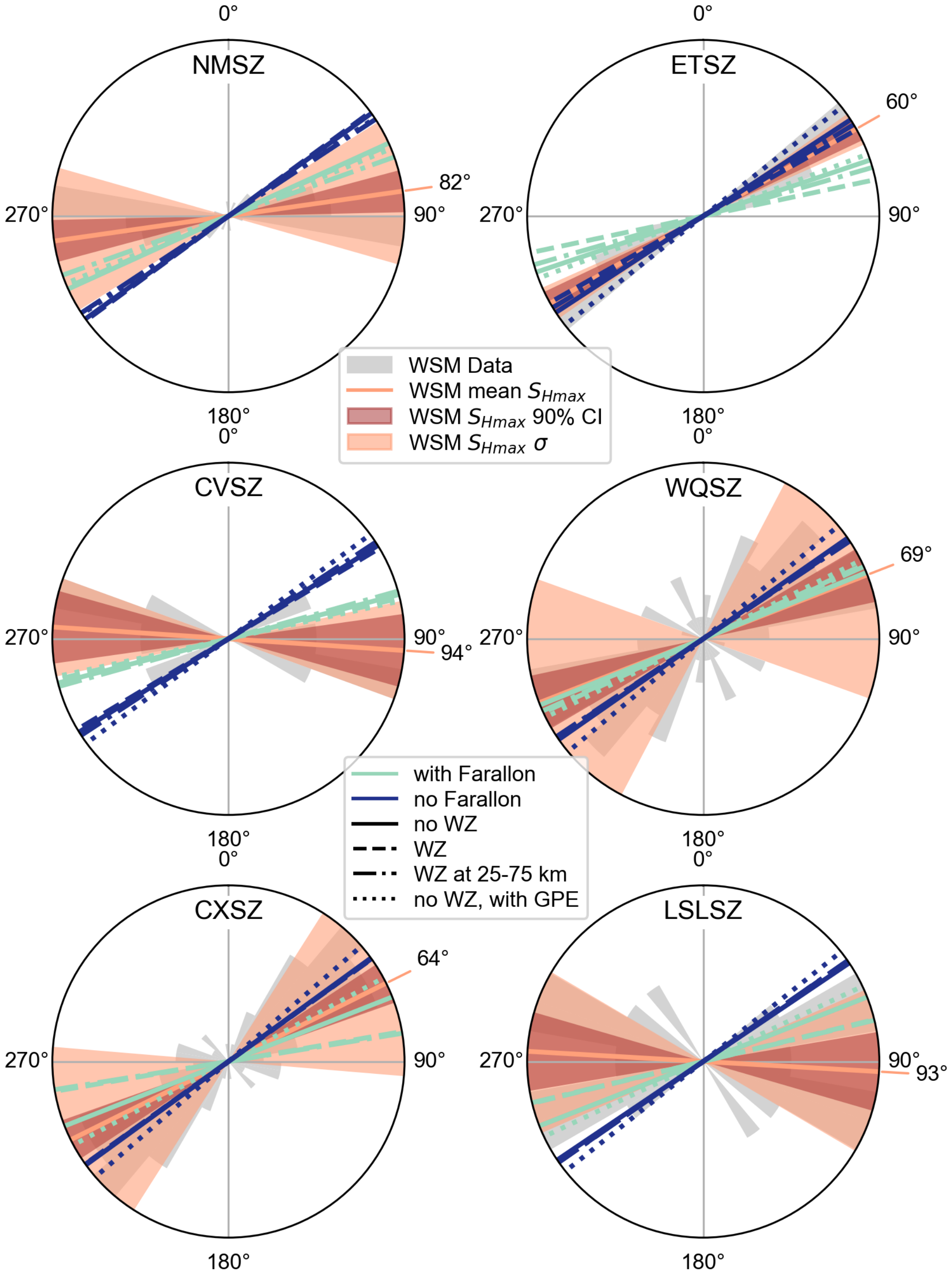

Figure C.5: S_{Hmax} orientations in different seismic zones. Gray: polar histogram of the local S_{Hmax} orientations from the WSM, binned every 10°. Orange colors: S_{Hmax} statistics from the WSM data (see legend). Mean WSM S_{Hmax} in each zone is labeled on the theta axis. Light blue lines: local S_{Hmax} from models with the Farallon slab (A0, A1, A1b, A0G). Dark blue lines: local S_{Hmax} from models with a neutralized slab (B0, B1, B1b, B0G). Line-styles differ for different weakzone cases (see legend). NMSZ: New Madrid Seismic Zone, ETSZ: Eastern Tennessee Seismic Zone, CVSZ: Central Virginia Seismic Zone, WQSZ: Western Quebec Seismic Zones, CXSZ: Charlevoix Seismic Zone, LSLSZ: Lower Saint Lawrence Seismic Zone.

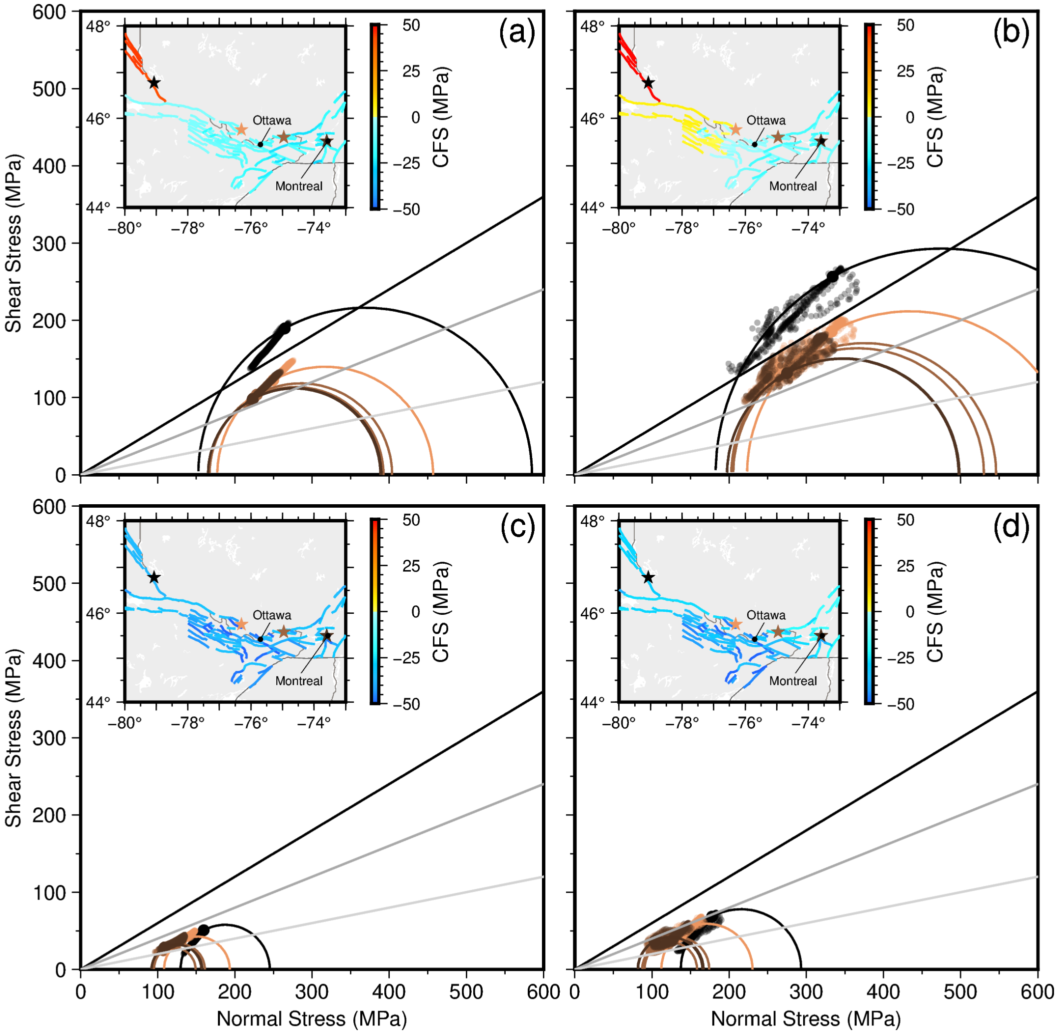

Figure C.6: Mohr circles (main plot) and Coulomb failure stress (map inset) for faults in the WQSZ, calculated assuming a $\mu = 0.55$. Fault locations from Rimando and Peace (2021) and Lamontagne et al. (2020). Fault strikes approximated using the best fitting great circle through the lineation. Unless otherwise specified, fault dips were assumed to be 56° (Bent et al., 2003; Rimando and Peace, 2021). Dip of the fault associated with the Timiskaming 1935 earthquake (black star) and nearby faults are from Bent (1996) (strike=146°, dip=45°). Mohr circles are drawn for four faults, using the stress tensor at the location of the corresponding star on the map: The Timiskaming fault of the M 6.1 1935 earthquake, the Rapide-du-Cheval Blanc Fault near the location of the M 6.3 1732 Montreal earthquake, the Lachute Fault (NE of Ottawa), and the Coulonge Fault (NW of Ottawa). Earthquake locations from Bent (2022) and Bent et al. (2003). Star colors correspond to Mohr circle colors. The cloud of points on each Mohr circle represent all possible stress tensors in the inset region given that fault's geometry. Black straight line is the Mohr-Coulomb failure criterion for $\mu = 0.6$; gray line is for $\mu = 0.4$; and light-gray line is for $\mu = 0.2$. (a) Results from model A0 (with Farallon, no weakzones). (b) Results from model A1 (with Farallon, with weakzones). (c) Results from model B0 (no Farallon, no weakzones). (d) Results from model B1 (no Farallon, with weakzones).

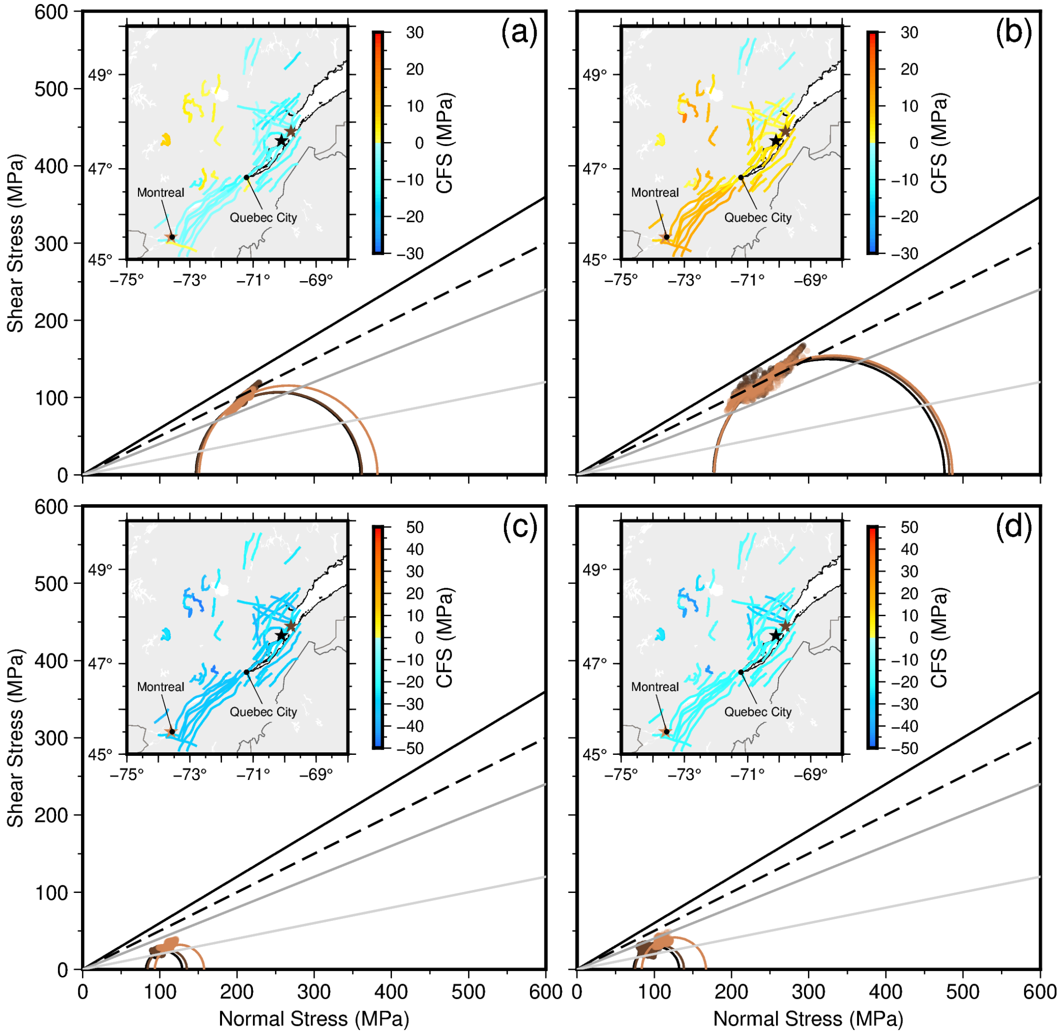

Figure C.7: Mohr circles (main plot) and Coulomb failure stress (map inset) for faults in the LSLRS, including the CXSZ, calculated assuming a $\mu = 0.5$. Fault strikes approximated for each fault location using the best fitting great circle through the lineation. Fault dips assumed to be 53°, consistent with the values of steeply dipping rift bounding normal faults for the LSLRS as reported by Bent et al. (2003) and Bent (1992). Mohr circles are drawn for the three faults closest to the epicenters of the 1663 M 7.0 and 1925 M 6.2 Charlevoix earthquakes and the M 6.3 1732 Montreal earthquake, using the fault's strike and dip and the stress tensor at the location of the corresponding star on the map. Star colors correspond to Mohr circle colors. Earthquake locations from Bent (2022). The cloud of points on each Mohr circle represent the shear vs. normal stress for all possible stress tensors in the inset region given that fault's geometry. Black straight line is the Mohr-Coulomb failure criterion for $\mu = 0.6$; dashed black line is for $\mu = 0.5$; gray line for $\mu = 0.4$; and light-gray line is for $\mu = 0.2$. (a) Results from model A0 (with Farallon, no weakzones). (b) Results from model A1 (with Farallon, with weakzones). (c) Results from model B0 (no Farallon, no weakzones). (d) Results from model B1 (no Farallon, with weakzones).

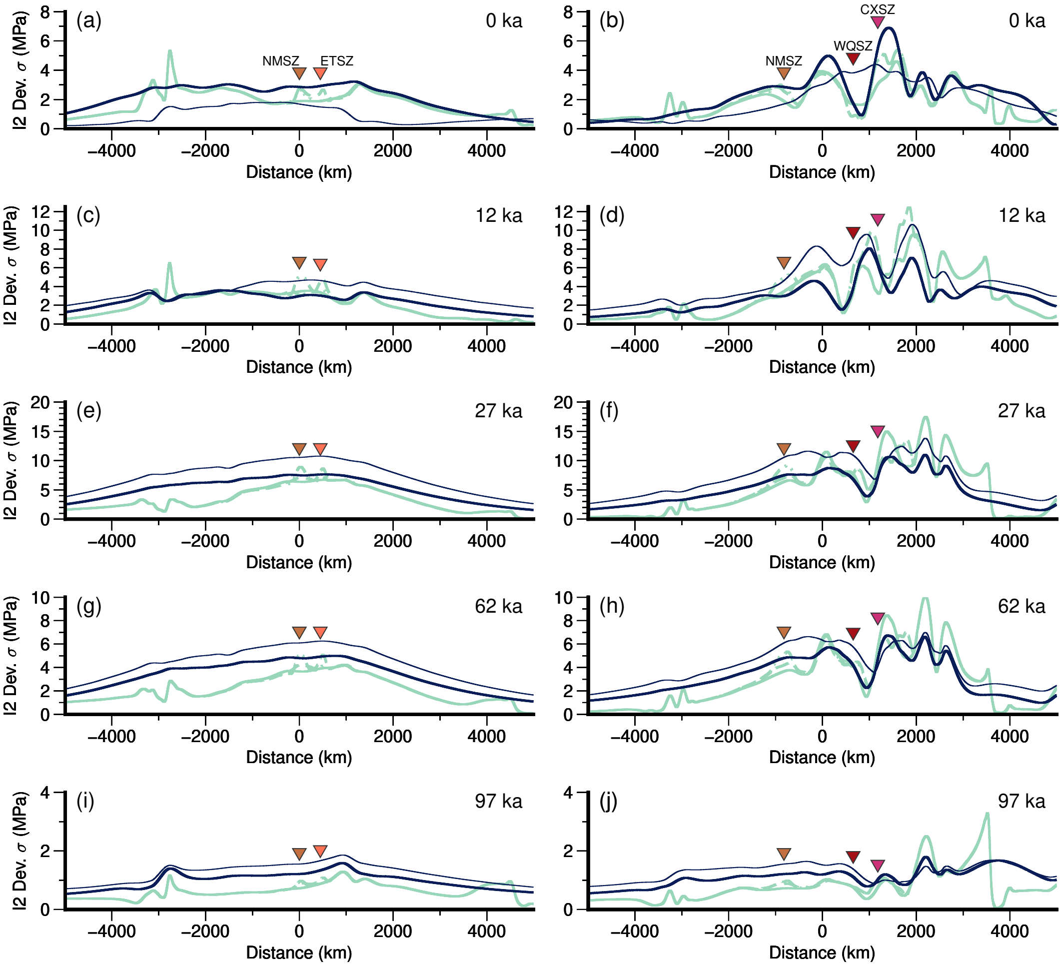

Figure C.8: Profiles of the second invariant of deviatoric stress magnitude induced by GIA for different times, pre-, syn-, and post-glaciation. Time in years before present is labeled in the upper right hand corner of each panel. Profiles are presented for models with 3D viscosity input (light green lines) with no weakzones (solid line; model GIA-A0), weakzones at different depths (dashed line; model GIA-A1), weakzones at 25-75 km depth (dashed-dotted line; model GIA-A1b), and 1D viscosity input (dark blue lines) from the radial average of model GIA-A0 (thick line; model GIA-1D-3Davg) and VM5a (thin line; model GIA-1D-VM5a). a,c,e,g,i) Stress profiles along line B-B' (see Figure 5.3 in the main text of Chapter 5 and Figure 4.4, orthographic panel in Chapter 4). New Madrid Seismic Zone (NMSZ) and Eastern Tennessee Seismic Zone (ETSZ) are labeled accordingly. b,d,f,h,j) Stress profiles along line A-A' (again, see main text). NMSZ, Western Quebec Seismic Zone (WQSZ) and Charlevoix Seismic Zone (CXSZ) are labeled accordingly.